Università degli Studi di Ferrara

DOTTORATO DI RICERCA IN
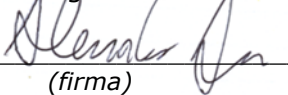## "SCIENZE DELL'INGEGNERIA"

CICLO XXVII

COORDINATORE Prof. Trillo Stefano

Positive Displacement Pumps: Pressure Modelling for Performance Analysis

Settore Scientifico Disciplinare ING-IND/13

Dottorando
Dott. Agazzi Alessandro

(firma)

Tutore
Prof. Dalpiaz Giorgio

(firma)

Anni 2012/2015

RIASSUNTO

La distribuzione della pressione all'interno di pompe volumetriche rotative varia periodicamente con la posizione del rotore; le conseguenti forze di pressione variabili rappresentano le principali fonti di vibrazioni e rumore. Questa tesi presenta diverse metodologie di modellazione per la simulazione dell'evoluzione di pressione in funzione della posizione del rotore in condizioni di lavoro, per questo tipo di pompe. Da un lato, viene sviluppato un approccio a parametri concentrati, applicato ad una pompa ad ingranaggi esterni per applicazioni automobilistiche; d'altro lato, viene studiato un approccio empirico, adottato nel caso di una famiglia di pompe a palette a cilindrata variabile.

Nel primo approccio, il volume fluido della pompa è suddiviso in volumi di controllo e viene risolto un sistema di equazioni di continuità. La metodologia di modellazione è generale e può essere applicata a qualsiasi pompa ad ingranaggi a denti diritti con profilo ad evolvente. I vari coefficienti di efflusso in regime laminare o turbolento sono stimati mediante opportune simulazioni fluidodinamiche CFD. Il modello è stato soddisfacentemente validato mediante il confronto con risultati sperimentali, in termini di efficienza volumetrica e di ripple di pressione in mandata, in differenti condizioni operative. Il modello validato ha poi permesso di svolgere un'indagine di sensibilità, utile per l'ottimizzazione di parametri progettuali e funzionali della pompa: profondità e larghezza della "Epsilon Groove", eccentricità delle ruote nel corpo pompa, caratteristiche e temperatura dell'olio. . I risultati di questa analisi saranno utili nell'ottimizzazione dell'efficienza e del comportamento dinamico.

Venendo all'approccio empirico, la modellazione della distribuzione di pressione non si basa in questo caso su leggi fisiche, ma sulla parametrizzazione di dati sperimentali: vengono individuate regole di correlazione tra le caratteristiche dell'evoluzione di pressione e i parametri geometrici e funzionali, relativamente ad una specifica

famiglia di pompe di diverse dimensioni. Come applicazione del modello empirico, è stata condotta un'analisi del regime di usura e lubrificazione nel contatto tra le palette e l'anello statorico; tale analisi è stata effettuata mediante un metodo originale basato sul modello di usura di Archard, che associa il coefficiente di usura alle forze di contatto ottenute mediante il modello empirico, al tasso di usura ed alla durezza del materiale, misurati sperimentalmente; i risultati ottenuti vengono confrontati con i risultati forniti da un modello di lubrificazione elasto-idrodinamica al fine di valutare lo spessore del meato ed il regime di lubrificazione. Questo metodo è applicato ad un caso industriale al fine di dare indicazioni per la scelta appropriata dei materiali.

Come risultato generale, entrambi gli approcci di modellizzazione producono risultati affidabili, utili per l'analisi delle eccitazioni vibro-acustiche, per l'ottimizzazione strutturale, nonché per la valutazione del regime di lubrificazione ed usura. Tuttavia si rileva che, da un lato, l'approccio a parametri concentrati permette di simulare il comportamento di pompe di diversa tipologia e di valutare l'effetto di una vasta gamma di modifiche, da prendere in considerare per l'ottimizzazione del progetto. D'altro lato, i modelli empirici sono meno flessibili rispetto ai modelli a parametri concentrati, in quanto sono applicabili solo a una famiglia di pompe; tuttavia, essi rappresentano strumenti efficaci per la R&S in ambito industriale, in quanto sono caratterizzati da tempi di sviluppo più rapidi e da un più facile impiego.

ABSTRACT

The pressure distribution inside rotary positive displacement pumps periodically varies with rotor position; the consequent variable pressure forces represent the main sources of casing vibration and noise emission. This dissertation presents different modelling methodologies for the simulation of pressure evolution in this kind of pumps, as a function of rotor position in working conditions: a lumped parameter approach is developed and applied to an external gear pump for automotive applications, while an empirical approach is studied and adopted in the case of a family of variable displacement vane pumps.

In the former approach, the fluid volume of the pump is divided in several control volumes and a system of continuity equations is solved. This modelling methodology is general and can be applied to any spur gear pump with involute profile. The flow discharge coefficients in laminar or turbulent regime are estimated by appropriate CFD simulations. The validation of the model has been satisfactorily carried out for comparison with experimental results in term of volumetric efficiency and outlet pressure ripple, in different operating conditions. Through the validated model, a sensitivity analysis has been carried out, useful for optimizing some design and operating parameters of the pump: depth and width of the "Epsilon Groove", gear eccentricity with respect to the pump casing, oil temperature and properties. The results of this analysis will be useful for the optimization of the efficiency and the dynamic behaviour.

On the other hand, the empirical approach for modelling pressure distribution is not based on physical laws, but on the parametrization of experimental data: correlation rules are established between the characteristics of the pressure evolution and the design and functional parameters of a specific family of pumps of different size. As a model application, the analysis of the wear and lubrication regime in the sliding contact between the vanes and the pressure ring

is developed; this analysis is carried out through an original methodology based on Archard's wear model, which associates the wear coefficient to the contact forces given by the empirical model, the wear rate and the material hardness, experimentally measured; the results are compared with the outcomes obtained from an EHD lubrication model in order to evaluate the film thickness and the lubrication regime. This method is applied to an industrial case in order to give indications for the proper selection of materials.

As a general result, both modelling approaches give reliable results, useful for the analysis of the vibro-acoustic excitations, the optimization of the structural design, as well as the assessment of wear and lubrication regime. It is worth noting that, on the one hand, the lumped parameter approach allows the simulation of the behaviour of pumps of different type and design and makes it possible to account for a wide range of modifications, to be considered for optimization purposes. On the other hand, empirical models are less flexible than lumped parameter models, as they are applicable only to a single family of pumps; however, they represent efficient tools for R&D in industrial environment, due to faster development time and more friendly use.

Preface

This preface is intended as a brief recap of the activities carried out during the four years of my PhD studies, when I have developed training and research activities addressing various issues in the field of Mechanics of Machines and Vibrations: modelling of pressure distribution in pumps, multi-body modelling of the dynamic behaviour of mechanical transmissions, methods for the functional design and optimization of mechanical drives and devices.

The main research issue -subject of the present PhD dissertation has concerned the development of modelling methodologies for the simulation of the variable pressure distribution in rotary positive displacement pumps, as well as applications of the models to the analysis of performances and to the functional optimization. In particular, variable displacement vane pumps for applications in machine tools and external gear pumps for applications in automotive transmission have been addressed. In this context, I have been involved in industrial projects in collaboration with companies. Firstly, the studies on the wear and lubrication regime in variable displacement vane pumps have been performed within a partnership between MechLav - Advanced Mechanics Lab of Ferrara Technopole - and Berarma srl (Casalecchio di Reno, BO, Italy), pump manufacturer. This project has been intended to study the type of lubrication regime present in the contact between the vanes and the pump stator, in order to find out the combination of materials giving the best performance in

terms of friction and wear. This work has led to the first publications of the PhD Candidate:

E. Mucchi, A. Agazzi, G. D'Elia, G. Dalpiaz (2012). Assessment of the lubrication regime in variable displacement vane pumps. In: Quinta Giornata di Studio "Ettore Funaioli". Bologna, 15/07/2011, p. 39-59, A cura di Umberto Meneghetti, Alberto Maggiore e Vincenzo Parenti Castelli, ISBN: 9788874885169.

E. Mucchi, A. Agazzi, G. D'Elia, G. Dalpiaz, "On Wear and Lubrication Regime in Variable Displacement Vane Pumps" WEAR Elsevier. Volume 306, Issues 1-2, 30 August 2013, Pages 36-46.

Secondly, during the development of lumped parameter models of the pressure distribution in gear pumps, I have been involved in a collaboration with TRW Automotive Italia Srl – Divisione Automotive Pumps (Ostellato, FE, Italy).

The research on the multi-body modelling of the dynamic behaviour of mechanical transmissions is mainly been carried out during a research period of 6 months as Visiting Researcher at Katholieke Universiteit Leuven (KU Leuven, Belgium), within European project COST Action TU 1105 "NVH analysis techniques for design and optimization of hybrid and electric vehicles." My supervisor during this short time scientific mission (STSM) was professor Wim Desmet (KU Leuven) who controlled the reaching of the project tasks. The experimental activities of the project were carried out in cooperation with LMS-Siemens, within the Belgian headquarters of Leuven. The main task of this STSM was the development of the flexible multi-body model of the gear test rig placed in LMS laboratory, characterized by high-precision components and the possibility of introducing defects, such as angular misalignments and eccentricities. These are accurately simulated as well as the variable meshing stiffness, the bearing stiffness as a function of speed and preload, the shaft flexural stiffness, the coupling stiffness. Moreover, several kinds

of gear mesh models, such as CAI, ISO, Calyx, Maatar, Velex and LDP (UDF customize solver), have been validated by comparison with experimental data measured by the test rig. The work performed during this STSM has led to the following proceeding paper:

A. Toso, A. Palermo, A. De Juan, R. Cerda, A. Agazzi, D. Mundo, W. Desmet, 2014, A comparison and experimental validation of gear contact models for spur and helical gears. International Gear Conferernce, 26-28 August 2014, Lyon, France, ISBN 9781782421948.

Subsequently I was involved in a research project in collaboration with Ducati Corse (Bologna, Italy) for the improvement of the dynamic performance of IC engine test benches. Two kinds of models have been developed and experimentally validated: a lumped-parameter torsional model of the whole transmission and a 3D finite-element model for the estimation of the modal properties of the flexible coupling. It has been possible to identify the trouble sources and to optimize the transmissions by means of the integration of the results given by the two models. This project produced a paper presented at ISMA 2015 conference:

M. Cocconcelli, A. Agazzi, E. Mucchi, G. Dalpiaz, R. Rubini, 2014, Dynamic analysis of coupling elements in IC engines test rig, Proceedings of ISMA International Conference 2014,15-17 September, Leuven, Belgium, ISBN 9781634395069.

A further topic of my doctorate activity has been related to methods for the functional design and optimization of mechanical drives and devices; concerning this activity, I have participated to three projects. Firstly, I was involved in the design of an innovative electric press brake for the bending of the metal sheets in the context of a research project supported by g.a.d.e. srl (Cologna, FE, Italy). The main features of the new machine are: a transmission pulley system producing the uniform distribution of the pressure force, so avoiding the deflection of the working beam; reduced tolerances in metal sheet

bending; low noise emissions; reduced maintenance; reduction of the bending cycle time, due to higher speed during the approaching and realising strokes; high efficiency and energy saving. MechLav of Ferrara Technopole was involved in the design of the force transmission system of the whole family of brakes (pressure force 400kN to 1800kN). The transmission system is composed of servo-electric motors, gearboxes, barrels, belts, idle pulleys fixed to the ground, idle pulleys fixed to the tool holder and finally a spring suspension system.

Moreover, I was involved in the project concerning the prototype design of a lock for delivery trucks, based on Radio Frequency IDentification (RFID). The project specifications were: reliable casing, resistant to corrosion and atmospheric agents; proof against tampering actions; allowing manual opening, either in case of malfunctioning or accidental closing; allowing the installation by an inexperienced user; simple and non-invasive installation on the rear door as well as on the lateral door; electromagnetic closing mechanism (simple and cheap).

The third project concerns the functional design of a cam mechanism for a long-cut pasta line, manufactured by Fava SpA (Cento, FE, Italy). The general aim of the project was reducing the number of the electric motors and reducing the friction, improving efficiency and performance. I was involved in the development of a software tool in MatLab environment, finalized to the design of the specific cam mechanisms employed in this line; given the mechanism specifications, the tool allows the cam synthesis and the computation of the contact forces between the cam and the follower.

CONTENTS

INTRODUCTION

The objective of this dissertation is the development of modelling methodologies for the simulation of the variable pressure distribution in rotary positive displacement pumps. The aim of these kind of models is the accurate dynamic simulation of the pressure evolution inside the pump and in the inlet and outlet ducts, as a function of rotor position in working conditions. Moreover, the variable pressure forces acting on all the components (the rotor, the pump casing, etc.) can be estimated. These results are important for the analysis of the vibro-acoustic excitations [56-65, 68-87], the optimization of the structural design [66-67,99], as well as the assessment of wear and lubrication regime.

Different approaches can be used for the modelling of pressure evolution. In this thesis, modelling methodologies based on a lumped parameter approach and an empirical approach are developed and applied in order to assess their specific features - pros and cons − as well as the possibilities of integration.

In **lumped parameter (LP) models**, the fluid volume of the pump is divided in several control volumes and a system of continuity equations is solved. Thus LP models have full physical meaning, taking into account all the design and functional parameters of the pump in a flexible and accurate manner; before a confidential use of the model, experimental validation is needed [20,65,87-89] in order to tune model

parameters. This approach allows the simulation of the behaviour of pumps of different type and design and makes it possible to account for a wide range of modifications, to be considered for optimization purposes.

On the other hand, **empirical models** are not based on physical laws but on experimental measurements: correlation rules are established between the design and functional parameters of a specific family of pumps of different size and the characteristics of the pressure evolution. Thus, empirical models are less flexible than lumped parameter models, as they are applicable only to a single family of pumps; however, they represent efficient tools for R&D in industrial environment, due to faster development time and more friendly use.

The main objectives of this thesis are the followings.

1. The **LP approach** for the modelling of the pressure distribution in rotary positive displacement pumps has been used in several literature works: papers [1-5, 20, 21] can be considered, among others, mainly referring to external gear pumps. **This thesis is intended to further develop this approach, to apply it to an industrial case and to assess its effectiveness by comparison to experimental results.** In addition, the use of CFD simulation for the characterisation of the flows inside the LP model is considered.
2. The **empirical approach** is a completely different method for the simulation of the pressure distribution. It has been recently proposed with the contribution of the PhD candidate [13, 15], as an efficient tool for R&D in industrial environment, due to fast development time and friendly use. **This thesis is intended to present in details this empirical methodology and its practical implementation** with reference to an industrial case study concerning a family of variable displacement vane pumps. Moreover, **its effectiveness will be assessed**.

3. **Aim of this thesis is also to compare these two modelling approaches, finding out their pros and cons as well as outlining their fields of application**.

4. As a further objective, a **sensitivity analysis will be carried out on the external gear pumps** by using the LP model, in order to assess the effects of the following functional and design parameters on the pressure evolution:

   o Oil temperature;
   o Gear eccentricity;
   o Epsilon groove depth;
   o Outlet epsilon groove extension.

   The results of this analysis will be useful for the optimization of the efficiency and the dynamic behaviour.

5. In addition, this thesis is intended **to develop an original methodology for the analysis of the wear and lubrication regime in the sliding contact between the vanes and the pressure ring** in variable displacement vane pumps. This methodology - based on Archard's wear model - makes use of the results of the empirical model and appropriately combines experimental and simulation data. The method will be **applied to an industrial case in order to give indications for the proper selection of materials**.

   The pressure distribution inside rotary positive displacement pumps periodically varies with rotor position; the variable pressure forces consequently represent the main sources exciting casing vibration and the reduction of the amount and rate of force variation can generally involve a reduction of casing vibration and noise emission. The LP approach is particularly valuable as a tool for the vibro-acoustical design and optimization. In fact, these models make it possible to estimate variable pressure forces in the design stage as a function of all geometrical parameters of rotor and housing, axial and radial clearances, oil physical properties and operational parameters. Moreover, these models can be the first element of a combined model

aimed at the complete dynamic simulation (casing vibrations as well as noise propagation), as a tool for vibro-acoustical optimization.

The lumped parameter approach (also called 1D approach) is probably the most used, as it requires limited computational effort, while it offers the chance to set and optimize several parameters; this approach is applied for example in Refs. [1-6,90], mainly dealing with external gear pumps. A further approach is the two-dimensional (2D) CFD modelling [7-10], which is more suitable for specific geometries, such as external and internal gear pumps, lobe pumps, georotor pumps; however, the 2D approach requires higher computational efforts and it has less flexibility in its settings when compared to the 1D approach. Finally, the three-dimensional (3D) CFD modelling is a more accurate approach than the previous ones, but it is obviously the most expensive in terms of computational efforts. Currently, the continuing improvements in CPU technology allow the wide utilization of this technique [11, 12].

In this dissertation a dynamic (time-dependent) analysis was required. Then, the 1D approach was adopted by implementation in Matlab codes. In fact, the 3D modeling, in this case, might lead to a very high computational effort; furthermore, the tight tolerances generate small geometries, which are difficult to mesh properly. The 1D approach gives the best compromise between computational efforts and setting flexibility; moreover, the code may be modified easily in a Matlab environment. In particular, a lumped parameter method based on continuity equations has been adopted, which is very fruitful when phenomena are time-dependent and the balance is taken over a finite entity ("macroscopic balance"). The model has to be validated by comparison to experimental data, in order to tune the model parameters. In this validation procedure, and together with the experimental data, 2D and 3D CFD models were developed. The 3D model simulates steady-state cases and makes it possible to check those parameters that are not measurable during experimental tests, as the laminar flows inside the pump and the flow discharge coefficients[100].

In this context, the aim of the 3D model is similar to a fluxing bench test, which is not feasible for this kind of pump.

As a completely different method, an empirical model can be adopted in order to predict the pressure evolution inside the pump by using an approach focused on industrial applications [13]. In fact, such a model is not based on physical laws but on an experimental campaign [14] concerning a specific family of pumps; however, it is fast to develop and easy to use and it is able to foresee the pressure trend by changing the most important parameters: pump nominal size (pump displacement), number of vanes, distributor design, working pressure and speed. Then, the pressure trend makes it possible to compute the pressure force between the vane tip and stator ring; this parameter is essential for the evaluation of the lubrication regime between this two components (this application is described in this thesis) [15]. Furthermore, the pressure ripple gives several information for the pump designers; in fact, these data are used for evaluation of the strengths in the shaft and in the stator ring. The pressure ripples also give some inputs about the pump dynamic behaviour and the vibration levels.

Overview of the Thesis – Both modelling approaches – LP approach and empirical one – have been developed for practical cases of industrial interest; moreover, model applications for estimating, improving and optimizing pump performances are presented. The thesis is divided into two parts: Part A deals with the development of lumped parameter models for the simulation of the pressure distribution in external gear pumps for automotive applications; in addition, it presents the use for the optimization of design and functional parameters; Part B concerns the development of an empirical model of the pressure distribution in variable displacement vane pumps, and its use for the assessment of the wear and lubrication regime in the vane-stator contact.

In more details, in Part A, Chapter A.1 introduces the universe of positive displacement pumps, then it presents the general characteristics of external gear pumps and it describes the tandem

pump under study as well as automotive dual clutch transmissions where it is employed. Afterwards, Chapter A.2 presents the development of the LP model: the system of continuity equations, the communication flows between the control volumes, the definition of the control volumes as a function of gear position, the oil physical properties, the characterization of the laminar flows through the comparison with the results of 2D and 3D CFD models, and eventually the experimental model validation. Chapter A.3 deals with the simulation results and the sensitivity analysis over the most relevant functional parameters, such as oil temperature, gear eccentricity, epsilon groove depth and outlet epsilon groove extension.

In Part B, Chapter B.1 describes the family of the variable displacement vane pumps under study and the experimental equipment. Thereafter Chapter B.2 explains the method for the empirical modelling of the pressure distribution by using the experimental data concerning three different pumps; the Matlab codes of the empirical model are also included in order to clearly define the implementation of the correlation rules between the design and functional characteristics of the pump and the parameters of the pressure evolution. The simulation results are then quantitatively assessed. Eventually, Chapter B.3 presents the analysis of the wear and lubrication regime in the sliding contact between the vanes and the pressure ring; this analysis is carried out through an original methodology based on Archard's wear model, which associates the wear coefficient to the contact forces given by the empirical model, the wear rate and the material hardness, experimentally measured; the results are compared with the outcomes obtained from an EHD lubrication model in order to evaluate the film thickness and the lubrication regime; the results are finally discussed.

The most relevant outcomes of this dissertation about the different modelling approaches and the analysis of pump performances are ultimately outlined in the Conclusions.

PART A
EXTERNAL GEAR PUMPS

NOMENCLATURE PART A

Latin Symbols

A Duct area.

$a(1)$ Density law coefficient n,1

$a(2)$ Density law coefficient n,2

$a(3)$ Density law coefficient n,3

$a(4)$ Density law coefficient n,4

$a(5)$ Density law coefficient n,5

B Dimension of the relief grooves.

b_t Gear width.

C_{flow} Flow discharge coefficient

D Hydraulic diameter

dt Increment of time.

h_f Lateral clearance between bushes and the lateral flank of the tooth.

h,l,w Height, length, width of a generic fluid film element.

h_t Radial height.

l_{FLF,i_i+1} Length of the equivalent pipe of the gear flank

l_{meanS1} Average length of the first tooth flank section 1

l_{meanS2} Average length of the first tooth flank section 2

$\bullet m_i$ General mass rate

$\bullet m_{in,i}$ General mass rate coming into reference volume i

$\bullet m_{out,i}$ General mass rate coming leaving reference volume i

p_i Pressure in tooth space i

$\bullet q_i$ General volumetric flow rate

Q_{drag} Drag flow rate

$Q_{laminar}$ Generic laminar flow rate

$Q_{turbolent}$ Generic turbulent flow rate

Q_{in}, Q_{out} Inlet and outlet flow rates

R_e Reynolds number

R_{g_ext} Tip radius

R_{g_int} Root radius

r_{root} Root radius.

r_{ext} Tip radius.

r_{S1} Radius of tooth section 1

r_{S2} Radius of tooth section 2

T Oil temperature

V_i Volume of the tooth space "i".

$v_{t\_average}$ Radial average speed

v_{rel} relative speed

Greek Symbols

β Oil bulk modulus.

Δp Pressure gradient

θ Rotational angle.

μ Oil dynamic viscosity.

ν Oil kinematics viscosity.

ρ Oil density.

ω Angular velocity.

Subscripts

i Denotes isolated tooth spaces of drive gears.

j Denotes isolated tooth spaces of driven gears.

Operators

$\big|_i$ Applied to the reference volume i.

$\dot{\ }$ First time derivative

CHAPTER A.1
DESCRIPTION OF THE GEAR PUMP UNDER STUDY

A.1.1.   About External Gear Pumps

The source of definitions, terminology and functioning concerning the pumps universe is the Hydraulic Institute Standards (HI), approved by ANSI (American National Standard Institute), which composed and defined the pumps classification as depicted in Figure 1 [16]. The classification of pumps is based on the mode of energy transfer between the mechanical parts of the pumps and the pumped fluid. There are two main families of pumps: the first one is kinetic pumps, which have several rotating elements called impellers, because they "impel" the kinetic energy to the fluid, further moving the fluid from the intake to the discharge. The second one is positive displacement pumps: these displace the media from an area to another. The suction side is usually called inlet and the discharge side outlet. The pump studied in this thesis is an external gear pump, which is a positive displacement pumps; the flow rate elaborated by this pump is guaranteed by the teeth meshing of the gear pair. Basically, the gear pump uses two identical gears rotating against each other (Figure 2), one gear is driven by a motor; when it is rotating it drives the idle gear. Each gear is supported by a shaft with bushings on both sides, and both gears are contained inside the pump housing; the sealing plates close the far end of the pump, preventing flow leakages.
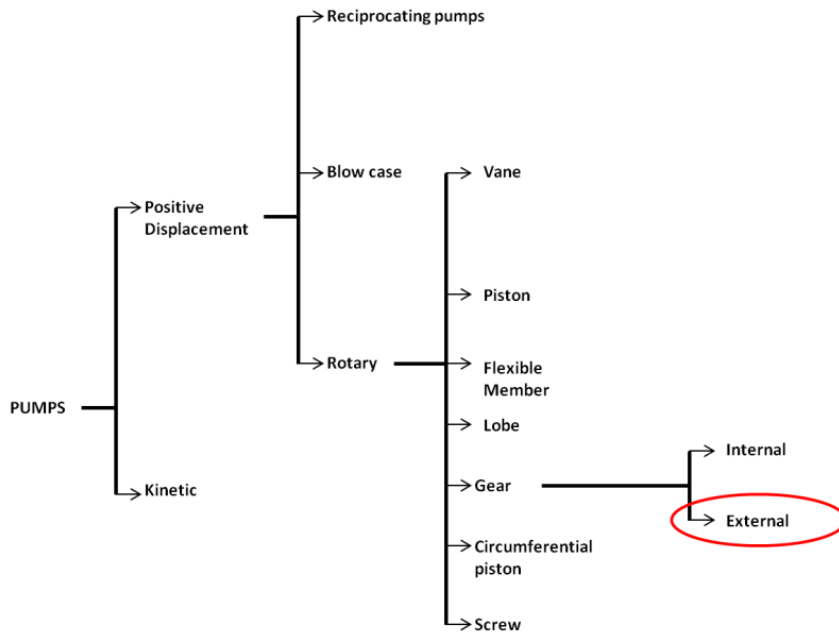
Figure 1. Types of pumps [101].
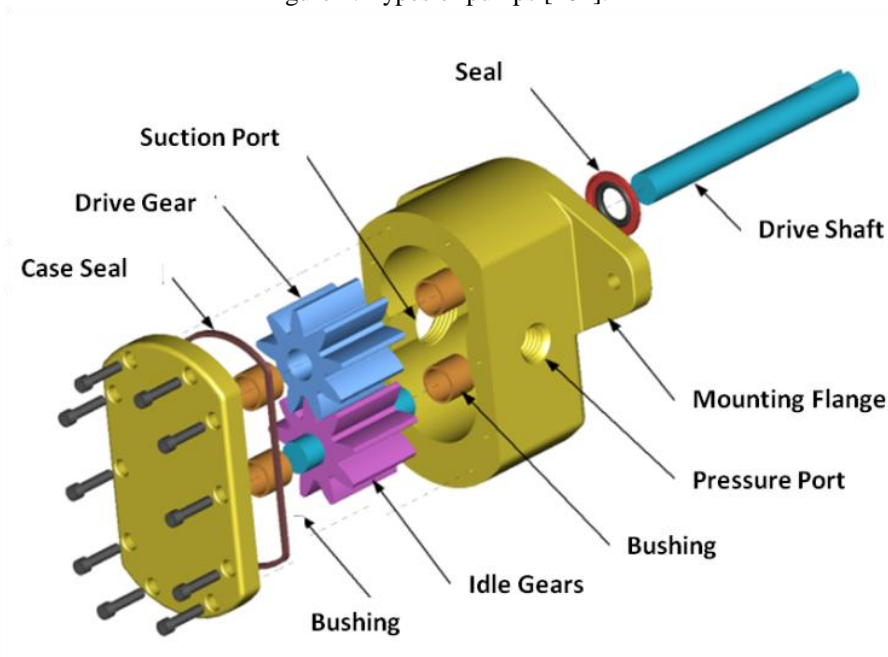
Figure 2. Assembly of the gear pump (https://en.wikipedia.org/wiki/Gear_pump).

Figure 3 illustrates how an external gear pump works. Phase 1 shows the suction phase: when the gears come out of mesh, they create an expanding volume on the inlet, which draws the flow into the gears cavity. Phase number 2 shows the liquid trapped between the gear cavities and the pump housing (called "pockets"). During the rotation of the system the liquid travels around the interior of the casing or, more precisely, inside the pockets between the teeth and the casing. Two basic type of clearances condition affect the pump efficiency: the first one is between the teeth tip and the pump housing; the second one is the axial clearance between the far end of the gear pair and the sealing plate of the pump housing. The designers must keep the proper clearance between the teeth tip and the pump housing, in order to avoid flow leakages, which lead to a decrease in efficiency. Furthermore, these clearances enlarge over the life span of the pump, due to the wear and tear of components. Due to these motives, a further challenge is foreseeing the wear rate and the definition of the proper running in process [1, 17, 18, 19]; in order to keep a high pump efficiency. Finally, phase number 3 of Figure 3 represents the liquid discharge: the meshing of the gears, forces the fluid through the outlet port under a high pressure.

Figure 3. Cross section of external gear pump and the main working phases(http://www.pumpschool.com/principles/external.asp).

This kind of pump has several advantages:

  - *High rotational speed (up to 4000rpm).*
  - *High pressures (up to 200bar).*
  - *Compact and stiff system.*
  - *Relatively quiet operation.*
  - *Its design can accommodate a huge variety of materials.*

External gear pumps share the same disadvantages of the other kinds of positive displacement pumps: they can only elaborate fluids (no solid allowed) and for a high volumetric efficiency, very tight design tolerances are required, causing an increase in manufacturing costs. Normally, three types of gears are used for external gear pumps: spur, helical and herringbone. Herringbone and helical gears typically offer a smoother flow and adapt well to high-capacity systems; their operation is also quieter than that of spur gears. Typically, the spur and herringbone gears have low axial forces; on the other hand, the helical gears generate stronger axial forces, thus compensation systems are needed.

Common external gear pump applications include:

  - Various fuel oil and lube oil.
  - Chemical additives and polymer metering.
  - Chemical mixing and blending.
  - Industrial and mobile industrial applications.
  - Acid and caustic substances.
  - Low volume transfer or application.

The materials of the pump components depend on the application; as we have already seen, this pump can work in very aggressive environments with highly corrosive liquids. Normally the pump housing and the seal plates can be made of cast iron, ductile iron, steel stainless steel, high alloys, composite (PPS Polypheynele Sulphide,

ETFE Ethylene Tetrafluoroethylene). For the internal parts, such as shafts and gears, the most common materials are steel and stainless steel; otherwise, high alloys, alumina ceramics, PTFE (Polytetrafluoroethylene) and composite PPS can be used in special applications. The bushing elements require low friction materials such as carbon, bronze, silicon carbide; however, materials that are resistant to abrasive elements and extreme high temperature are not readily available. This type of pump has been thoroughly researched and developed, but researchers and designers still face huge challenges in order to improve its dynamic behaviour. For instance, the pressure distribution within the pump is essential for understanding its dynamic behaviour [2, 20, 21], because it is the main excitation source of the system. Sometimes the dimension of the pump allows the measurement of pressure distribution [20], but the experimental approach is not convenient in this case, and the pump dimensions do not permit to tackle the problem performing experimental measurements. Thus, simulation models become cheaper and more useful. Normally the positive external gear pump are well suitable in DCT system (Dual Clutch Transmission) due to their cheapness and global efficiency, especially if they are coupled with an electric motor controlled by ECU, which allows to set several strategy for energy saving.

A.1.2.   Dual Clutch Transmission (DCT)

Nowadays, the search for better performances in automotive industry has led to a greater focus on the efficiency of the transmissions. This target can be reached by working on driveline frictions, speed of gearshift during run-up or run-down maneuvers, continuity in transmission torque and power loss due to the absorption by the auxiliary systems. Among the nimblest and most advanced gearbox designs is the Dual Clutch Transmission (DCT), also called "semi-automatic transmission". It basically offers the function of two manual gearboxes in a single package. The DCT is a transmission gearbox in which the clutches and gears are engaged by a sophisticated hydraulic system and an electronic control unit. The clutches have a

basic multi-plate wet clutch design (Figure 4) and operate independently; one clutch is linked to the odd gears shaft while the second clutch is connected to the shaft where the even gears pairs are placed (Figure 5). In some DCT designs, the clutch plates are not bathed in oil for cooling purposes; this kind of design is called "multi-plate dry clutch design", and it is restricted to low-torque engines (typically ≤ 350Nm). The dual clutch systems differ for clutches installation as well; three variants are currently used in automotive applications. The original design features a concentric arrangement, where both clutches share the same plane (Figure 6b)). The second implementation has two single-plate dry clutches, which are side-by-side from the perpendicular view, but are still sharing the center line of the crankshaft (Figure 5). The latest variation uses two separate, but identical-sized clutches; these are arranged side-by-side when viewed head-on (along the length of the input shaft and crankshaft center line), and share the same plane when viewed perpendicularly. The latter arrangement was developed by Honda for use in motorcycles and, differing from the other two variations, it is driven via a gear from the engine crankshaft (Figure 7).
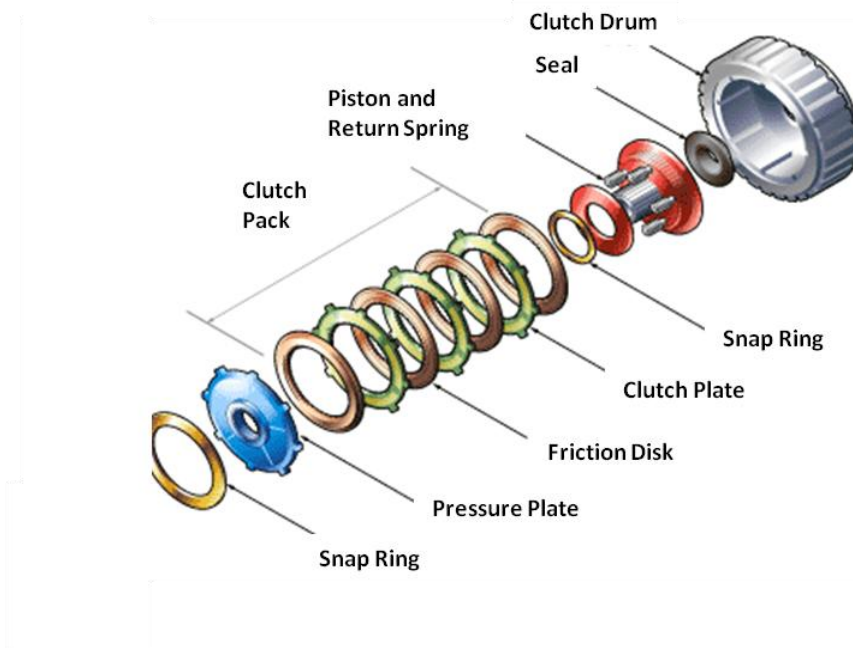
Figure 4. Basic multi plates clutch design (http://auto.howstuffworks.com/dual-clutch-transmission1.htm).
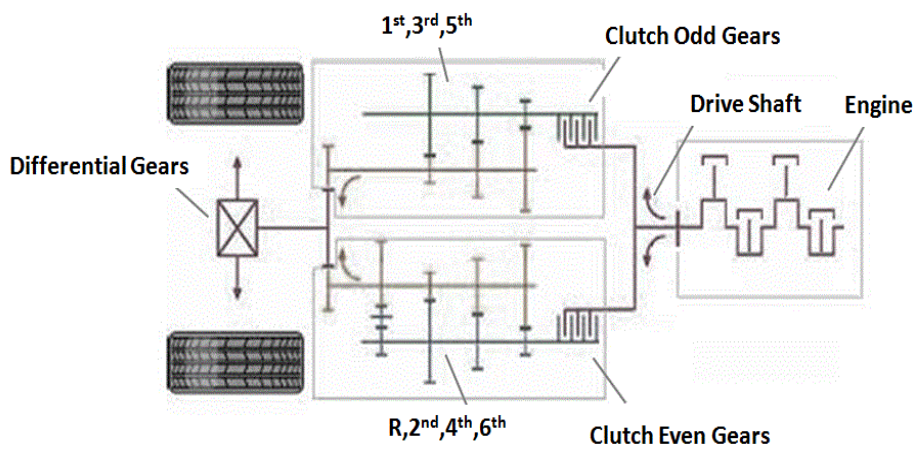
Figure 5. Dual clutch system(http://totalcarmagazine.com/tech/2013/04/09/dsg_dct_co_double_clutchin/).

Figure 6 suggests how the actuation system works. The clutches are driven by the pressure of the fluid, which acts respectively against the coil spring of clutch number 2 and the diaphragm spring of clutch number 1. This actuation mechanism, in essence, pushes a series of stacked clutch plates and friction discs against a fixed pressure plate. The friction discs have internal teeth that are sized and shaped to mesh with splines on the clutch drum. The drum is also connected to the gear set that will receive the transfer force. To disengage the clutch, the fluid pressure inside the piston is reduced. This makes the springs relax, reducing the pressure between the clutch pack and the pressure plate. This system avoids typical problems of single-clutch transmissions such as "shift shock" and "torque interrupt", because a refined control strategy is implemented in the ECU (Electronic Control Unit); therefore, the ECU is able to understand the driver when the latter demands an up- or downshift. For instance, if the second gear is engaged, the speed is increasing and the driver keeps pushing the throttle, the third gear will be pre-selected (Figure 8). When the driver changes gear, the even gears clutch disengages, and the odd gears clutch is immediately activated; the power is instantly transferred through the inner transmission shaft, with the upshifts typically taking a mere 8 ms. Many professional pilots have declared that the DCT offers the most dynamic acceleration of any transmission on the market.
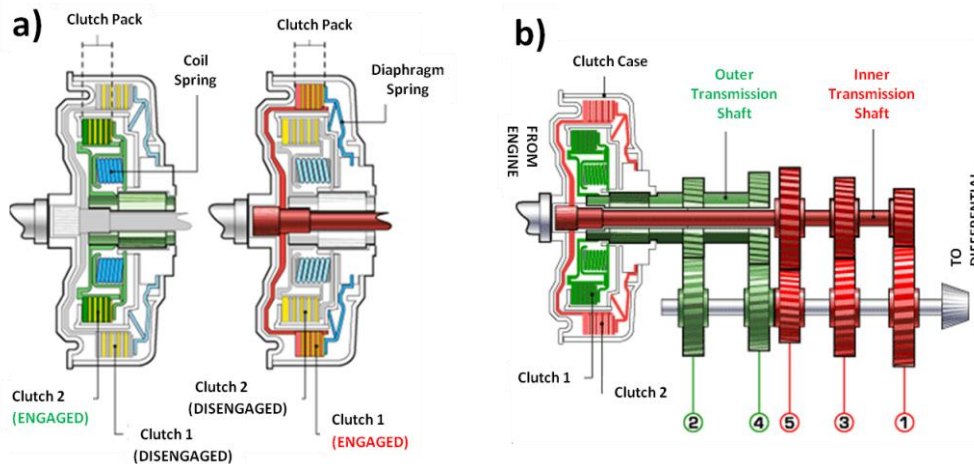
Figure 6. a) Clutches of DCT transmission. b) basic arrangement of DCT with 5 gears(http://auto.howstuffworks.com/dual-clutch-transmission1.htm).
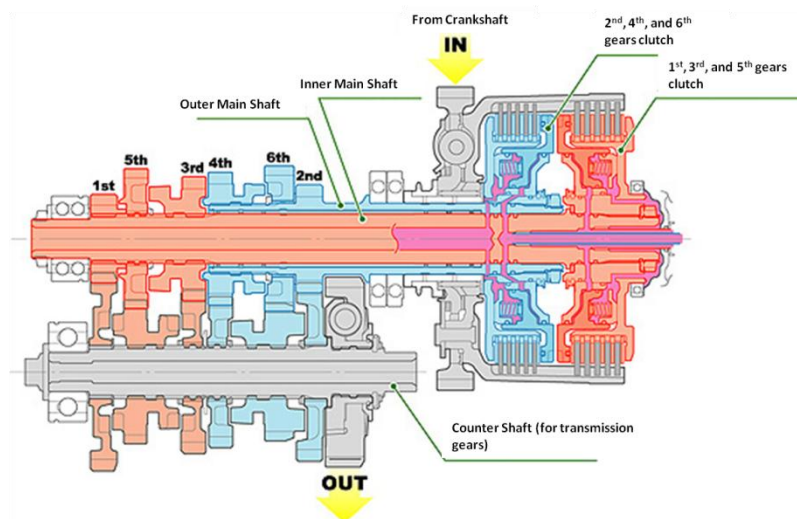
Figure 7. DCT for motorcycle application (http://www.hondaprokevin.com/automatic-motorcycles-dct-review-dual-clutch-transmission-specs-auto-clutch-bikes-model-lineup-overview/).

A similar approach is used while slowing down: for example, when the driver is in third gear and is braking, the ECU pre-selects the lower gear; as the driver shifts down, it makes it possible to transfer the torque through the even gears shaft.
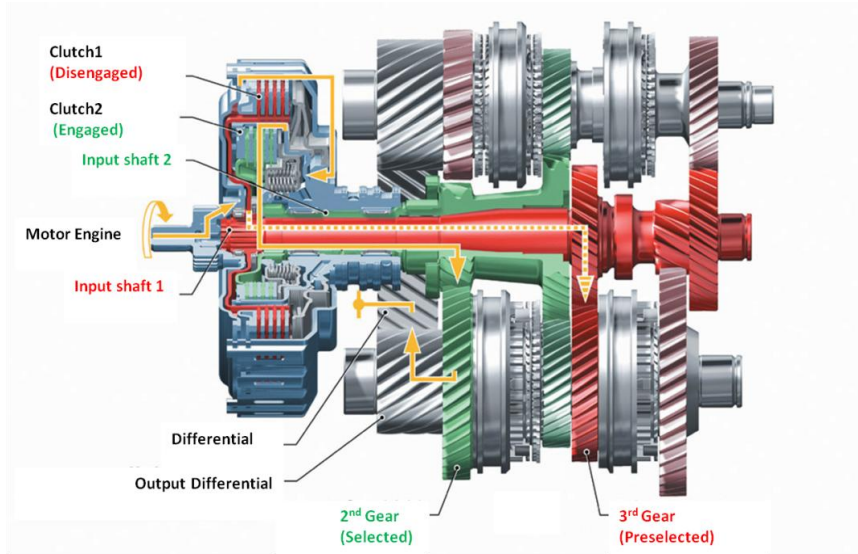
Figure 8. Picture of DCT system during up shift, from 2nd to 3rd gear
(http://sidratuls.blogspot.it/2012/09/dual-clutch-transmission-of-bugatti.html).

The most compelling advantage of DCTs is probably the improvement in fuel consumption; since the power flow from the engine to the transmission is not interrupted, fuel efficiency increases dramatically and CO_2 emission is reduced. Several tests show that a six-speed DCT can deliver up to a 10% increase in relative fuel efficiency, when compared to a conventional five-speed automatic gearbox. The peculiarities of the DCT have led the manufacturers of high-performance cars to a widespread adoption; however, some automakers are still wary of the additional costs associated with modifying production lines to accommodate a new type of transmission. This factor could initially drive up the costs of DCT-equipped cars, which might discourage cost-conscious consumers; this, however, has not stopped DCTs from reaching an adoption rate of ~15% in Europe.

Finally, the advantages of DCT systems are:

- *No power interruption when shifting gears*
- *Lower fuel consumption*
- *Better drive dynamics*
- *Better comfort.*
- *Drive faster and faster*
- *Greater efficiency during the entire lifespan of the car*

There are some disadvantages as well:

- *Increased system complexity (mechanics and control strategy).*
- *Increased weight, due to the number of components.*
- *Increased production costs.*
- *Need for special lubricants.*

The interest in dual-clutch transmissions is particularly strong among OEMs in Europe and major markets in Asia (China in particular). Currently, only 15% of the cars in Europe and 4% in the world are equipped with DCT. If the automotive company will manage to reduce the disadvantages of DCT transmission through design improvements, this kind of transmission might prevail on the market due to its own benefits. For wet-clutch DCTs, the development of a numerical model that can foresee the dynamic behavior and the performance of the pump system is very useful for reducing the development costs, the experimental tests and the number of prototypes.

A.1.3. Tandem Pumps for Applications in DCT

The heart of the hydraulic system of a DCT is the positive displacement pump. The company TRW decided to apply an external, positive displacement gear pump (called "DL-382") because this solution gives the best compromise in terms of efficiency, durability and manufacturing costs, even though the external gear pump has a fixed displacement and the regulation of the flow is only possible by setting

the rotational speed. The positive displacement pump moves a unit of fluid, which is trapped within a pumping element that physically displaces it from the inlet to the outlet environment. The pump layout and the design of the coupled hydraulic system, allow two operational modes (Figure 9): with (*mit speichern laden*) or without (*ohne speichern laden*) the charging of the reservoir. The pump is made of two gears pairs (Figure 10): the bigger one is always linked to the low-pressure hydraulic system, which lubricates the clutches, and keeps them at an optimal temperature. The smaller one feeds the high-pressure hydraulic system when the reservoir needs a higher pressure (29bar). Otherwise, when the reservoir has not to be feed, a by-pass valve is enabled, thus the gear pumps discharge in a common pipe at the lower pressure level, in order to increase the cooling system efficiency and the global efficiency. An electric brushless machine powers the driver shaft, which connects the gears of the high and low-pressure pumps rigidly. There is no clutch in between the motor and the shaft, so there is always the chance to switch from *"mit speichern laden"* mode to *"ohne speichern laden"* without wasting part of the power from the motor through a dissipation valve.
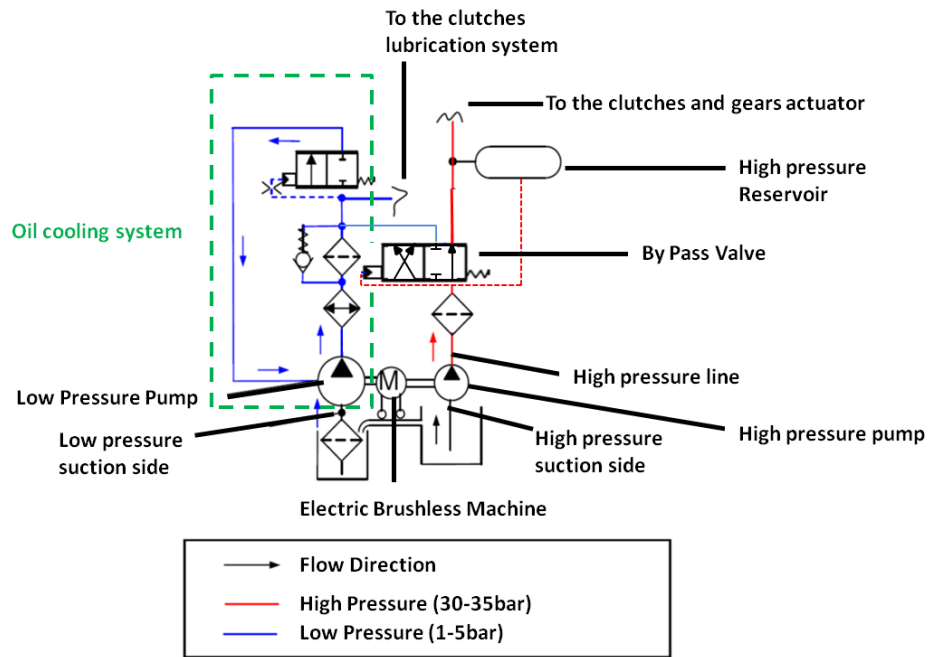
Figure 9. Oil-dynamic DCT system.
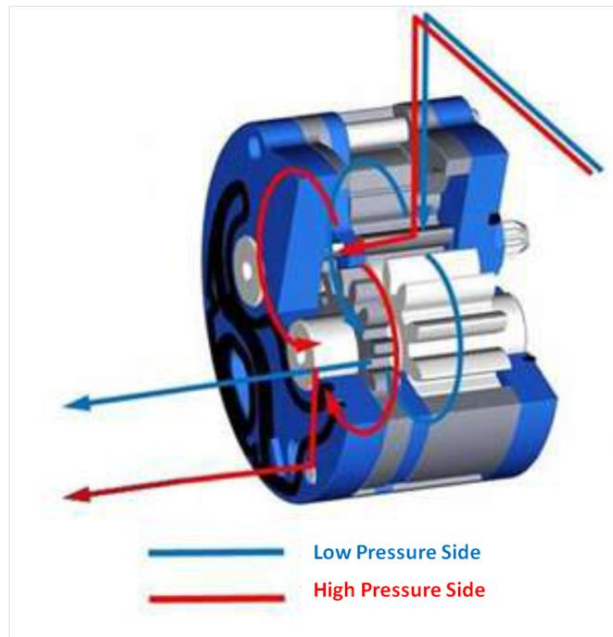
Figure 10. Cross Section of "DL-382".

The technical feature of the pumps are listed in Table 1
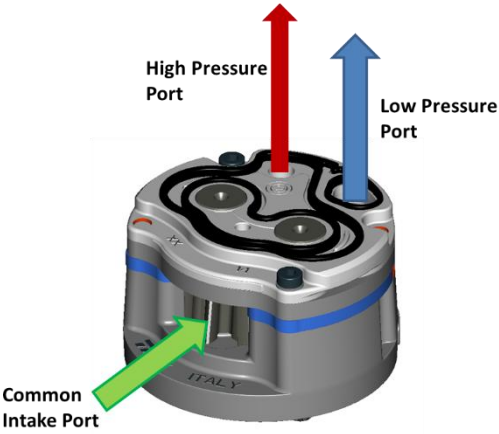
HIGH PRESSURE PUMP	
Displacement	0.8cc/rev
Rated Pressure	30 bar
Max allowable pressure	43bar
Maximum flow rate	3l/min
Number of teeth	17
Gear type	Spur Gear
LOW PRESSURE PUMP	
Displacement	5.33cc/rev
Rated Pressure	3 bar
Max allowable pressure	5bar
Maximum flow rate	20l/min
Number of teeth	11
Gear type	Helical Gear

Table 1. Technical features of DCT tandem pump.

The pump layout leads to several advantages:

- *Reduction of assembly components.*
- *Simplify the assembling procedure.*
- *Low weight and dimension.*
- *Energy saving.*

The pump layout leads to several advantages:

– *Reduction of assembly components, thus a simpler assembling procedure.*
– *Low weight and dimension.*
– *Greater energy savings.*

The rotational, positive displacement pumps need an axial compensation force, in order to avoid any contact between the rotor and the seal plates; nevertheless, the leakage flows must be limited. This is always a big challenge for designers, who keep pushing for high-efficiency systems. Designers are always looking forward for innovative solutions that can reduce the power loss and flow leakages. In this case, there is also an additional issue due to the double operational modes ("*mit speichern laden*", "*ohne speichern laden*"). Figure 11 shows the axial pressures acting on the pump plates. On the upper surface of the top plate, there are two acting forces: the first one is due to the bolt tightening, and the second contribute is the force resulting from the upper pump pressure. On the lower surface of the top plate, the internal upper pump pressure pushes against the resultant external compensation force. The middle plate is pushed from the top by the upper pump internal pressure and from the bottom by the lower pump internal pressure. Finally, the lower plate is pressed against the electric motor flange by the lower pump internal pressure and by the bolt tightening forces. The bolt tightening preload and the compensation area on the upper plate are fundamental for the proper sealing of the pump in both operational mode; the external compensation force must always be higher than the overall force caused by the pump internal pressure. Figure 12 shows the pressurized area on the top of the upper plate; the oil is kept inside this area by a rubber seal with 80 Shore_A hardness.
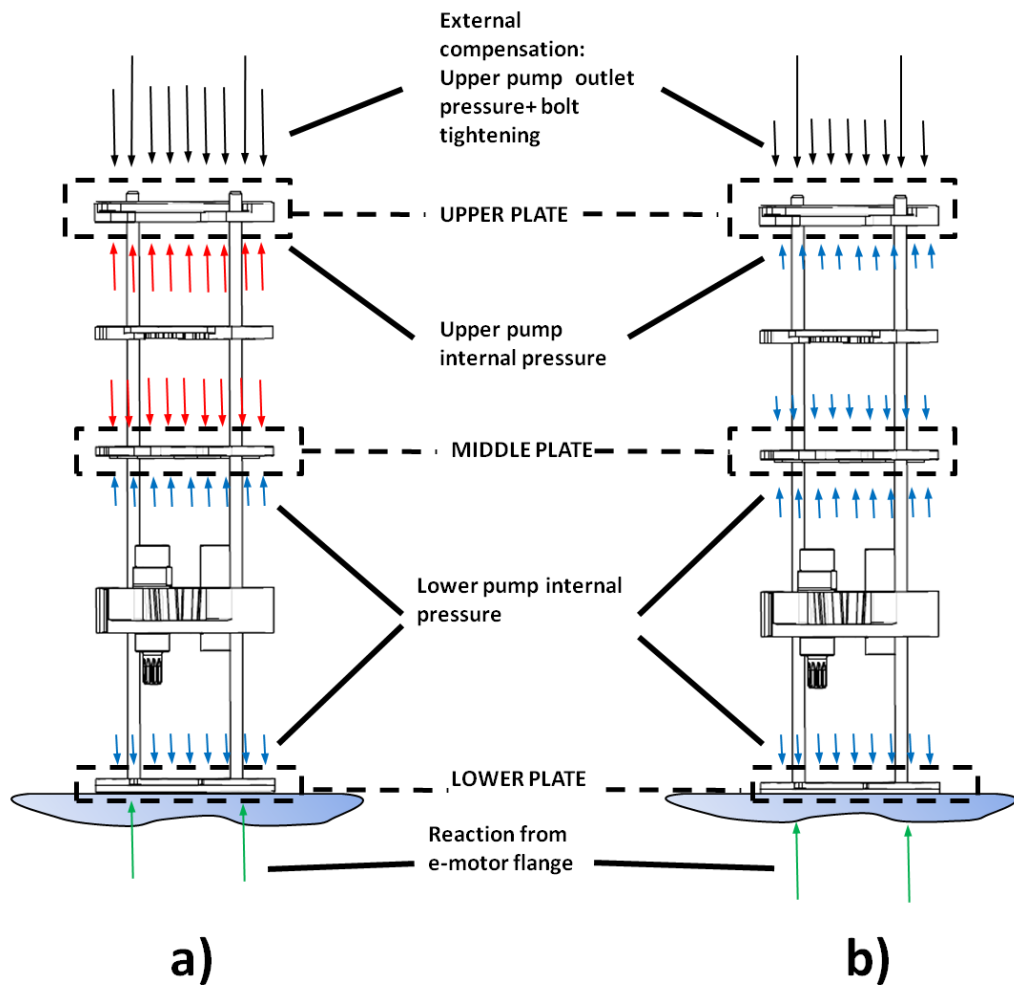
Figure 11. Pressure balance of tandem pump. a) "*mit speichern laden*", b)"*ohne speichern laden*".
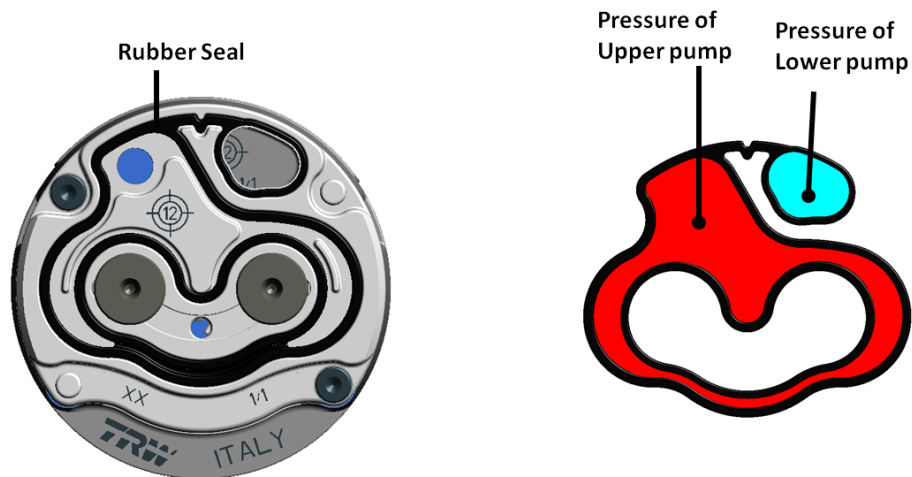
Figure 12. Front view of the upper plate and compensation area.

The electric machine that powers the DLL 382 pump is a brushless synchronous motor, powered by a DC source via an integrated inverter-switching power supply. The inverter produces an AC signal that drives the motor; alternated current does not imply a sinusoidal waveform, but the motor control unit, using additional sensors and electronics, can generate the current signal with several waveforms. The signal can be modified in terms of amplitude, waveform and frequency, in order to obtain the best performance for each and every working condition. These features reduce mechanical losses, avoid the creation of sparks due to the lack of sliding contact when speed increases, and reduce maintenance. Brushless motor commutation can be implemented in software using a microcontroller or microprocessor computer, or may alternatively be implemented in analogue hardware, or in digital firmware using an FPGA (field programmable gate array). Commutation with electronics instead of brushes allows a greater flexibility and capabilities not available with brushed DC motors. Those include speed limiting, "micro-stepped" operation for slow and/or fine motion control, and supplying a holding torque when the pump is stationary. Brushless engines need a speed sensor (called pick up, and acting as a Hall effect sensor) or a very accurate resolver in order to provide the rotor position to the controller.

The wide array of solutions available to manage the control strategy of a brushless motor leads to the adoption of this machine in several applications such as: industrial positioning and actuation applications, [22], assembly robots, [23] brushless stepper or servo motors. The latter are used to position a part for assembly or a tool for a manufacturing process, such as welding or painting. Brushless motors can also be used to drive linear actuators [24], extruder drive motors and feed drives for CNC machine tools [25]. The pros and cons of the brushless engines are:

Pros:
- Increased lifespan of electric machines, as the lack of sliding contacts (which are the weakest link) causes less electromagnetic noise
- High reliability and low maintenance.
- High versatility (the motors can be used for several applications, due to the use of a programmable control unit).
- High power to weight ratio and reduced dimensions.
- Higher efficiency, as the controller makes it possible to operate in optimal conditions.
- Reduced heat generation, when compared to other electrical machine.
- The permanent magnets are fixed to the rotor and are made of low-density material, in order to obtain a lower rotational inertia, assisting in speed and acceleration control.
- Permits overload in terms of speed and torque.

Cons:
- Expensive hardware and control units.
- High operational temperature could lead to demagnetization of permanent magnets.
- Eddy currents flow through the stator windings, dissipating energy because of Joule effect, and generating an opposite torque (against the turning direction).

The stator of the brushless electric motor has six polar pairs fixed to the housing (Figure 13). The AC current that flows through these coils generates a strong magnetic field next/adjacent to the rotor. The rotor has eight permanent magnets mounted on it, which produce a magnetic field. When the current flows through the stator coils, the rotor starts to rotate, because the rotating magnetic field produced by the stator causes the magnetic field of the permanent magnets to rotate. In order to keep the rotor rotating, the electronic control commutes the current direction, preventing the alignment of the magnetic field.
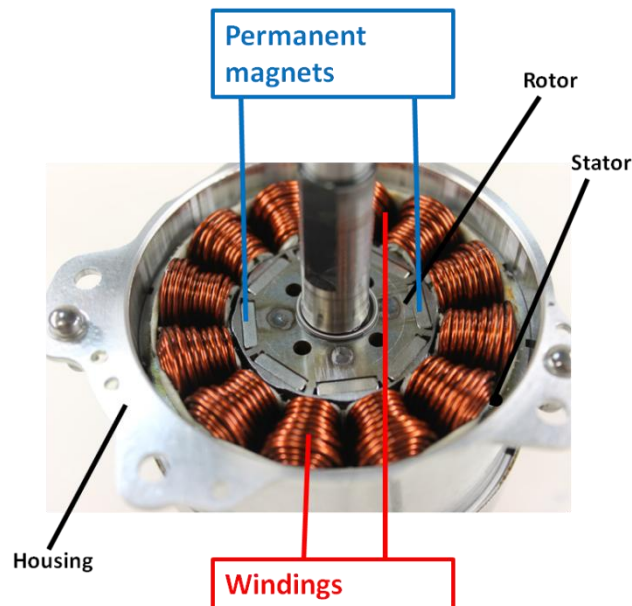
Figure 13. Brushless electric motor hardware.

The ECU has a strategy to control the electric machine; this strategy is based on the rotor position, indeed the control unit by knowing the absolute rotor position feed the phases in the proper manner. The control system requires a sensor position as encoder or a resolver.

The objectives of the control strategy are:
- *Keeping the right way of rotation.*
- *Reducing the rotor torsional oscillation when in a steady state.*
- *When not in a steady state, keeping the rotational speed within a narrow range, in order to reach the target speed in a fast way.*

Table 2 reports the brushless motor features, while Figure 14 contains the developed torque for different temperature conditions.

Feature	Value
Number of permanent magnets	8
Number of coil pairs	6
Number of windings per coil	30
Number of phases	3
Cables diameter	1.12mm
Rotor length	22mm
Stator diameter	78mm
Peak torque	2.2Nm @ 75 A, -30 °C

Table 2. Brushless motor features.
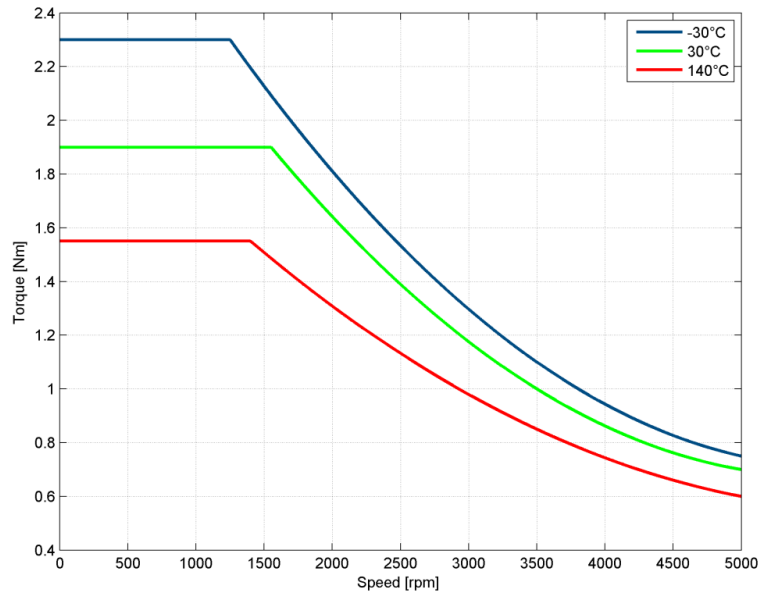
Figure 14. Torque curve of brushless engine for different working temperature.

The assembly scheme of the whole system is reported in Figure 15.
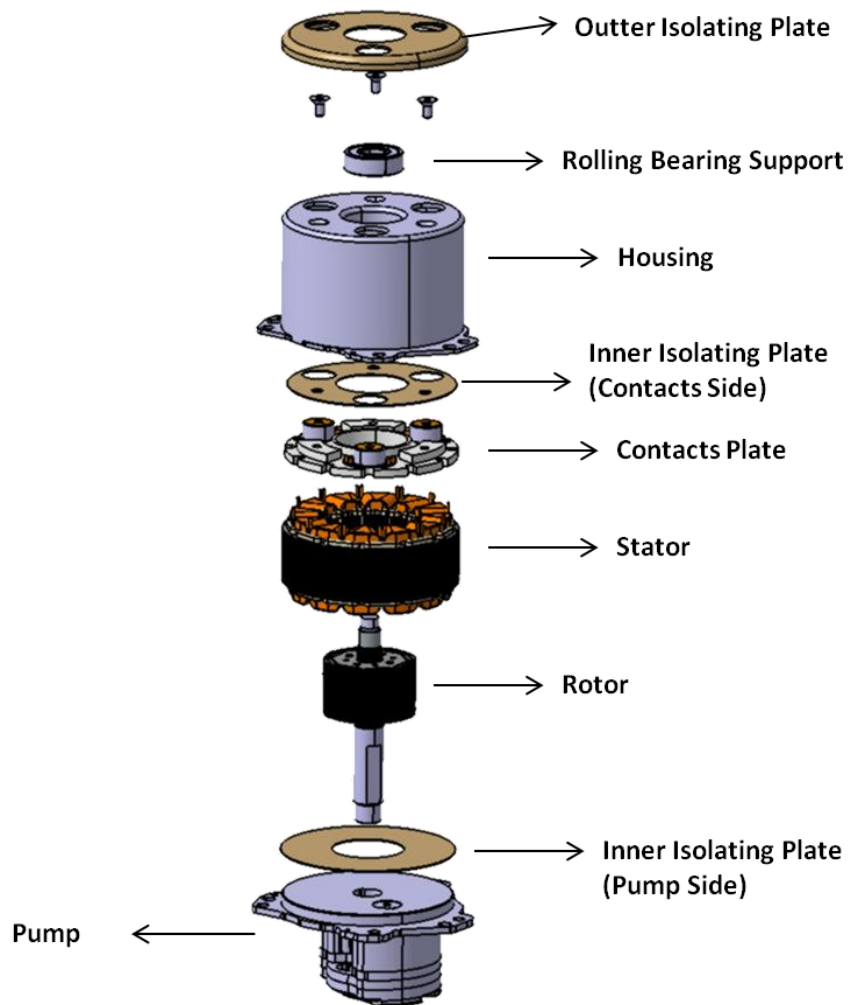
Figure 15. Fixing scheme of "DL 382" elettro-pump.

CHAPTER A.2
MODELLING AND VALIDATION OF PRESSURE DISTRIBUTION

A.2.1.   Introduction

The aim of this chapter is the definition and the validation of a robust, flexible and efficient model in order to foresee the pressure distribution within external gear pumps.

The second paragraph (A.2.2) introduces the description of the LP model, defining the continuity equations and the subdivision of the fluid domain in several control volumes. The third paragraph (A.2.3) focuses on the flow rates (laminar, turbulent, drag and drainage) between the control volumes. Furthermore, a detailed analysis of the evolution of the control volumes over the gear position has been performed in paragraph A.2.4. The fifth paragraph (A.2.5) describes the oil physical properties and the formulation used in order to express such properties. The sixth paragraph (A.2.6) introduces a CFD model for characterization of the laminar flows of the LP model: basically, the CFD model proves the hypothesis of the laminar flows on tooth flanks and tooth tips. The last paragraph (A.2.7) contains the validation procedure of the LP model.

A.2.2.   Modelling the Hydraulic System by Control Volumes

In this dissertation the LP approach was chosen, by using a commercial flexible tool such as Matlab in order to model the pressure distribution within external gear pump. In this case the LP model was preferred respect to a sophisticated 3D model, due to the lower computational effort; furthermore, the tight geometrical tolerances of the gear pump lead to generate small geometries, which are difficult to mesh properly. The flexibility of the LP approach, gives the best

compromise in term of computational efforts and modification of the simulation parameters. Typically, the lumped parameter method is based on continuity equations, thus is able to catch phenomena which are time-dependent and characterized by a "macroscopic balance" over a finite entity. The validation procedure of the LP model requires a comparison to experimental data, in order to reach the target by using the tuning parameters methodology. Furthermore, the LP model require some hypothesis concerning the flow rates which are taken into account, in particular the laminar flow hypothesis were justify by the development of 2D and 3D CFD models. In this context, the aim of the 2D and 3D model is similar to a fluxing bench test, which is not feasible for this kind of pump. Figure 16 schematically presents the methodology for the LP model development.
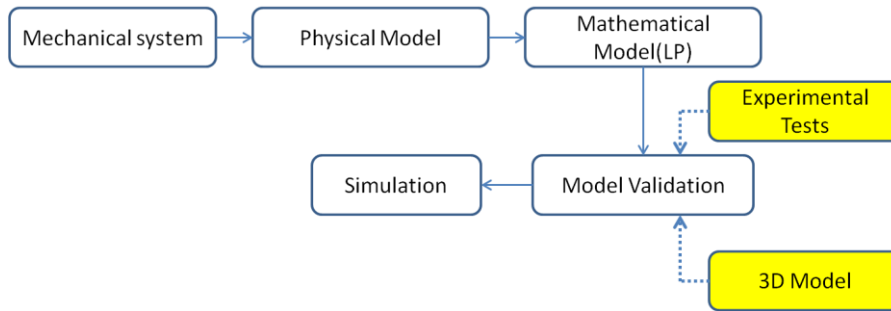
Figure 16. Flow chart of the modeling process.

The lumped parameter models are based on the macroscopic phenomena that characterize the mechanical systems; furthermore, they can be identified by a low number of degrees of freedom (DOFs). Concerning the LP model, the overall fluid domain is divided in several control volumes, and respecting the mass conservation equation is the cornerstone of this approach. In essence, these control volumes are a kind of tank receiving and giving flows from the neighboring control volumes, where the fluid properties are assumed as uniform and time-dependent only. Eq(1) reports the conservation mass equation of for a generic control volume (Figure 17) [20].

$$\frac{dp_i}{dt} = \frac{1}{V_i} \frac{dp}{d\rho}\bigg|_{p=p_i} \left[\sum \dot{m}_{in,i} - \sum \dot{m}_{out,i} - \rho|_{p=p_i} \left(\frac{dV_i}{dt} \right) \right] \qquad (1)$$
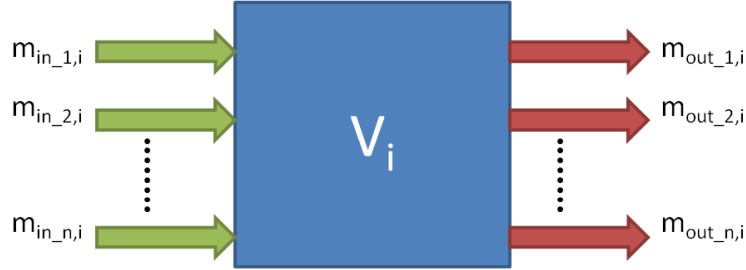
Figure 17. Mass flow balance in generic control volume.

The mass conservation equation asserts that the time derivate of the volume pressure is proportional to the inverse of the control volume, the density derivative of the pressure, and finally to the overall sum of the flows minus the product between the control volume fluid density and the time derivative of the control volume. In the case study, this equation can be simplified and switched to the angle domain. The pump works in a steady condition, and the rotational speed of the shafts is constant as well; indeed, in this case it is easy to switch from the time domain to the angle domain. The angular rotational speed ω is defined as the rate of change of angular displacement, Eq(2); thus, the time derivatives of Eq(3) become angle derivatives, with a further contribution of the rotational speed, as shown in Eq (3).

$$\frac{d\vartheta}{dt} = \omega \qquad (2)$$

$$\frac{dp_i}{d\vartheta} = \frac{1}{\omega V_i} \frac{dp}{d\rho}\bigg|_{p=p_i} \left[\sum \dot{m}_{in,i} - \sum \dot{m}_{out,i} - \rho|_{p=p_i} \left(\frac{\omega dV_i}{d\vartheta} \right) \right] \qquad (3)$$

Eq(3) is obtained by applying the continuity equation and the steady state fluid equation, under the hypothesis of adiabatic and isentropic transformation. It can be simplified further, as the lower pressure levels reached by the pump suggest that the fluid can be considered as an incompressible fluid; this aspect leads to consider the density derivate of the pressure parameter as a constant called Bulk modulus. Finally, the mass flow rate can be stated as a volumetric flow rate, Eq(4) thus the continuity equation implemented in the mathematical model get as Eq(5).

$$\dot{m}_i = \rho \dot{q}_i \qquad (4)$$

$$\frac{dp_i}{d\vartheta} = \frac{1}{\omega V_i} \beta \rho \left[\sum \dot{q}_{in,i} - \sum \dot{q}_{out,i} - \left(\frac{\omega dV_i}{d\vartheta} \right) \right] \qquad (5)$$

After having illustrated the basic equation of the mathematical model, let us move to the description of the high-pressure pump model of Figure 18. The entirely fluid domain is divided in 37 control volumes and 2 environments, at a constant pressure (Figure 19). The first control volume is the inlet volume, which represents the tank containing the pump; 34 of the 37 volumes represent the gear pump pockets; the last two volumes are, respectively, the outlet pump volume and the outlet pipe; the latter links the outlet volume of the pump to the tank, and is where the pressure regulation valve is placed. The tank and the drainage are considered as a volume with a steady pressure (10000Pa); the tank volume is connected to the outlet pipe volume and the intake volume, while each gear pocket volume is connected with the drainage volume. These assumptions have two different explanations; firstly, the tank has the highest volume of the system and is not pressurized, so it is not affected by the outlet and inlet pressure; secondly, the drainage flows can be considered negligible, as they must get through the axial clearances, which are characterized by a high hydraulic resistance. Using the relation present in Eq(5) it is possible to determine the pressure variation of the fluid contained in the control volume Vi , caused by the imbalance between the inlet and outlet flows

($\sum q_{in,i}$-$\sum q_{out,i}$) and the volume variation ($dV/d\theta$). The mass gain indicates the overall flow entering and leaving the control volume, obtained considering the contribution of the connections linked to the control volume. In order to solve Eq(5), the calculations of the terms on the right side of equation, i.e. the volume and its variation and the inlet and outlet flow rates, has to be performed for each control volume. The number of control volumes involved in the pressure calculation remains constant during the whole integration period but the flow rate exchanged by control volumes can vary with respect to angular coordinate. Finally, the mathematical model is composed by a system of 37 ordinary differential equations (ODE) reported in Eq(6)

$$\begin{cases} \dfrac{dp_1}{d\vartheta} = \dfrac{1}{\omega V_1}\beta\rho\left[\sum \dot{q}_{in,1} - \sum \dot{q}_{out,1} - \left(\dfrac{\omega dV_1}{d\vartheta}\right)\right] \\[2ex] \dfrac{dp_2}{d\vartheta} = \dfrac{1}{\omega V_2}\beta\rho\left[\sum \dot{q}_{in,2} - \sum \dot{q}_{out,2} - \left(\dfrac{\omega dV_2}{d\vartheta}\right)\right] \\[2ex] \dfrac{dp_3}{d\vartheta} = \dfrac{1}{\omega V_3}\beta\rho\left[\sum \dot{q}_{in,3} - \sum \dot{q}_{out,3} - \left(\dfrac{\omega dV_3}{d\vartheta}\right)\right] \\[1ex] ..... \\ ..... \\ ..... \\[1ex] \dfrac{dp_{37}}{d\vartheta} = \dfrac{1}{\omega V_{37}}\beta\rho\left[\sum \dot{q}_{in,37} - \sum \dot{q}_{out,37} - \left(\dfrac{\omega dV_{37}}{d\vartheta}\right)\right] \end{cases} \qquad (6)$$
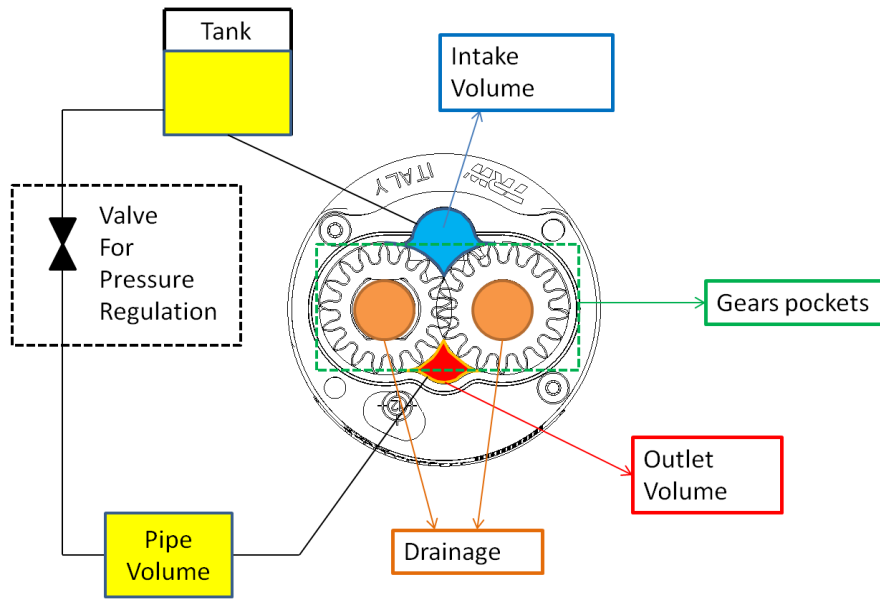
Figure 18. Scheme of high pressure fluid domain.
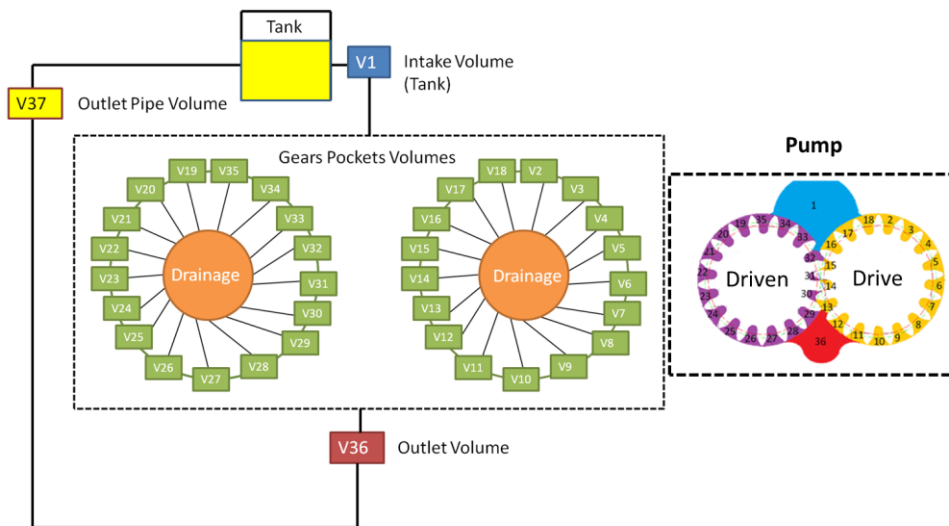
Figure 19. Scheme of the Lumped parameter model of the high pressure test bench line.

A.2.3.   Flow Rates

This section deals with the description of the entering and leaving flows of the control volume. Normally there are two types of flows that describe the behaviour of the fluids in the pipes. The first type is the laminar flow, where the fluid moves slowly in layers in a pipe, without mixing with other layers. Then there are the turbulent flows, where considerable mixing occurs, and flow velocities are high. Laminar and turbulent flows can be characterized and quantified by the Reynolds number as defined in Eq(7), which depends on the flow speed, hydraulic diameter and dynamic viscosity.

$$R_e = \frac{vD}{\mu} \qquad (7)$$

The Reynolds equation suggests that both fast flows and pipes with large cross-sections lead to high turbulences, where considerable mixing of particles occurs. On the contrary, high-viscosity flows tend to "stick" to solid surfaces, thus the motion of particles is very orderly and in straight lines parallel to the pipe wall. Under $2000 R_e$, flows are considered laminar; when they exceed $4000 R_e$ turbulent. Inside the $2000{\sim}4000 R_e$ range flows cannot be considered neither laminar nor turbulent; they are usually called transitional flows. The mathematical approaches for the modelling of laminar and turbulent flows are different. The laminar flows are well modelled using the Poisulle Eq(8),

$$Q_{La\min ar} = \frac{wh^3 \Delta p}{12\mu l} \qquad (8)$$

Considering Eq(8) for two control volumes at different pressures and connected by a pipe with a geometry as in Figure 20, the volumetric laminar flow rate passing through the pipe depends on the following parameters:

- *w = pipe width*
- *h= pipe height.*
- *ΔP= pressure gradient.*
- *µ= dynamic viscosity.*
- *l= pipe length.*
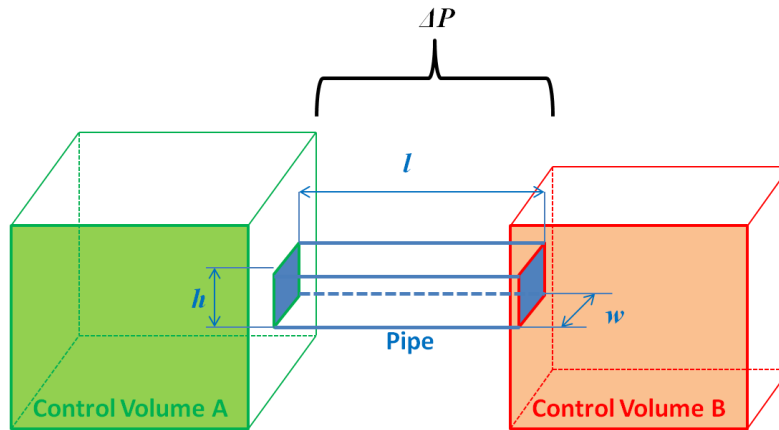
Figure 20. Representation of two control volumes (A, B) connected by single pipe.

The turbulent flows increase when all of the following conditions are satisfied:

- Pipe with a large cross-section area and short length;
- Low viscosity fluids;
- High pressure gradient. Keeping in mind the scheme in Figure 20, the volumetric flow rate of turbulent flows is defined as Eq(9).

$$Q_{Turbolent} = C_{flow} A \sqrt{\frac{2\Delta p}{\rho}} \qquad (9)$$

Where:

- *C_{flow}= flow discharge coefficient*
- *A= pipe cross-section area (hw).*
- *ΔP= pressure gradient.*
- *ρ= fluid density.*

The comparison between Eq(8) and Eq(9) suggests that turbulent flows are not conditioned by fluid viscosity; moreover, the proportionality due to the pressure gradient is not linear, but goes with the square root, and finally the length of the pipe does not affect the flow rate. The cross-section of the connection pipe influences both kinds of flow, but turbulent flows are conditioned by a further parameter "C_{flow}" called "flow discharge coefficient". The flow discharge coefficient is a parameter that can assume values from 0 to 1; however, for most turbulent flows this range can be reduced to $(0.6 \div 0.7)$. The laminar and turbulent flows are not sufficient for the pump characterization, and there is a further aspect to keep in mind that is independent of the pressure field. The majority of rotary pump machines have two main components: the rotor and the stator. The first component rotates, while the second one is fixed to the ground. When considering the relative velocity, the gaps between components and the fluid viscosity, drag flows inside the pump will have to be taken into account. Typically, the drag flows involve the adjacent rotating volumes that displace and pump the fluid from the inlet to the outlet. Considering the external gear pump and the two adjacent pockets, two drag flows will have to be taken into account. The first one is allowed by the existing gap between the gear tip and the pump housing, while the second one is permitted by the axial clearance of the gear flank and the sealing plates. The drag flow rates depend on the relative speed between the rotating component and the fixed part; it is identified by the dimension of the clearances or gaps in the assembly, well shown in Figure 21 and Figure 22.
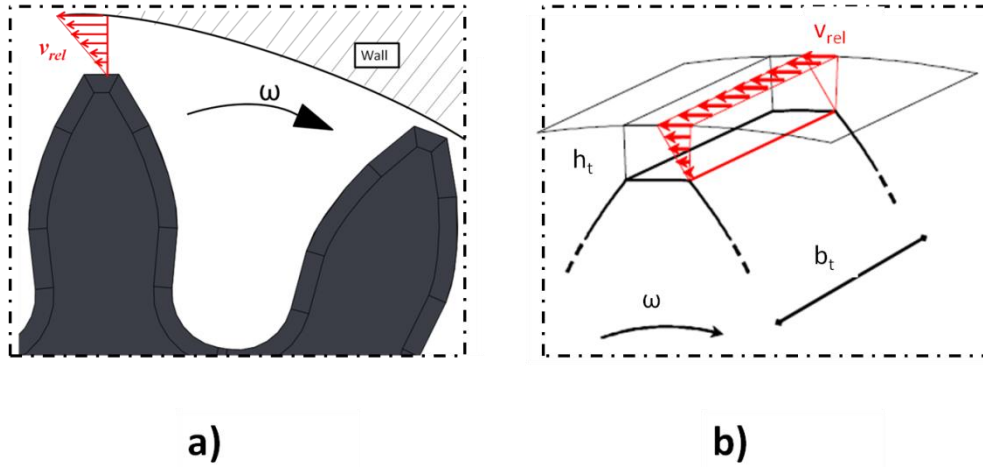
Figure 21. Geometrical definition of the drag flow. a) Speed field, b) Flow rate representation.

The mathematical modelling of these flows is quite simple, and is based on the adhesive fluids phenomenon. The fluid particles that are in contact with the solid surfaces have the same speed as the solid walls; thus, if we consider the relative motion between the inner stator circumference and the teeth tip, the speed field trough the tip clearance is defined as Figure 21*a)*. Where the minimum relative speed is zero and it is located on the teeth tip, and the maximum relative speed is on the inner surface of the inner stator surface, the magnitude of the maximum relative speed is the tangential speed on the external radius of the gear teeth, as reported in Eq(10):

$$v_{rel} = \omega \; r_{ext} \qquad (10)$$

The drag flow rate is computed by the integration of the speed field trough the tip clearance Figure 21*b)*; in this case, where the cross-section area is rectangular, the drag flow rate traded by two adjacent pockets rate on the teeth tip is expressed as Eq(11).

$$Q_{drag} = \frac{v_{rel} h_t b_t}{2} \qquad (11)$$

A similar approach can be exploited also for drag flows on the gear flank, but in this case there are two speed fields: the first one in the radial direction (Figure 22 a)), and the second one in the axial direction(Figure 22 b)). The radial speed field leads to an average tangential speed that is applied on the teeth flank length, and then the tangential average speed is used as the maximum speed of the axial velocity field. Finally, these flank drag flows can be expressed as Eq(12):

$$Q_{drag} = \frac{v_{t\_average} h_f \left(R_{g\_ext} - R_{g\_int} \right)}{2} \qquad (12)$$
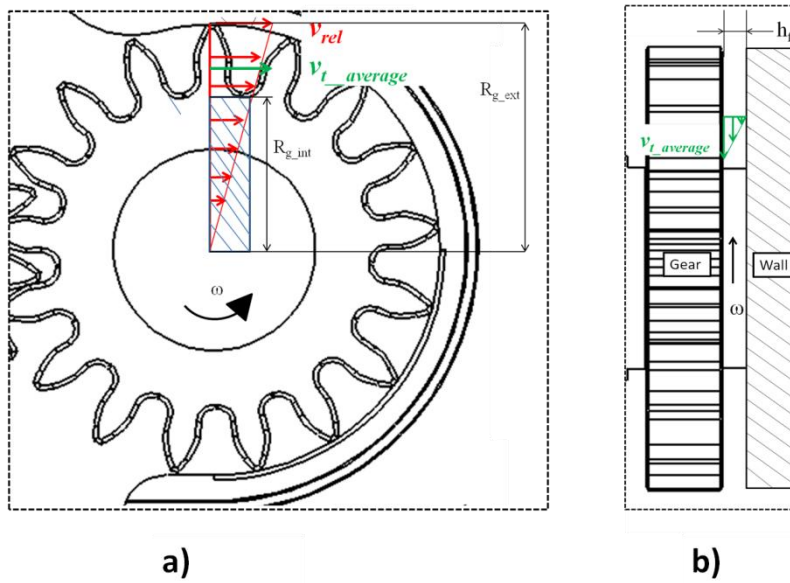
Figure 22. Drag Flow on the gears flank. a) Front view, b) lateral view.

In the following lines, we will define the overall flow rates considered in the model; in order to simplify comprehension, two control volumes will be taken as a reference. The first one belongs to the drive gear, while the second one is the control volume of the driven gear, which establishes the trapped volume during the teeth meshing (Figure 23).
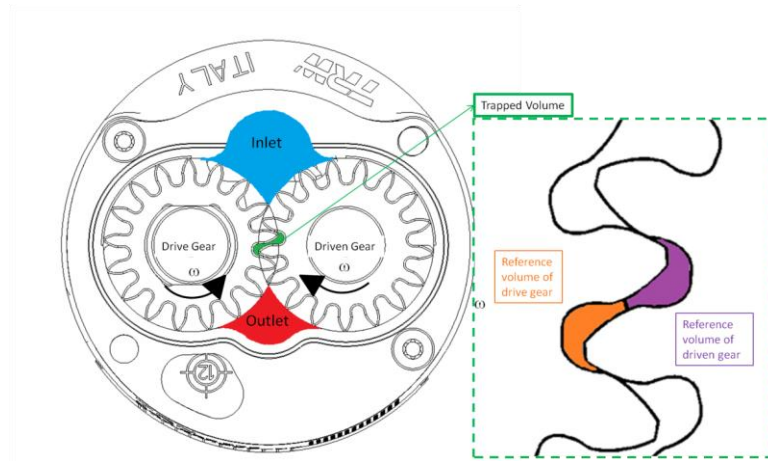
Figure 23 Reference volumes of drive gear (orange) and driven gear (violet).

The scheme of Figure 24 contain the flows of the reference volume. Before describing the scheme, a brief introduction to the nomenclature is necessary for a better understanding (Table 3).
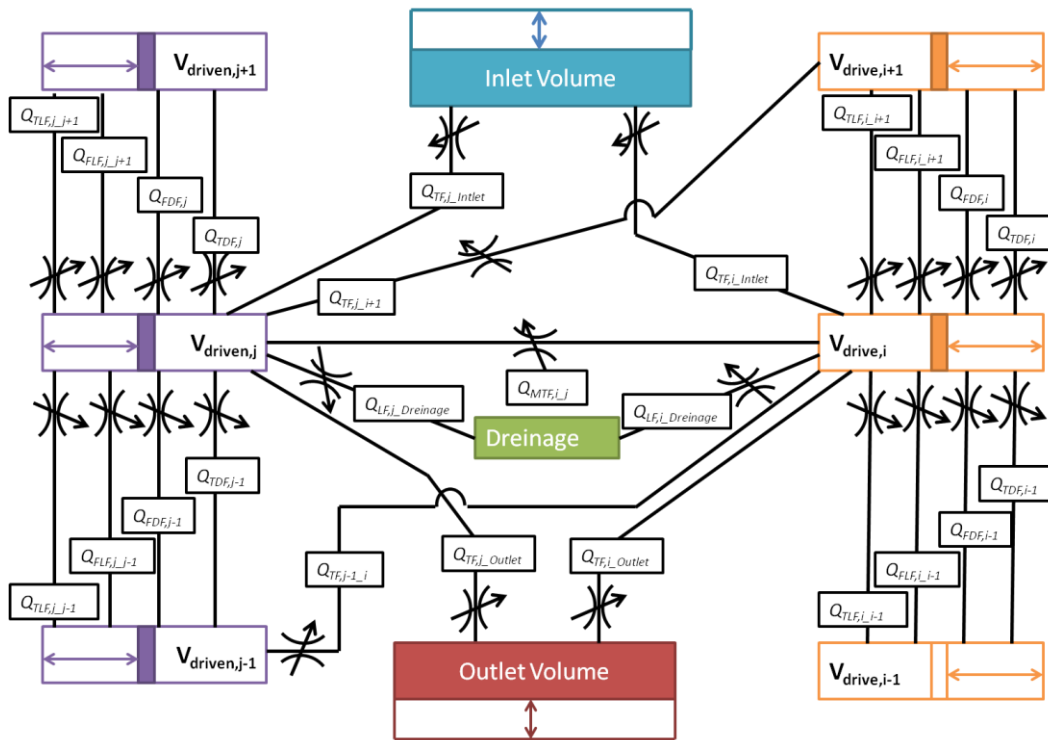
Figure 24. Scheme of exchanged flows by reference volumes.

Nomenclature	Description
LF	Laminar Flow
TF	Turbulent Flow
MTF	Meshing Turbulent Flow
TLF	Tip Laminar Flow
FLF	Flank Laminar Flow
FDF	Flank Drag Flow
TDF	Tip Drag Flow

Table 3. Nomenclature of the model flow rates.

The two indexes i and j, are respectively associated to the drive gear and the driven gear. The three types of flows are indicated with capital letters; T is used for turbulent flows, L for laminar flows and D for drag flows. Considering the rotational directions of the pump gears, the *+1* indexes represent the control volumes that precede the reference

volumes i and j; on the other hand, -1 indicates the volumes that follow the reference volumes. It is clear, looking at Figure 24, that each control volume of the gear pockets is linked with eight different volumes and thirteen flows are needed for a proper definition of a continuity equation. Taking the reference volume of the drive gear, let us see how these flows are allocated to the eight volumes. There are four flows for each adjacent control volumes (preceding volume: Q_{TLF,i_i+1}, Q_{TLF,i_i+1}, $Q_{FDF,i}$, $Q_{TDF,i}$; following volume: $Q_{TLF,i-1\_i}$, $Q_{TLF,i-1\_i}$, $Q_{FDF,i-1}$, $Q_{TDF,i-1}$), due to the axial and radial clearances which the gear teeth have in respect to the pump housing. Furthermore, the reference volume of the drive gear is linked with two control volumes of the driven gear by two turbulent flows (Q_{TF,i_j}, $Q_{TF,j-1\_i}$). Finally, the three remaining flows concern the connection with the outlet (Q_{TF,i_Outlet}), inlet (Q_{TF,i_Inlet}) and drainage volumes ($Q_{LF,i\_Drainage}$). Figure 25 represents the numbering system of the control volumes of the gear pump pockets and the inlet and outlet volume. The flow parameters that will be displayed in the following pages are referred to the control volume number 18 for the drive gear and number 35 for the driven gear.
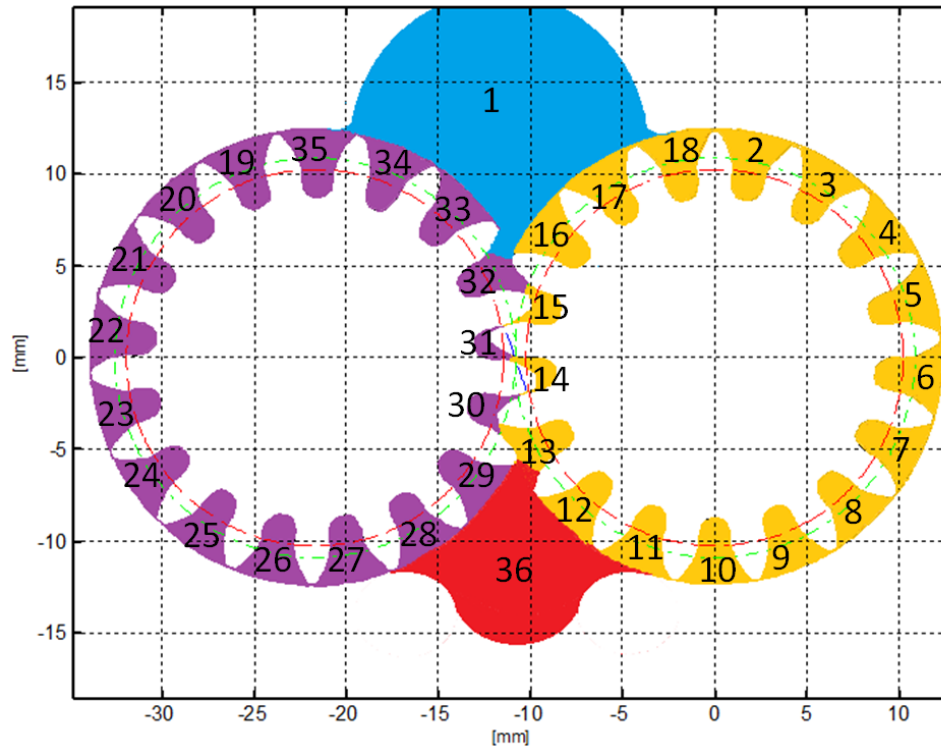
Figure 25. Numbering system of gear pump control volumes-

Let us start to see the laminar and drag flows exchanged by the adjacent gear pockets (Figure 26).
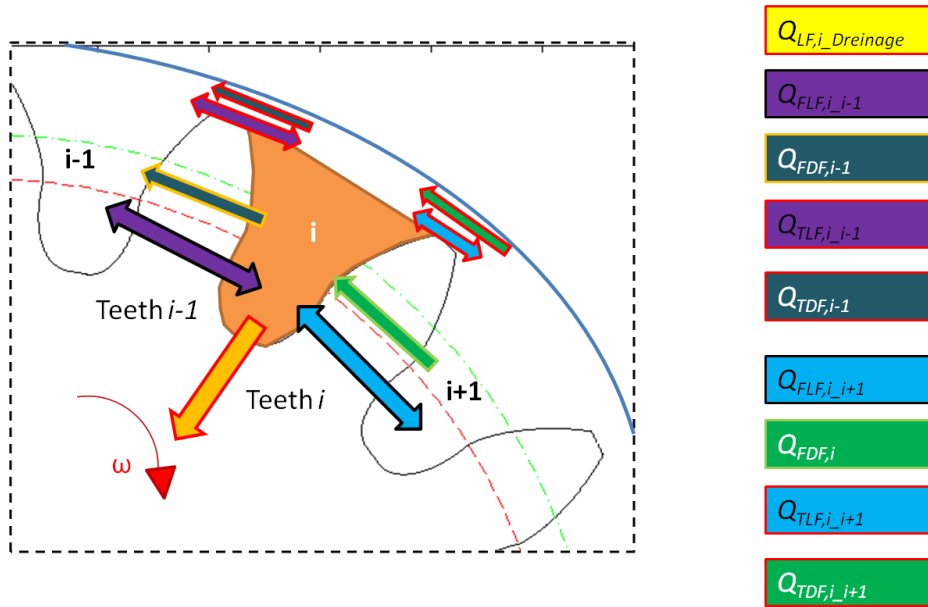
Figure 26. Laminar and drag flows of adjacent gear pockets.

The first flow analyzed, is the drainage flow($Q_{LF,Drainage}$), as it is fundamental for the hydrodynamic bushing that supports the gear shafts. The flow rate moves from the pockets to the gear center, where the hydrodynamic bushing is located. This flow is usually quite low, even when there is a high-pressure gradient between the drainage volume and pockets. This is due to the small height of the equivalent drainage pipe. The features of the equivalent drainage pipe are steady during the gear pump rotation; they are reported in Table 4. The geometrical feature of the pipe are displayed in Figure 27. It is clear, looking at the image, that the pipe height is the axial clearance, the pipe width is the peripheral step computed in correspondence of the minimum teeth radius, and the pipe length is the distance between the minimum teeth radius and the pump shaft radius.

Feature of equivalent drainage pipe	Value
Height	5µm
Width	3.2mm
Length	3.2mm

Table 4. Features of equivalent drainage pipe.
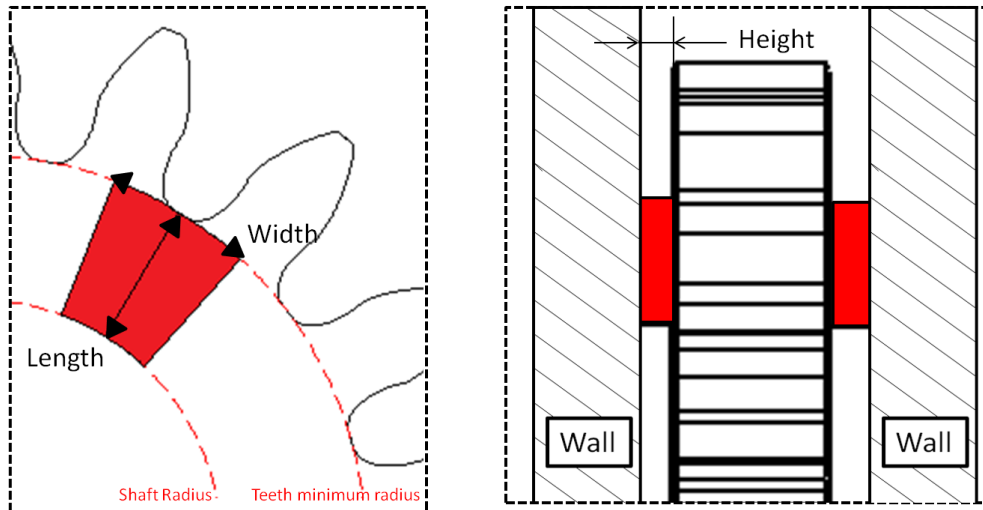
Figure 27. Geometrical feature of equivalent drainage pipe.

The second flow to analyze is the flank laminar flow, which has a variable geometry during rotation. That happens because on the upper and on the middle plate, which contain the high-pressure pump gear pair, there are two milling grooves. The first one is located on the inlet side, while the second one is on the outlet side; the latter is called "epsilon groove" due to its design (Figure 28). The grooves on the inlet side are as deeper as those on the outlet side, although the grooves on the upper plate are deeper when compared to the grooves on the middle plate. The depth of the milling machinery on the middle plate is 0.2mm and 0.5mm on the upper plate. The minimum height of the equivalent pipe defined on the flank teeth is defined by the axial clearance, which is 0.05mm. Figure 29 displays the trend of the heights of the equivalent pipe for the reference volume "i". The ascending and descending curves

that connect the minimum and maximum heights of the flank laminar flow are defined by using polynomial laws. The polynomial laws have been identified by a validation procedure.
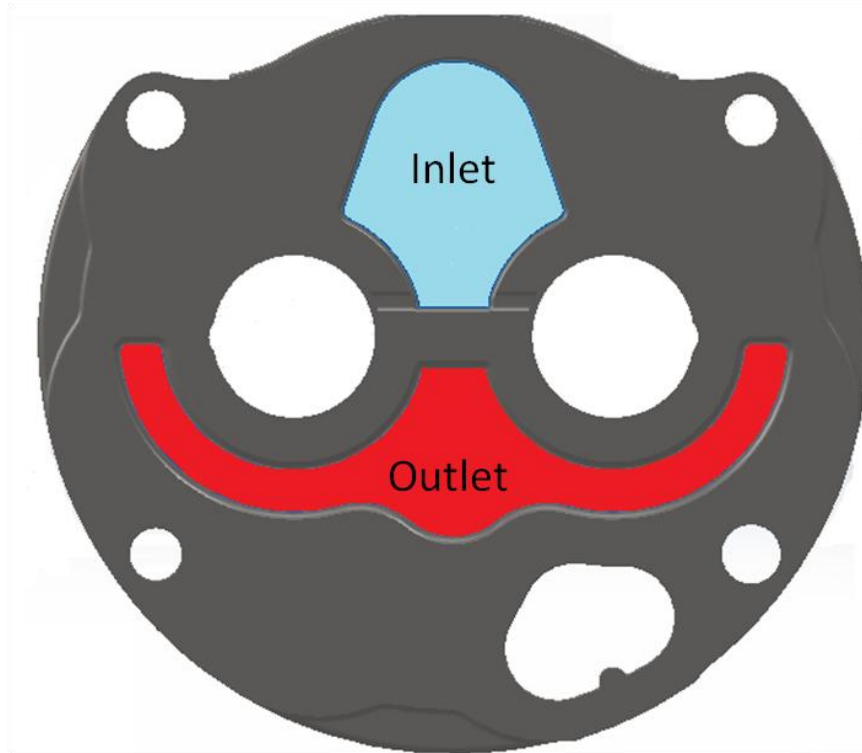
Figure 28. Milling grooves (cyan for inlet and red for outlet) on the middle plate.
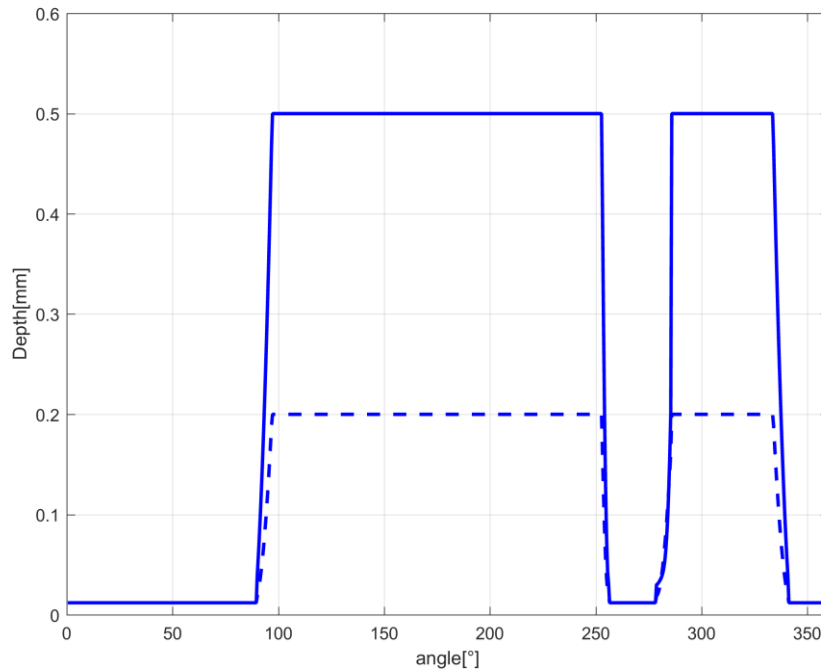
Figure 29. Depth of the equivalent pipe for the control volume "i" (straight line for upper side and dotted line for the lower side)

The equivalent pipe has a further variable parameter during the pump rotation, as the pipe width is conditioned by the gear meshing. As it will be explained later on, the control volume of the gear pockets is variable during rotation, thus also the equivalent pipe on the gear flank must be properly defined. When a gear tooth is included between two control volumes that are not involved in the meshing process, the axial clearances on the upper and middle plate are constant. For that reason, the equivalent pipe width can be expressed as the difference between the maximum and minimum teeth radius; on other hand, the value of the maximum teeth radius is replaced by an average value. The average value is computed by using the maximum radius of the control volumes that contain the teeth as shown in Figure 30. Considering the control volumes "i+1", "i" and the teeth included in between as a

reference, the trend of the equivalent pipe width for the reference teeth is shown in Figure 31.
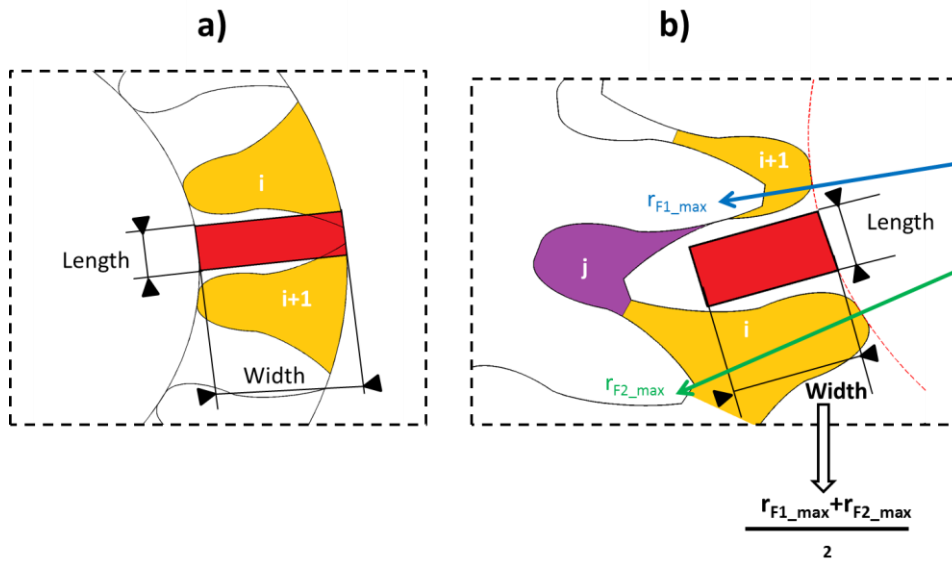
Figure 30. Flank equivalent pipe during non-meshing phase a) and meshing phase b)
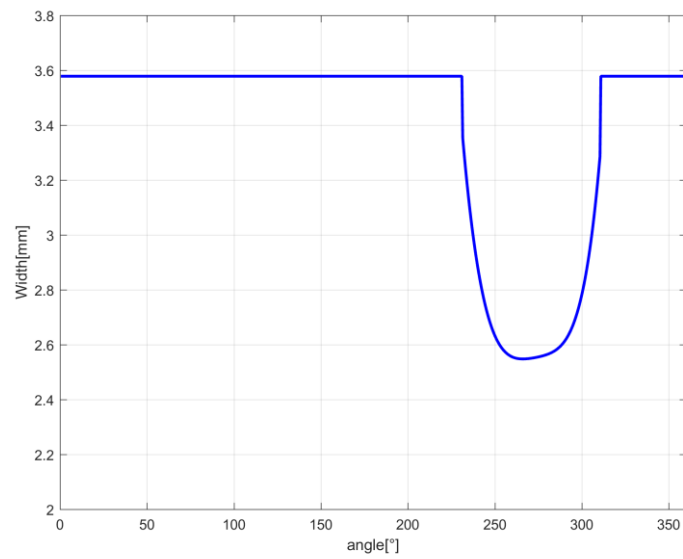
Figure 31. Width of the equivalent pipe on the teeth flank, for the reference tooth "i".

The length of the equivalent pipe of the gear flank is kept constant during pump rotation; this value is compute by means of a weighted average. The teeth flank has been divided in three sections: the first one is delimited by the root radius and the start of the trochoidal profile; the second one is the tooth profile that contains the whole trochoidal profile; the last profile is the teeth tip which joins up the trochoidal profile and the tip diameter. For each section, an average length is computed, and the equivalent pipe length is then obtained by using the weighted average in respect to the section width, as shown in Figure 32. The length of the equivalent pipe of the gear flank is represent by Eq(13). The features of the equivalent pipe of the gear flank are summarized in Table 5

$$l_{FLF,i\_i+1} = \frac{(r_{S1} - r_{root})l_{meanS1} + (r_{S2} - r_{S1})l_{meanS2} + (r_{S3} - r_{S2})l_{meanS3}}{(r_{S1} - r_{root}) + (r_{S1} - r_{S2}) + (r_{S1} - r_{S3})} \quad (13)$$
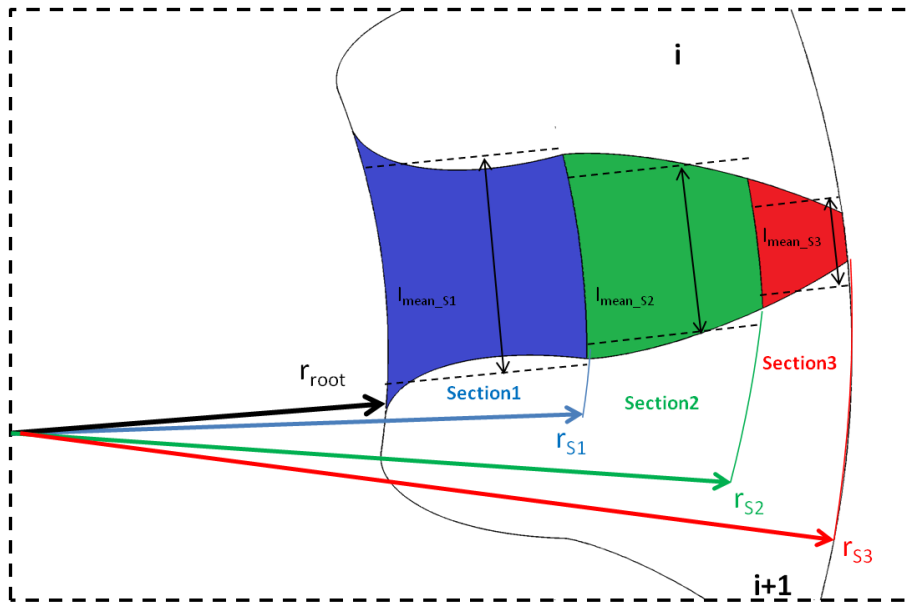
Figure 32. Sections of the gear teeth flank for evaluation of the equivalent pipe length.

Feature of equivalent gear flank pipe	Value
Height upper side	From 0.05mm to 0.5mm
Width upper side	From 3.58mm to 2.55mm
Length upper side	1.785mm
Height lower side	From 0.05mm to 0.2mm
Width lower side	From 3.58mm to 2.55mm
Length lower side	1.785mm

Table 5. Features of the equivalent gear flank pipe.

The second flow which involves the gear flank is the drag flow ($Q_{FDF,i}$); the fundamental parameters for this type of flow are the axial clearance between the teeth and the seal plates and the extension of the velocity field. The epsilon groove and the gear meshing process make these parameter variable during the pump rotation, thus the approach implemented for the flank turbulent flow has been used also in these case. In essence, the heights of the equivalent flank pipes are the values of the axial clearances (Figure 29), and the width represents the extension of the velocity field (Figure 33).
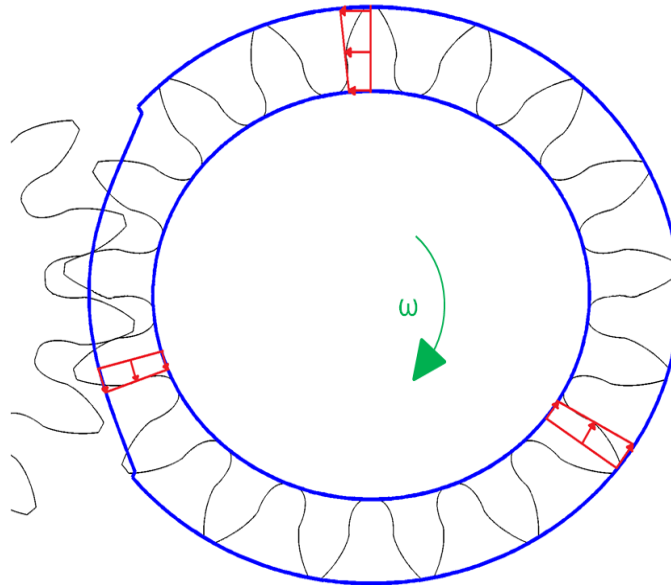
Figure 33. Diagram of the velocity field extension for the drag flow on the gear flank.

Let us move to analyzing the flows on the teeth tip. The laminar and the drag flows on the teeth tip are defined only when the teeth are included between the low-pressure seal (LPS) and the high pressure seal (HPS) Figure 34. Taking into account the angular reference from Figure 34, the angular extension of the teeth tip flow for both gears (drive and driven) is almost 297 degrees (-20.9° to 196.6°). The equivalent laminar flows pipes have only the pipe height as a parameter. It is variable if a flow exists, while the pipe width and pipe length are steady; the former is the gear width, while the latter is the length of the tooth tip.
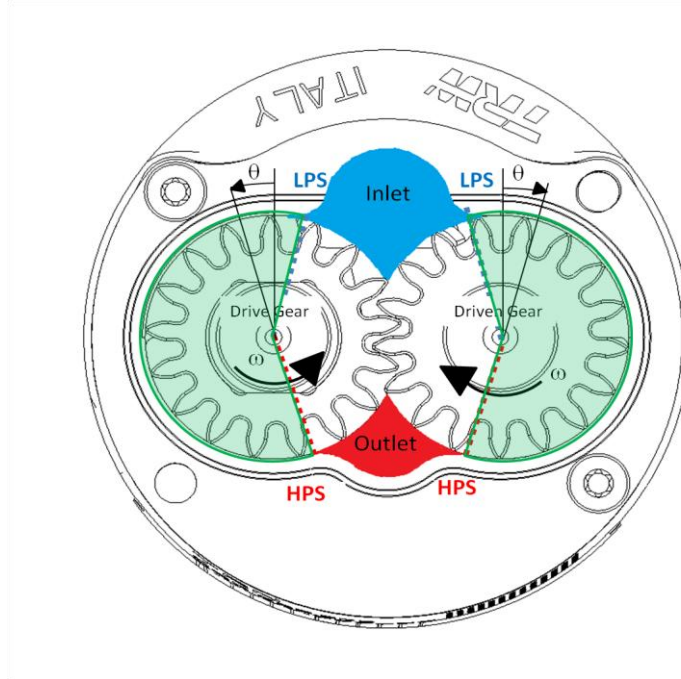
Figure 34. Angular extension of the teeth tip flows.

The pipe height is variable during rotation, because in operating conditions the pressure distribution around the gears moves the latter from their nominal position; thus, the eccentricity and the radial clearance between the gears and the gear housing generate a variable equivalent pipe (Figure 35). The pump designers computed and provided a set of eccentricity values for the pump gears; these values depend on the pump function mode and on the pump housing wear

rated. For validation purposes, the eccentricity values estimated for the "Mit" operational mode (X=-0.01mm Y=0.04mm) and the nominal dimension of the pump housing were considered; the case wear rate has been neglected. The trend of the equivalent pipe height is represented in Figure 36. The relevant feature of the teeth tip laminar flow are summarized in in Table 6. The geometrical features of the laminar tip flow have been used for the drag flows too.
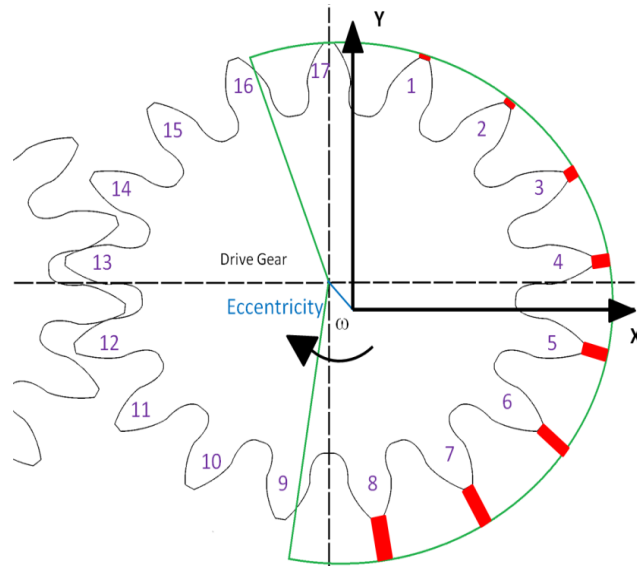
Figure 35. Representation of the equivalent pipe on the teeth tips.
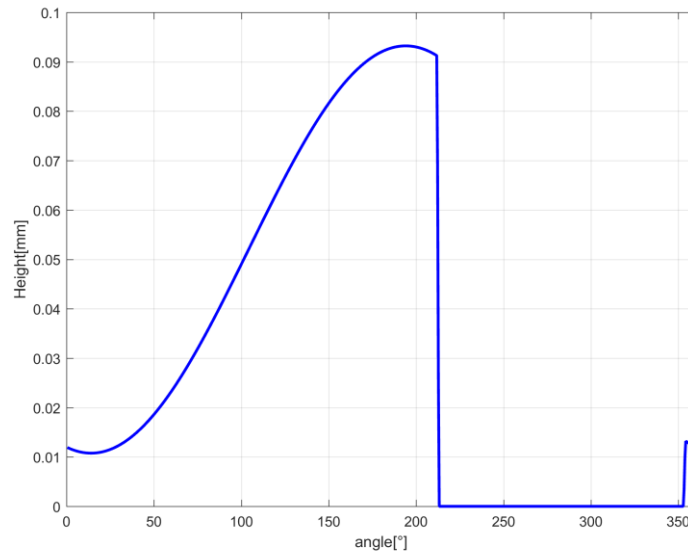
Figure 36. Height of equivalent pipe on the gear teeth, for the reference tooth "i".

Feature of equivalent pipe on the teeth tip	Value
Height	From 0mm to 0.094mm
Width	4mm
Length	0.47mm

Table 6. Feature of the equivalent pipe on the teeth tip.

The descriptions of the laminar and drag flows are concluded; the next flows it is going to be the turbulent flows. Considering the drive gear control volume "i", there are four turbulent flows to analyze. The first flow analyzed concerns the connection with the outlet environment (Q_{TF,i_Outlet}); this connection starts when the pockets of the control volume "i" cross the HPS line, and ends when the control volume "i" is linked to the control volume "j-1" of the driven gear. These phases are represented in Figure 37. The turbulent flow depends on the cross-section area of the connection surface. In this particular case, the connection surface height is steady and depends on the gear width, while the cross-section width can be either a segment or an arch (Figure 38). The width is a segment when the teeth of the driven gear

goes through the control volume "i"; otherwise, it is an arch of a circumference. The segment length is obtained in a simple manner; it is the minimum distance between the teeth profiles of the drive and driven gears that are approaching the meshing phase. On the other hand, the extension of the arch of circumference is defined by the teeth tip and the HPS line.

The cross-section area trend for the outlet flow is represented in Figure 39.
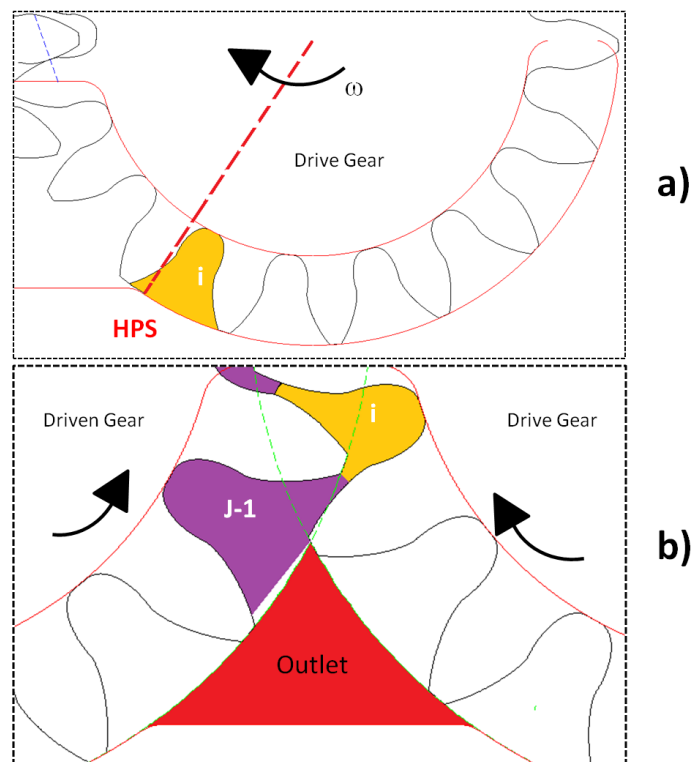
Figure 37. a) Beginning of the connection between the control volume "i" and outlet volume. b) Ending of connection between the control volume "i" and the outlet volume.
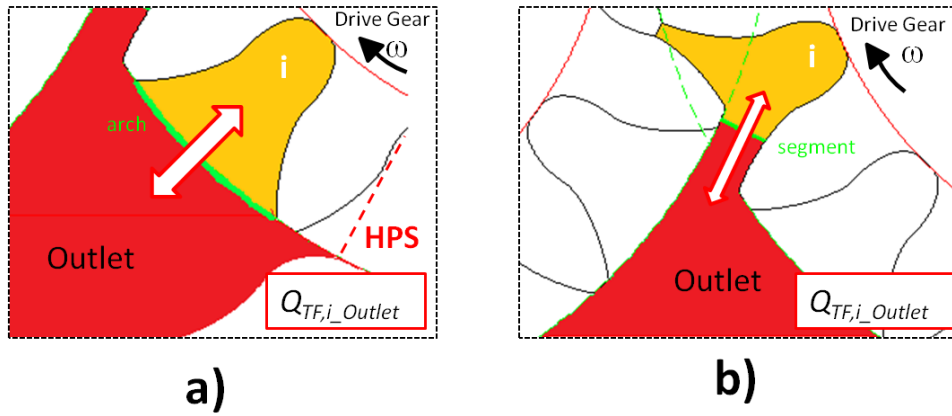
Figure 38. Representation of the $Q_{TF,i\_Outlet.}$ for the both section area width a) arch b) segment.
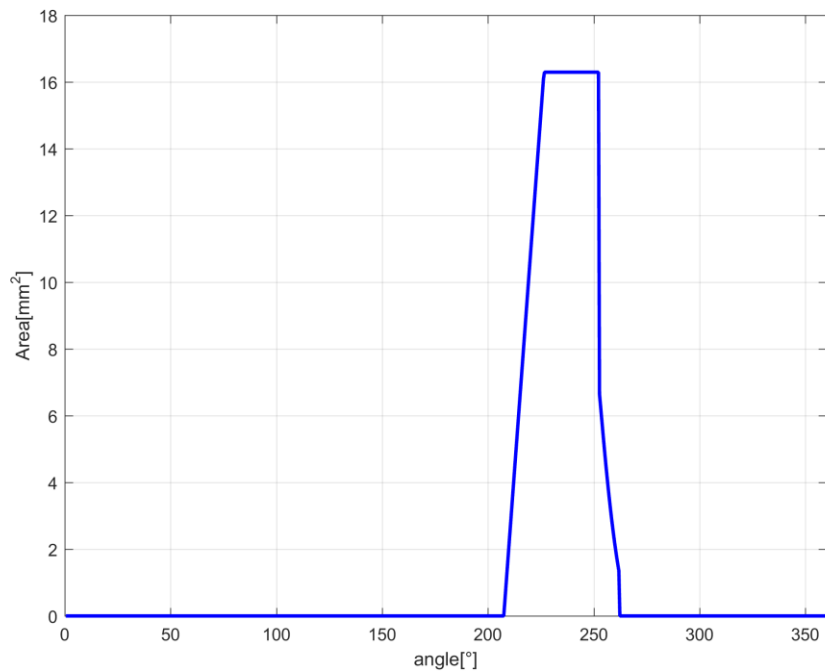
Figure 39. Cross-section area of the turbulent outlet flow, for the reference volume "i".

The minimum distance approach has been used also for the Q_{TF,i_j}, Q_{TF,i_j-i} flows. During the pumping phase, the reference control

volume "i" communicates with the outlet volume, and starts to decrease its dimensions. This decrease is due to the penetration of the tooth "j" of the driven gears within the control volume "i"; this fact causes the hydraulic resistance of the outlet flow (Q_{TF,i_Outlet}) to increase, and it generates a further turbulent flow Q_{TF,i_j} (Figure 40). The cross-section area of this flow is characterized by the lateral clearance between the teeth flank, and Figure 41 represents the trend of this area for the control volume "i" during pump rotation.
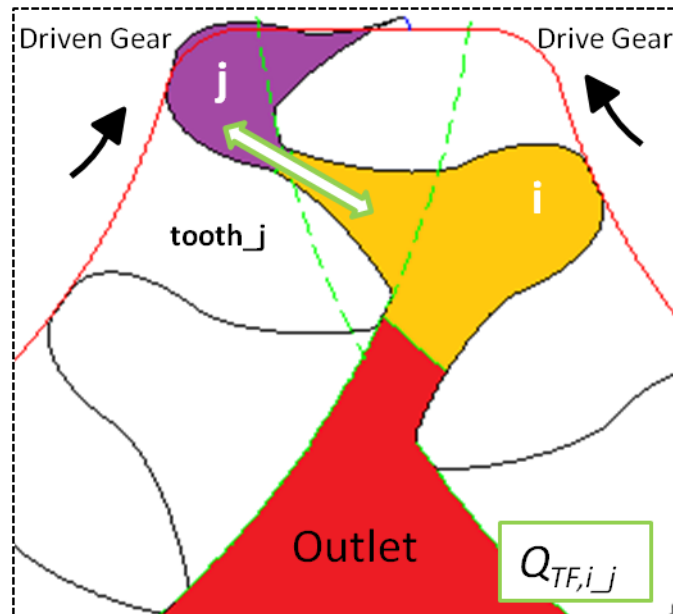
Figure 40. Representation of the $Q_{TF,i\_j\ flow.}$
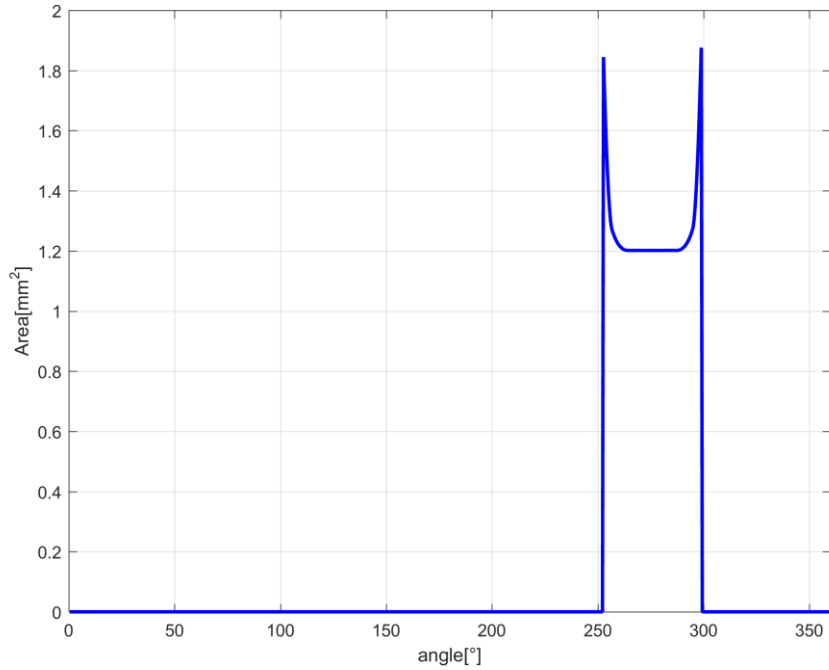
Figure 41. Trend of the connection Area between the reference volume "i", "j".

Since the reference volume "i" ends its connection with the outlet volume, when a new connection begins, $Q_{TF,i\_j\text{-}1,}$ must be taken into account. When the "i-1" tooth meshes the "j" tooth, the connection area between the "i" and "j-1" volumes does not exist, and the communication cannot be allowed. The $Q_{TF,i\_j\text{-}1}$ connection resumes when the "i-1" and "j" teeth stop meshing each other, and ends when the control volume "j" starts to communicate with the inlet volume. The flow is represented in Figure 42, while the flow interruption during the meshing phase and the trend of cross-section are shown respectively in Figure 43, Figure 44.
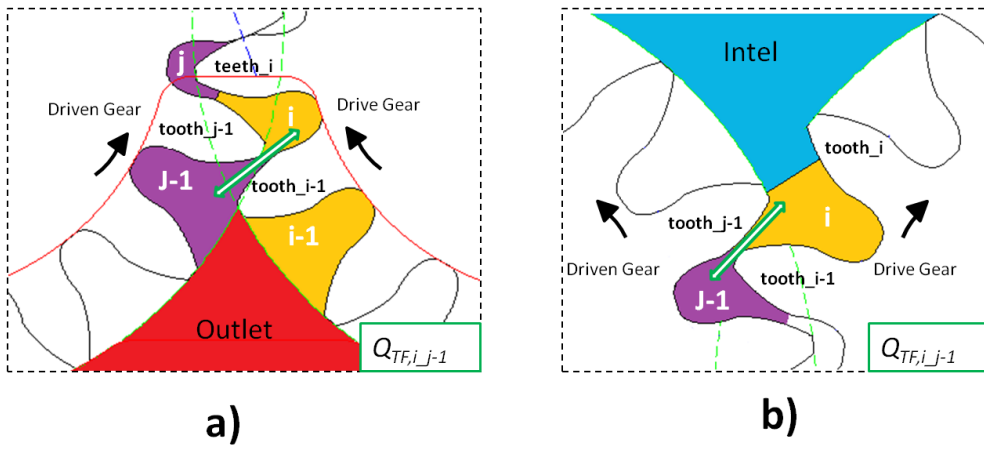
Figure 42. a) Q_{TF,i_j-1}, Beginning condition. b) Q_{TF,i_j-1}, ending condition
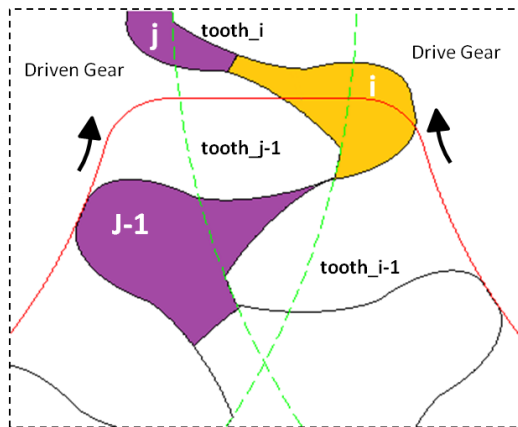
Figure 43. Interruption of the Q_{TF,i_j-1}, flow due to the gears meshing.
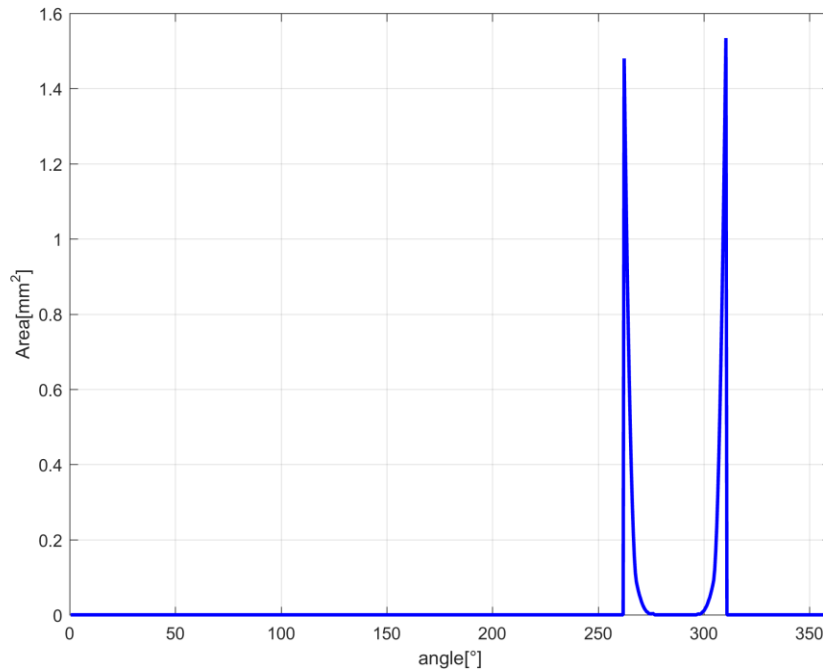
Figure 44. Connection area between volume "i" and "j-1".

The last flow analyzed is the turbulent flow between the control volume "i" and the inlet volume (Q_{TF,i_Inlet}). This flow is responsible for the pump suction; it starts when the control volume "i" communicates with the inlet volume, and finishes when the "i-1" tooth crosses the low pressure sealing line, LPS (Figure 45). As we have already seen in the case of the Q_{TF,i_Outlet} flow, the width of the cross-section area is defined by using the minimum distance approach. This approach is used during the increasing phase of the control volume "i"; on the other hand, when the volume reaches a steady condition, the width of the cross-section area is an arch of circumference. The communication area between the control volume of the drive gear and the inlet volume is represented in Figure 46. Finally, Figure 47 contain the trend of communication area between the inlet volume and the reference volume "i".
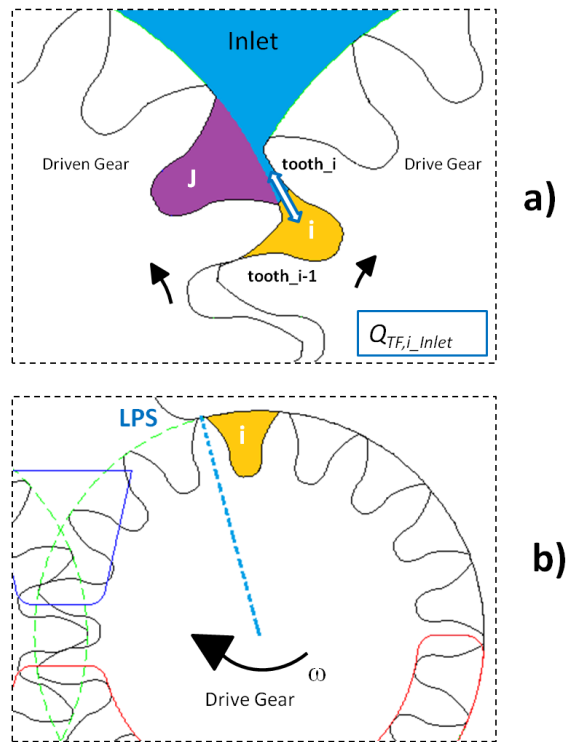
Figure 45. a) Beginning of connection between the control volume "i" and the inlet volume. b) Ending of the connection between the control volume "i" and outlet volume.
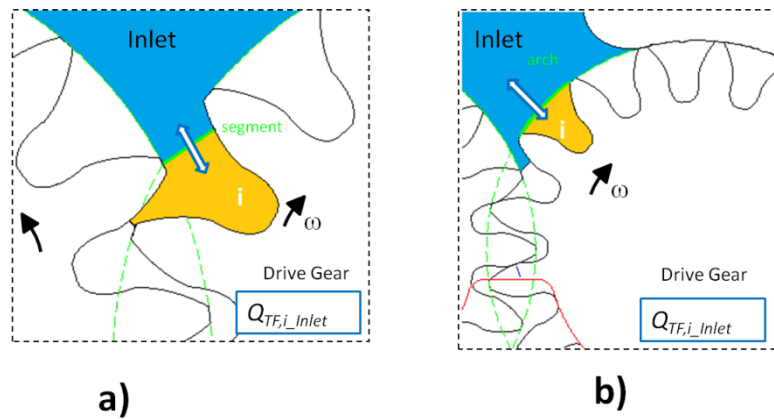

Figure 46. . Representation of the $Q_{TF,i\_Inlett.}$ for the both section area width a) segment b)arch.
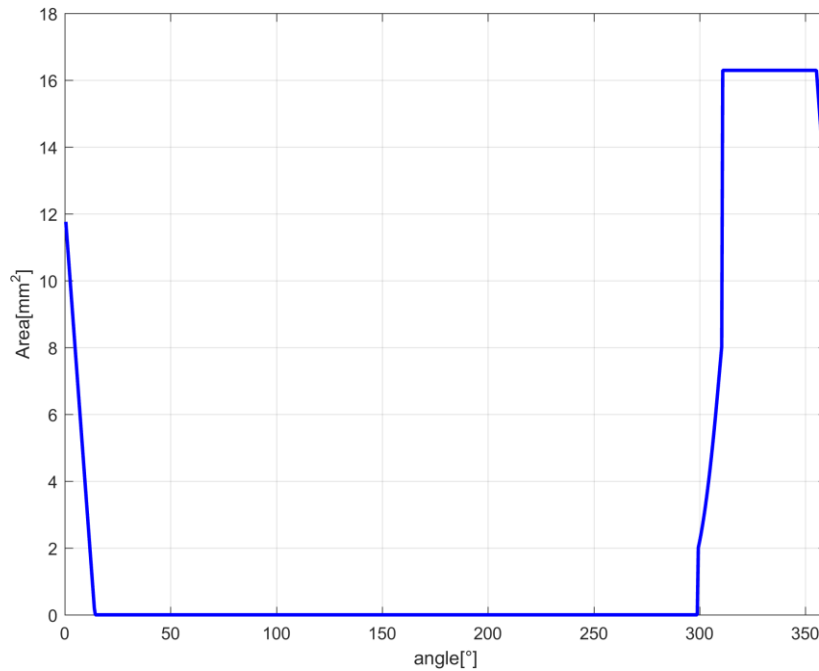
Figure 47. Cross-section area of the turbulent inlet flow, for the reference volume "i".

A.2.4. Definition of the Control Volumes as a Function of Gear Position

In this chapter, we will describe the control volumes that define the external gear pump model. The proper definitions of these volumes is essential for the model to be correct; they are the value of the control volume and the volume variation ($dV/d\theta$). The high-pressure pump model contains 37 control volumes. Only one of them is steady during a complete rotation (Outlet pipe volume) of the gear pump; the remaining 36 volumes, define the pumping action of the external gears pump by means of the geometry variation. The first volumes analyzed are the gear pockets volumes of the drive and driven gears. The cross-section area of the gear pockets volumes is defined by the empty space between two consecutive teeth (Figure 48); this area varies during the pump

rotation, because of the meshing phase. The decrease of the cross-section area is due to the teeth penetration, and the cross-section area geometry is obtained by calculating the minimum distance between the profiles of the teeth that are meshing together (Figure 49).
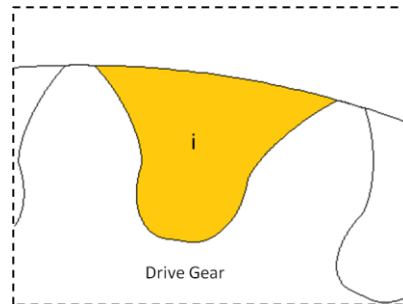

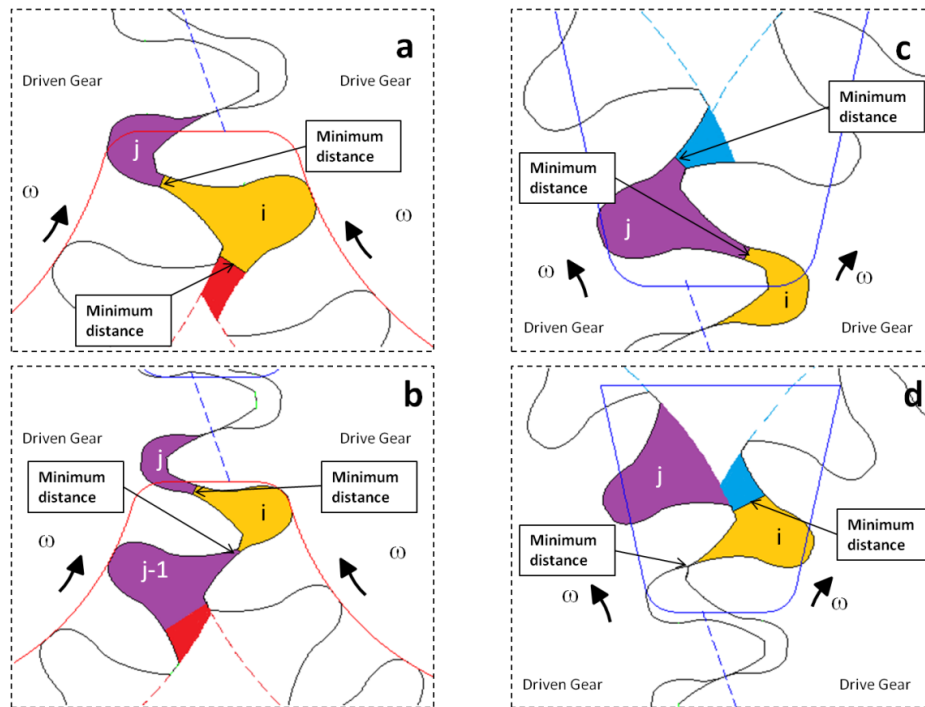Figure 48. Definition of the gear pocket cross_section area. For the reference volume "i"

Figure 49.Definition of the cross_section area of the gear pockets volume. a) Decreasing of the gear pocket "i", b) Decreasing of the gear pocket "j-1",c) Increasing of the gear pocket "j", d) Increasing of the gear pocket "i".

The definition of the cross-section area of the gear pockets made using the minimum distance approach involves also the definition of the inlet and outlet volume. Indeed, in order to preserve the continuity of the oil volume during the meshing phase, the part excluded by the new definition of the gear pockets (The red and blue area of Figure 49) must be associated respectively to the outlet volume if the gear pocket is decreasing (beginning of the meshing) its own volume, or to the inlet volume if the gear pocket is increasing (ending of the meshing phase) its own volume. A further feature that can be taken into account for the definition of the cross-section area is the radial clearance between the gear teeth and the pump housing. It causes a sinusoidal contribution in the definition of the gear pocket volume, due to the eccentricity between the gear position and the gear housing; in this particular case, this factor is negligible. Finally, the last feature of the gear pockets volume definition is the volume height, which has two contributions. The first one is steady and corresponds to the gear height; the second one is variable, and depends on the epsilon groove. As we have seen in the previous chapter for the laminar flow on the gear flank, the epsilon grooves increase the height of the gear pocket volume. The trend of the drive and driven gear pockets control volume "i" and "j" are represented in Figure 50.
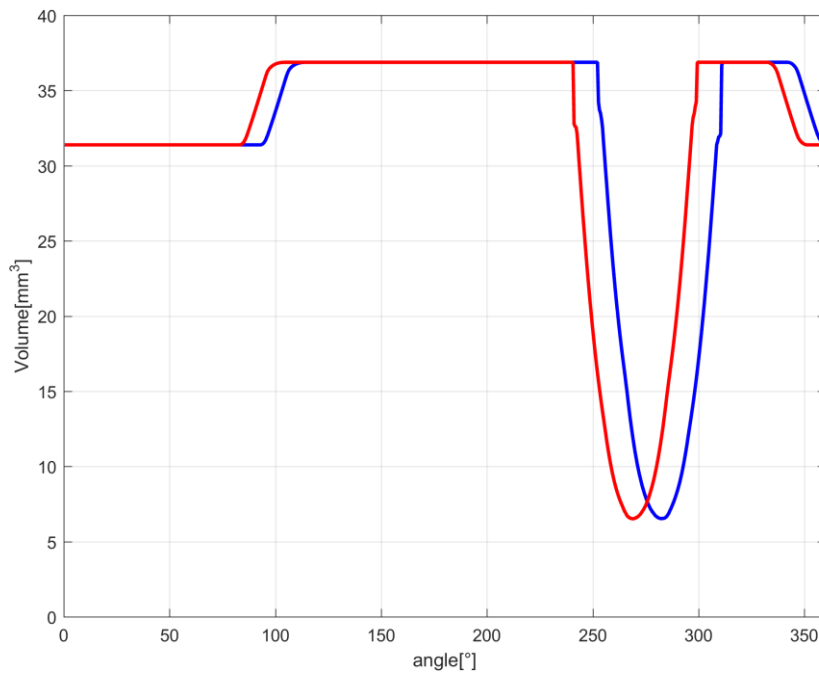
Figure 50. Control volume values for the reference pocket of the drive gear (blue line) and for the reference pocket of driven gear (red line).

The first control volumes increment is due to the epsilon groove on the outlet side: the gear pockets begin to put themselves forward on the milling grooves; after that, the gear pocket volumes reach their maximum values. Just as the meshing phase begins, the gear pockets start to pump the oil to the outlet volume by decreasing their volumes. During the release meshing phase, the gear pockets volumes return to their maximum values. Finally, there is a further reduction of the volumes when the cross-section areas of the gear pockets are no longer influenced by the epsilon groove of the inlet side. The evolution of the gear pockets volume during a complete run of the gear pump defines the evolution of the gear pockets volume derivative, but there are some aspects that need to be examined carefully, in order to avoid non-physical phenomena. First, when considering the beginning of the meshing phase, the gear pocket volume trend decreases sharply (Figure 51 a)); this leads to a sudden variation in the volume derivative (Figure

51 c)). This kind of discontinuity is not physical, but depends on the definition of the control volume; thus, the first value of the volume derivative has been neglected. The same observation must be done for the meshing releasing where the volume suddenly stops increasing (Figure 51 b), c)). This kind of sharp trends leads to a pressure spike in the gear pocket volume and in the pump pressure ripple. On the other hand, the volume variations due to the epsilon grooves are very smooth, and do not lead to a derivative discontinuity.
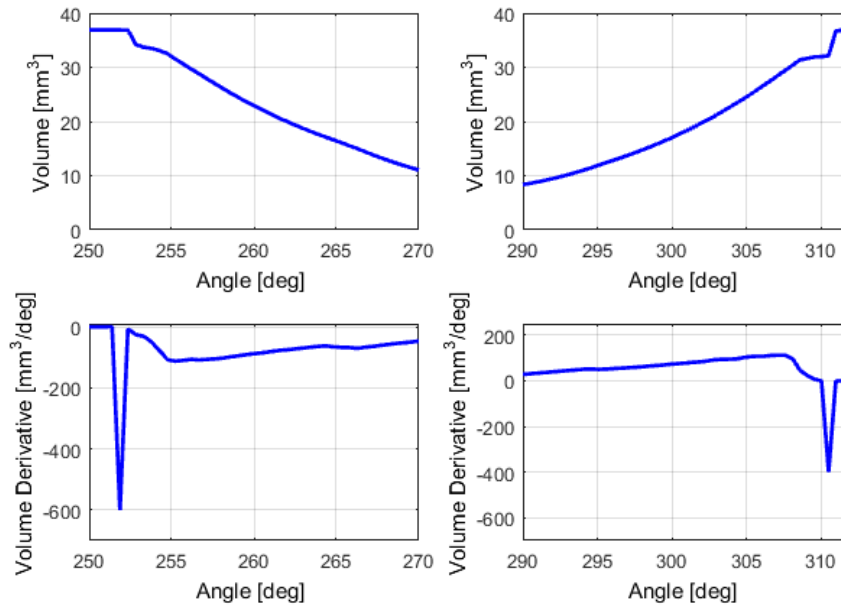
Figure 51. Sudden variations in volume derivative of gear pocket volume. a) Gear pocket volume "i" during the beginning of the meshing phase, b) Gear pocket volume "i" during gear meshing release. c) Derivative discontinuity due the definition of the gear pocket volume "i" during the beginning of the meshing phase. d) Derivative discontinuity due the definition of the gear pocket volume "i" during the releasing of the meshing phase.

The volume derivatives of the gear pockets "i" and "j", which have been implemented in the numerical model, are shown in Figure 52.
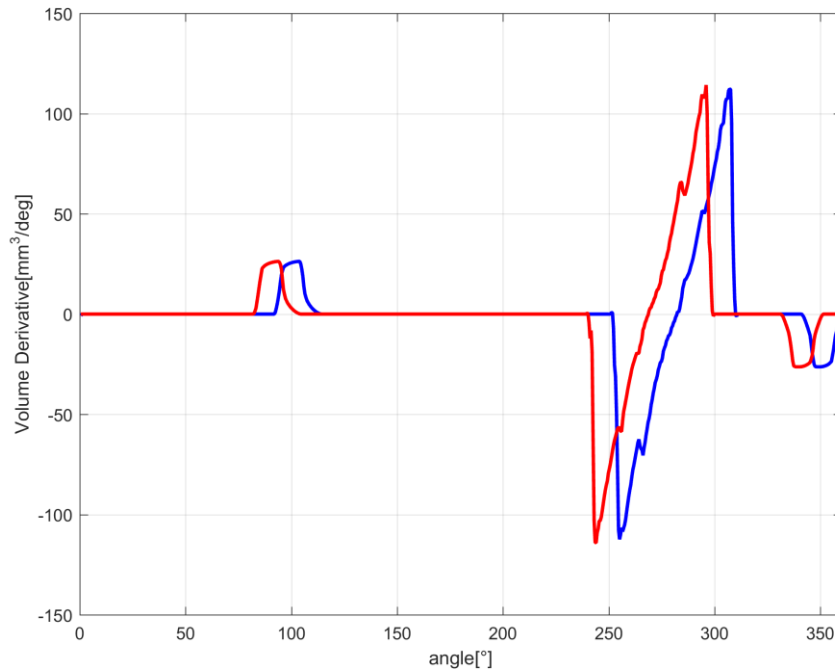
Figure 52. Values of the volume derivatives for the reference pocket of the drive gear (blue line) and for the reference pocket of driven gear (red line).

The second volume we analyzed is the outlet volume, which is relevant for the pumping action. This volume is composed by two contributes; the first is steady, while the second one varies during a pump rotation. By looking at a front view of a high-pressure pump, the cross-section area of the first contribute is represented in Figure 53 and its value is 45,42mm, while the height is defined by the gear width and the epsilon groove depth (4,7mm). Furthermore, this steady portion of the outlet volume is linked to the outlet pipe volume through a 6mm-wide hole. The volume contribute of the second portion is less relevant than that of the first portion, but it is essential for the pumping action, as it determines the derivative terms of the outlet volume. The second contribute of the outlet volume is due to the oil volume conservation during the meshing phase of the gear teeth. The definition of the gear pocket volumes made using the minimum distance approach during the

meshing phase leads to associating a portion of the oil volume to the outlet volume, in order to preserve the overall oil volume into the high pressure pump, as it is shown in Figure 53 b) for a drive gear pocket and Figure 53 c) for a driven gear pocket. This issue can be sorted out as explained in reference [20], where the derivative term of the second outlet volume contribution is taken into account in the continuity equation of the gear pocket volume. Unfortunately, this subdivision of the oil volume might introduce spikes in the derivative term of the outlet volume; that is not physically correct; thus, a smoothing method for the derivative term is needed. The outlet volume and the derivative of the outlet volume are shown respectively in in Figure 54, Figure 55.
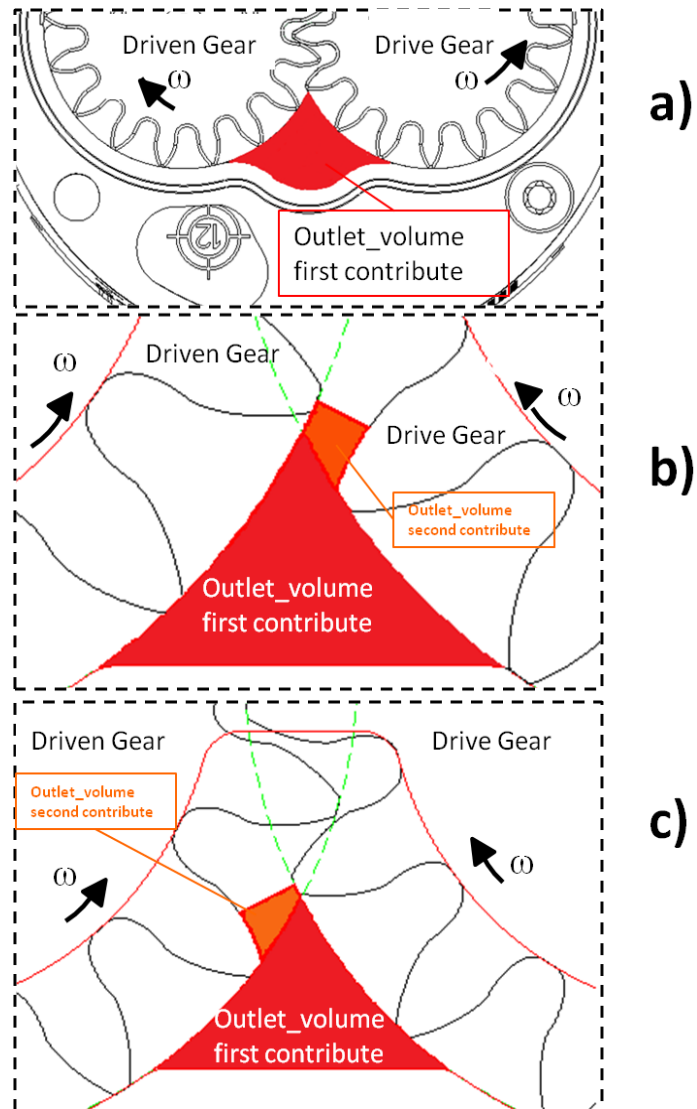
Figure 53. Definition of the outlet control volume, a) steady contribute, b) second contribute of the drive gear, c) second contribute of the driven gear.
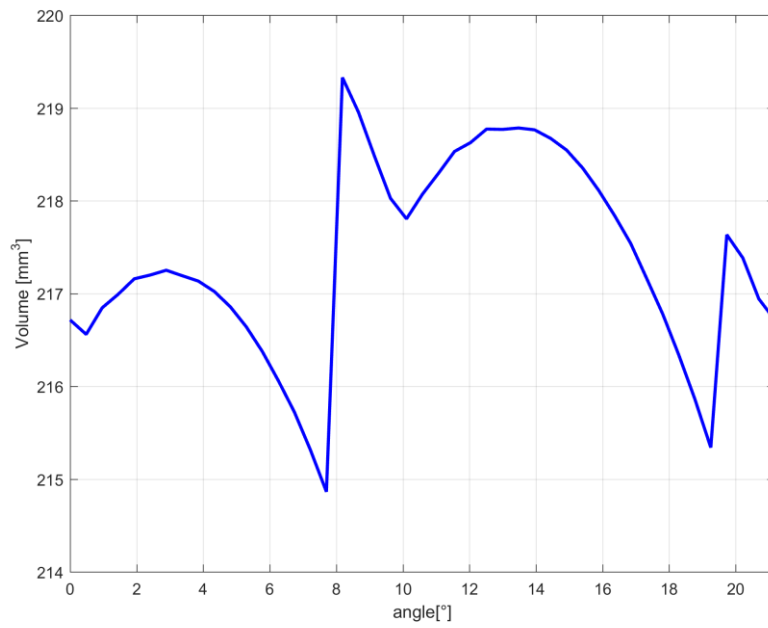
Figure 54. Outlet Volume values during a complete turn of the gear pump.
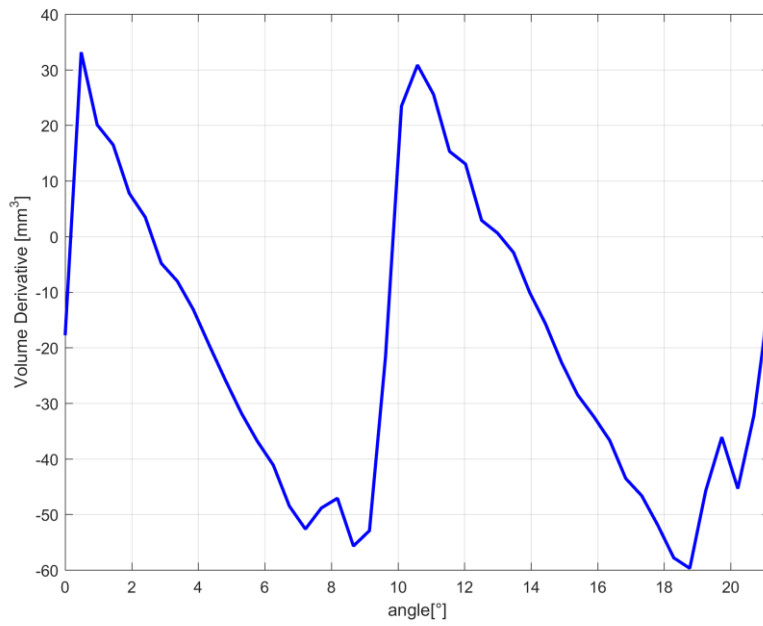

Figure 55. Derivative of the outlet volume during a complete turn of the gear pump.

The third volume involved in the model is the inlet volume, which moves the oil pump from the oil reservoir to the gear pocket volumes. As we saw previously for the outlet volume, the inlet volume is also composed by two contributes. The main volume contribute is steady during the pump rotation (Figure 56 a); on the other hand, the smaller, but most important contribute for the volume derivative point of view, is defined by the partitioning of the overall oil volume during the meshing release (Figure 56 b), c)). The cross-section area of the first contribute is bigger than the cross-section area of the outlet volume, and its estimated value is 108mm^2; this area is also the connection area to the oil reservoir. The height of volumes contributions is defined by the gear width and the epsilon groove depth (4,7mm). The height values for the inlet control volume (Figure 57) and the volume derivate obtained through the smoothing method (Figure 58) lead to a pressure ripple characterized by a low amplitude.
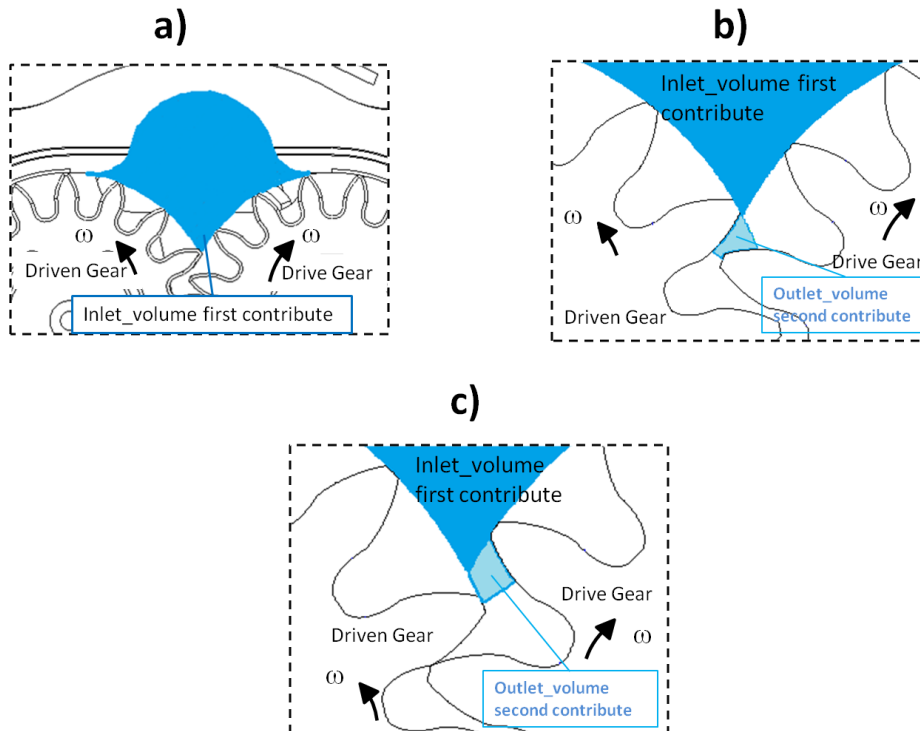

Figure 56. Definition of the inlet control volume, a) steady contribute, b) second contribute of the drive gear, c) second contribute of the driven gear.
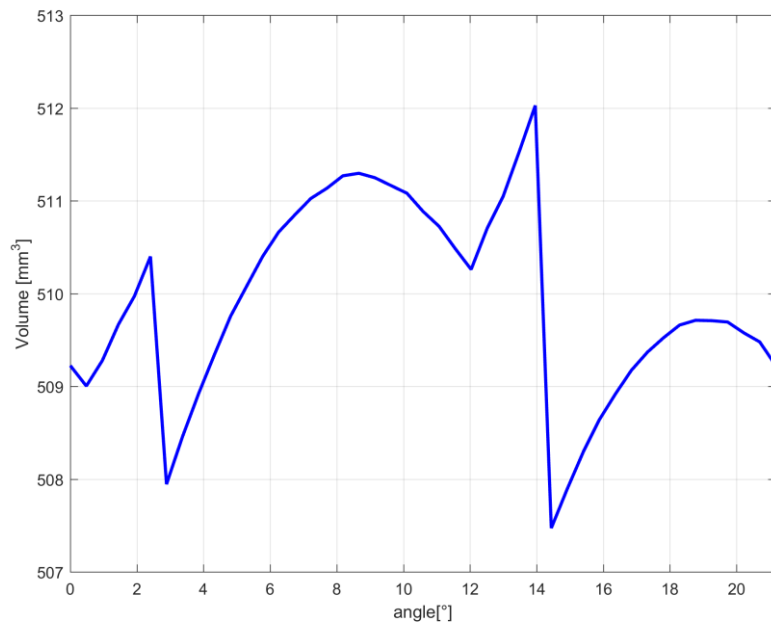
Figure 57. Inlet Volume values during a complete turn of the gear pump.
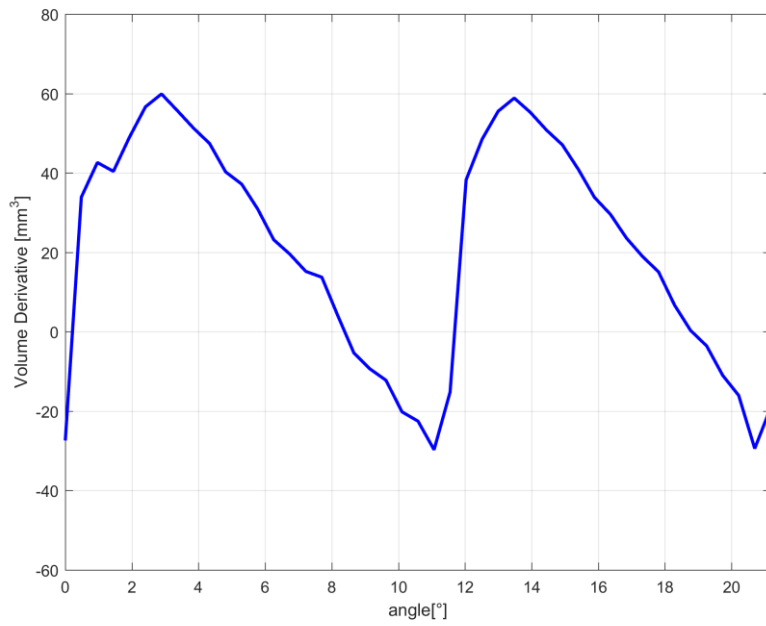

Figure 58. Derivative of the outlet volume during a complete turn of the gear pump.

Finally, the last control volume we will consider is the flexible pipe that starts from the outlet volume of the gear pump and finishes to the oil pressure servo control valve. The flexible pipe intercepts several components, such as the pressure transducer, the oil filter, the positive displacement flow meter and the servo control valve. The modifications of the pipe section caused by these components have been neglected in this model; thus, the principal features of these control volume are the flexible pipe diameter (6.5mm), the overall pipe length (2,9m) and, of course, the pipe volume ($9.62*10^{-5}m^3$). Figure 59 shows the components placed on the outlet pipe of the test bench.
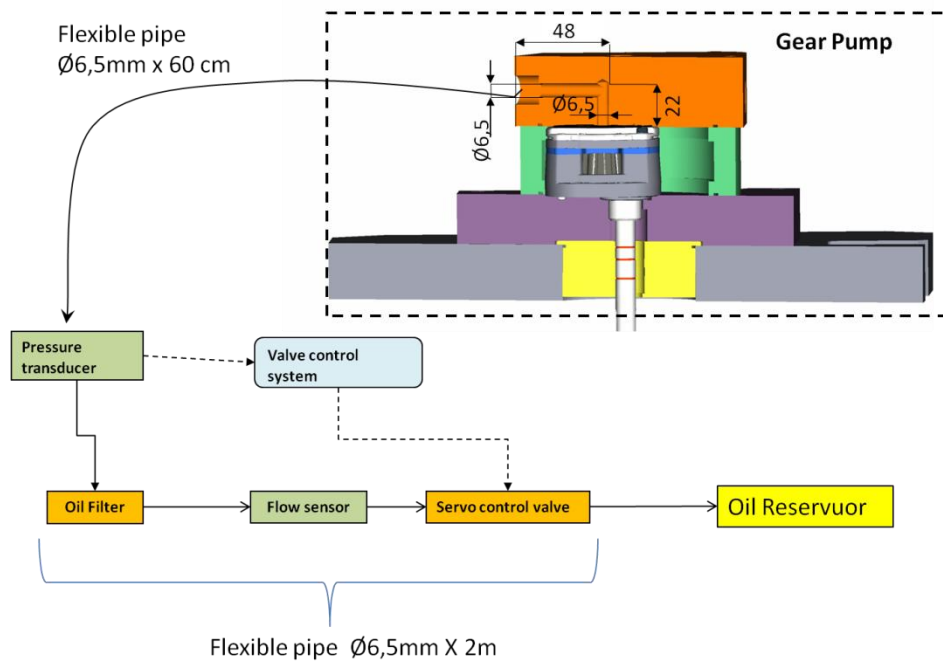

Figure 59. Scheme of the flexible pipe path.

A.2.5. Oil properties

The control volumes continuity equations of the contain three fundamental oil properties. The first property is the oil density, which appears in the turbulent flow equations. The oil manufacturer provides the thermodynamics equations, Eq(14), for the oil density evaluation in function of pressure and temperature.

$$\rho(p,T) = \frac{\rho(T)}{1 - a(1)\ln\left(\dfrac{a(2) + a(3)T + a(4)T^2 + a(5)T^3 + p}{a(2) + a(3)T + a(4)T^2 + a(5)T^3}\right)} \tag{14}$$

The numerator of Eq(14) ($\rho(T)$) is the oil density at the atmospheric pressure in function of the temperature only; these values are represented in Figure 60. On the other hand, the denominator terms are engineering coefficients and the oil pressure (p).
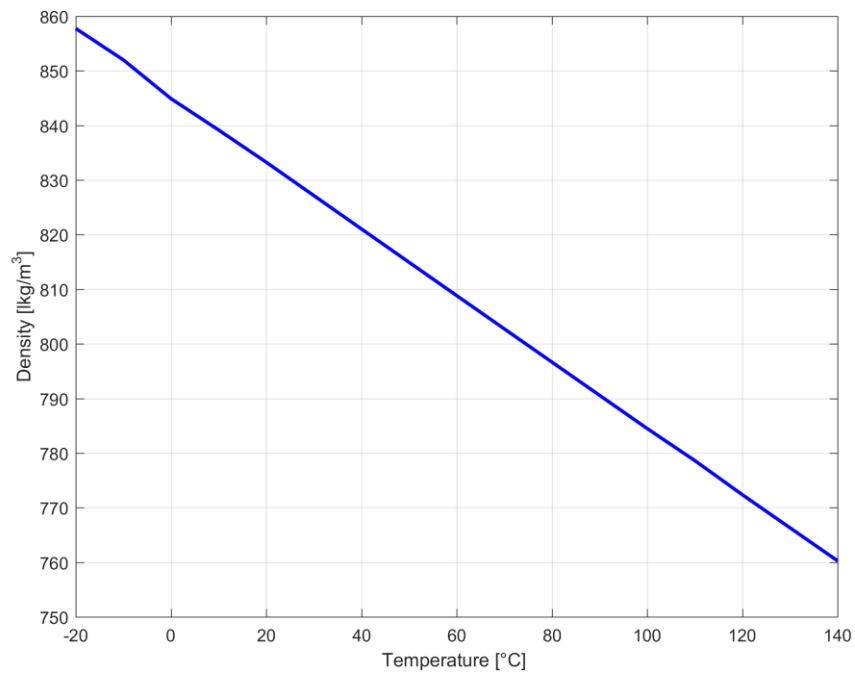

Figure 60. Oil Density in function of the environment temperature.

The engineering coefficient are not affected by the oil temperature or the environment pressure; Table 7 contains the value of the engineering coefficients a(1),a(2),a(3),a(4),a(5).

Coefficient	Value
a(1)	0.104708137
a(2)	6571.272275[bar]
a(3)	-28.35782332[bar/K]
a(4)	0.045352774[bar/K^2]
a(5)	-2.63 10^{-5} [bar/K^3]

Table 7. Engineering coefficients of oil density equation.

Considering a test temperature of 30°C, and the pressure gradient between the inlet and outlet environments of the gear pump (29bar), the oil density has been considered as a steady parameter (Figure 61).
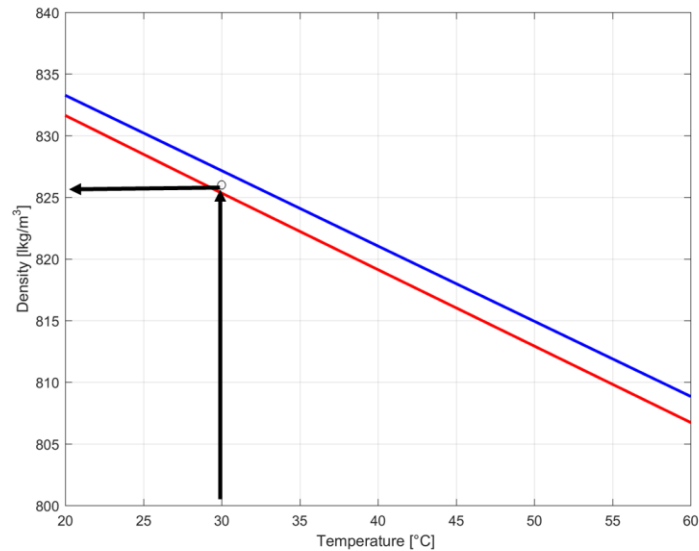

Figure 61. Oil pump density for 1bar (red line) and for 30bar (blue line) working pressure.

Figure 61 shows the oil density of the oil pump in function of the temperature and pressure. There are no remarkable differences between the working conditions; that is as expected, because in this pressure range the oil can be considered a non-compressible fluid. The

density used in the model is 826kg/m³. The second thermodynamics property of the oil is the resistance of the oil to a uniform compression; it is called bulk modulus ß. The temperature and the pressure condition this parameter, and Eq(15) defines the bulk modulus values in function of the oil pressure and the oil temperature.

$$\beta(p, T) = \left(\frac{a(1)}{a(2) + a(3)T + a(4)T^2 + a(5)^3 + p} \frac{\rho(p, T)}{\rho(T)} \right)^{-1} \quad (15)$$

Even in this case the temperature and pressure range of interest do not affect the bulk modulus (Figure 62); thus, this parameter is considered steady, and the set value in the numerical model is 1.37*10⁻⁹Pa.
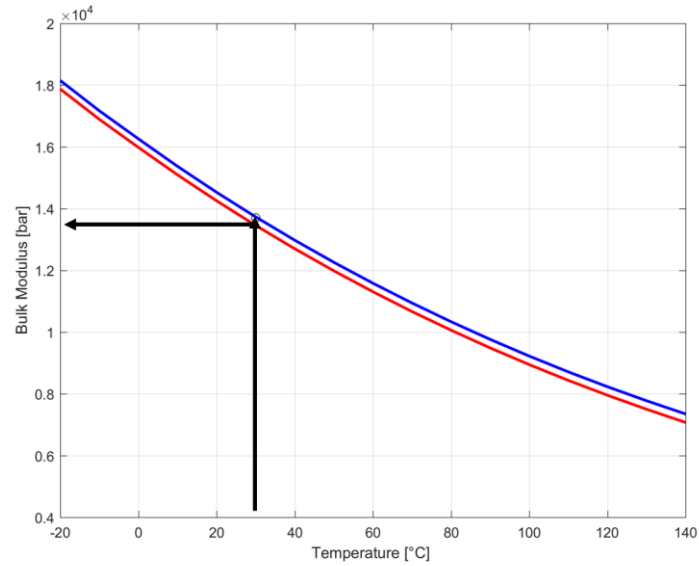

Figure 62. Values of bulk modulus at 30°C for two different pressure conditions 1bar (red line) and 30bar (blue line).

The last oil feature is the dynamic viscosity, which is defined by the well-known Eq(16).

$$\mu = \frac{\nu(T)}{\rho(p, T)} \quad (16)$$

v(T) is the kinematic viscosity in function of the oil temperature, while the denominator of Eq(16) is the oil density, which in this particular case has been considered as a constant value. Thus, Figure 63 displays the trend of the dynamic viscosity.
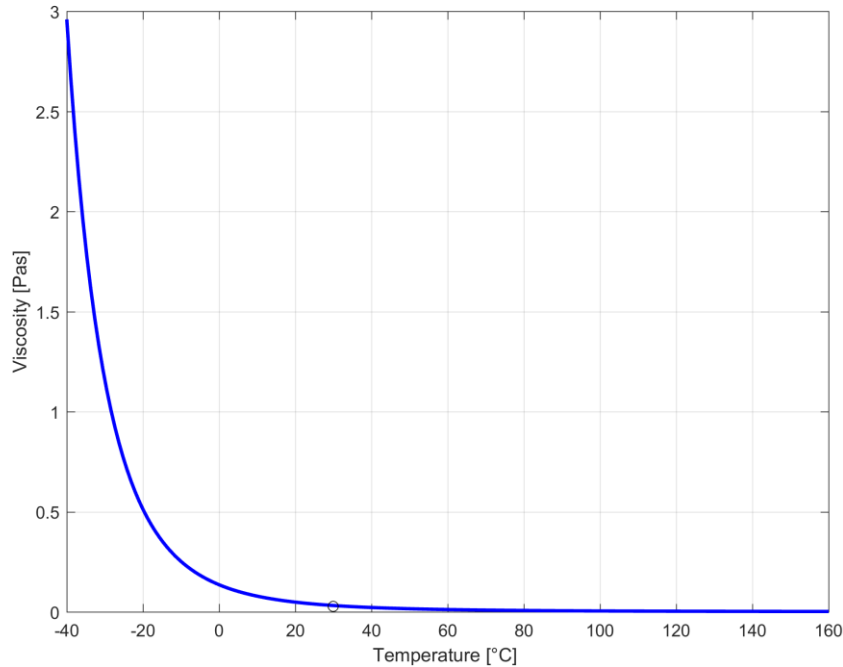

Figure 63. Dynamic viscosity trend of the oil pump.

The oil viscosity is a fundamental parameter for the reliability of the numerical model. Indeed, the oil viscosity determines the laminar flows that cause the oil leakages from the outlet environment to the inlet environment, thus defining the pump efficiency. The value obtained for the dynamic viscosity is 0,0278Pas.

A.2.6. Characterization of the Laminar Flows by CFD Simulations

The small dimensions of the pump do not make it possible to evaluate the axial and radial flows by using experimental tool, thus a

CFD numerical model has been helpful in order to identify the type of flows (laminar of turbulence) which passing through the axial and radial clearances between the gear teeth and the pump housing The CFD models have been also usedful for the validation of the laminar flows that pass through the. Concerning the CFD modeling, two models have been developed by the Fluid Machinery and Energy System Group of the University of Ferrara. First, a 2D model was develop in order to validate the hypothesis of the laminar flow on the teeth tips. This model considers the geometry of a single tooth within a straight duct (Figure 64); furthermore, the model boundary conditions evaluate the wall effect of the duct partitions and the gradient pressure applied between the duct far end. The model aim at the evaluation of the flows, which passes through the gear tip and find out how the pressure gradient and the clearance between the gear tip and the duct wall (Figure 65) affect these flows. Several simulations have been performed, in order to analyze the pressure range 4.3kPa-1MPa and the clearance range 5µm-1.36mm. The pressure range was divided in ten pressure levels; for each level, fifteen gaps were investigated. Table 8 summarizes the pressure level and the gaps between the teeth tip and the pipe wall.
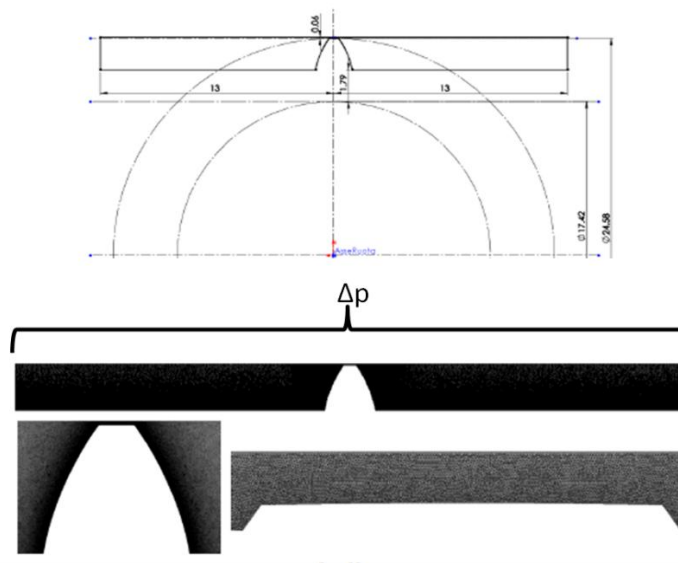

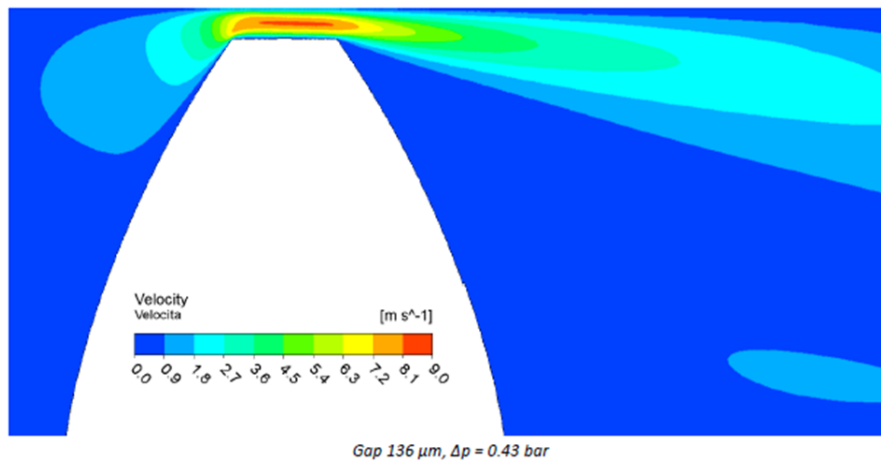Figure 64. Representation of the 2D CFD model.

Figure 65. Simulation result flow velocity for 136μm gap and pressure gradient 0.43bar.

Pressure Gradient levels	Teeth tip gaps
43kPa	5µm
50kPa	10µm
60kPa	15µm
75kPa	20µm
100kPa	25µm
430kPa	30µm
500kPa	40µm
600kPa	60µm
750kPa	80µm
1000kPa	100µm
	125µm
	130µm
	136µm

Table 8. Pressure gradient level and teeth tip gaps investigated with the 2D CFD model.

Figure 66 shows the results of the 2D model, from which it is clear that, for small gaps (5-15µm) the spread of flow rates due to the pressure gradient is close. On the other hand, when considering the results for

the 20-136μm range, the spread of the flow rates is more relevant. The trends of Figure 66 are well reproducible with third-order polynomial laws; this implies that, the laminar flow hypothesis on the teeth tips is correct. Figure 67, Figure 68 show the good matching between the simulation results and the third order polynomial laws. No further 2D models have been developed for the flows that pass through the teeth flank, because the height and the width of the oil meatus are comparable to the teeth tip meatus. The fruitful experience of the 2D CFD simulation lead to the development of a 3D CFD model, in order to compare the ratio between the laminar flow on the teeth flank and the laminar flow passing through the teeth tip. The 3D CFD model is suitable for a better comprehension of the laminar flows behavior on the seal zone before the epsilon grooves. The seal zone is essential for reaching high volumetric efficiencies and a proper pressure field around the gears. This zone is characterized by high pressure gradients and small clearances; thus, strategic clearance ranges and pressure gradients were investigated.
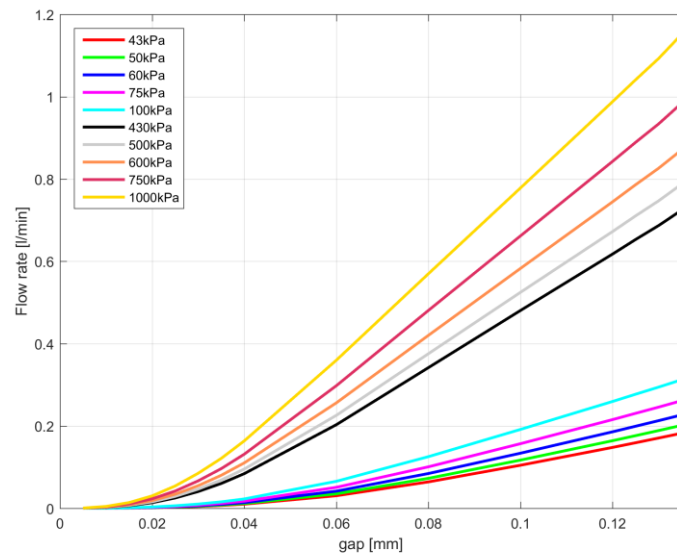

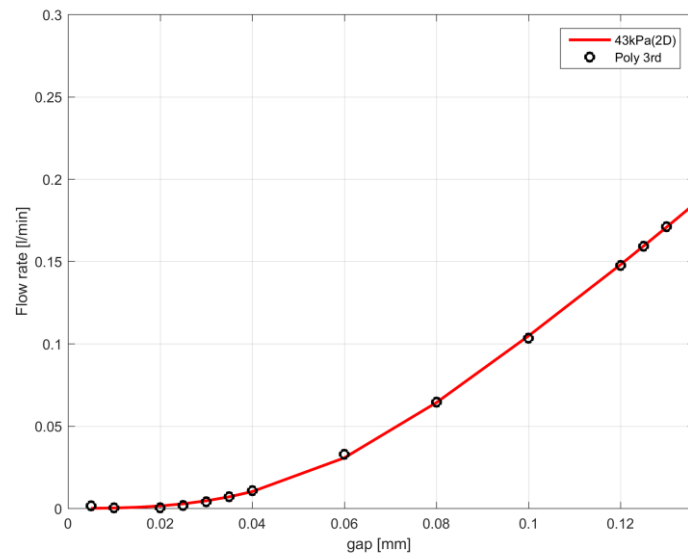Figure 66. 2D CFD model results (flow rate on the tip) for gap range 5-136μm.

Figure 67. Comparison between gear tip flow rate computed by CFD 2D (43kPa) and 3rd order polynomial law.
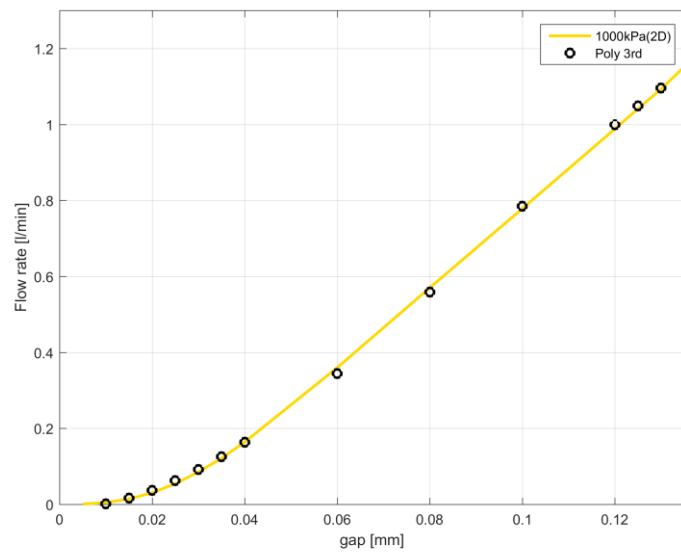

Figure 68. Comparison between gear tip flow rate computed byCFD 2D (1000kPa) and 3rd order polynomial law.

The aims of the 3D CFD model are firstly the evaluation of the teeth tip and flank flows, and secondly the verification of the laminar hypothesis for both types of flow. The definition of a hydraulic resistance in a linear pipe has been used for the 2D model as well as for the 3D model. The geometry of the hydraulic resistance is due to the gear teeth geometry and the radial and axial clearance of the gear pump(Figure 69).

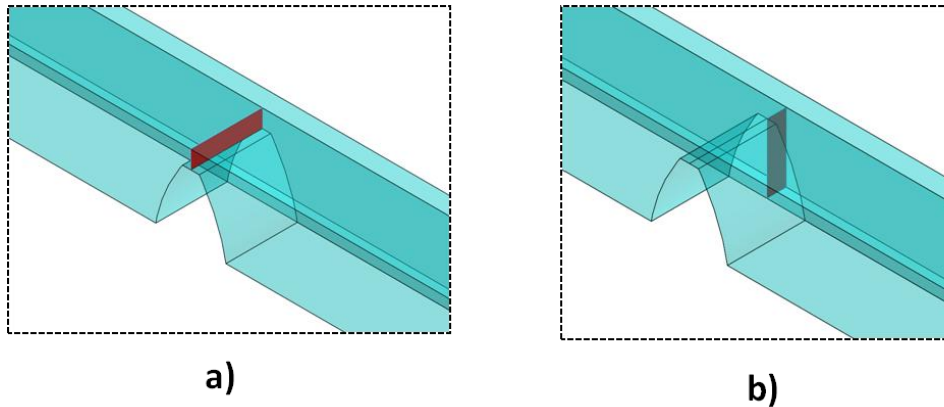a)   b)

Figure 69. 3D CFD model representation. a) radial clearance, b) axial clearance.

The axial clearance is the additional parameter within the 3D model, but the sensitivity analysis has been made again on the radial clearance, in order to reduce the number of simulations. The sensitivity of the axial clearance has been neglected, as the range of the radial gaps (5-136μm) can be used for the axial gaps as well; thus, considering that the height and the weight of the oil meatus are comparable for both cases, the sensitivity analysis of the radial clearance is sufficient to reach the objectives. The axial clearance was kept constant (5μm), but seven different values for the radial clearance were investigated (Table 9). Five simulations were made for each radial gap, in order to analyze five different pressure levels (Table 9).

Pressure Gradient levels		Teeth tip gaps
430kPa		5µm
500kPa		10µm
600kPa		20µm
750kPa		40µm
1000kPa		60µm
		80µm
		100µm
		136µm

Table 9. Pressure gradient level and teeth tip gaps investigated with the 3D CFD model.

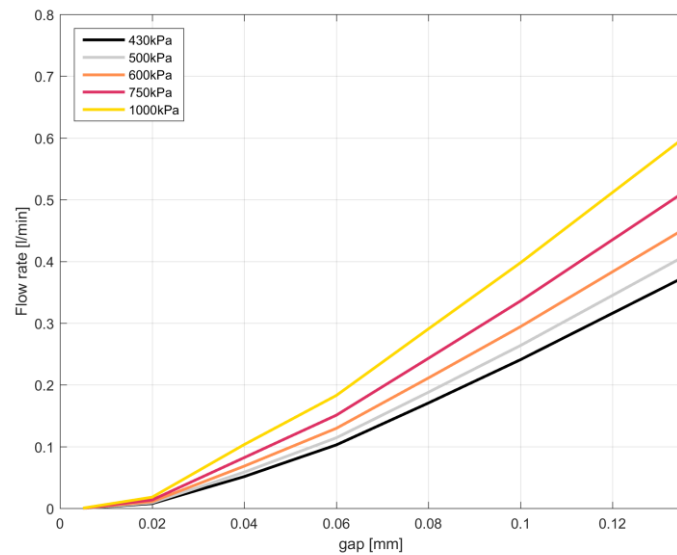The gear tip flow rates evaluated by using the 3D CFD model are displayed in Figure 70.

Figure 70. Gear tip flow rates computed by the 3D model, for radial clearance range 5-136µm

The results follow the third order polynomial laws as expected (Figure 71, Figure 72); the flow rates are lower when compared to a 2D model, because the 3D model takes into account the lateral flow passing through the tooth flank. The gear tip flow rates increase their value

when there are high radial gaps and a high pressure levels as well; the increase of the gear flank flow rates is due to the gradient pressure only (Figure 73). The high values of the gear flank flow rates for a tight radial clearance are due to the comparable dimensions of the tip and flank oil meatus. On the other hand, for high radial gaps values, the hydraulic impedance on the gear flank becomes more relevant compared to the gear tip hydraulic impedance; thus, in general the flow prefers following the path with the lower impedance.
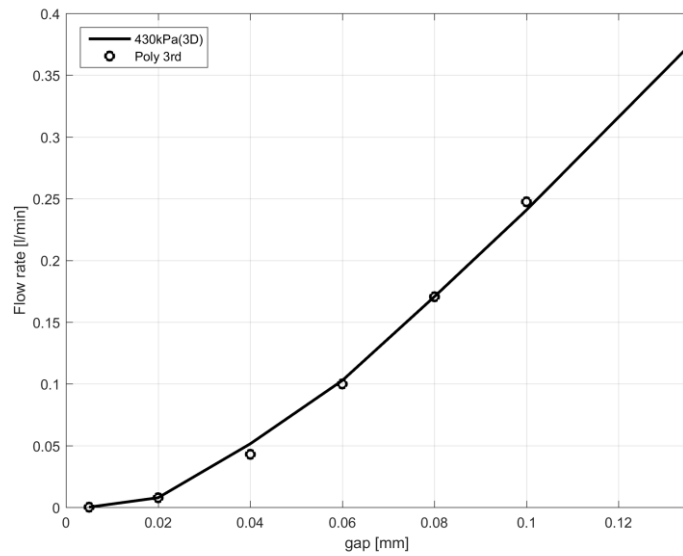

Figure 71. Comparison between gear tip flow rate computed by CFD 3D (430kPa) and 3rd order polynomial law.
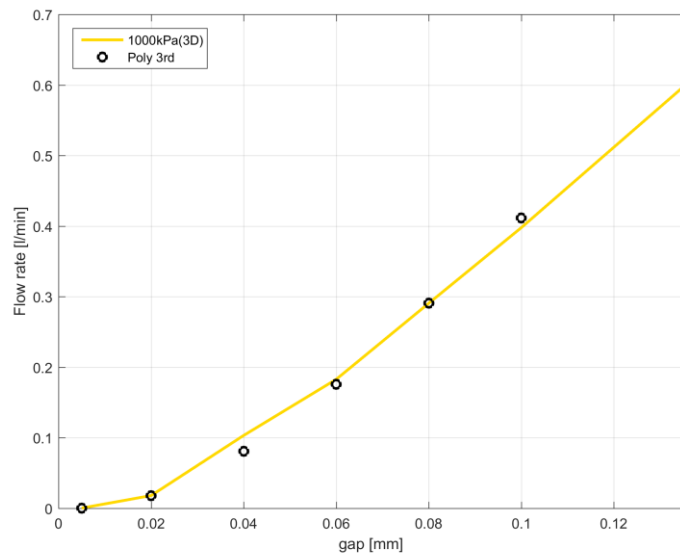
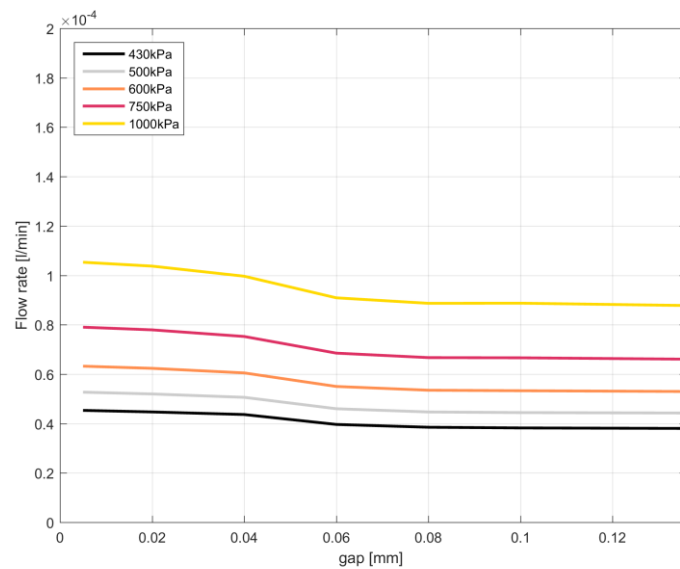Figure 72. Comparison between gear tip flow rate computed by CFD 3D (1000kPa) and 3rd order polynomial law.

Figure 73. Gear flank flow rates computed by the 3D model, for radial clearance range 5-136μm.

A.2.7.   Model Validation by Comparison with Test Results

The model validation, uses the experimental data obtained through the TRW test bench described in the previous chapter (A2.4, Figure 59). The working conditions for the experimental test are defined by TRW standard trial procedures, but in this particular case a specific middle plate has been designed. Typically, the epsilon groove on the middle plate is shallower than the epsilon groove on the upper plate; thus, in order to avoid non-symmetrical features in the mechanical system, the epsilon groove on the upper and middle plate have the same depth (0.2mm). The TRW standard trial procedure reproduces the "*mit speichern laden*" operational mode; this operational mode makes it possible to separate the outlet pipelines of the high pressure and lower pressure gear pump. The outlet pipe decoupling reduces both the lower pressure pump effects on the high-pressure pump and, especially, the pressure ripple of the outlet pipe. This operational mode represents the best compromise for the validation of the single model of the high-pressure pump where the low-pressure pump effects are neglected. The validation procedure is based on the comparison between the model and the experimental results concerning the inlet, outlet flow rate ratio (volumetric efficiency) and the outlet pressure ripple. The main features of the experimental test are: the gears rotational speed is 3020rpm; the outlet working pressure is 30 bar; the oil temperature is 30°C and the gears eccentricity are 0,01mm in X direction and 0,04mm in Y direction (Figure 74).
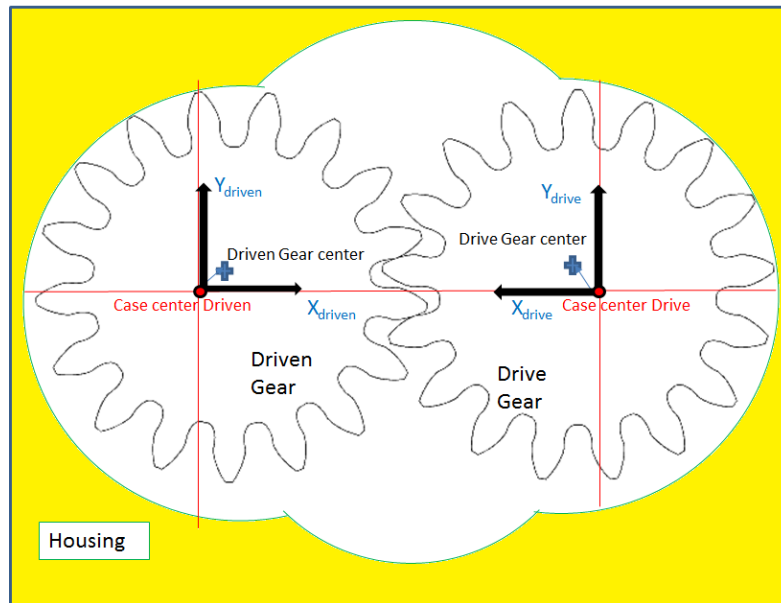
Figure 74. Overstate representation of eccentricity concept.

The first result that is analyzed, before starting the validation procedure, is the pressure trend within the reference volumes of the drive and driven gear, in order to confirm the truthfulness of the results. The trend is displayed in Figure 75; the first volume which is pressurized is the reference volume of the driven gear (red line); this volume increases its own pressure when it ceases to communicate with the inlet volume; after a half pitch delay, the pressure of the drive gear reference volume also increases. The reference volumes take 50° to reach the working pressure condition (30bar), but after this rotation the control volumes are not influenced by the epsilon groove yet, thus a pressure overshoot arises. The pressure overshoot represents the starting point of the pressure ripple; the amplitude of the pressure ripple has a decreasing trend until it reaches the ripple level of the outlet pipe. The pressure ripple of the drive and driven gear are clearly out of phase; this condition persists until both volumes begin to communicate with the outlet pressure environment. The first volume that is affected by the meshing phase is the reference volume of the driven gear; the meshing phase causes a reduction of the volume that

establishes the pumping action of the gear pump. During the pumping action the pressure of the reference volume of the driven gear increase and then drop dramatically until to reach the inlet pressure level. The pressure trend of the reference volume of the drive gear follows the trend of the driven gear, because during the meshing phase these volumes are strictly connected. After the pressure drop, the pressure level considerably oversteps the 1bar threshold, causing the oil cavitation; but this observation is not reliable, because no cavitation models have been implemented [91-97]. The pressure trends obtained by the numerical model can be considered reliable in terms of pressure level and shape.

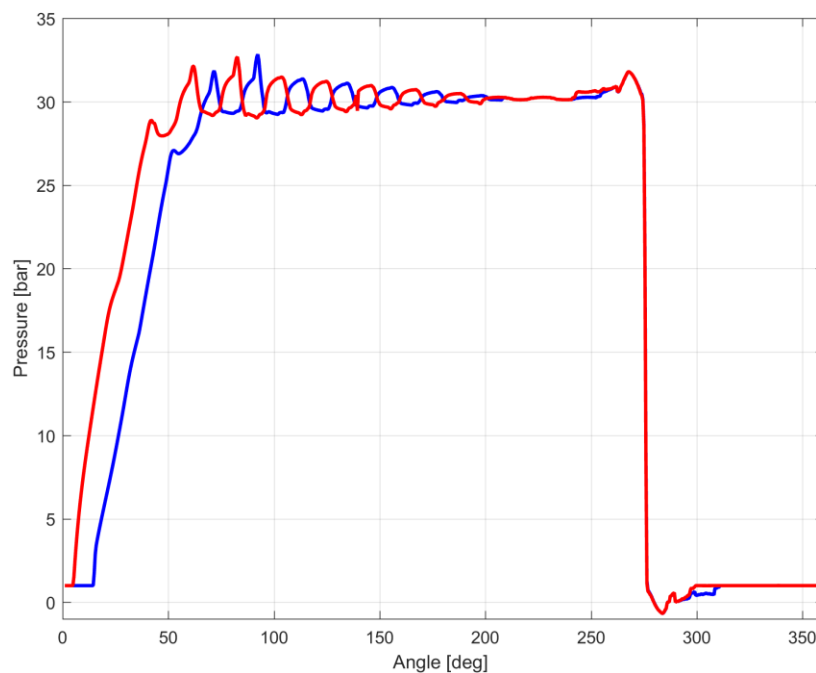Figure 75. Simulation Results: Pressure trend within the reference control volumes of the drive gear (blue line) and driven gear (red line).

After the analysis of the pressure trend in the reference volume, it is possible to analyze the pressure ripple on the outlet pipe. The comparison between the simulation result and experimental test is displayed in Figure 76. A further comparison has been done in the

frequencies domain by performing the FFT of the time signals (Figure 77). The FFT comparison of experimental and simulation results shows that the spectrum of the experimental results contains several contributes which are not displayed in the simulation results; in both cases, the most important contribute is due to the 17th order (855,7Hz), which is the gear pump meshing order. The experimental and the simulation signal contain contributes which are multiple of the gear meshing order: 1712Hz (2nd meshing order), 2567Hz (3rd meshing order), 3423Hz (4th meshing order); the error percentage for the most important meshing order contributes are contained in Table 10. The percentage of the first, third and fourth errors are acceptable; on the other hand, the gap between the second meshing orders is wide. The experimental results point out that the lower pressure pump affects the dynamic behavior of the high pressure gear pump even in the "*mit speichern laden*" operational mode. In fact, the experimental spectrum of the pressure signal contains the first (553,7Hz) and second (1107Hz) meshing order contribution of the lower pressure gear pair. Furthermore, the spectrum of the experimental results contains the first and second order of the pump rotational speed (probably due to system unbalances); finally, each meshing order has side band contributes: the double sidebands are centered and spaced +/- 50,7Hz (Rotational speed) around the meshing orders. The side band effects are typically due to the gears eccentricity, which leads to an amplitude modulation where the envelope goes with the rotational speed. The comparison between the experimental and numerical results indicates that the numerical model needs to be improved by taking the lower pressure pump effects and pump rotor dynamic effects into account, the numerical model can be considered validated, because it is able to catch the main contributions of the experimental pressure signal.
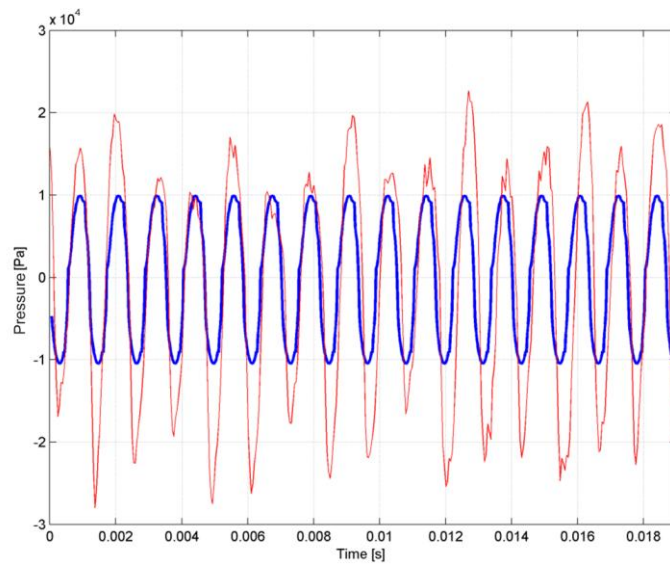
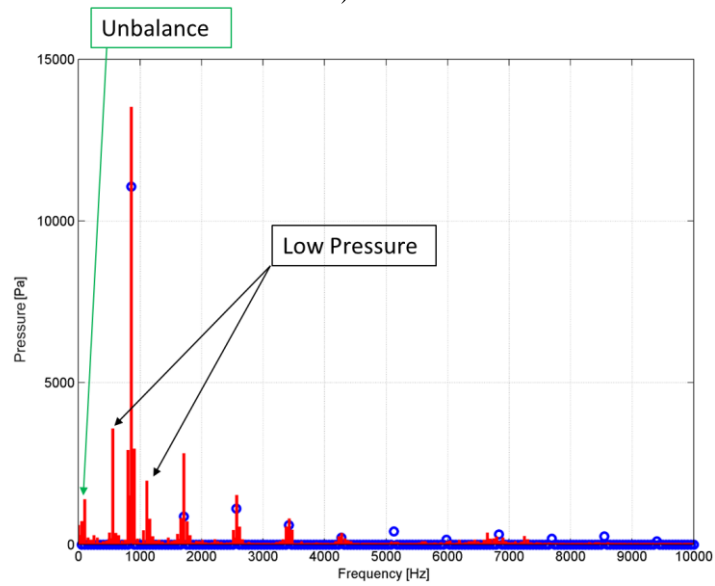Figure 76. Pressure ripple comparison between simulation (blue line) and experimental (red line) results.

Figure 77. FFT comparison of simulation and experimental results.

Meshing Order	Percentage error (Amplitude)
1st (855m7Hz)	-18%
2nd (1712Hz)	-69%
3rd (2567Hz)	-27%
4th (3423Hz)	-25%

Table 10. Percentage error of the meshing order amplitudes.

The second parameter used during the validation is the volumetric efficiency of the gear pump, which is based on the ratio between the outlet and inlet flows. The inlet flow rate during a whole pump rotation is shown in Figure 78; the mean value of the inlet flow rate is 2.43l/min. On the other hand, Figure 79 shows the outlet flow rate and the relative mean value (2.36l/min). The simulation leads to a volumetric efficiency value of 0.976; when compared with the value of 0.98 calculated using the experimental tests, the inlet and outlet flow rates can be considered correct.
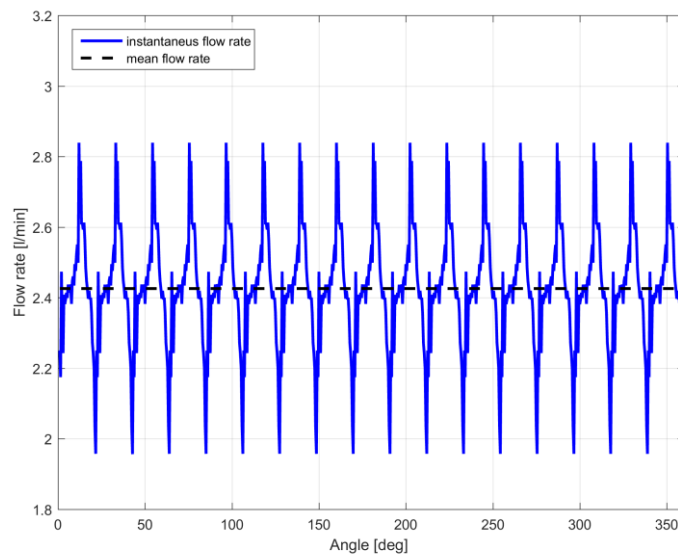

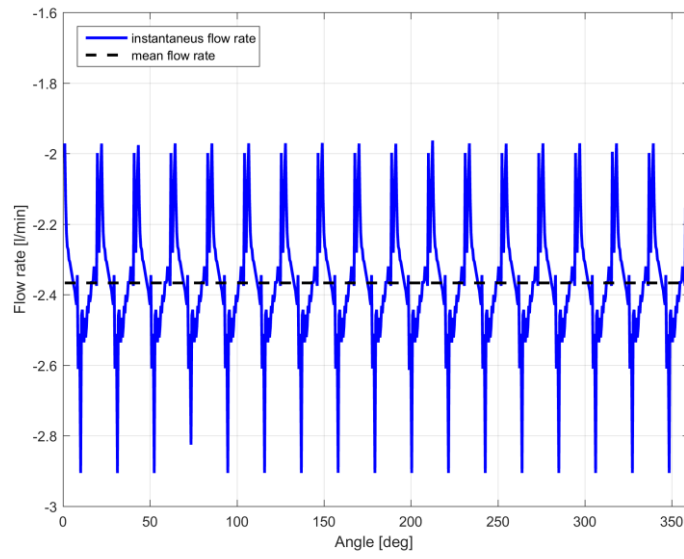Figure 78. Inlet flow rate trend (blue line) and the mean value of the inlet flow (black dot line).

Figure 79. Outlet flow rate trend (blue line) and the mean value of the outlet flow (black dot line).

CHAPTER A.3
SIMULATION RESULTS AND SENSITIVITY ANALYSIS.

A.3.1.   Introduction

This chapter contains the simulations developed in order to find out the sensitivity of the model for several parameters. The parameters that were investigated are:

1. *The oil temperature.*
2. *Gear Eccentricity.*
3. Epsilon Groove Depth.
4. Epsilon Groove Exstensions.

The oil temperature (A.3.2) affects the fluid viscosity, the Bulk modulus and the fluid density. The physical properties of the oil obviously have an intense effect on the drag flows. After the oil temperature (A.3.3), the focus has been moved on the gear eccentricities, which have an effect on the radial clearances between the tip of the gear teeth and the pump housing; these clearances define the gaps where the laminar tip flows and radial tip flows pass through, conditioning the pump volumetric efficiency. The third and fourth parameters concern the epsilon groove geometry; the depth (A.3.4) of the grooves and the epsilon groove extensions (A.3.5). The epsilon groove has a significant effect on the flows that pass through the axial clearance; furthermore, these flows are responsible for the oil leakages between the inlet and outlet volume, which affect the volumetric efficiency dramatically. The sensitivity analysis was fundamental to see how the model parameters affect the pressure distribution and the pump flows; it was also useful for detecting the key areas of the pump and the range that favor good performances. In this paragraph it is

possible to find for each parameter the analysis concerning the pressure of the gear pockets, the flows of the control volumes, the outlet and inlet pressure trend and the pump efficiency. Furthermore, we also tried to explain how the model modification affects the simulation results. The sensitivity analysis contained in this chapter, highlights the effects on the pump dynamics and pump volumetric efficiency; due to variation of some design parameters. The effect on the system dynamic has been appreciated by looking at the outlet pressure ripple and the pressure distribution, on the other hand the consequences on the volumetric efficiency were performed on the flows rate analysis. The sensitivity analysis gives the pro and cons of the single pump design modification, but without any target for optimization analysis in term of dynamic performances and pump efficiency, no further pump configurations were investigated. The results that will be exposed in the following paragraph concern the 18th reference volume (drive gear) and the 35th volume (driven gear) (Figure 25).

A.3.2.   Sensitivity to Oil Temperature

The first analysis concerns the variation of the physical properties of the oil due to temperature. In the previous chapters, the effects of temperature on the physical properties were explained in detail; thus, Table 11 contains the set up values for the three temperature levels (30°C, 45°C, 60°C), these range has been chosen because the pump costumer, for NVH tests require that the oil temperature must be included into the temperature range of 30-60°.

Oil Temperature	Oil Density	Oil Viscosity	Oil Bulk Modulus
30°C	825kg/m^3	0.0278Pas	1.37*10^{-9}Pa
45°C	817kg/m^3	0.0162Pas	1.26*10^{-9}Pa
60°C	808kg/m^3	0.0103Pas	1.16*10^{-9}Pa

Table 11. Oil Physical properties.

First, the pressures within the outlet pipe were compared; the results of the simulations for the three temperature levels are displayed in Figure 80. The comparison shows how oil temperature affects the outlet pressure: basically, the high temperatures lead to an increase in the amplitude of the pressure ripple. On the other hand, looking at the spectra of the pressure ripple (Figure 81), the ratios between the amplitudes of the meshing harmonics are not affected by oil temperature.
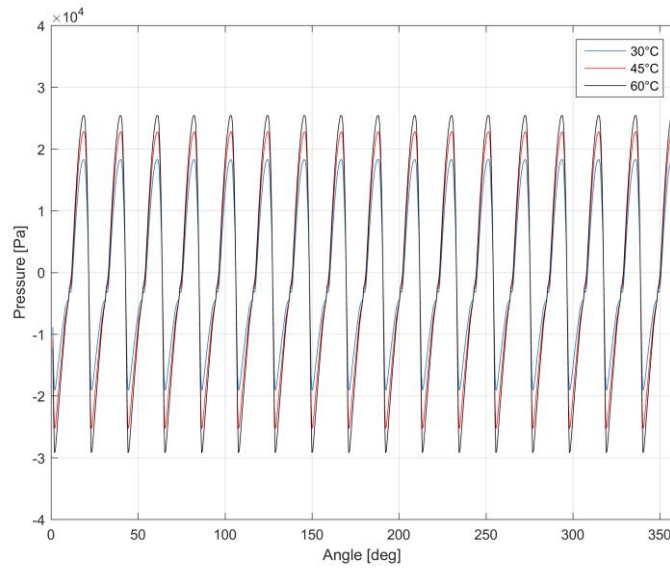

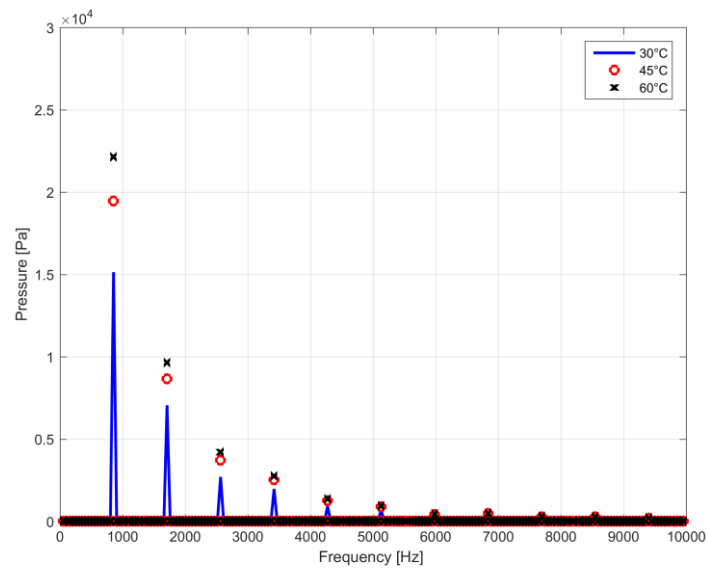Figure 80. Outlet pressure comparison (30°C,45°C,60°C).

Figure 81. Spectrum of the pressure ripple, for three temperature level. (30°C,45°C,60°C)

Furthermore, the increment of the oil temperature leads to a boost even in the outlet flow oscillation, which explains the outlet pressure ripple observed previously. Figure 82 represent the comparison between the results of the simulations for each oil temperature levels: the rise of the temperature leads an increase in the flow oscillations and the average values of the outlet flow. Thus, a lower fluid viscosity decreases the pump efficiency. The mean value of the outlet flows is: 2.21 l/min (30°C), 2.10 l/min and 1.91 l/min (60°C); their respectively volumetric efficiencies are: 0.94, 0.90 and 0.85. The results concerning the higher oil temperature show that, for several instances, the outlet flow assumes positive values; in this case, positive values mean that there are leakage flows which reach the inlet environment.
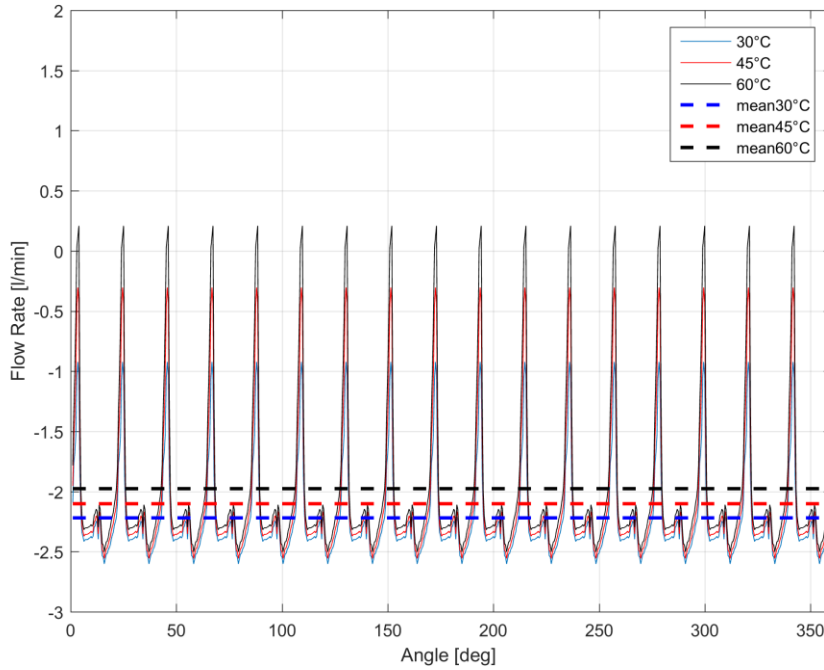
Figure 82. Outlet flow comparison (30°,45°,60°).

There are further flows that contribute in the efficiency decrease for high oil temperatures; these flows are the laminar flows that pass through the radial and axial clearances between the gear teeth and the pump housing. Considering the reference control volume of the drive gear (Control Volume n.18 of Figure 25), when this volume is contained between the LPS and HPS angles, it is able to exchange flows with the following pocket (Volume n.17) by the axial and radial clearances. The average values of the axial and radial flows exchanged between control Volume n.18 and control Volume n.17, determine the pump efficiency; in fact, negative values of average flows imply oil flow leakage from the outlet environment to the inlet environment. Figure 83 and Figure 84 display respectively $Q_{FLF,17\_18}$, for the upper and lower flank of the gear tooth; on the other hand, Figure 85 shows the $Q_{TLF,17\_18}$. Figure 85 helps to explain the previous statements concerning the decreasing of the pump efficiency with the rising of the temperature. When considering

the 0° to 196° range, it is clear how the increase of the temperature facilitates the flow leakage from the control Volume n.18 to control Volume n.17. Furthermore, the $Q_{FLF,17\_18}$ flows are characterized by a positive peak in correspondence of the 272°-277° angle band. During this phase, the control volume is passing from the outlet environment to the inlet environment, and the Volume n.18 is receiving a flow from the Volume n.17; thus, there is a mass flow from the outlet environment to the inlet environment. The same approach can be used for the driven gear; the flows ($Q_{FLF,34\_35}$; $Q_{TLF,34\_35}$) of the reference control volume of the driven gear (Volume n.35) are displayed in Figure 86, Figure 87 and Figure 88. The last flows that needs to be analyzed for evaluating the pump efficiency is the drainage flow, which is basically a laminar flow; for that reason, it is affected by the oil viscosity. The drainage flows of the references volumes are plotted in Figure 89 and Figure 90; they are fundamental for the lubrication of the hydrodynamic bushings and respect to the other laminar flow, the average flow rate values are always negative (Table 12), thus these flows represent always a leakage zone which reduce the pump efficiency. Finally, Table 12 reviews the average values of the $Q_{FLF,17\_18}$; $Q_{TLF,17\_18}$, $Q_{FLF,34\_35}$; $Q_{TLF,34\_35}$ flows, when the reference control volumes passing within the angle band defined by the LPS and HPS angles.
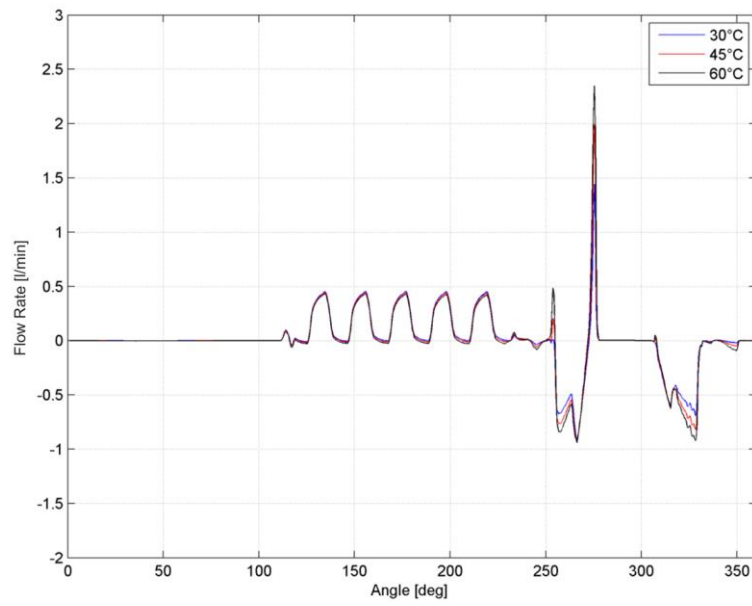
Figure 83. Comparison of $Q_{FLF,17\_18}$ flows for three temperature levels (Upper tooth side).

Figure 84. Comparison of $Q_{FLF,17\_18}$ flows for three temperature levels (Lower tooth side).

Figure 85.Comparison of $Q_{TLF,17\_18}$ flows for three temperature levels.

Figure 86 Comparison of $Q_{FLF,34\_35}$ flows for three temperature levels (Upper tooth side).
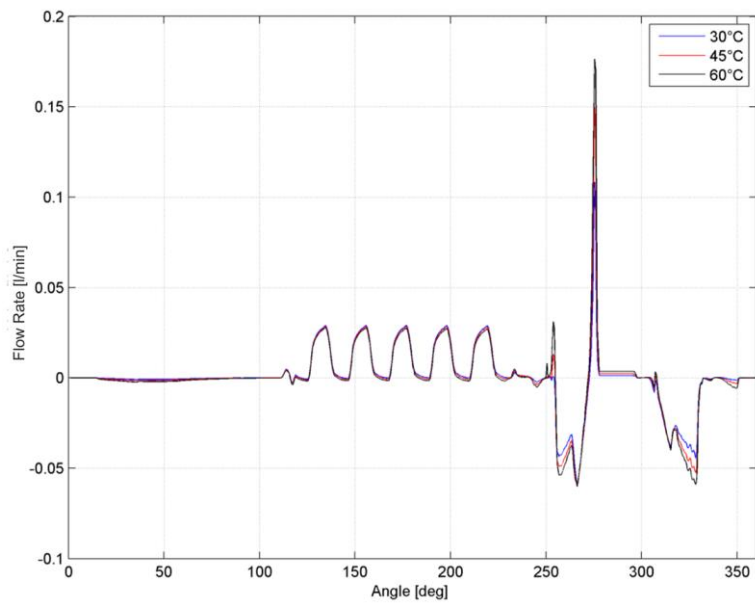
Figure 87. Comparison of $Q_{FLF,34\_35}$ flows for three temperature levels (Lower tooth side).
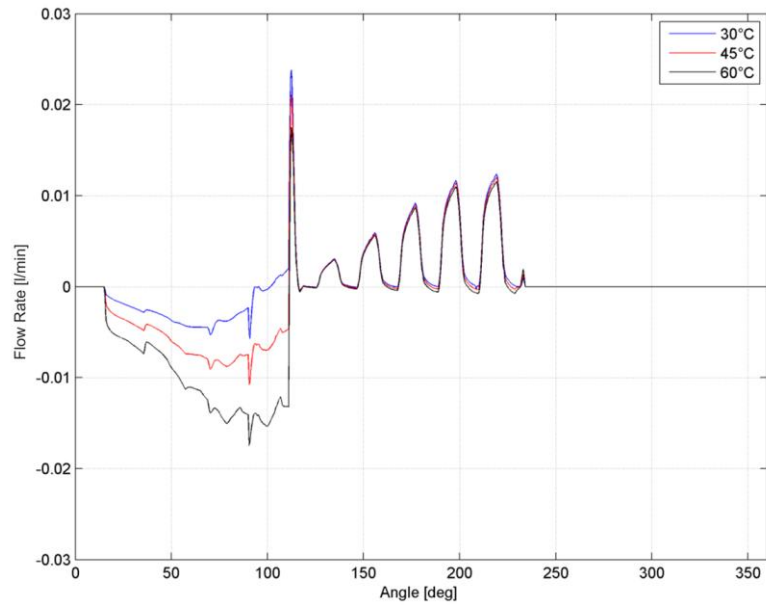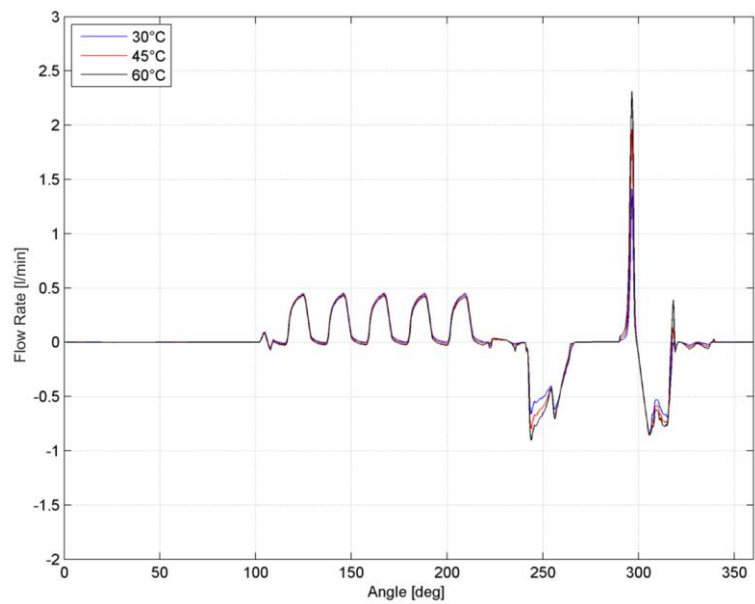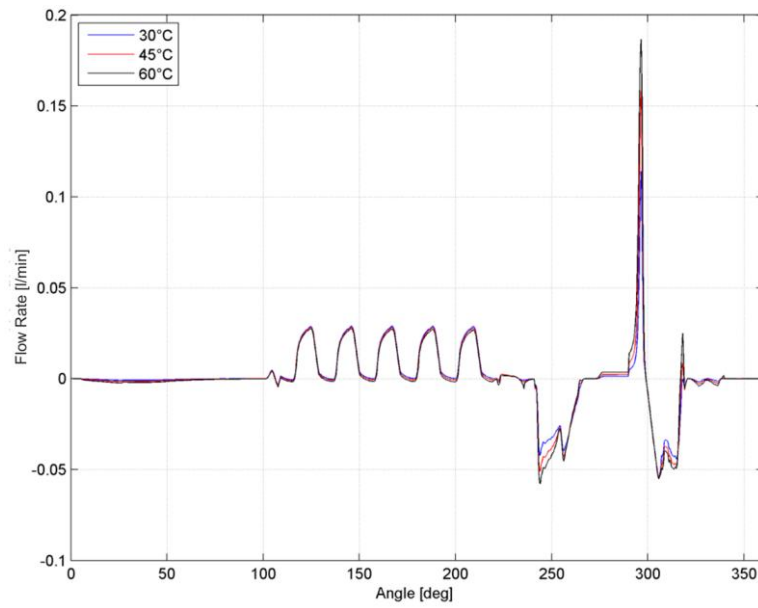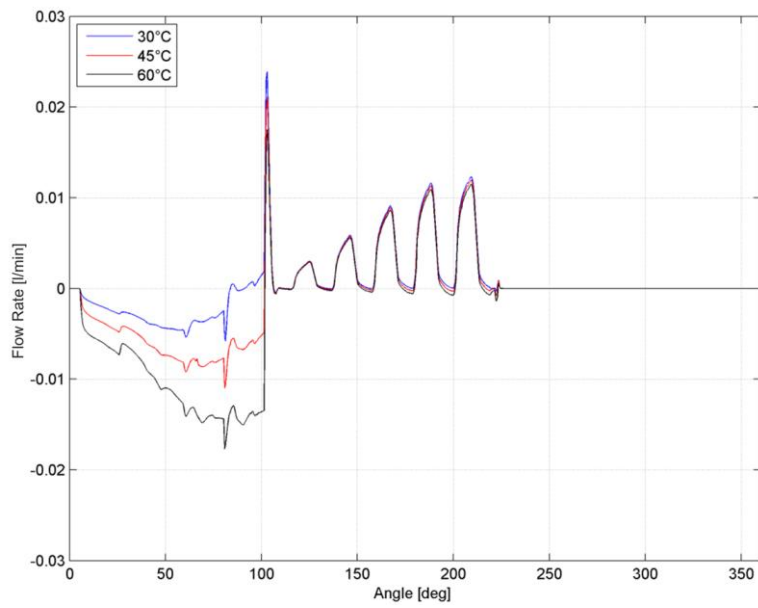

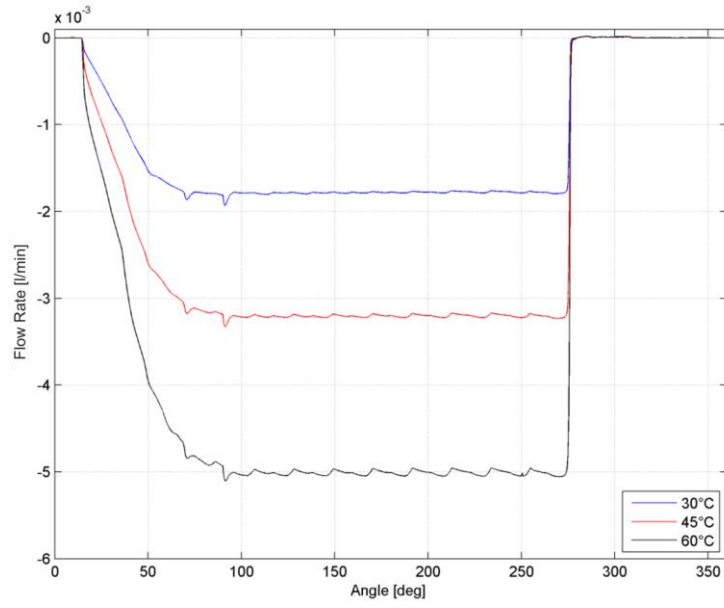Figure 88. Comparison of $Q_{TLF,34\_35}$ flows for three temperature levels.

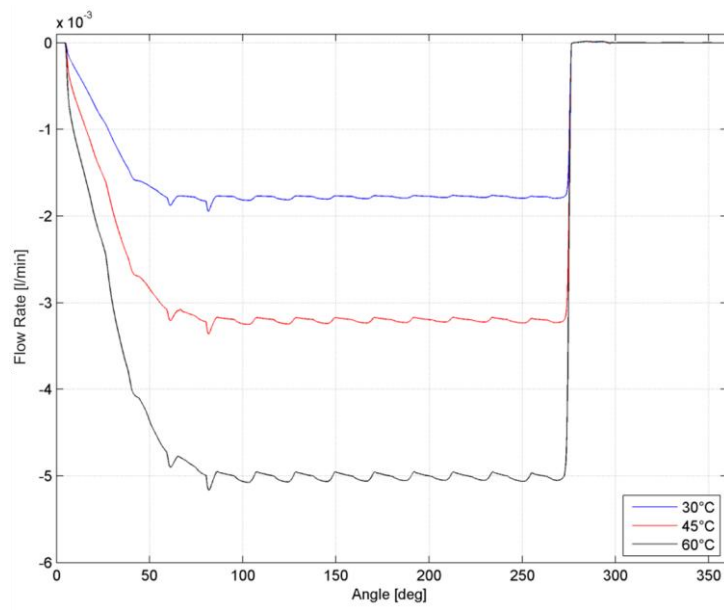Figure 89. Comparison of $Q_{LF,Dreinage\_18}$ for three temperature levels.

Figure 90. Comparison of $Q_{LF,Dreinage\_35}$ for three temperature levels.

Reference Control Volume of drive gear	30°C	45°C	60°C
Average $Q_{FLF,16\_17}$(Upper Side)	0.09650l/min	0.09110l/min	0.08420l/min
Average $Q_{FLF,16\_17}$(Lower Side)	0.006l7l/min	0.00550l/min	0.00490l/min
Average $Q_{TLF,16\_17}$	0.00084l/min	-0.00071l/min	-0.00270l/min
Average $Q_{LF\_17Dreinage}$	-0.00160l/min	-0.00210l/min	-0.00330l/min
Reference Control Volume of driven gear	30°C	45°C	60°C
Average $Q_{FLF,33\_34}$(Upper Side)	0.00960l/min	0.00902l/min	0.00828l/min
Average $Q_{FLF,33\_34}$(Lower Side)	0.00600l/min	0.00550l/min	0.00480l/min
Average $Q_{TLF,33\_34}$	0.00089l/min	-0.00081l/min	-0.00300l/min
Average $Q_{LF\_34Dreinage}$	-0.00160l/min	-0.00220l/min	-0.00340l/min

Table 12. Comparison of the average laminar flows for three temperature levels.

It is going to analyze the pressure within the gear pockets. An investigation of the pressure trend of the meshing reference volumes has been performed first, followed by an analysis of the variation of the pressure distribution in function of the oil temperature for each reference volume of the gear pump. The three Figures (Figure 91, Figure 92 and Figure 93) represent the simulation results for the three different temperature level (30°C, 45°C and 60°C); the results are displayed in the most interesting angular range (40°-280°), when the reference volume reaches the outlet pressure level. The solid blue line is the pressure trend within the reference volume of the drive gear; the solid red line is the pressure of the reference volume of the driven gear; finally, the solid black line represents the pressure within the outlet volume. The simulation results show a comparable behavior among the different temperature levels; in fact, the output pressure trend seems to be aligned with the pressure ripple of the driven gear. Furthermore, the frequency content of the control volume of the driven gear differs from the pressure ripple of the drive gear. This behavior arose when different depths of the upper and lower epsilon grooves were introduced. Moreover, the time needed to align the drive and driven gear pressure ripples with the outlet pressure, becomes longer when the oil temperature decreases; this behavior is probably due to the pressure overshoot during the pressurization of the control volume.
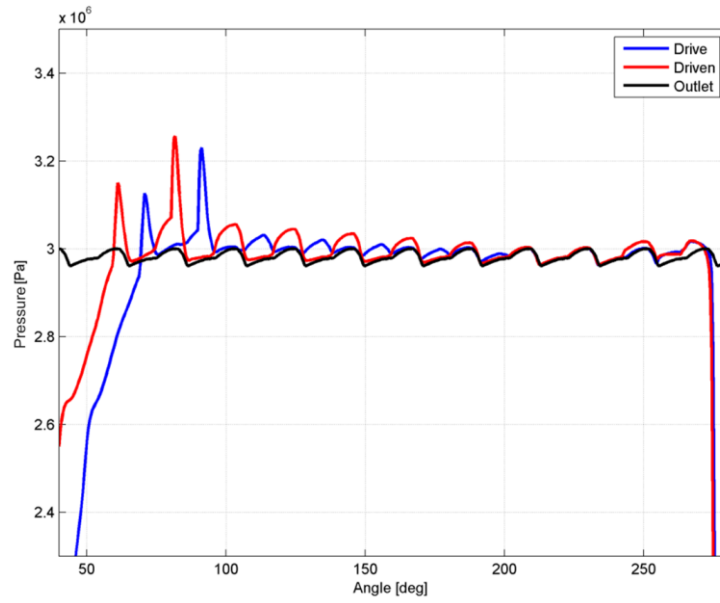
Figure 91. Pressure level of the reference volume and outlet volume; oil temperature (30°).
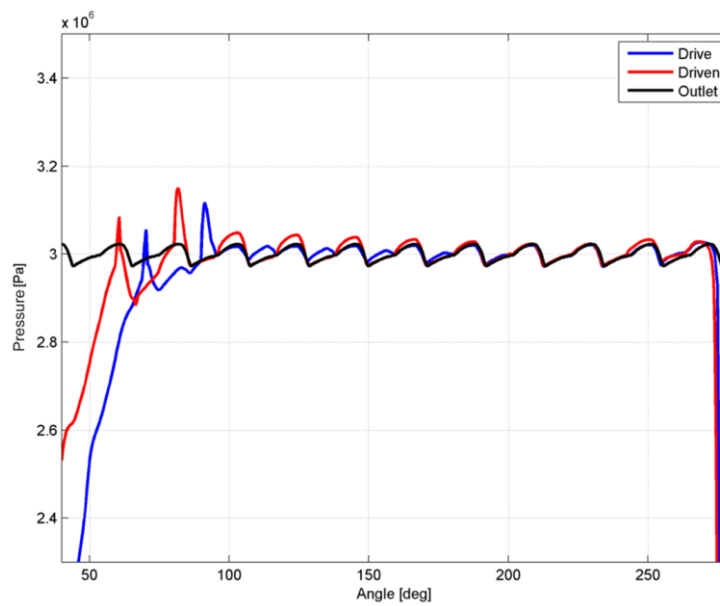
Figure 92. Pressure level of the reference volume and outlet volume; oil temperature (45°).
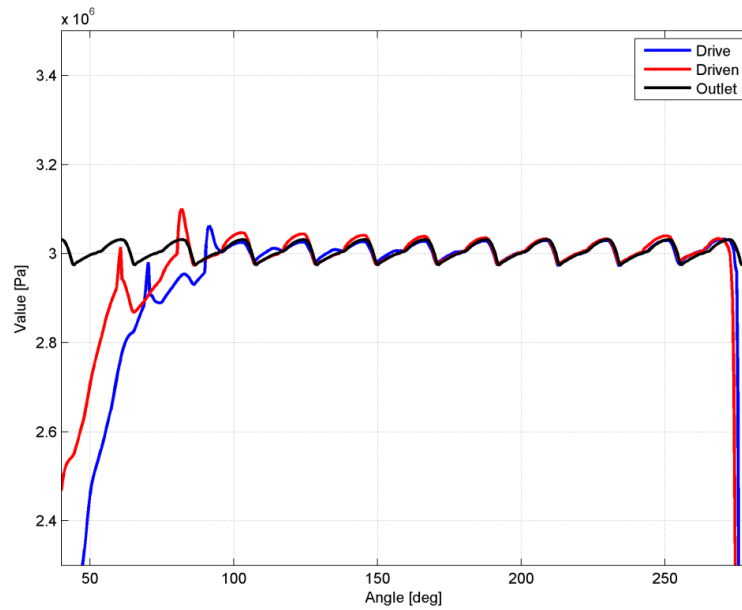
Figure 93. Pressure level of the reference volumes and outlet volume; oil temperature (60°).

The second analysis deals with the comparison of the pressure level in function of the oil temperature for each reference volume. The comparison concerning the control volume of the drive gear is shown in Figure 94, while Figure 95 displays the comparison for the reference volume of the driven gear. The results observation leads to the same conclusions for both volumes; the pressure overshoots are reduced by high oil temperature levels, as the reduction of the oil viscosity facilitate the leakage flows through the axial and radial clearances. Moreover, the reduction of the oil viscosity has a relevant effect during the release of the teeth meshing (273-300deg), where the control volume derivative increases and the pressure drops dramatically below the atmosphere pressure level. The amplitude of the pressure decay can be reduced if the control volumes (during the meshing phase) are able to draw oil from a high-pressure environment such as the outlet volume; the suction action can be facilitating by a low-viscosity oil. Figure 96 and Figure 97 show the effect of the oil viscosity during the meshing phase.

Figure 94. Evolution of pressure within the control volume of the drive gear for three temperature level.

Figure 95. Evolution of pressure within the control volume of the driven gear for three temperature level.

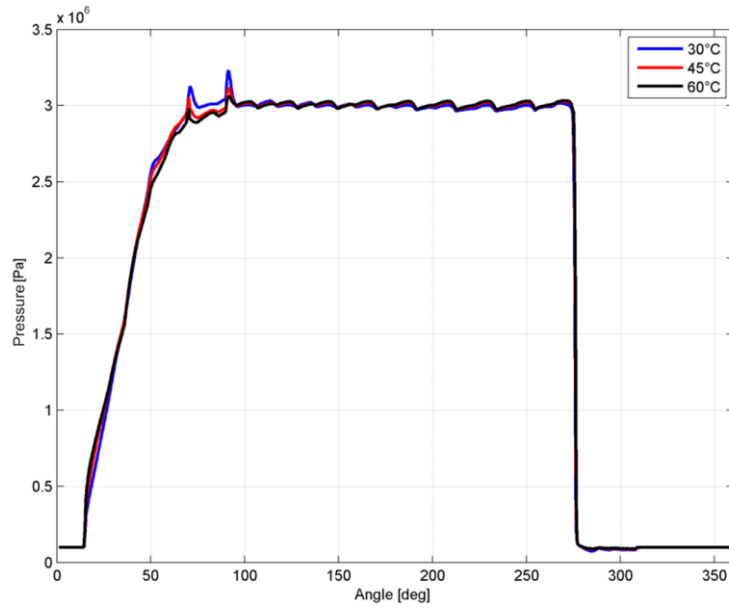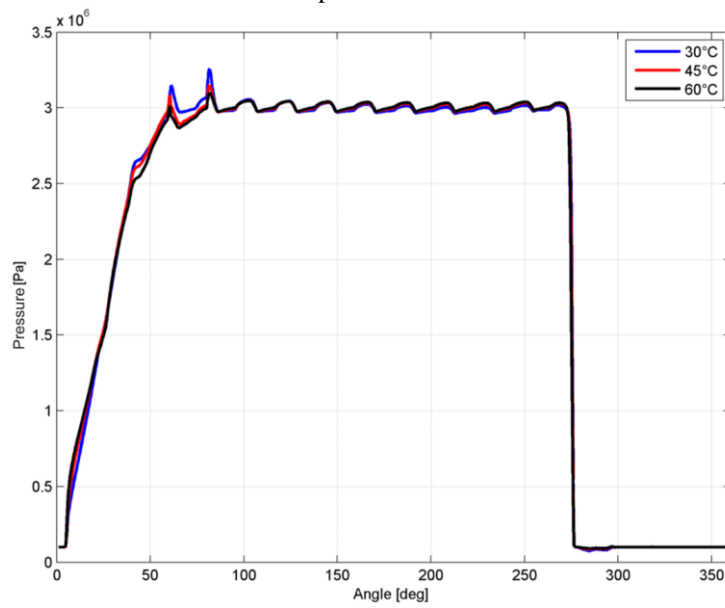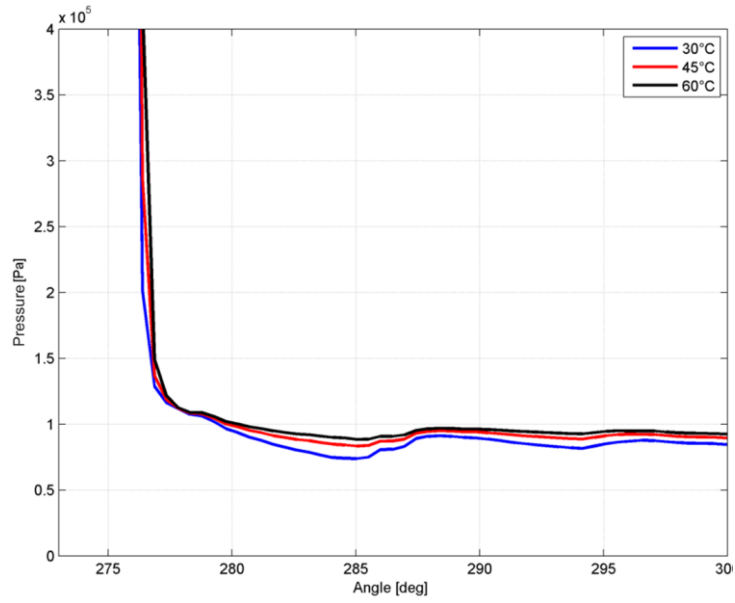Figure 96. Evolution of pressure within the control volume of the drive gear, during the meshing release, for three temperature level.
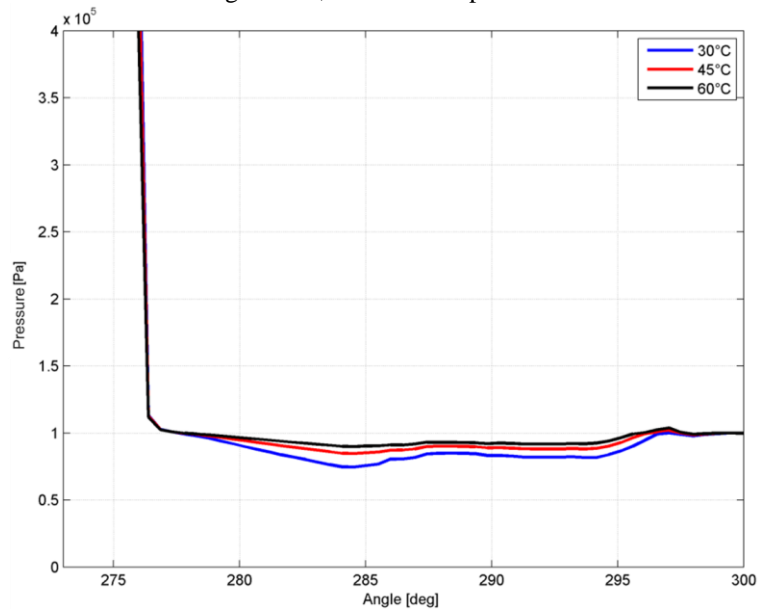

Figure 97. Evolution of pressure within the control volume of the driven gear, during the meshing release, for three temperature levels.

A.3.3. Sensitivity to Gear Eccentricity

The second analysis carried out with the numerical model deals with the effects of the gears eccentricity with respect to the pump housing. Also in this case three different pump configurations have been studied; an oil temperature of 30°C has been taken as a reference. The three cases are named: Zero eccentricity, where the radial clearances were kept constant; Standard eccentricity, where the tightest clearances were chosen; Intermediate eccentricity, which is situated between the other two cases. The eccentricity affects the laminar flows as well as the drag flows, because the variation of the radial clearances leads to modifying the hydraulic impedance of the laminar flows and the geometrical parameters of the drag flows. The eccentricity should have a significant effect on the beginning of the sealing zone, before the epsilon groove; in this particular area, the axial clearances are very tight, thus lower gear eccentricity values could increase the leakage flows from the radial clearances, reducing the pump efficiency. Figure 98 highlights the eccentricity level for the drive gear; considering the standard reference view (where the drive gear is placed on the right side), the eccentricity steps tend to push the gears against each other and towards the lower pressure sealing points (LPS). Considering the axes reference of Figure 98, Table 13 contains the eccentricity values of the three step that have been analyzed. The trend of the radial gap between the reference tooth of the drive gear and the pump housing due to the eccentricity steps is displayed in Figure 99. Before looking at simulation results, we must briefly comment Figure 99. The blue solid line represents the radial gap in the Zero eccentricity case, while the red line depicts the Intermediate eccentricity case, and finally the black solid line is the Design condition. The radial gap for the Zero eccentricity condition is steady, while in the Intermediate and Design conditions the gap increases from LPS to HPS. Thus, two angular intervals can be defined: the first from 354° to 104°, and the second from 104° to 212°. The first interval represents the angular domain near the LPS, where the Zero Eccentricity condition has the

higher radial gap. In the second interval, which is closer to HPS, the Standard configuration has the higher radial gap.
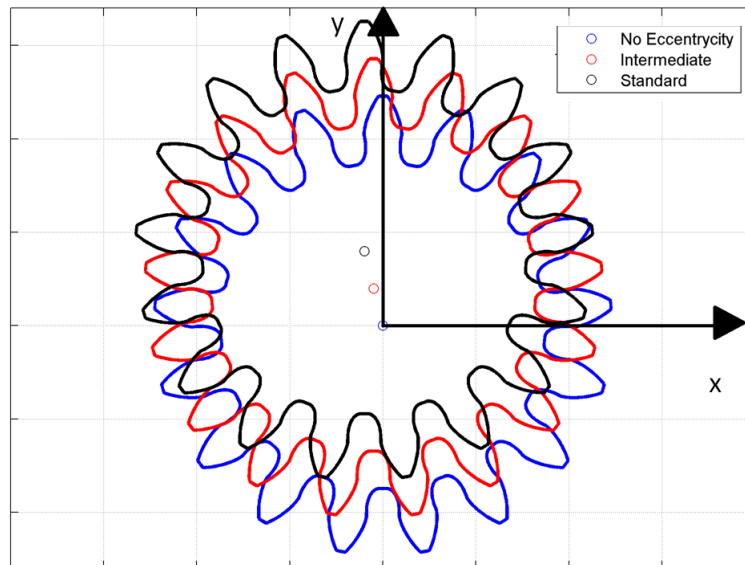
Figure 98. Eccentricity step of the drive gear (Exaggerated).
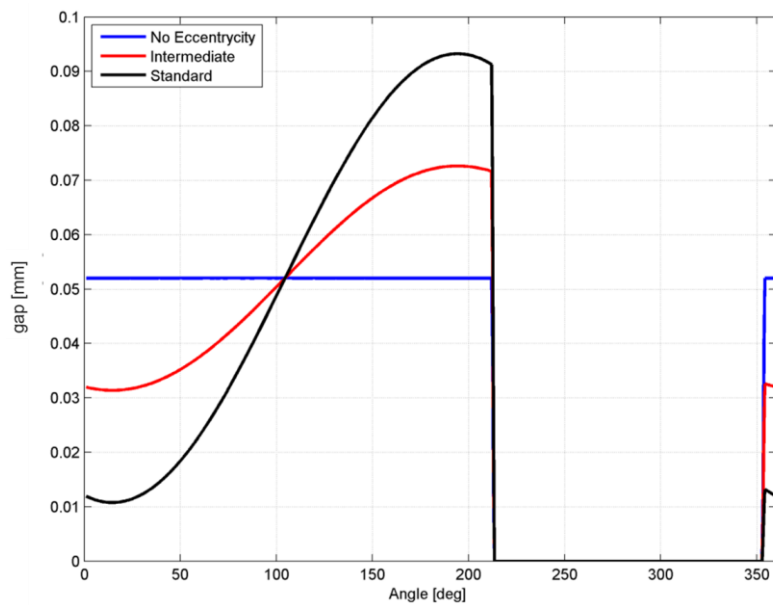
Figure 99. Comparison of the radial gaps for three different eccentricity step.

Drive gear	Zero Eccentricity	Intermediate Eccentricity Step	Design Eccentricity
X_axis	0,000mm	-0,005mm	-0,010mm
Y_axis	0,000mm	0,020mm	0,040mm
Driven gear	**Zero Eccentricity**	**Intermediate Eccentricity Step**	**Design Eccentricity**
X_axis	0,000mm	0,005mm	0,010mm
Y_axis	0,000mm	0,020mm	0,040mm

Table 13. Table of the eccentricity steps.

Let us now analyze the simulation results, as it was done in the previous paragraph for the oil temperature sensitivity. The three eccentricity configurations do not seem to affect the outlet pressure ripple (Figure 100 and Figure 101), as no remarkable differences have been found in the time signal and frequency analysis; yet, it affects the outlet flows and the pump efficiency as expected (Figure 102). Basically, the low sealing effect of the Zero eccentricity configuration reduces the average value of the outlet flow, but it does not affect the frequency content of the ripple flow. The pump efficiency results are respectively 0.81 for Zero eccentricity configuration, 0.90 for Intermediate and finally 0.94 for Design configuration.
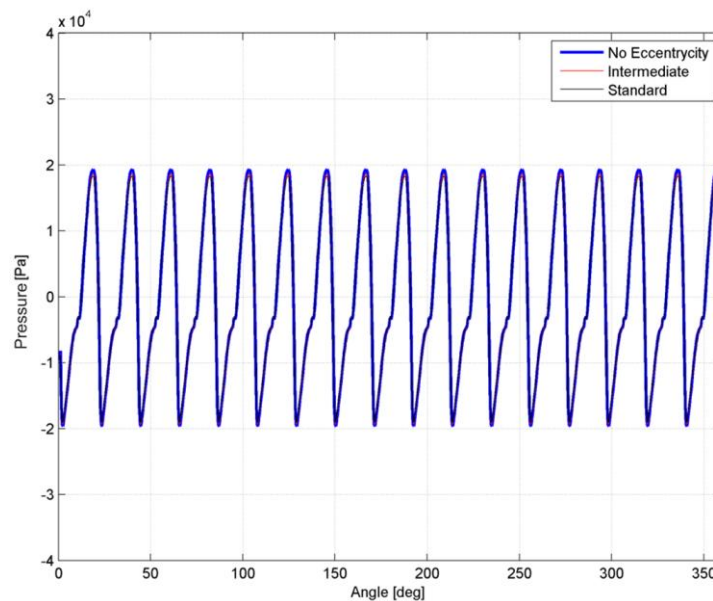
Figure 100. Outlet pressure comparison (No Eccentricity, Intermediate, Standard)
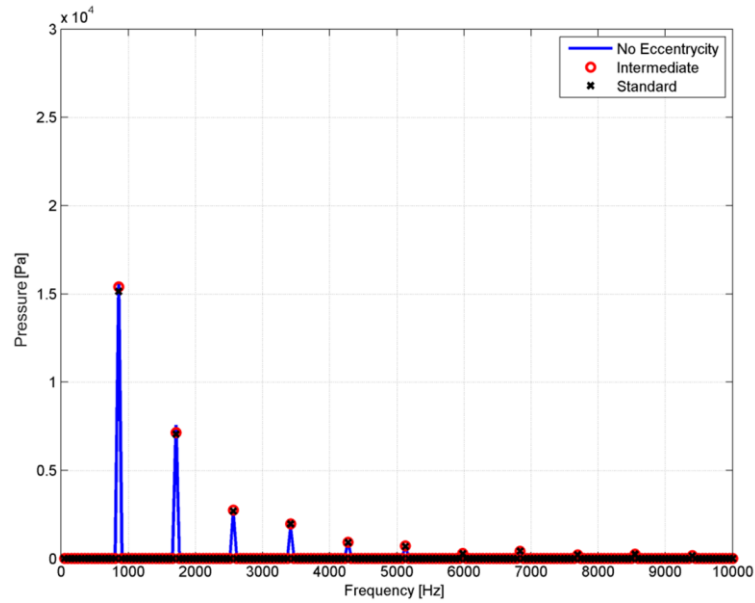
Figure 101. Spectrum of the pressure ripple, for three different eccentricity configuration.
(No Eccentricity, Intermediate, Standard).
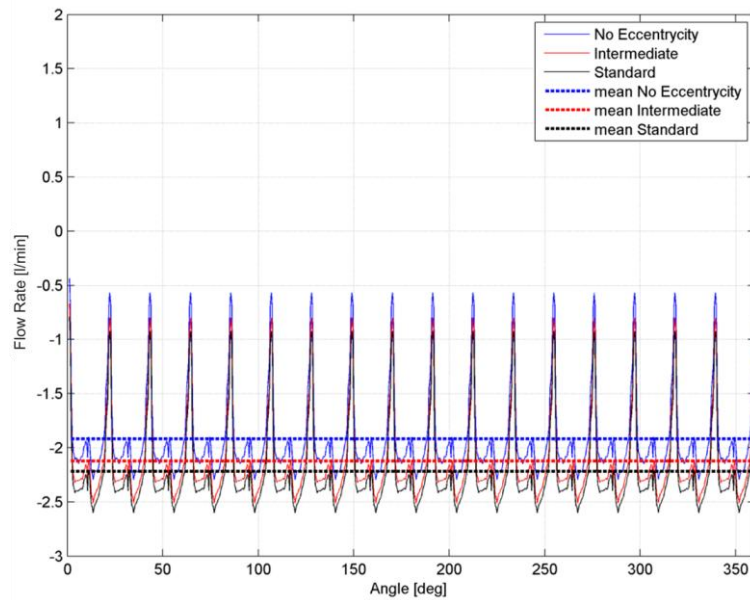
Figure 102. Outlet flow comparison (No Eccentricity, Intermediate, Standard).

In this case, the flows that are affected by the radial clearances are responsible of the pump efficiency; thus, a more accurate analysis

has been performed on those flows. At the beginning the focus was dedicated on the laminar flows of the reference volumes $Q_{TLF,16\_17,}$ $Q_{TLF,33\_34}$. Figure 103 and Figure 104 clarify how the large clearances near the LPS zone facilitate the oil leakages to the inlet volume while reducing the flows oscillation near the HPS zone. Remarkable attention must be paid to the $Q_{TDF,16\_17,}$ $Q_{TDF,33\_34}$ drag flows (Figure 105, Figure 106) as well, in order to evaluate the pump efficiency. It is interesting to see how the different eccentricity configurations affect the pressure within the pump reference volumes.
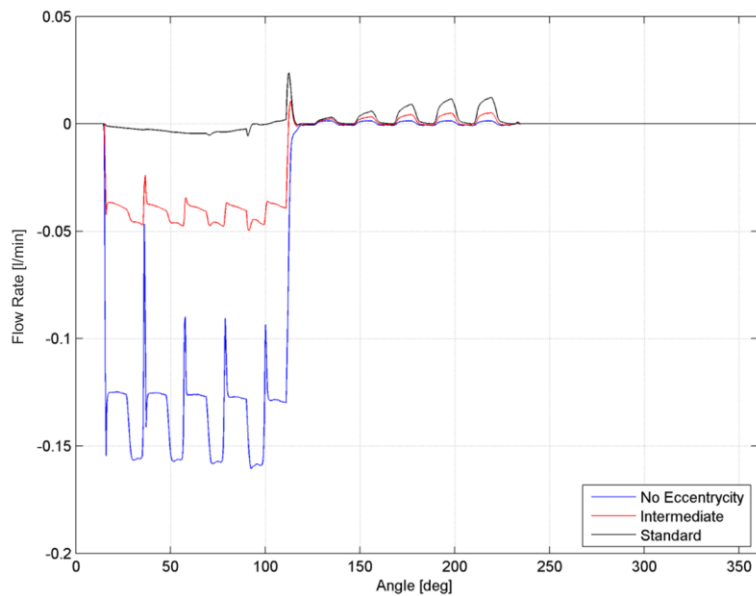
Figure 103. Comparison of $Q_{TLF,17\_18}$ flows for three eccentricity step.
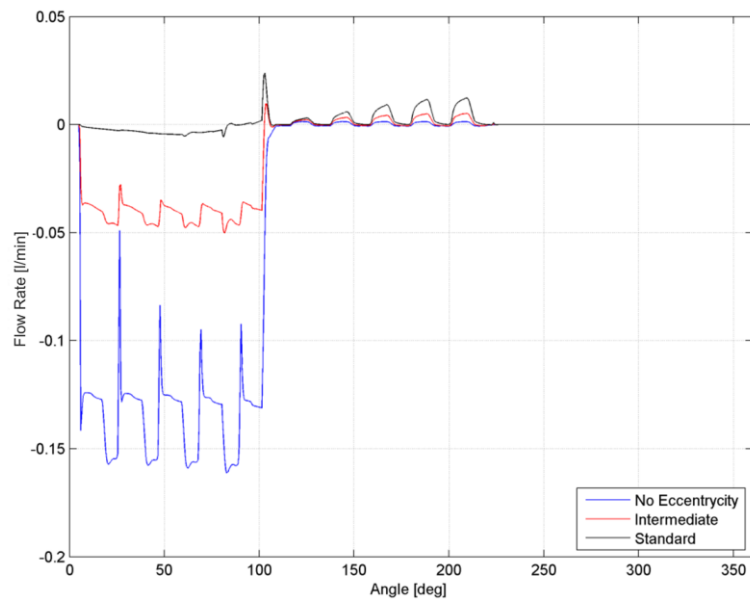
Figure 104. Comparison of $Q_{TLF,34\_35}$ flows for three eccentricity steps.
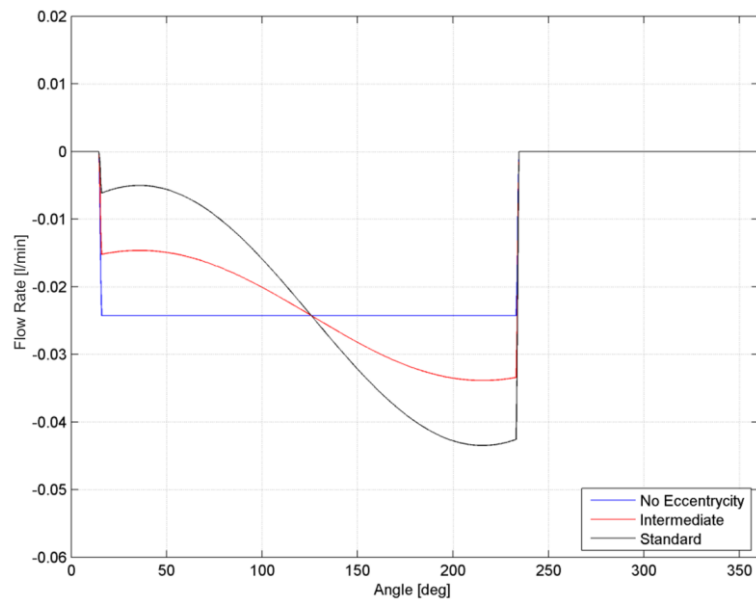
Figure 105. Comparison of $Q_{TDF,17\_18}$ flows for three eccentricity steps.
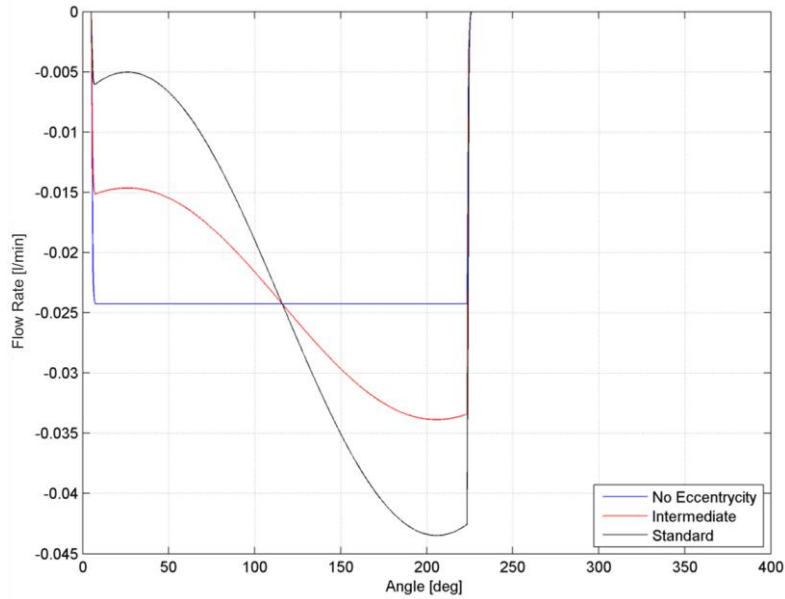
Figure 106. Comparison of $Q_{TDF,34\_35}$ flows for three eccentricity steps.

Following the same logical thread of the previous paragraph , the study of the pressures trend (focusing on the sealing zone) of the meshing volumes has been done for the Intermediate eccentricity condition and the Zero eccentricity condition (Figure 107, Figure 108). The results underline that the proper sealing of the standard condition (Figure 91) facilitates the pressurization of the gear pocket, reducing the delay to 30° from the worst condition (Zero Eccentricity). The disadvantages of the quick pressurization process are the pressure overshoot and the high amplitude levels of the pressure ripples in the first moments of the pressurization process. Moreover, the eccentricity does not affect the phase shift between the pressure ripple of the meshing volumes during the first moment of the pressurization process. A further overview is reported in Figure 109, Figure 110, where for each reference volume the simulation results have been compared to each other. These comparisons emphasize the concepts expressed in the previous lines.
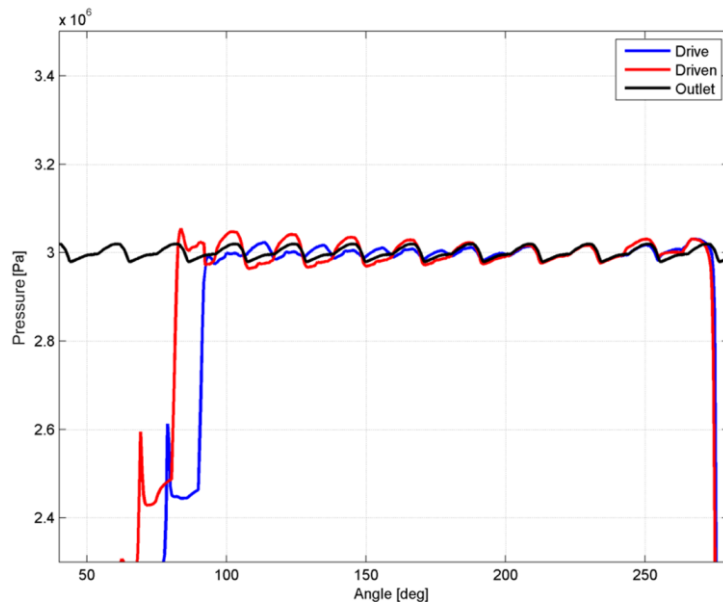
Figure 107. Pressure level of the reference volumes and outlet volume; Zero Eccentricity.
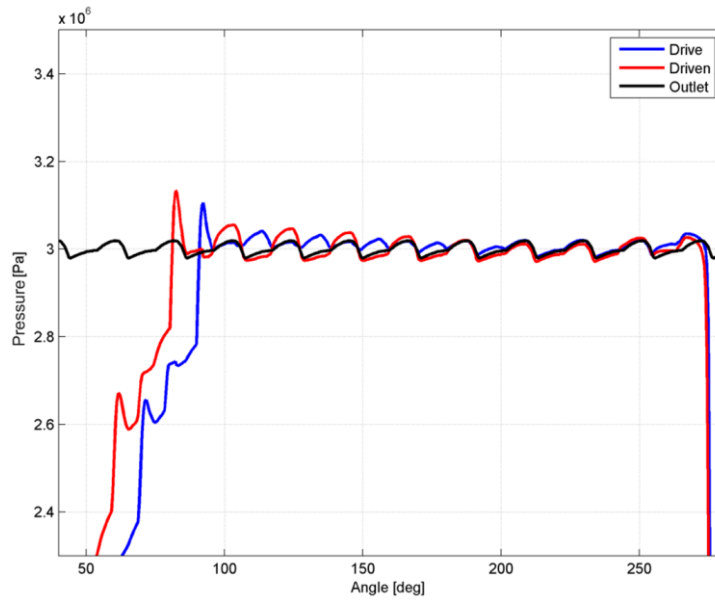
Figure 108. Pressure level of the reference volumes and outlet volume; Intermediate configuration.
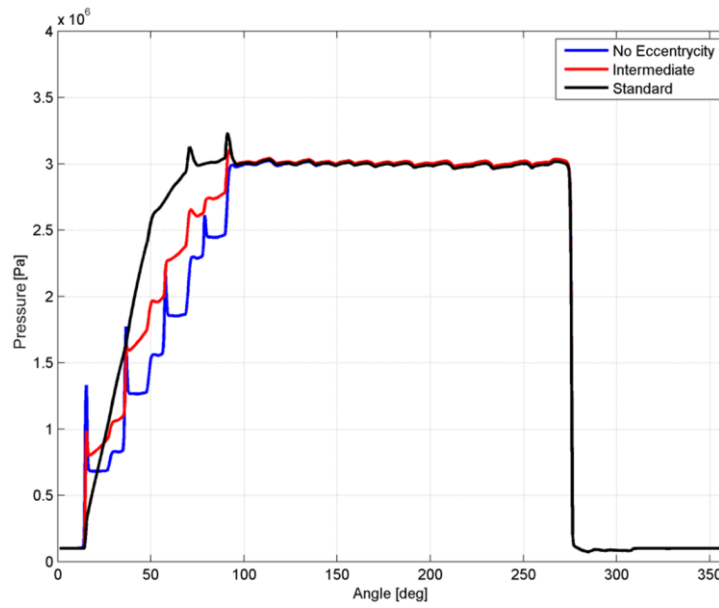
Figure 109. Evolution of pressure within the control volume of the drive gear for three eccentricity configurations.
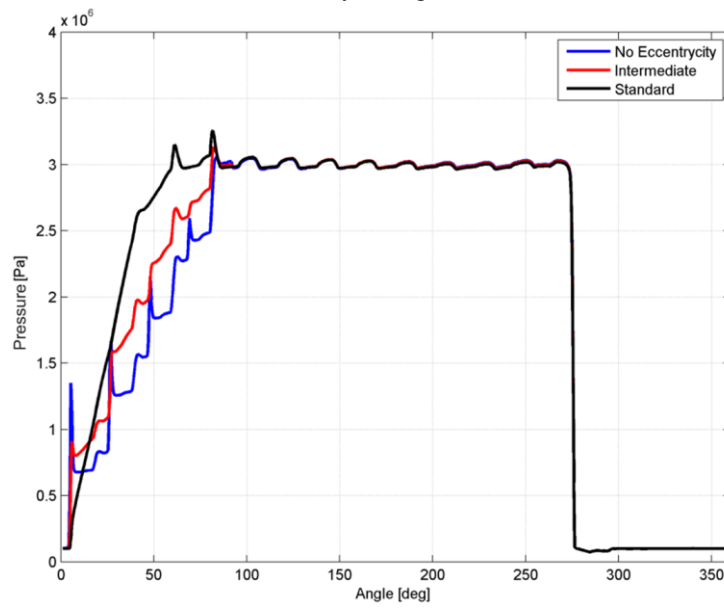
Figure 110. Evolution of pressure within the control volume of the driven gear for three eccentricity configurations.

Looking at the pressure within the control volume it is clearly evident that the gear eccentricity dramatically affects the pressure trend during the pockets pressurization; the different pressure distributions also have an effect on the $Q_{FLF,17\_18}$, $Q_{FLF,34\_35}$ axial laminar flows, which depend on the pressure gradient. Figure 111, Figure 112, Figure 113 and Figure 114 show the sensitivity of the gear eccentricity on the laminar axial flows. Furthermore, the gear eccentricity does not affect the phase shift between the pressure ripple of the reference volume during the first moment of the pressurization process. Finally, the last overview concerns the $Q_{LF,Dreinage\_18}$, $Q_{LF,Dreinage\_35}$ (Figure 115, Figure 116) drainage flows, which contribute to the reduction of the pump efficiency. The quality estimation of the pump efficiency has been performed by computing the average values of the studied flow rates within the sealing zone. These values are contained in Table 14.
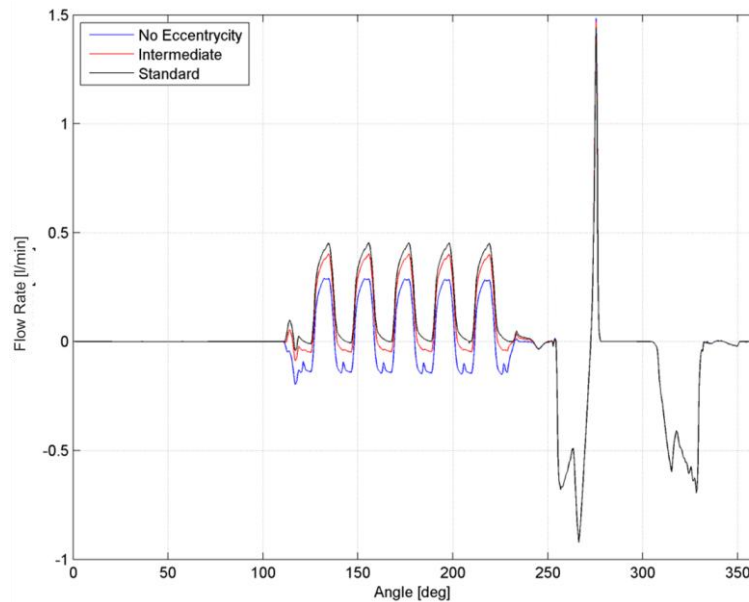
Figure 111. Comparison of $Q_{FLF,17\_18}$ flows for three eccentricity configurations (Upper tooth side).
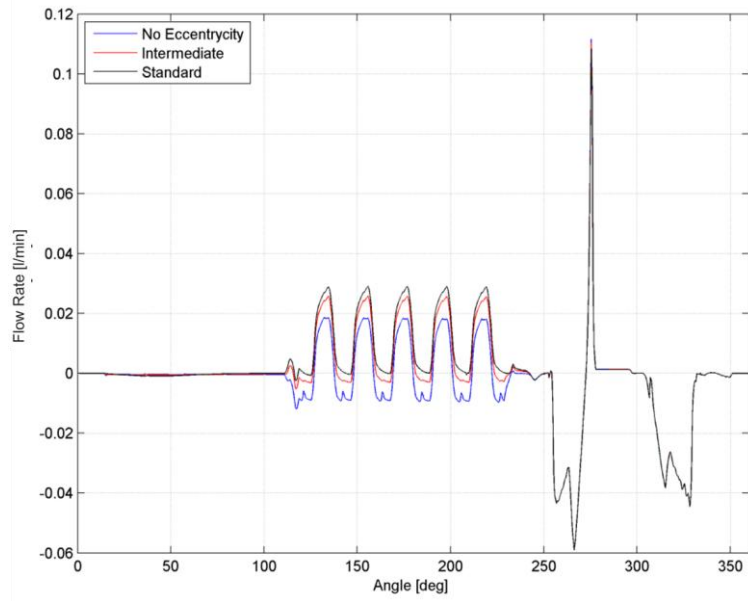
Figure 112. Comparison of $Q_{FLF,17\_18}$ flows for three eccentricity configurations (Lower tooth side).
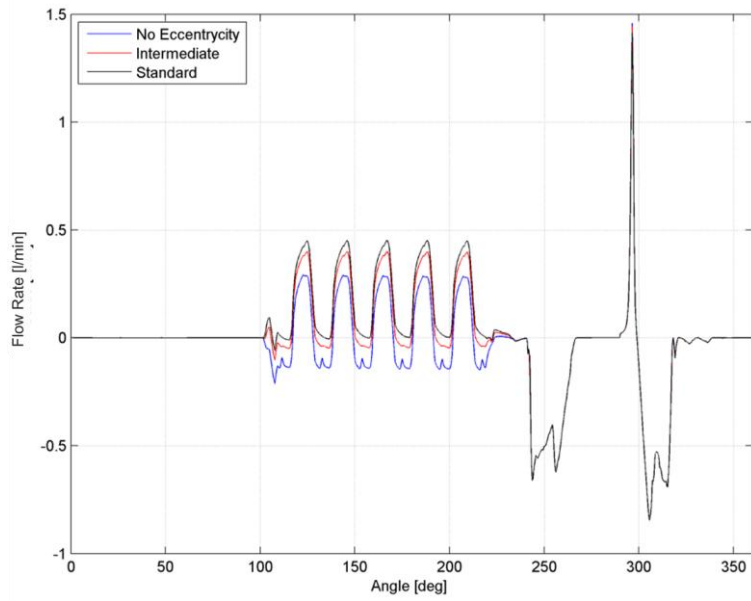
Figure 113. Comparison of $Q_{FLF,34\_35}$ flows for three eccentricity configurations (Upper tooth side).
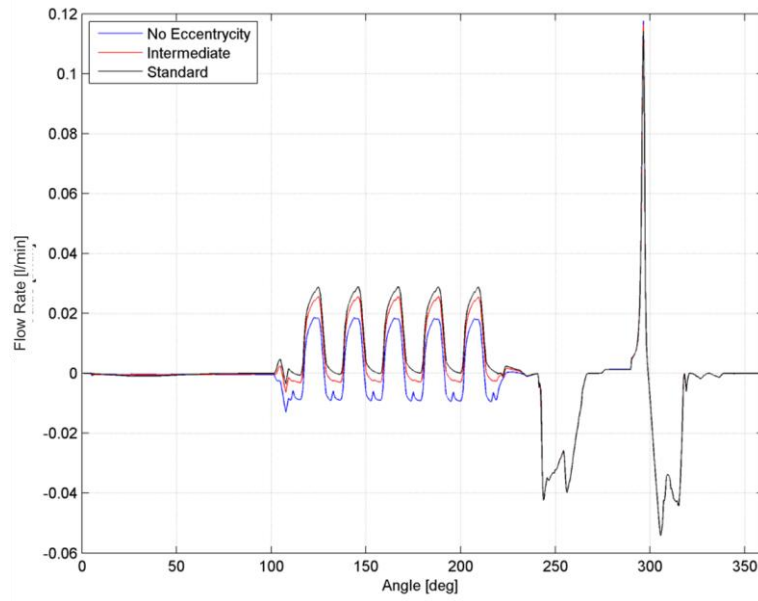
Figure 114. Comparison of $Q_{FLF,34\_35}$ flows for three eccentricity configurations (Lower tooth side).
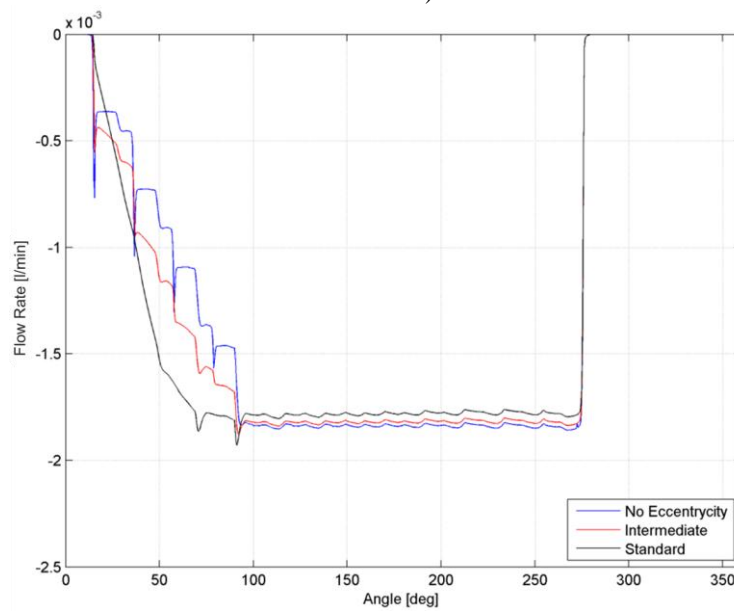
Figure 115. Comparison of $Q_{LF,Dreinage\_18}$ for three eccentricity configurations.
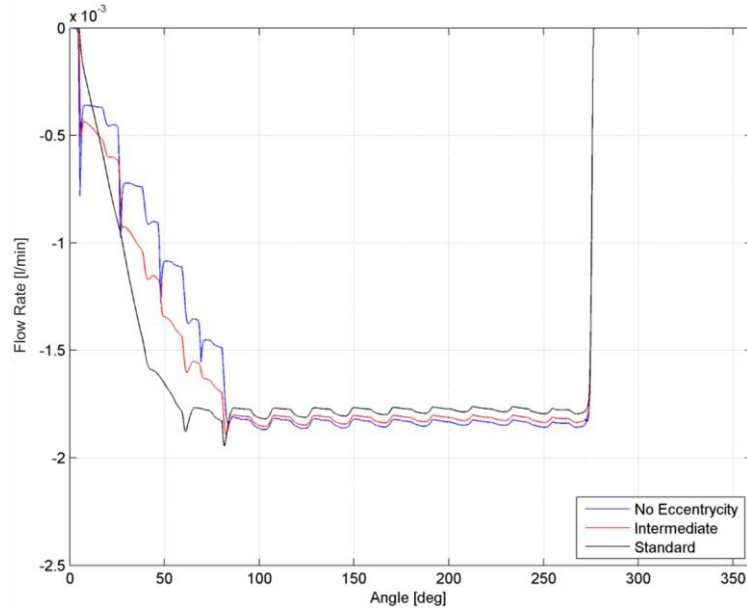
Figure 116. Comparison of $Q_{LF,Dreinage\_35}$ for three eccentricity configurations.

Reference Control Volume of drive gear	Step1	Step2	Step3
Average $Q_{FLF,16\_17}$(Upper Side)	0.01694l/min	0.07122l/min	0.09650l/min
Average $Q_{FLF,16\_17}$(Lower Side)	0.00093l/min	0.00443l/min	0.006l7l/min
Average $Q_{TLF,16\_17}$	-0.05994ll/min	-0.01734l/min	0.00084l/min
Average $Q_{TDF,16\_17}$	-0.00231l/min	-0.00231l/min	-0.00230l/min
Average $Q_{LF\_17Dreinage}$	-0.00154l/min	-0.00164l/min	-0.00160l/min
Reference Control Volume of driven gear	**Step1**	**Step2**	**Step3**
Average $Q_{FLF,33\_34}$(Upper Side)	0.01620l/min	0.06842l/min	0.00960l/min
Average $Q_{FLF,33\_34}$(Lower Side)	0.00090l/min	0.00422l/min	0.00600l/min
Average $Q_{TLF,33\_34}$	-0.54732l/min	-0.01663l/min	0.00089l/min
Average $Q_{TDF,33\_34}$	-0.00231l/min	-0.00231l/min	-0.00230l/min
Average $Q_{LF\_34Dreinage}$	-0.00154l/min	-0.00164l/min	-0.00160l/min

Table 14. Comparison of the average laminar flows for three eccentricity configurations.

A.3.4.   Sensitivity to the Epsilon Groove Depth

The next analysis is focused on the epsilon grooves: in particular, the effects of three different depths of the epsilon grooves have been investigated. The levels that were analyzed are: design depths 0.5mm

on the lower side and 0.2mm on the upper side, which is the intermediate condition; the second level (called "minimum depths"), where the height of the upper and lower grooves are respectively 0.25mm and 0.1mm; in the last level (called "maximum depths"), the dimensions of the standard depths were doubled. The epsilon groove depths for the three scenario are listed in Table 15. Figure 117, Figure 118, Figure 119 and Figure 120 represent the axial clearances (upper and lower side) between the tooth flank and the pump housing, for the reference tooth of the drive and driven gear. The ascending and descending curves that connect the minimum axial clearances (0.012mm) and the height of the epsilon grooves are polynomial laws, which have been properly scaled for minimum and maximum depths cases. Considering the simulation results analyzed so far, an important effect on the outlet and gear pockets pressure ripple is expected, as the epsilon groove extensions goes from the sealing zone up to the meshing zone, and a considerable difference in terms of groove depth means a substantial variation in terms of laminar and drag flows. A further indication that can be obtained from the previous paragraph concerns the higher depth of the upper side, which determines the lowest hydraulic impedance of the system and the best way for the oil to pour out. The simulation has been performed by keeping the other geometrical pump features and the oil physical properties constant.

Epsilon Grooves	Design	Minimum Depths	Maximum Depths
Upper side	0,5mm	0,25mm	1,00mm
Lower side	0,2mm	0,10mm	0,40mm

Table 15. Setting of the epsilon grooves, for the sensitivity analysis.
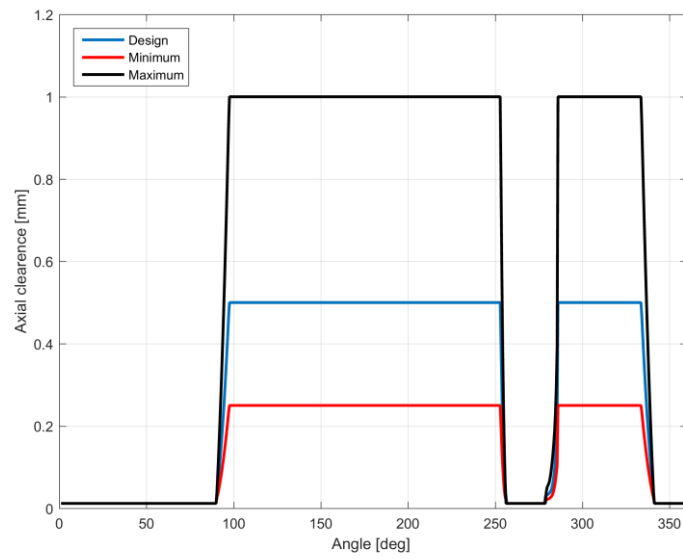
Figure 117. Axial clearance of the reference tooth of the drive gear (Upper side).
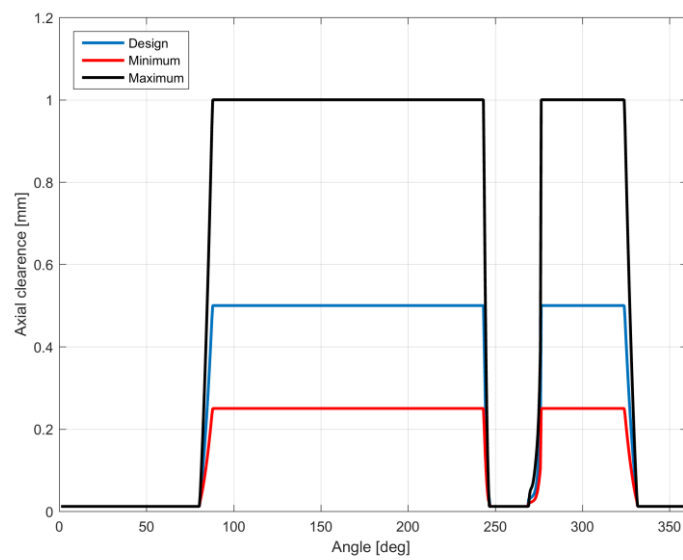
Figure 118. Axial clearance of the reference tooth of the driven gear (Lower side).
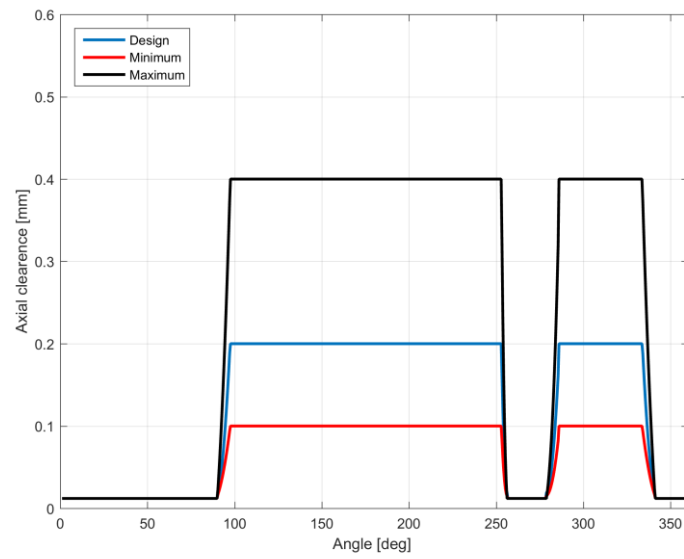
Figure 119. Axial clearance of the reference tooth of the driven gear (Upper side).
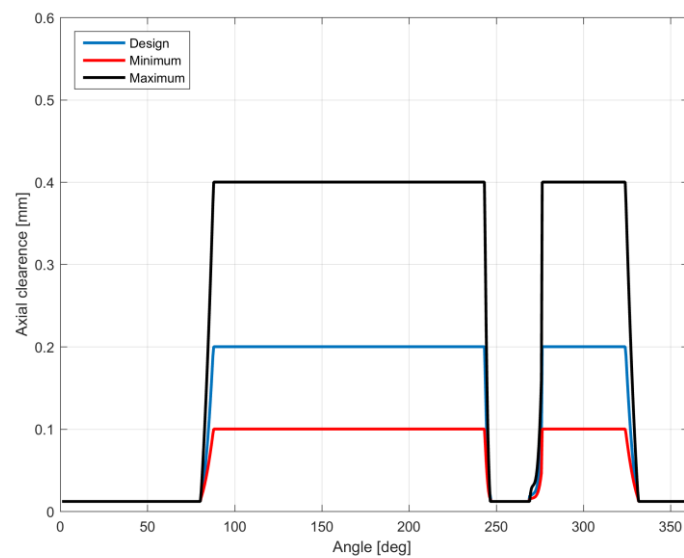
Figure 120. Axial clearance of the reference tooth of the driven gear (Lower side).

The analysis of the outlet pressure and outlet flow (Figure 121, Figure 122) points out that the tight axial clearances avoid leakages

between the outlet and inlet environment during the teeth meshing phase, inducing pressure ripple and flow oscillation with low amplitude levels. Furthermore, the minimum epsilon groove height case has the highest efficiency, because of its average outlet flow value; on the other hand, the maximum eccentricity case represents the worst case in terms of pump efficiency. Figure 122 clearly shows the worst case, in which the outlet flow assumes positive values in several points; in those moments, the outlet volume is drawing oil from the outlet pipe, because the meshing volumes are moving a flow from the outlet environment to the inlet environment. The pump efficiency values are respectively 0.94 for the design case, 0.98 for the minimum epsilon grooves height and finally 0.81 for the worst case. The frequency analysis of the outlet pressure ripple (Figure 123), shows the variation of the signal frequency content due to the epsilon groove height; essentially, the epsilon groove height affects the pressure ripple amplitude, as well as the relative ratios between the main order amplitudes of the pressure signal. This is the first case that shows this particular trend and Table 16 contains the amplitude ratios, taking the amplitude of the first meshing order as a reference.

Epsilon grooves configuration	1°meshing Order	2°meshing Order	3°meshing Order
Design	1	2.15	5.61
Minimum	1	2.89	10.86
Maximum	1	2.07	6.01

Table 16. Relative ratios of the main order amplitudes.
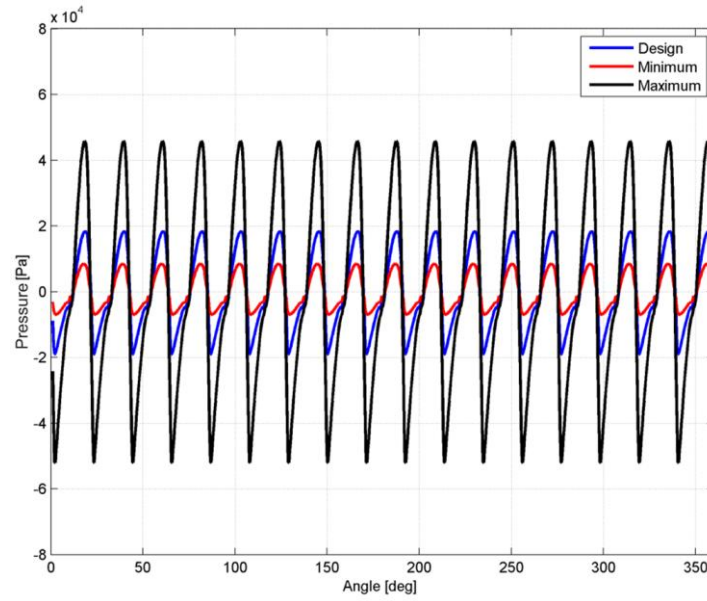
Figure 121. Outlet pressure comparison (Design, Minimum height, Maximum height).
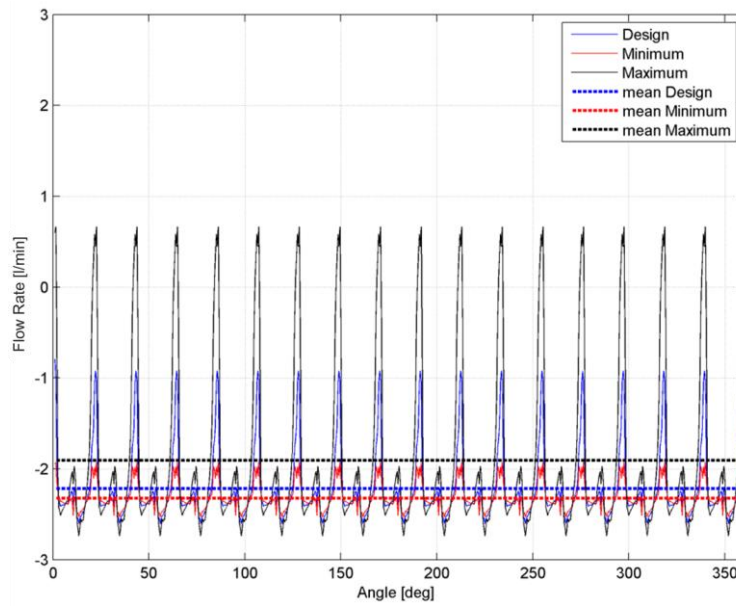
Figure 122. Outlet flow comparison (Design, Minimum height, Maximum height).
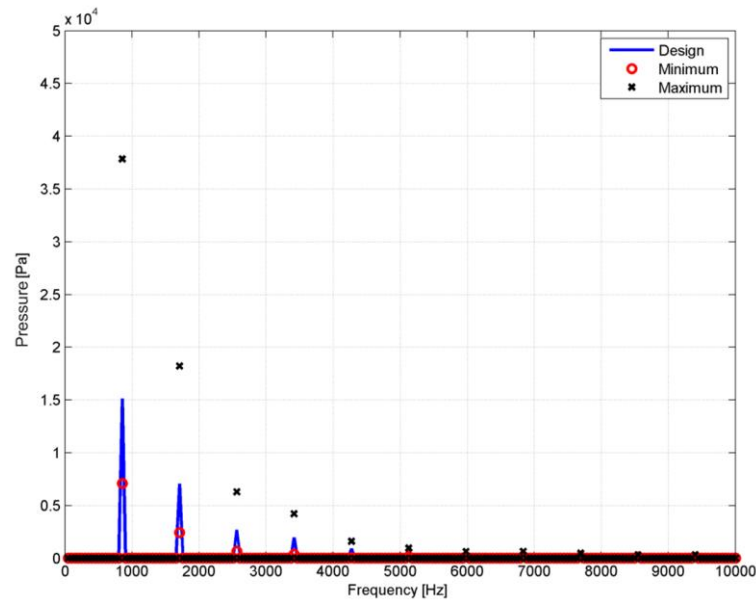
Figure 123. Spectrum of the pressure ripple, for three different epsilon grooves height configuration. (No Design, Minimum, Maximum).

It is going to analyze the behavior of the laminar flows and the axial drag flows, in order to understand what is effect the different designs of the epsilon grooves inside the sealing zone have on the pump efficiency. The first flows analyzed are $Q_{FLF,17\_18}$, $Q_{FLF,34\_35}$. (Figure 124, Figure 125,Figure 126 and Figure 127); these flows do not seem to affect the pump efficiency, when looking at sealing zone. Increasing the grooves depth increases the amplitude of the flow oscillation; yet, the absolute values inside the sealing zone have always a positive sign, thus no leakage is expected. On the contrary, the axial drag flows ($Q_{FDF,17\_18}$, $Q_{FLF,34\_35}$) (Figure 128, Figure 129, Figure 130, Figure 131) have an opposite behavior in respect to the laminar flows, as they are not influenced by the pressure gradient but their magnitudes are defined only by the groove depths.
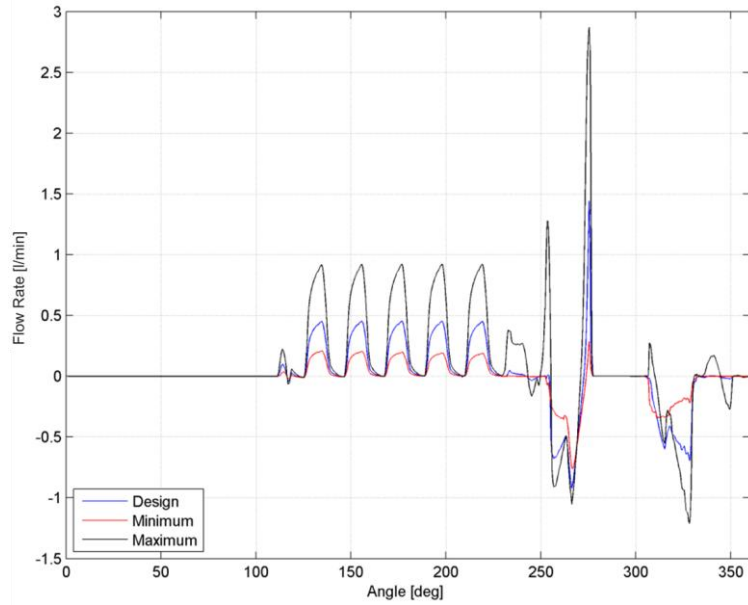
Figure 124. Comparison of $Q_{FLF,17\_18}$ flows for three different epsilon groove heights configuration (Lower tooth side).
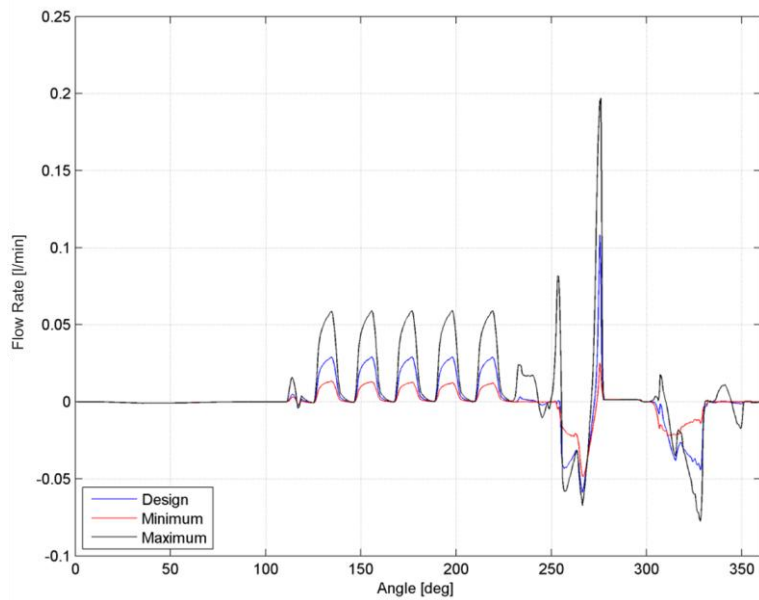
Figure 125. Comparison of $Q_{FLF,17\_18}$ flows for three different epsilon groove heights configuration (Upper tooth side).
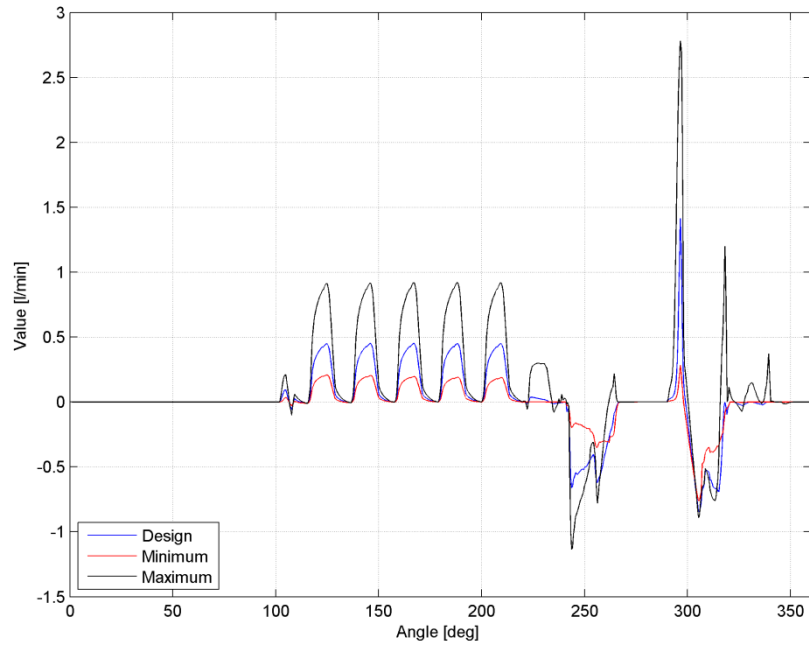
Figure 126. Comparison of $Q_{FLF,34\_35}$ flows for three different epsilon groove heights configuration (Lower tooth side).
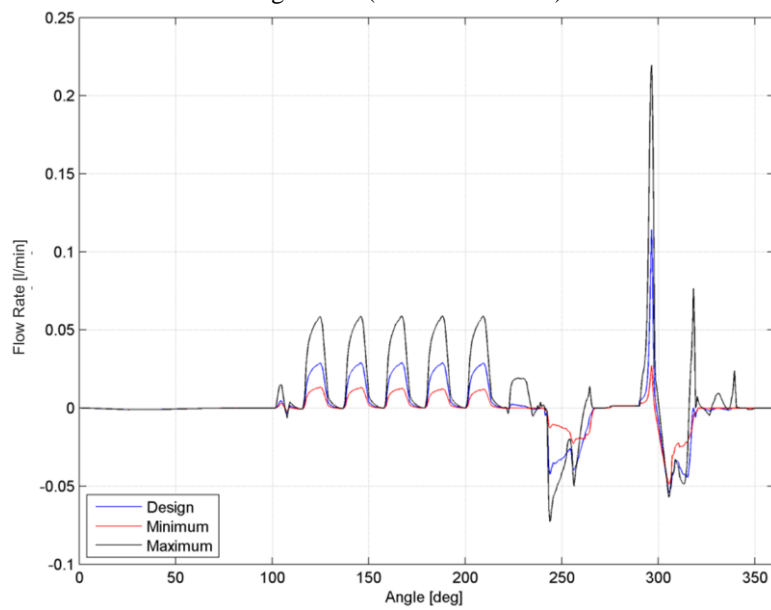
Figure 127. Comparison of $Q_{FLF,34\_35}$ flows for three different epsilon grooves height configuration (Upper tooth side).
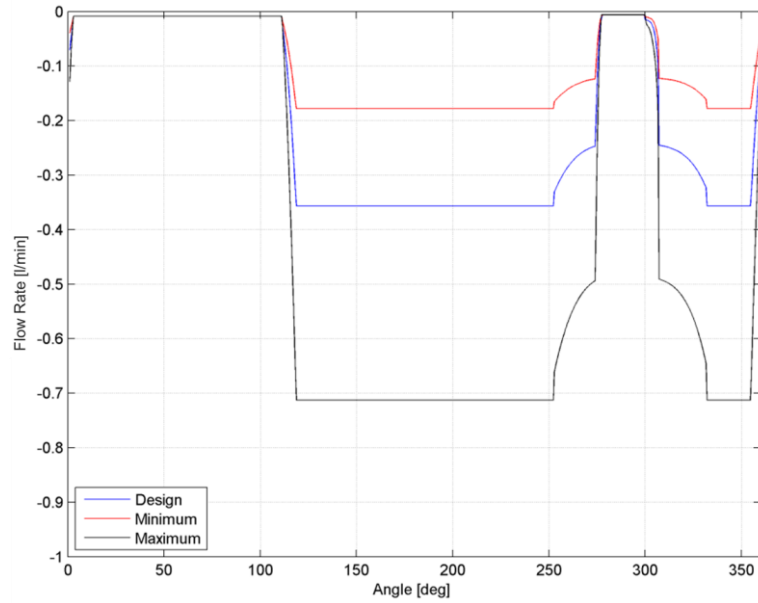
Figure 128. Comparison of $Q_{FDF,17\_18}$ flows for three different epsilon grooves height configuration (Lower tooth side).
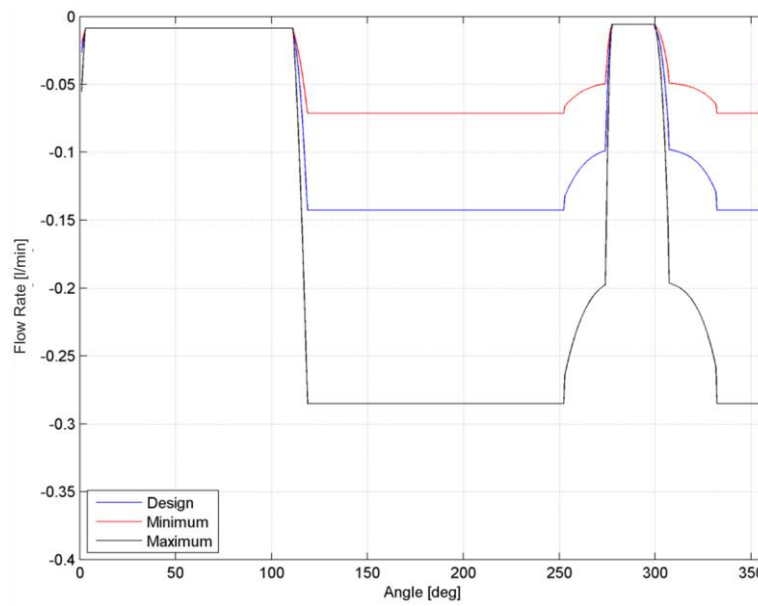
Figure 129. Comparison of $Q_{FDF,17\_18}$ flows for three different epsilon grooves height configuration (Upper tooth side).
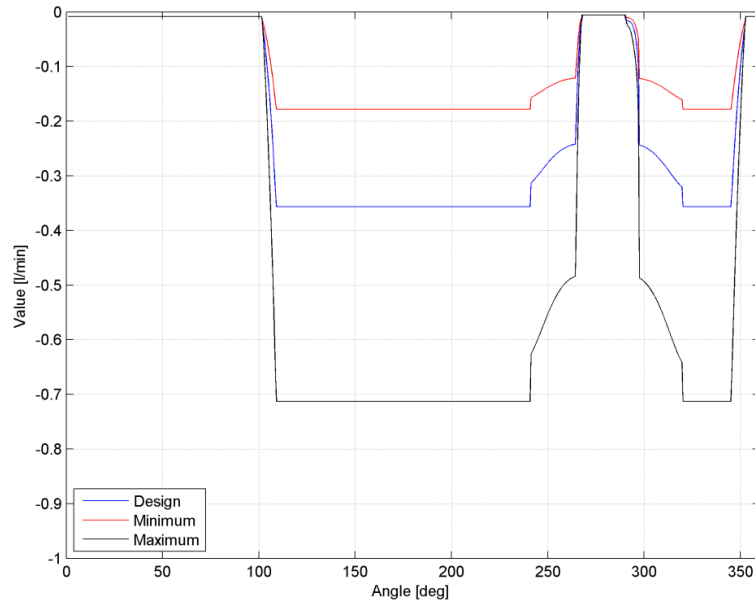
Figure 130. Comparison of $Q_{FDF,34\_35}$ flows for three different epsilon grooves height configuration (Lower tooth side).
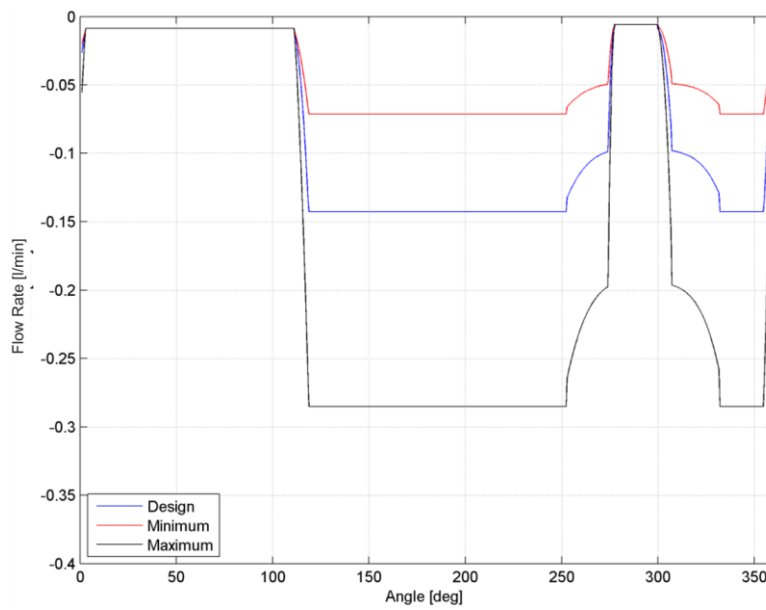
Figure 131. Comparison of $Q_{FDF,34\_35}$ flows for three different epsilon grooves height configuration (Lower tooth side).

The results observed so far suggest that the different behaviour of the axial laminar flows within the sealing zone also affects the laminar flows which passing through the clearances between the gear tip and the pump housing. Figure 132, Figure 133 display the comparison between the $Q_{FLT,17\_18}$, $Q_{FLT,34\_35}$ for the epsilon groove depths. The trend of the tip laminar flows has an opposite behaviour in respect to the flank flows; when a high amplitude oscillation occurs on the flank, a low amplitude oscillation arises on the tip and vice-versa. The configuration with the deepest epsilon grooves sets a low hydraulic impedance for the axial flows; thus, when a pressure gradient occurs between two adjacent pockets, the oil tends to pass through the axial clearance instead of the gear tip clearance. Nevertheless, the magnitude of the axial flows is always higher than that of the radial flows. We will now focus on the pressure trend within the reference control volumes of the drive and driven gears in the far end cases of groove depth (Figure 134, Figure 135). These cases differ from the design case because the pressure ripple of the drive and driven gear have the same frequency content. A further consideration concerns the pressure ripple: essentially, the epsilon grooves, which are characterized by a small depth, delay the achievement of the outlet pressure level; the pressure amplitude oscillations tend to decay slowly after the first overshoot, due to the gear pocket pressurization. In conclusion, the high axial clearance facilitates the pockets pressurization by reducing the pressure ripple within the sealing zone. The separated comparison of reference volume pressure ripples (Figure 136, Figure 137) gives additional points. Firstly, the tight clearances case enhances the pressure level on both reference volumes during the meshing phase; this is due to the high hydraulic impedances, that prevent the oil from leaking into the inlet environment. Secondly, during the meshing release the gear pockets struggle to draw oil from the inlet or outlet environment; thus, a low pressure level occurs, causing a greater risk of cavitation. The average flows analysis for pump efficiency estimation was not necessary in this case, as the main oil leakages that arise during the meshing phase happen through the bridge that separates the outlet and inlet grooves.
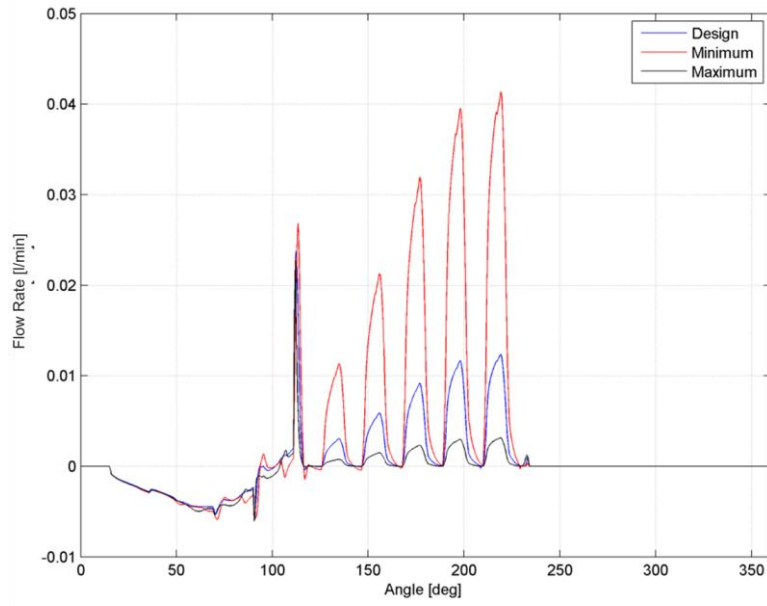
Figure 132. Comparison of $Q_{TLF,17\_18}$ flows for three different epsilon grooves height configuration (Drive gear).
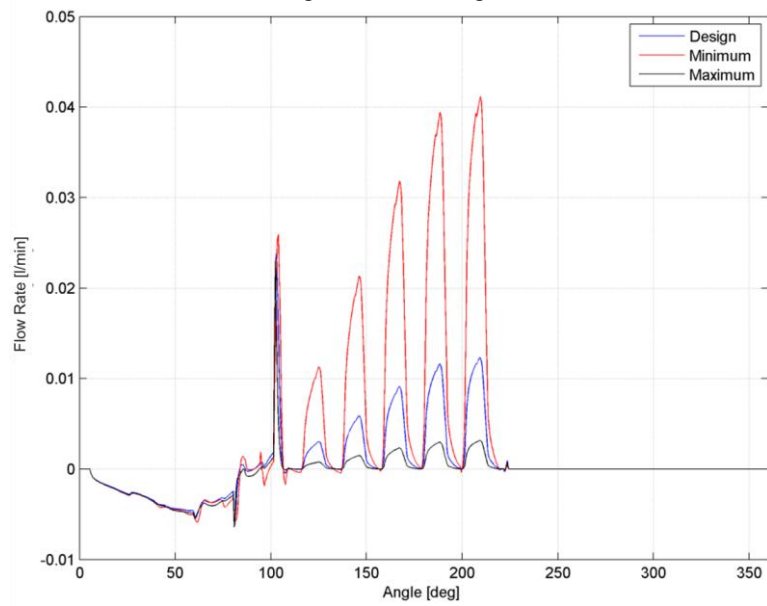
Figure 133. Comparison of $Q_{TLF,34\_35}$ flows for three different epsilon grooves height configuration (Driven gear).
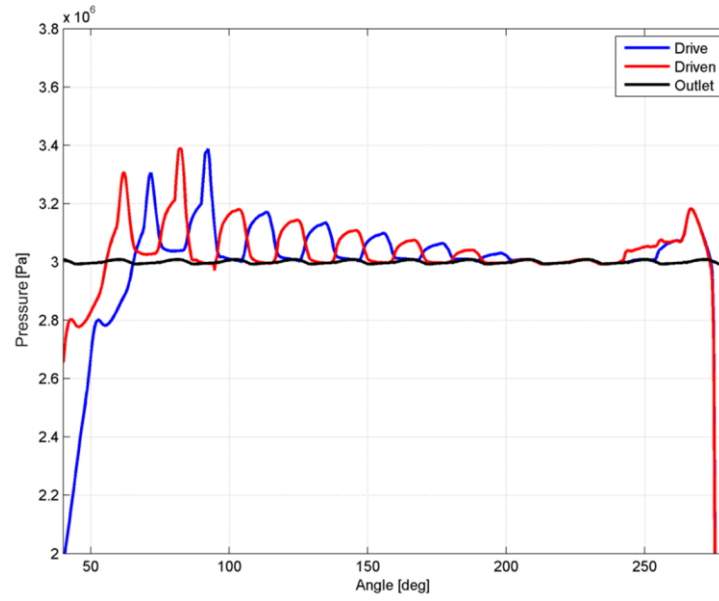
Figure 134. Pressure level of the reference volumes and outlet volume; Minimum depth of the epsilon grooves.
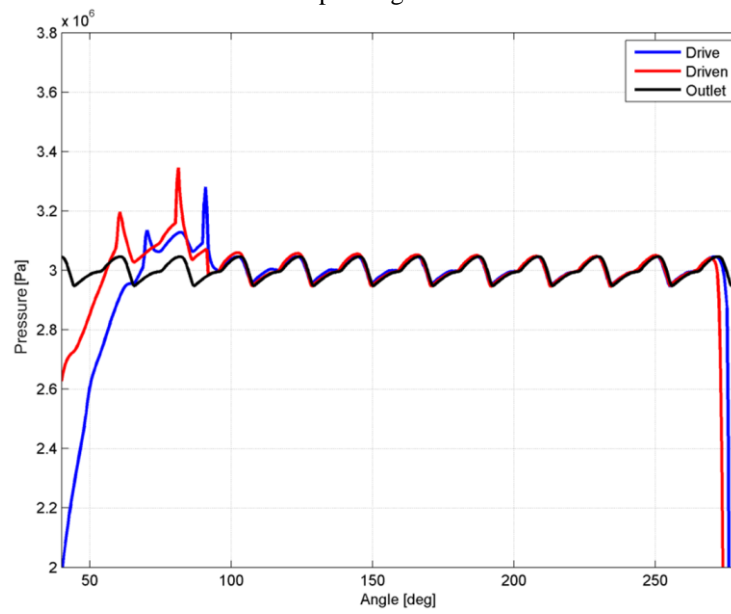
Figure 135. Pressure level of the reference volumes and outlet volume; Maximum depth of the epsilon grooves.
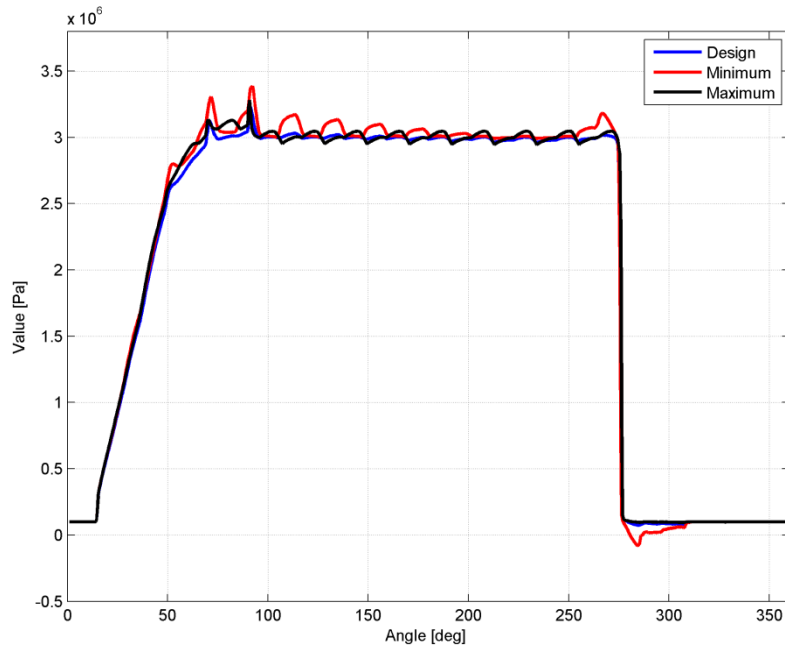
Figure 136. Evolution of pressure within the control volume of the drive gear for three different epsilon groove depths.
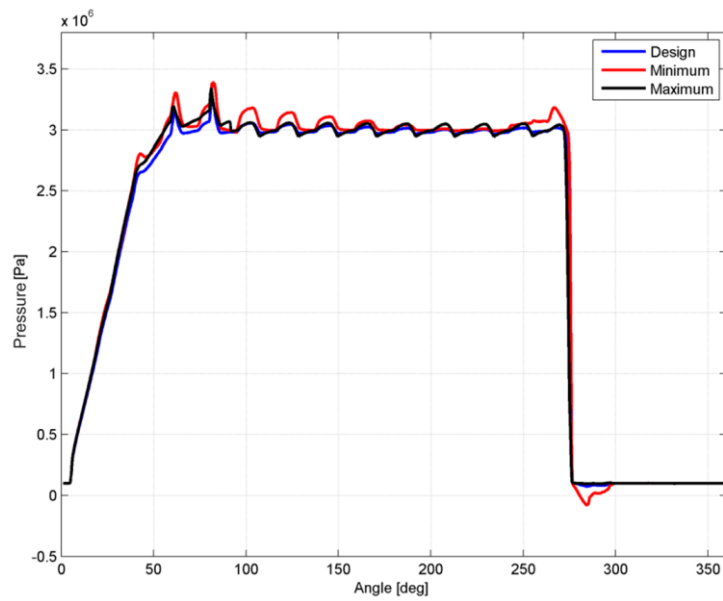
Figure 137. Evolution of pressure within the control volume of the driven gear for three different epsilon groove depths.

A.3.5.   Sensitivity to the Outlet Epsilon Groove Extension

The last paragraph deals with the effect of the outlet epsilon groove extensions. The epsilon groove extension leads to modify the axial laminar and drag flow within the sealing zone; thus, no remarkable differences in terms of pump efficiency can be expected. The modifications should affect the gear pockets pressure level: in fact, the epsilon groove characterized by the maximum extension should reduce the outlet pressure level within the gear pockets. This behavior is due to the low hydraulic impedance, which allows the oil leakage up to the epsilon groove begin; yet, the oil cannot reach the inlet environment, and the pump efficiency remains almost constant. Also in this case, three different conditions have been analyzed. The first refers to the standard design; in the second one, the epsilon groove extension has been reduced (45° of delay in respect to the gear centers); finally, the widest extension of the epsilon groove has been investigated. The three different designs are displayed in Figure 138. The outlet epsilon grooves modifications are applied on the upper plate and the middle plate as well. The axial clearances due to the different outlet epsilon groove extensions have been reported in Figure 139, Figure 140, Figure 141 and Figure 142; the epsilon groove depths have been kept equal to those of the design configuration (0.2mm on the lower side and 0.5mm for the upper side). The polynomial laws which link the minimum axial clearance value to the maximum clearance value and the inlet groove designs were not modified.
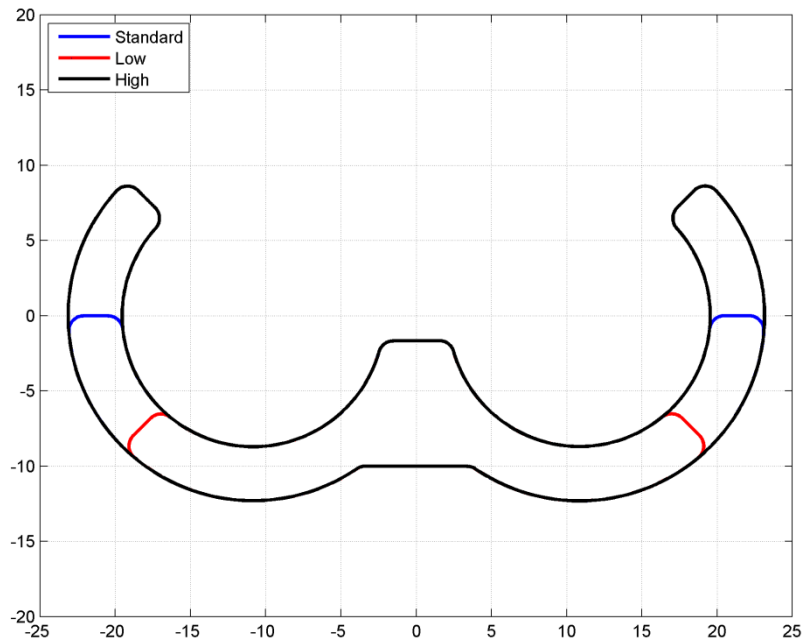
Figure 138. Epsilon groove designs. (Standard, Low extension, High extension)
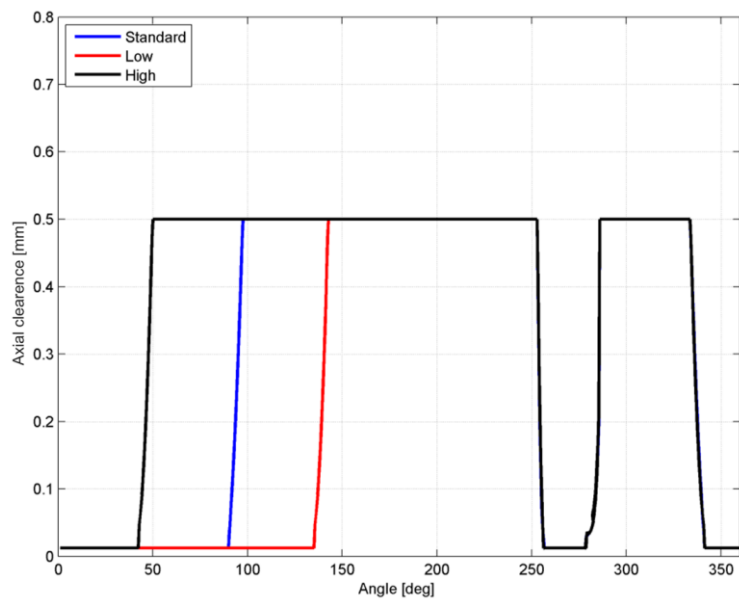
Figure 139. Axial clearance of the reference tooth of the drive gear (Upper side).
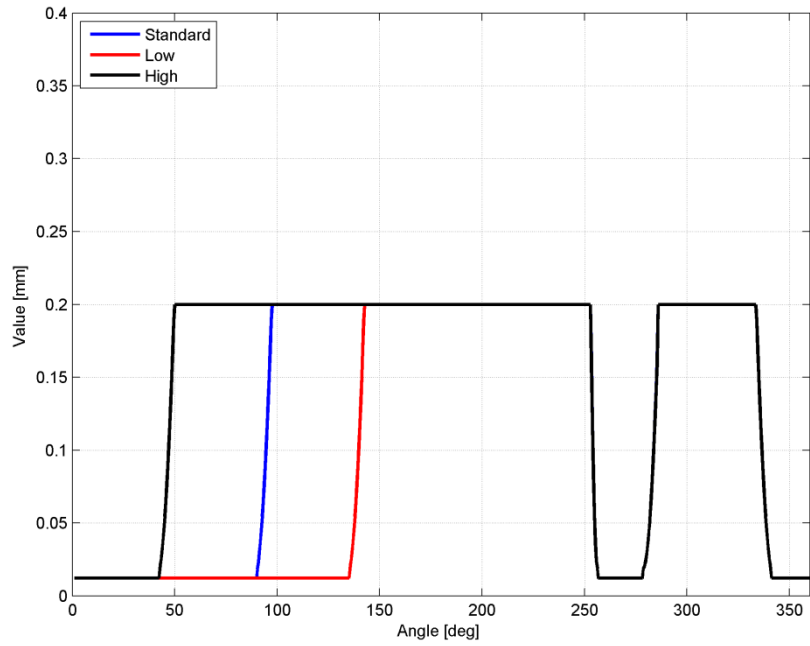
Figure 140. Axial clearance of the reference tooth of the drive gear (Lower side).
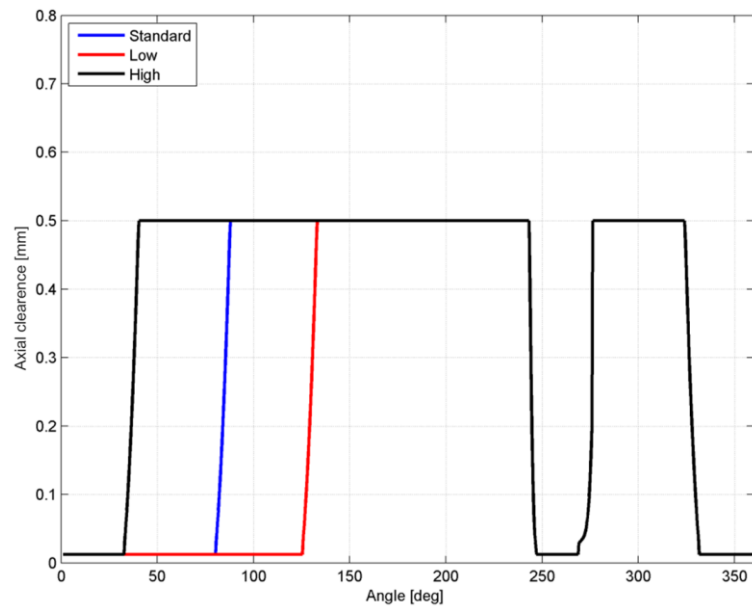
Figure 141. Axial clearance of the reference tooth of the driven gear (Upper side).
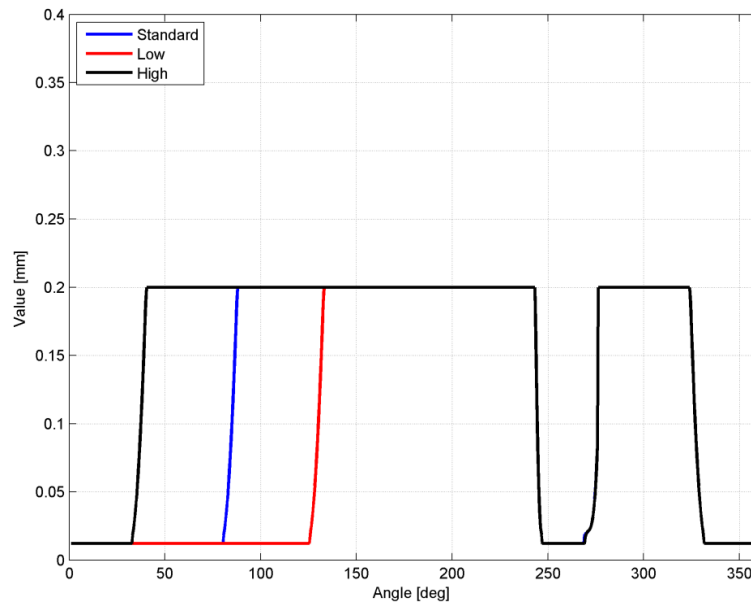
Figure 142. clearance of the reference tooth of the driven gear (Lower side).

It is going to analyze the results for the outlet pressure ripple (Figure 143, Figure 144); it is really interesting to see how the different epsilon groove extension is able to affect the outlet pressure ripple. The spectrum analysis shows the different frequency content among the different configurations; in particular, the standard extension determines the amplification of the even meshing order. On the other hand, the configurations that begin further from the gear center line accentuate the odd meshing order. Basically, the outlet pressure trend during a circular pitch rotation is characterized by two sections with a positive slope; the wider extension of the epsilon groove reduces the derivative value of the first section, and increases the value of the second section. Furthermore, the wider epsilon groove extensions have high positive and negative peak values. The trend of the outlet flow is coherent with the outlet pressure ripple, but the difference in terms of pump efficiency is not as remarkable as expected (0.94 Standard, 0.93 Low, 0,93 High).
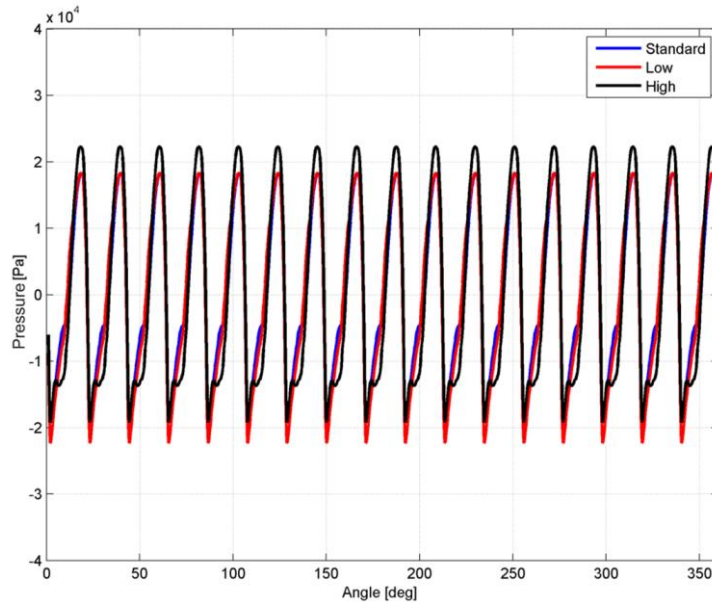
Figure 143. Outlet pressure comparison.
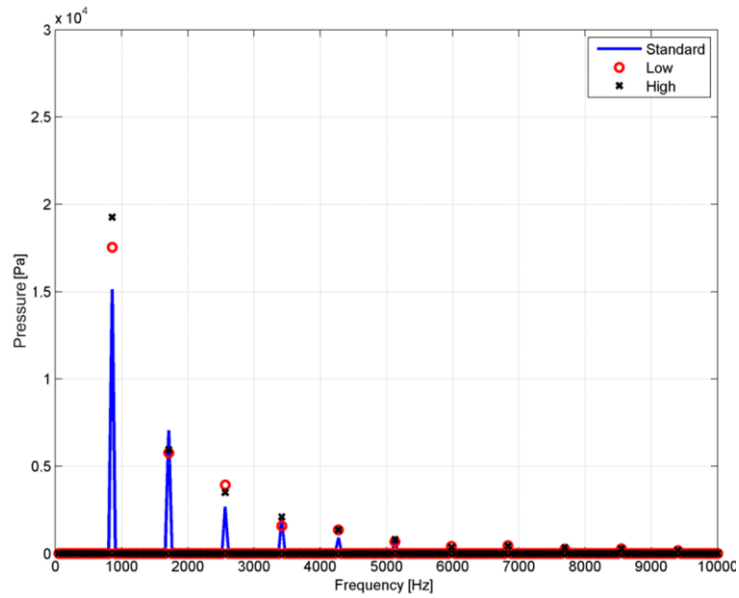
Figure 144.Spectrum of the pressure ripple, for three different e Epsilon groove extension .
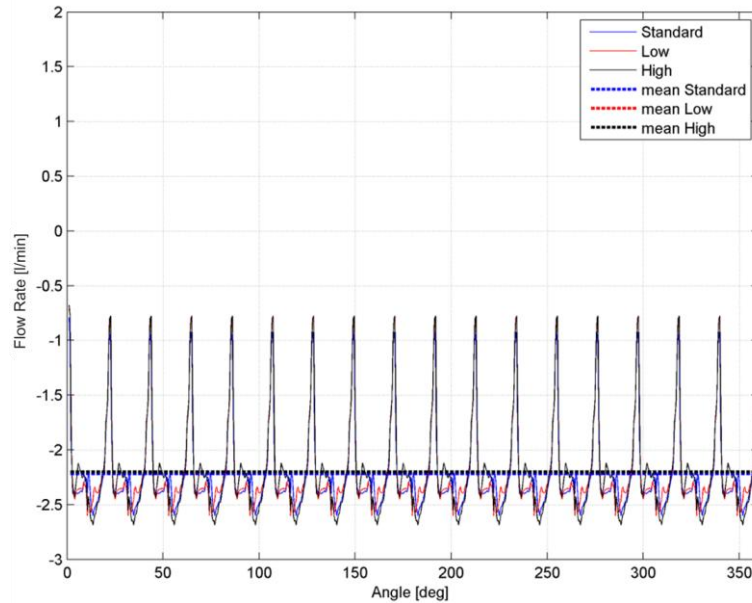
Figure 145. Outlet flows comparison between three different epsilon groove extension.

Further information is given by the axial laminar flows (Figure 146, Figure 147, Figure 148 and Figure 149). The study of the laminar flows confirms both the phase shift due to the different extension and the two main effects on the flows oscillations within the sealing zone. The first effect is the variation of the positive peak trend: higher extensions add a further harmonic contribution on the flow trend peaks and lead to reaching negative values in initial oscillations. The epsilon groove extensions affect the radial laminar flows as well (Figure 150, Figure 151); in fact the lower extension of the epsilon groove makes for the same zone the hydraulic impedance of the radial flows comparable with the axial hydraulic impedance. On the other hand, the wider epsilon groove extensions make the flows passing through the radial clearances negligible, while the positive flow peak is reduced due to the volume getting in front of the epsilon groove earlier. The last analysis concerns the pressure within the gear pockets during a complete pump turn.
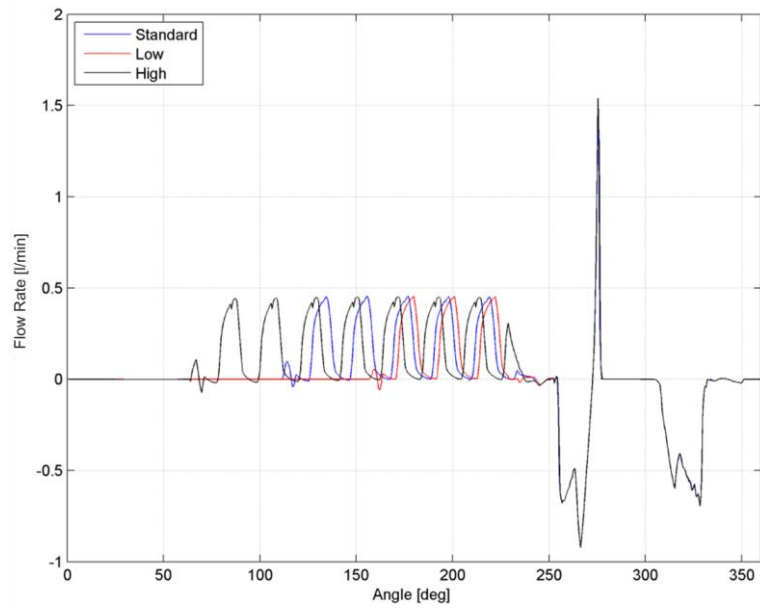
Figure 146. Comparison of $Q_{FLF,17\_18}$ flows for three different epsilon groove extensions (Lower tooth side).
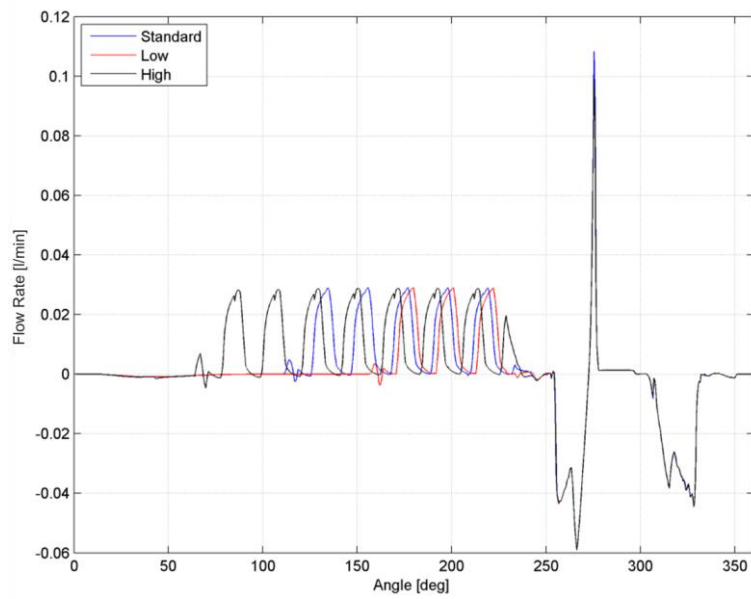
Figure 147. Comparison of $Q_{FLF,17\_18}$ flows for three different epsilon groove extensions (Upper tooth side).
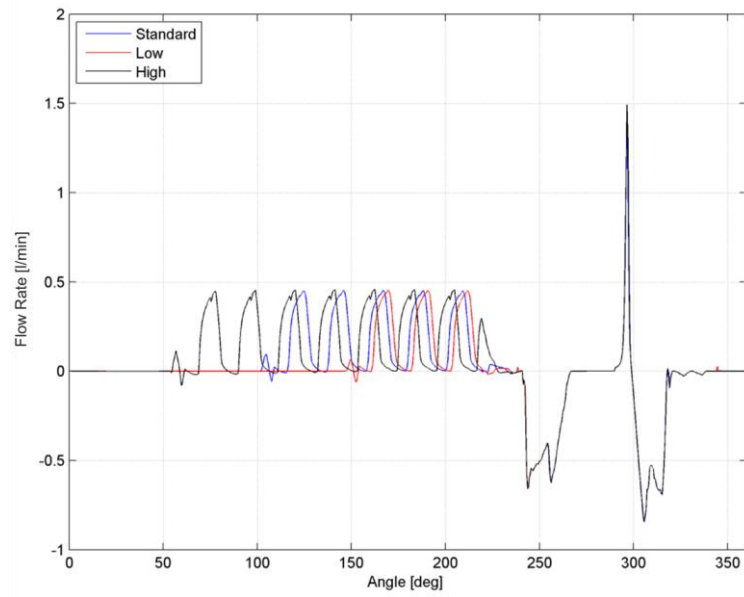
Figure 148. Comparison of $Q_{FLF,34\_35}$ flows for three different epsilon groove extensions (Lower tooth side).
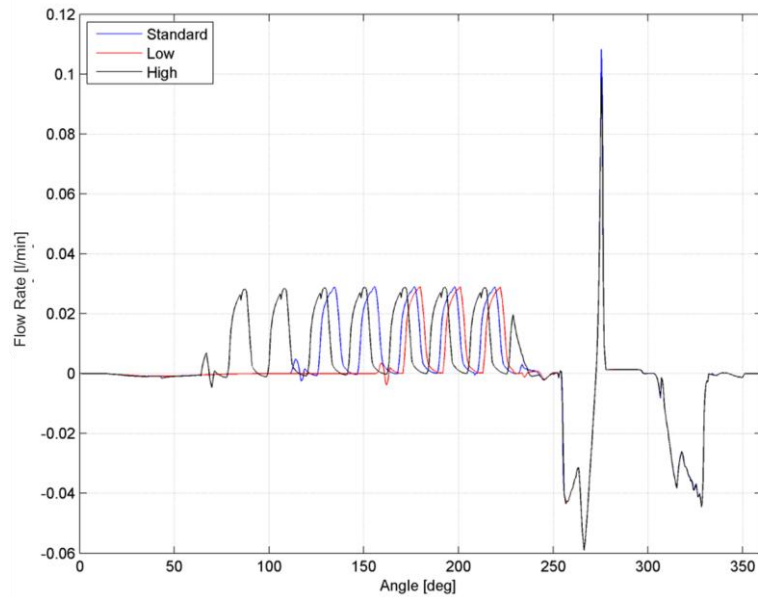
Figure 149. Comparison of $Q_{FLF,34\_35}$ flows for three different epsilon groove extensions (Upper tooth side).
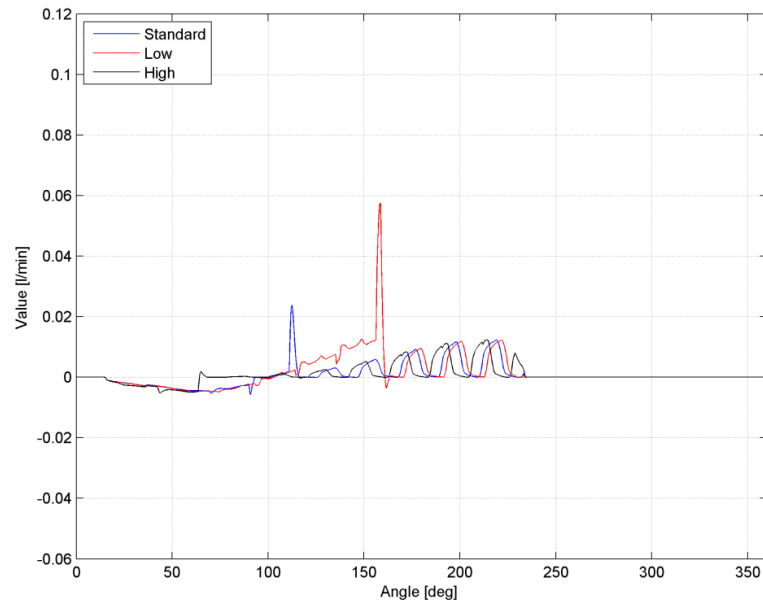
Figure 150. Comparison of $Q_{TLF,17\_18}$ flows for three different epsilon grooves extension (Drive gear).
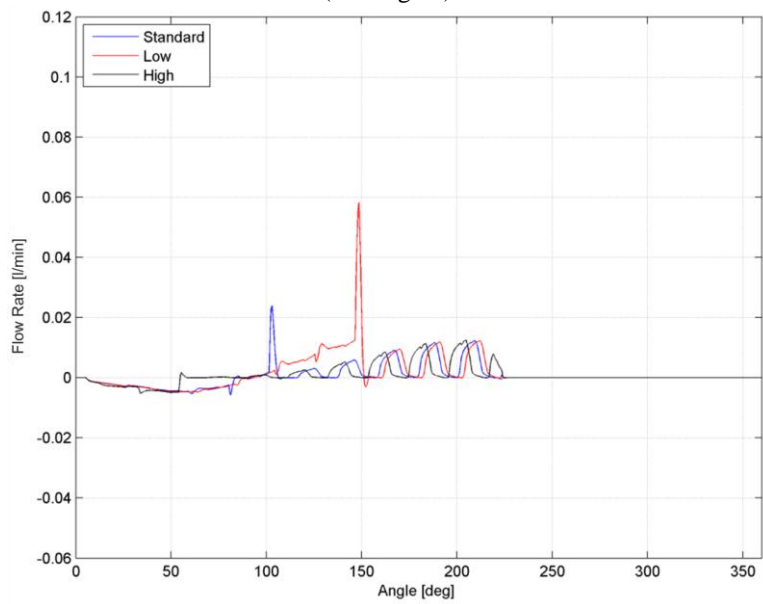
Figure 151. Comparison of $Q_{TLF,34\_35}$ flows for three different epsilon grooves extension (Drive gear).

The epsilon grove extensions affect the overshoot pressure level dramatically: in fact, the filling in advance of the gear pocket (due to the wider epsilon groove configuration) induces a very sharp spike during the pressurization process. The delay of the epsilon groove beginning, reduces the peak of the pressurization process; this behavior is caused by the wide radial clearances between the gear tooth and the pump housing. The increasing of the epsilon groove extension makes it possible to extend the outlet pressure level within the gear pockets when they are sealed by the pump housing. Finally, the separated comparison between the drive and driven gear pocket results shows a peculiar behavior: the curves match respectively at 212° for the drive gear and 190° for the driven gear; this angle corresponds to the moment in which the reference pockets begin to communicate with the outlet environment.
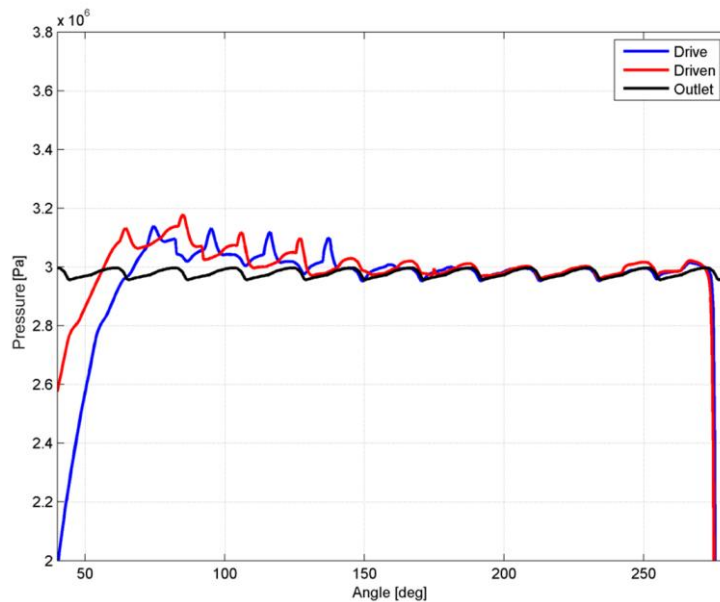
Figure 152. Evolution of pressure within the control volume for the lower extension of the epsilon groove.
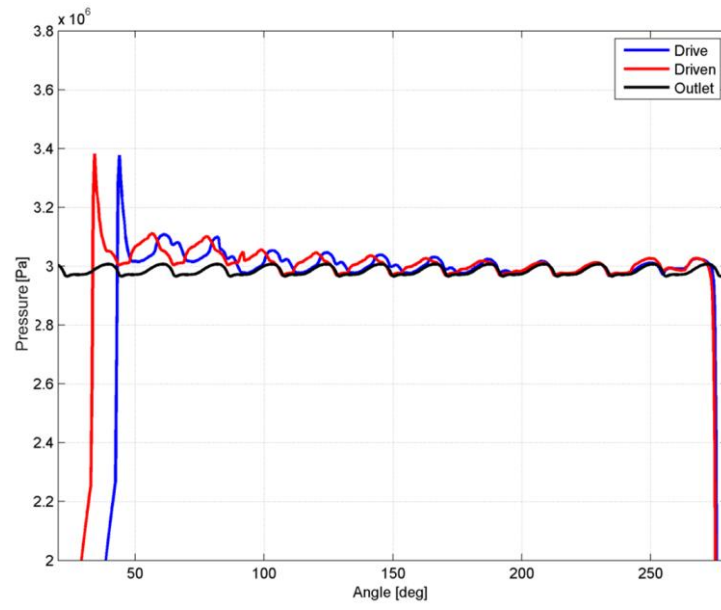
Figure 153. Evolution of pressure within the control volume for wider epsilon groove configuration.

Part B

VARIABLE DISPLACEMENT VANE PUMPS

NOMENCLATURE PART B

Latin Symbols

$A_v(\theta)$ Cross-section area at angular position θ.

A_{11} Amplitude value of the first term of the pressure ripple trend

A_{22} Amplitude value of the second term of the pressure ripple trend

A_{33} Amplitude value of the third term of the pressure ripple trend

b Vane thickness.

c_{dep} Coefficient of the cubic depressurization law, for evaluation of vane space pressure trend.

E' Young's Modulus parameter for EHD model.

E_A Young's Modulus of the vane pump material.

E_B Young's Modulus of the stator ring material.

F_{Inlet} Normal contact force between the vane tip and stator ring for the inlet section.

$F_{Inl-Out}$ Normal contact force between the vane tip and stator ring for the I-O section.

F_N Normal contact force.

F_{Outlet} Normal contact force between the vane tip and stator ring for the outlet section.

$F_{Out-Inl}$ Normal contact force between the vane tip and stator ring for the O-I section.

F_{V-B} Pressure force acting on the vane bottom.

F_{V-B} Vane centrifugal force.

F_{V-T} Pressure force acting on the vane tip.

f_{i1} Beginning angle of pressurization phase of vane space

f_{i2} Ending angle of pressurization phase of vane space

f_{ib} Angle within range f_{i1} and f_{i2}

H Material hardness.

G Non dimensional material parameter for EHD model

h_0 Minimum lubricant thickness.

l Contact length

K Generalized wear coefficient.

m_v Mass of the vane pump.

k_{i_peaks} Coefficient of the of the damped harmonic function of the vane space pressure trend (peaks)

$k_{i\_valleys}$ Coefficient of the of the damped harmonic function of the vane space pressure trend (valleys)

$p(\varphi)_{dep\_f}$ Cubic trend of the depressurization phase of the vane space

$p(\varphi)_{peaks\_period}$ Pressure trend (peaks) of the damped harmonic function of the vane space pressure trend.

$p(\varphi)_{ripple}$ Pressure ripple trend of the vane space pressure trend.

$p(\varphi)_{valleys\_period}$ Pressure trend (valleys) of the damped harmonic function of the vane space pressure trend.

$pf_{3\min}$ Last pressure value of the first interval of the depressurization phase of the rotor hole pressure trend

$pf_{5\max}$ Last pressure peak of the depressurization phase of the depressurization phase of the rotor hole pressure trend

p_{ripple_end} Last pressure value of the pressure ripple interval

$p(fif_{g1})$ Pressure trend during the first interval of the depressurization law, for rotor hole pressure trend.

$p(fif_{g2})$ Pressure trend during the second interval of the depressurization law, for rotor hole pressure trend.

$p_H(\varphi)$ Pressure within the rotor hole during a complete pump revolution.

$p_{V-S}(\varphi)$ Pressure within the vane space during a complete pump revolution.

p_b Pressure trend during pressurization phase of vane space

p_{es} Working pressure level

p_{max} Pressure overshoot, value for vane space pressure trend

$p_{max\%}$ Percentage of overshoot pressure

$p_{max\%\_250bar}$ Percentage of overshoot pressure for 250bar working pressure level

$p_{max\%\_210bar}$ Percentage of overshoot pressure for 210bar working pressure level

p_{min} Pressure undershoot, value for vane space pressure trend.

$R^{'}$ Reduced radius of curvature of EHD model.

R_A Curvature radius of the vane tip.

R_B Curvature radius of the stator ring.

R_{a1} Roughness of the first contact surface foe EHD model.

R_{a2} Roughness of the second contact surface foe EHD model.

R_m Mean distance between the center mass of the vane and shaft rotational axis.

s Sliding distance.

s_{Inlet} Vane sliding distance on the Inlet section of the stator ring.

$s_{Inl-Out}$ Vane sliding distance on the I-O section of the stator ring.

s_{Outlet} Vane sliding distance on the Outlet section of the stator ring.

$s_{Out-Inl}$ Vane sliding distance on the O-I section of the stator ring.

s_{total} Total sliding distance

t time

t_{test} Total testing duration time.

t_{tip} Thickness of the vane tip.

u Velocity parameter of EHD model.

U Non dimensional speed parameter of EHD model

V Wear volume

V_{vane_pump} Displacement of vane pump

$v_{sliding}$ Sliding average velocity

W	Non dimensional load parameter.
w	Vane width.
z_{vane}	Number of vane

Greek Symbols

α	Pressure viscosity coefficient.
α_{11}	Phase value of the first term of the pressure ripple trend
α_{22}	Phase value of the second term of the pressure ripple trend
α_{33}	Phase value of the third term of the pressure ripple trend
δ	Pressure tolerance for evaluation of PGP index
μ_0	Viscosity at atmospherich pressure and operational temperature
υ_A	Poisson's ratio of vane pump material.
υ_B	Poisson's ratio of vane stator rig material.
φ	Rotational angle
ω	Angular velocity of the pump rotor

Subscripts

i	Denotes isolated vane space

CHAPTER B.1
DESCRIPTION OF THE VANE PUMP UNDER STUDY AND EXPERIMENTS

B.1.1. Design and Operation of the Variable Displacement Vane Pump

A further study concerning positive displacement pumps will be illustrated in this Part B. In this case, the studied pump is a variable displacement vane pump. This kind of pumps are generally used for applications which require medium-high oil pressure level (up to 250bar) such as: shaping and machining tools, earthmoving machines and good lifts. Positive displacement vane pumps belong to the rotary pump category; they are composed of two main components: the first one is the rotor, in which the vanes are mounted in slots ending in holes and they are kept free to slide in radial direction; the second component is a stator which acts as a sliding track for the pump vanes (Figure 154). These pumps are based on a simple principle: basically, an oil volume is carried from the inlet environment to a higher pressure environment (outlet); this volume is defined by the shaft radius, two adjacent vanes, the inner radius of the stator ring and the vane width. The variable displacement pumps have many advantages in terms of energy saving and control strategy; in fact, the pressure and the outlet flow rate are tuned on the system requirements. These pumps are typically mounted in closed loop hydraulic systems; when the target pressure is reached, the pump can vary the displacement, adjusting the outlet flow in order to keep the outlet pressure steady, avoiding energy dissipation.
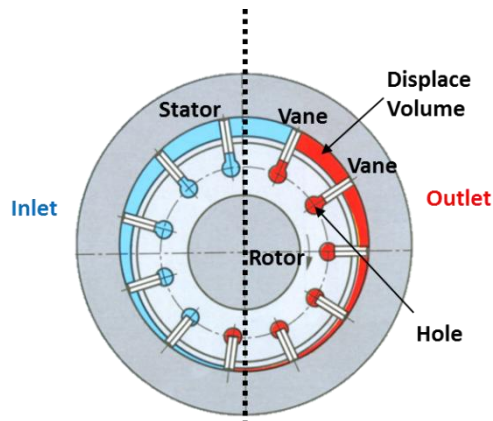
Figure 154. Scheme of a typical positive displacement vane pump.

The possibility of different working displacement conditions (full flow, zero flow) is allowed by the pump architecture which admits two different relative positions between the rotor and the stator rig (Figure 155). In the first case the pump supplies the maximum flow rate allowable; on contrary, in the second instance, the flow rate is almost zero, just keeping the outlet pressure level.
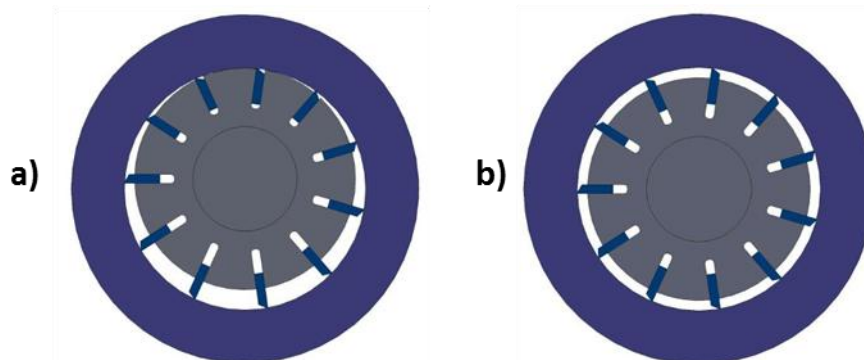
Figure 155. Pump working conditions. a) Full flow, b) Zero flow.

Let us focus the attention on the auto compensation system which regulate the outlet flow; Figure 155 displays a typical variable positive displacement pump where there are a control piston and two tuning screws. Looking at Figure 156 is possible to see the red area where the outlet pressure acts on the inner surface of the stator rig; the outlet

pressure distribution generates a force called F_o, which can be divided in two components: the first along the vertical direction, F_v, and the second one along the horizontal direction, F_h. Since the horizontal component is lower than the reaction force of the spring, F_s, the stator rig is forced to keep the nominal position. When the system reaches the outlet pressure and the users do not require hydraulic power, in the very first moments the pump is still displacing flow to the outlet pipe, thus the pressure tends to increase. As a consequence, forces F_v and F_h also increase and F_h becames higher than F_s; thus the stator ring is pushed coaxially to the rotor, decreasing the outlet flow. The pressure level which determines the zero flow condition is selected by the spring preload applied by the tuning screw n.3. This principle of pressure control is called also "direct pressure control".
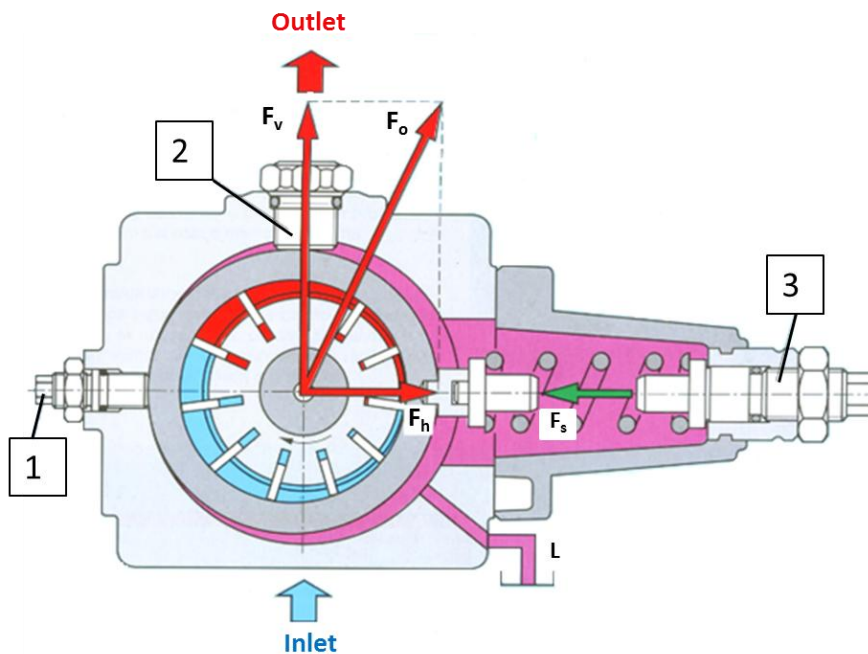
Figure 156. Variable displacement vane pump. (1,3) Tuning screws, (2) control piston.

The flow in variable displacement pumps can be regulated with a further control strategy, by mounting a pressure control valve on the outlet duct (Figure 157). Basically, the pressure stator ring is pushed by two pistons positioned in opposite direction. The first piston is directly linked to the outlet pipe environment, the second piston is

connected with the regulation valve and there is a spring which pushes the piston against the pressure ring in case of low pressure level. Normally, in full flow condition, the same pressure pushes on the both pistons, but due to the bigger section of piston B the stator rig is led to the maximum eccentricity position. When the requested pressure is reached, the piston of the regulation valve is pushed, compressing the spring within the valve, thus piston B is not pushed anymore by the outlet pressure but from a lower pressure level. The horizontal force balance in this situation allows the coaxial positioning of the stator ring respect to the shaft rotor, reducing the outlet flow. This condition is shown in Figure 158.
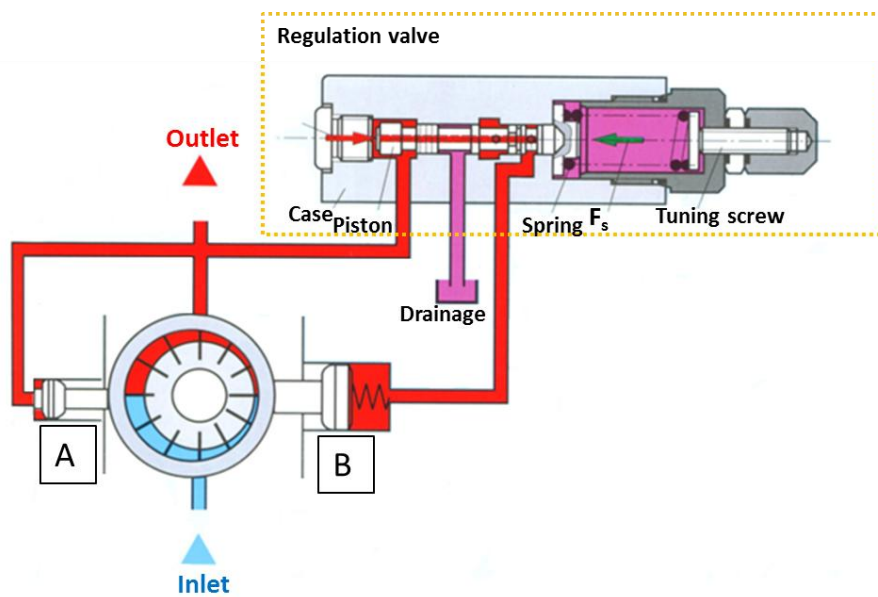
Figure 157. Variable displacement pump with pressure regulation valve.
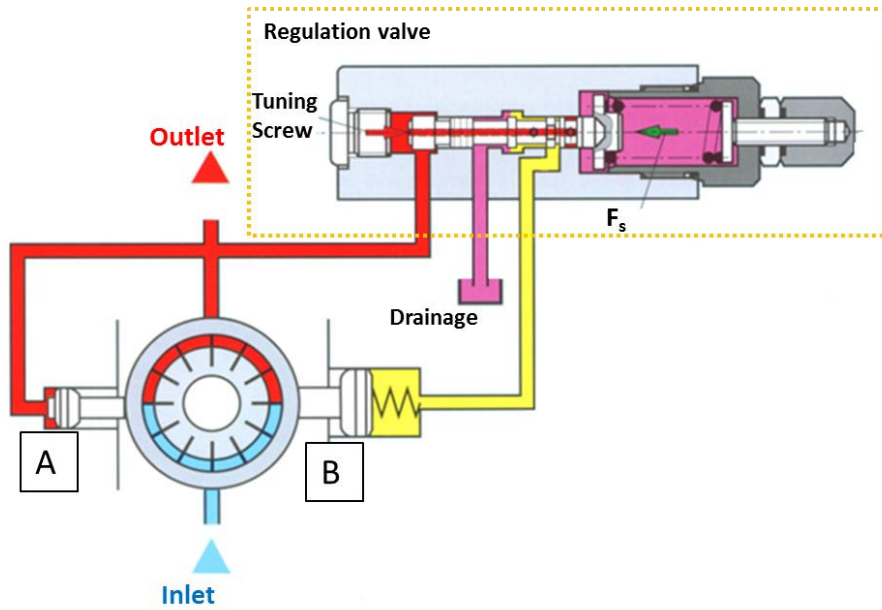
Figure 158. Variable displacement pump - zero flow working condition.

The characteristic curve of variable displacement vane pumps, depicted in Figure 159, shows that the maximum eccentricity, corresponding to full flow condition, is maintained till the cutoff pressure is reached. The small slope of the first part of the curve is due to hydraulic losses. Once the cutoff pressure is reached, the eccentricity and the flow rate decrease; the slope of the second part of the curve is determined by the spring stiffness. This procedure can be reversed when the working pressure decreases under the cutoff value. Eq(17) makes it possible to compute the displacement of the vane pump; z_{vane} is the number of vanes, w_{rotor} is the rotor width and A_v represents the frontal surface of the trapped vane space at the angular position θ. The volume of the trapped vane space (Figure 160) depends on design parameters, such as external rotor diameter, rotor width in axial direction, inner pressure ring diameter, as well as on the eccentricity between rotor and pressure ring.

$$V_{vane\_pump} = A_v(\vartheta)\, z_{vane}\, w_{rotor} \qquad (17)$$
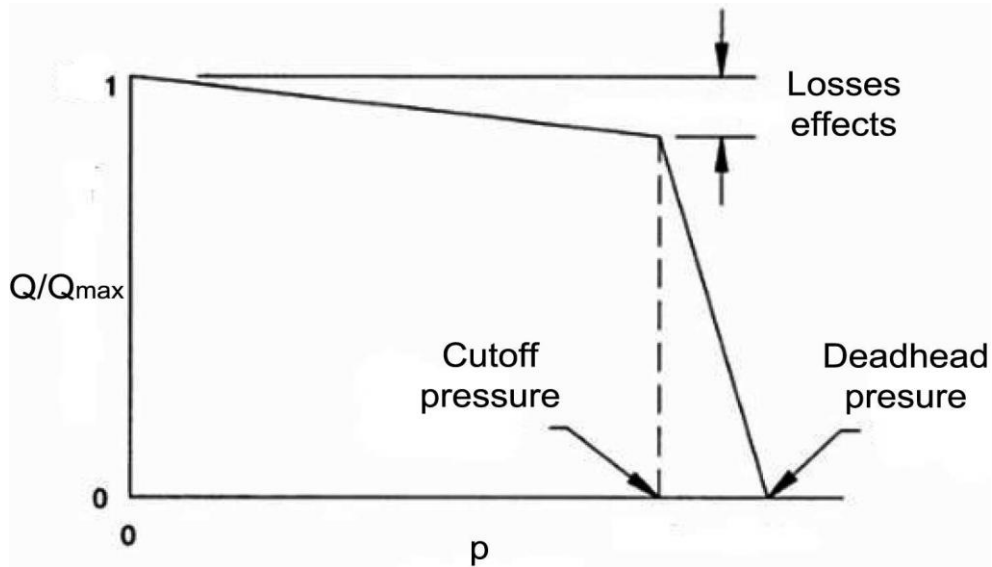
Figure 159. Variable displacement vane pump characteristic curve.
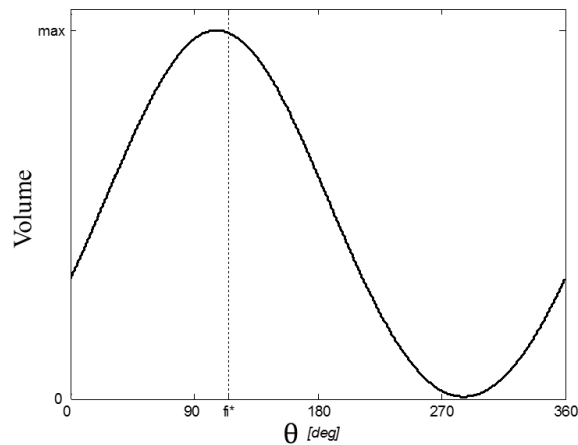
Figure 160. Typical trend of the trapped vane space volume.

Figure 161 shows the pump under study, manufactured by BERARMA s.r.l (Casalecchio di Reno(BO)). Basically, the pump is composed of a body, a cover plate (in which the inlet and outlet ducts are obtained), two port plates - the first one positioned on the body side and the second one on the cover side (in order to optimize the balancing of the axial forces) - the pump rotor and the radial sealing component, called stator ring.
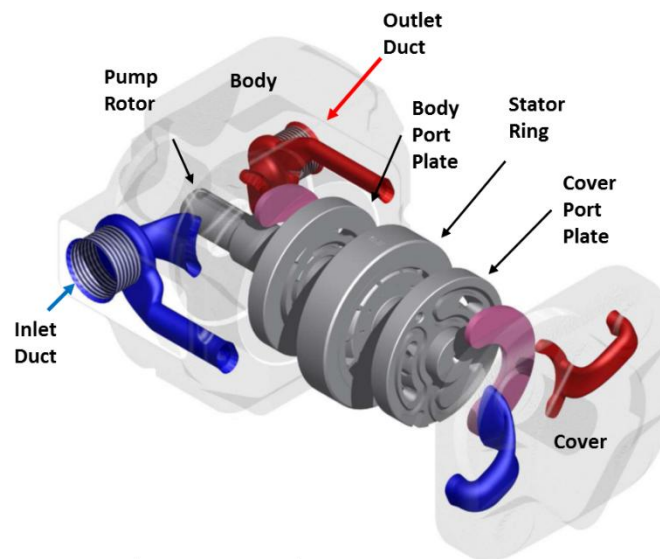
Figure 161. Design of the pump manufactured by BERARMA s.r.l.

B.1.2.   Test Bench and Experimental Set-Up

This paragraph contains the description of the test bench which has been used for the development and validation of the empirical model. The scheme of the test rig is reported in Figure 162. The electric motor is linked to the variable displacement pump by means of a transmission line, composed of a clutch (for emergency decoupling), a torque transmitter and an elastic joint, in order to allow misalignment between the transmission line and the pump shaft. The pump is linked to two reservoirs. The first one is the inlet reservoir characterized by the atmospheric pressure; the pipe line which connects the inlet environment to the pump inlet port contains an oil filter which avoids the aspiration of debris due to wear. The second reservoir is linked to the pump outlet port; this outlet pipe line contains a tuning valve which sets the outlet flow. Finally, the inverter allows the setting of pump rotational speed. The test rig has several sensors: two piezoelectric sensors (Kistler, model 6207) are mounted for the evaluation of the pressure level within one vane space and one rotor hole. For this purpose, a specific rotor shaft (Figure 163) has been designed; this rotor

has two ducts which intercept a vane space and a rotor hole; these ducts make it possible to measure the pressure signals by means of two separate pressure chambers, obtained by O-ring gaskets (Figure 164). The tracking of the shaft rotation has been performed via proximity sensor Balluff BES 516324S4C; the electric motor torque has been measured with torque sensor Staiger Mohilo 0160, mounted on the transmission line (Figure 165).
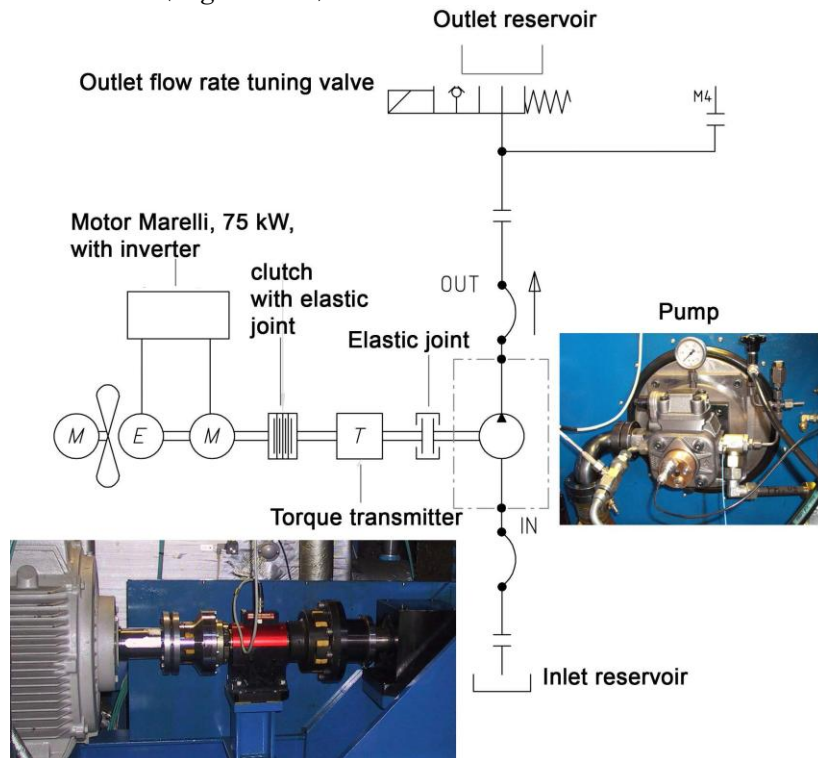
Figure 162. Scheme of the test rig.
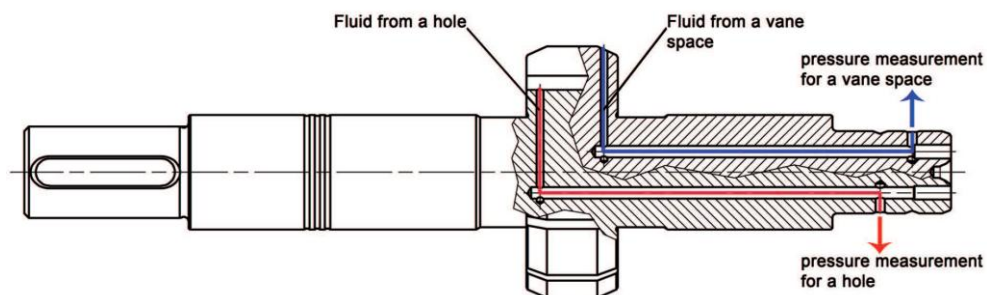
Figure 163. Special shaft pump for evaluation of vane space and hole pressure.
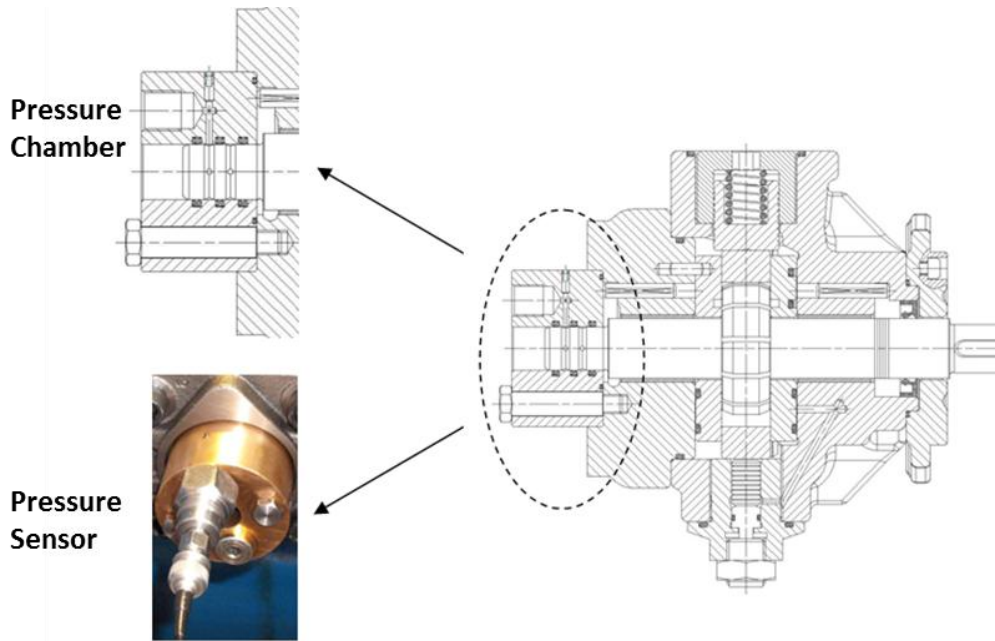
Figure 164. Specific cover plate for the pressure measurement in the vane space and the hole.
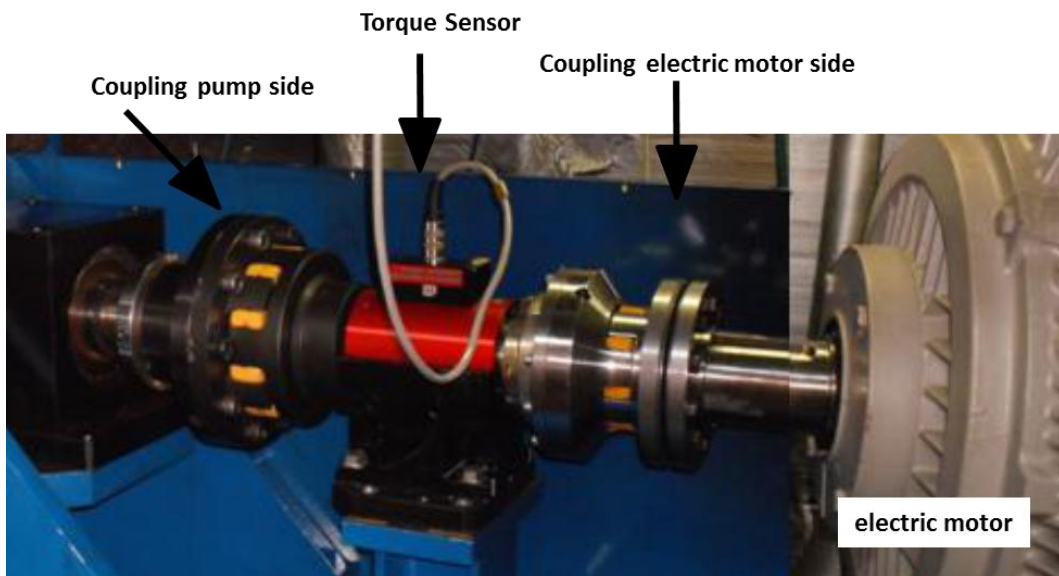
Figure 165. Positioning of the torque sensor

Figure 166 displays the experimental results concerning the pressure trends in the vane space and in the hole.
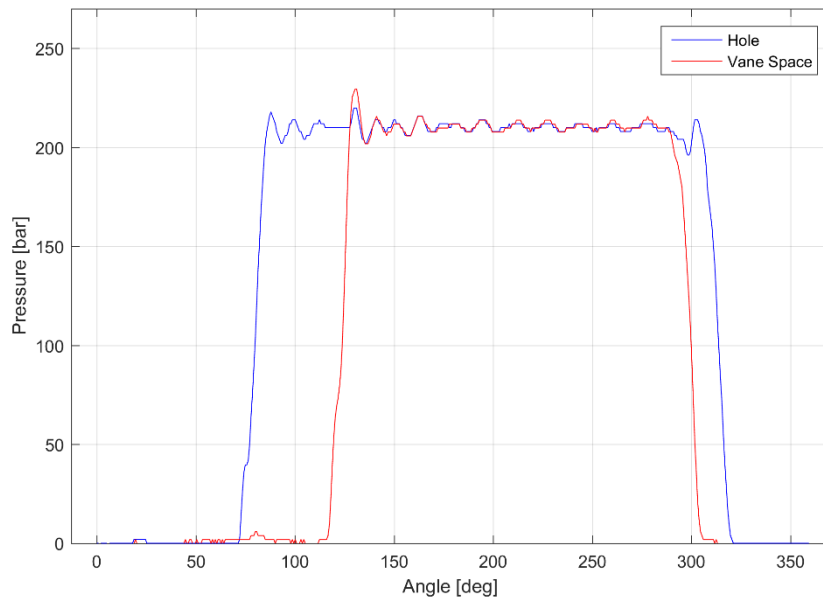
Figure 166. Typical pressure trend inside the hole and the vane space.

The pressure trends of Figure 166 can be divided in four sections; the first section is characterized by the inlet pressure in which the vane space and the hole are linked with the inlet environment via the circumferential ducts - called "distribution ducts" - obtained on the port plates (Figure 167) located on the inlet side. The external distribution duct feeds the vane spaces, on the other hand the internal one feeds the rotor shaft holes. During this phase the vane space volume is increasing, so drawing oil from the inlet manifold; when the vane space and the hole start to communicate with the outlet environment the pressurization process begins, thus the pressure increases. When the outlet pressure level is reached, while the vane space and the hole are still communicating with the outlet distribution ducts, the pressure assumes the typical ripple trend; this is the third section. Finally, the last section is the depressurization process: a quickly pressure drop occurs till the achievement of the inlet pressure level; in this phase the vane space volume is decreasing and the vane space is pumping the oil to the outlet duct. In this pumps, the outlet distribution duct of the

rotor shaft holes is generally more extended than the outlet distribution duct of the vane spaces, because this reduces the oil leakage by increasing the sealing of the vane spaces during the pressurization and depressurization phases. Typically, the distributor ducts have extensions called "carvings" at the far ends; these carvings make it possible to decrease the pressure overshoot during the transition from the inlet to outlet environment and the transition outlet-inlet as well. Furthermore, the feeding of the rotor shaft holes by means of the distribution duct avoids the introducing of spring elements in order to guarantee the contact between the vanes and the stator ring.
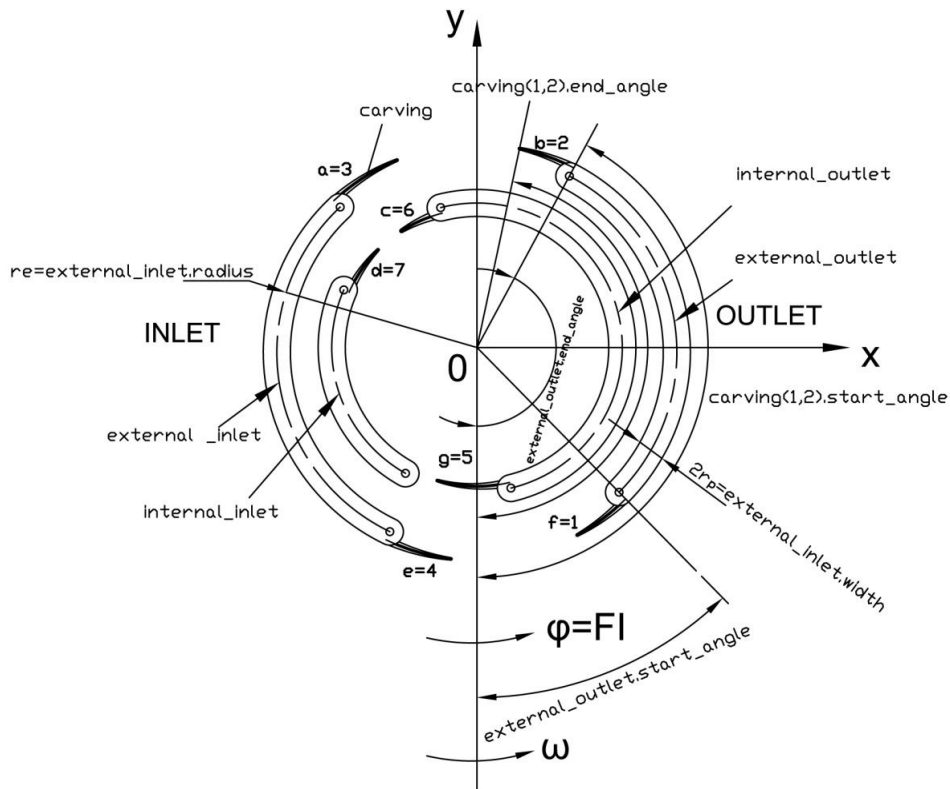
Figure 167. Distribution ducts of the port plates.

CHAPTER B.2
EMPIRICAL MODEL

B.2.1.   Introduction

In order to evaluate the pressure evolution within the vane spaces and holes in operational conditions, an empirical model can be develop with the approach described in this chapter. Then, the pressure trends make it possible to compute the pressure force between the vane tip and stator ring; this parameter is essential for the evaluation of the lubrication regime between these two components. Furthermore, the pressure ripple gives several information for the pump designers: in fact these data are used for the evaluation of strengths in the shaft and the stator ring. The pressure ripple can also give some inputs about the pump dynamic behavior and the vibrations levels.

In this chapter the attention will be focus on the description of the empirical model for the evaluation of the pressure evolution within the vane spaces and the holes. Paragraph B.2.2 contains the model input parameters. Paragraph B.2.3 describes the parametrization of the pressure evolution, explaining how the experimental data have been used in order to build up the empirical model. Paragraph B.2.4 is focused on the model implementation using the Matlab code. Finally, the last paragraph B.2.5 shows the validation process of the empirical model. This model is based on experimental data, obtained by an experimental campaign evaluating the effects of several parameters on the pressure trends. These parameters are: pump nominal size (pump displacement), distributor design, number of vanes, working pressure and shaft speed. The variation of the shaft eccentricity has not been considered, because the full flow condition is the heaviest and the most interesting working condition. Figure 168 shows the reference system which has been used in order to display the experimental and numerical results for both pressure trends, within the vane spaces as well as the holes. The zero value of angular coordinate φ is located on the opposite side of the control piston; considering the reference vane

space *i*, the alignment of the vane with the origin of angular coordinate determines the zero position of the reference vane space.
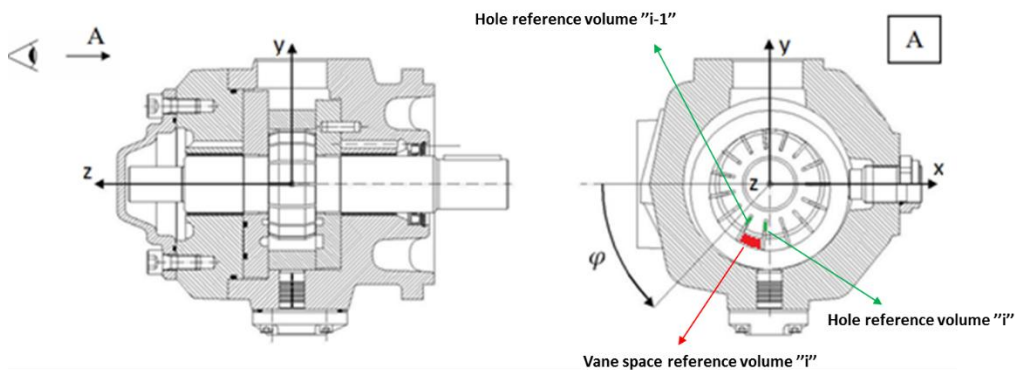
Figure 168. Reference system of the empirical model.

On the other hand, the coordinate reference system for the evaluation of the stator ring eccentricity is defined in Figure 167.

As already said, the model has been developed in Matlab environment, taking into account these characteristic pump parameters:

- Pump displacement, which affects the pressure overshoot and undershoot.
- Design of the distributor ducts, which affects the advance and the delay of the pressurization and depressurization phases.
- Number of vanes, which influences the frequency content of the pressure ripple.
- Working pressure level, which is responsible of the outlet pressure mean level and of the overshoot and undershoot in the pressure trend.

The model is based on the matching of the experimental results, thus no physical formulations have been implemented but only the correlation laws between the pump parameters and the pressure trend. In particular, looking at the experimental results, there are some parameters - such as pressurization angles (beginning and ending), stabilization pressure angle, pressure overshoot angle, depressurization angle (beginning and ending), overshoot pressure level - which are well correlated to the working pressure level. In the following lines a

preliminary and general introduction to the effects of the pressure working level over the pressure distribution will be presented. Moreover in order to emphasize the concepts, several qualitative graphs which are not refer to a numerical simulation or experimental results will be used. Firstly the focus has been pointed on the linear correlation between the working pressure and the pressurization trend, Figure 169 shows how high pressure anticipates the beginning of the pressurization process and delays the reaching of the outlet pressure.
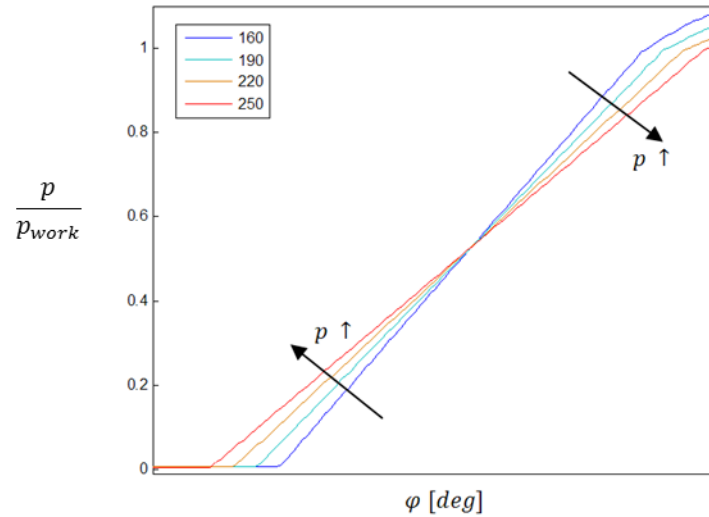
Figure 169. Pressurization laws for different working pressure levels (160-250bar).

Also the depressurization phase is affected by the working pressure level, in fact higher pressure extends the angular interval of this phase, how Figure 170 depicts.
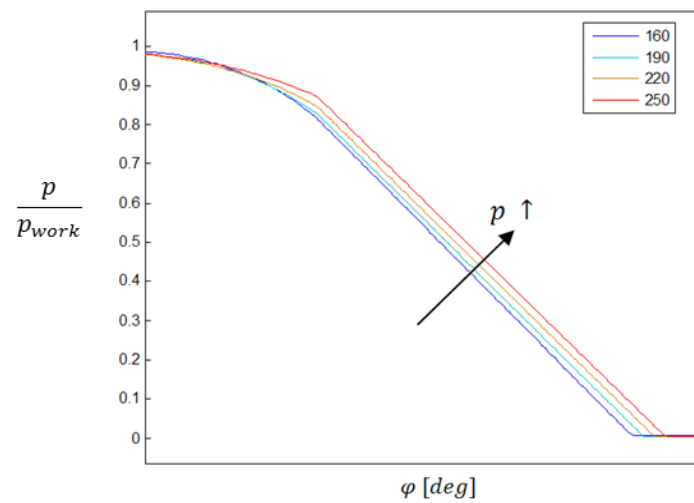
Figure 170. Depressurization laws for different working pressure levels (160-250bar).

Finally, there are two further parameters which can be considered linearly dependent on the working pressure level: the overshoot pressure - which decreases for high working pressure level - and the pressure overshoot angle - which grows proportionally to the working pressure level. These observations are displayed in Figure 171.
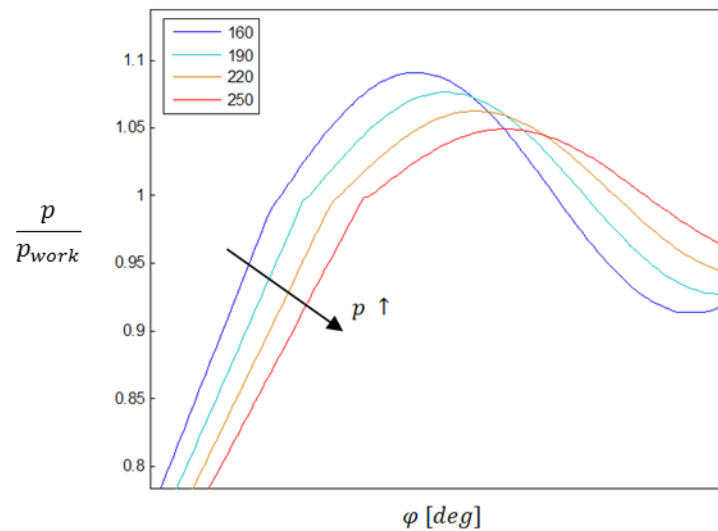
Figure 171. Pressure overshoot for different working pressure levels (160-250bar).

B.2.2.   Model Inputs

This paragraph presents the input data required by the empirical model in order to obtain the pressure trend within the vane spaces and the holes. The first parameters to set are the pump displacement, the working pressure level and the number of vanes. In second instance, the model needs the distributor geometry, that is to say all the geometrical parameters of the distributor ducts, such as extension, width, depths, positions, as well as the port plate diameter. Table 17 contains an example of the typical angles of the distributor ducts.

Nomenclature	φ [deg]
Vane spaces	
fi_external_outlet_start	134.3
fi_external_outlet_end	241.8
fi_external_outlet.carving_start	118.0
fi_external_outlet.carving_end	258.0
fi_external_inlet_start	314.1
fi_external_inlet_end	67.8
fi_external_inlet.carving_start	293.0
fi_external_inlet.carving_end	83.0
Nomenclature	**φ [deg]**
Holes	
fi_internal_outlet_start	103.5
fi_internal_outlet_end	284.5
fi_internal_outlet.carving_start	73.5
fi_internal_outlet.carving_end	302.8
fi_internal_inlet_start	336.5
fi_internal_inlet_end	60.5
fi_internal_inlet.carving_start	315.2

Table 17. Input data for the characterization of the distributor ducts (Pump 32cc).

Furthermore, rotor and stator characteristics must be taken into account; these parameters are: rotor external diameter, rotor internal diameter (where the holes are placed), rotor width, stator internal diameter and rotor eccentricity. Moreover, the vane geometrical parameters are required. Finally, the rotational speed is the last parameter to set up in order to launch the simulation.

B.2.3.   Parametrization of the Pressure Trend

The empirical model is based on the subdivision of the pressure trend in several sections. This approach makes it possible to implement the correlation laws in order to match the numerical results with the experimental ones. The model evaluates the pressure trend in the vane spaces and in the rotor holes.

Concerning the pressure trend in the vane spaces, it can be basically subdivided in four intervals (Figure 172). The first interval (1st) is characterized by a steady pressure level where the mean value is the relative inlet pressure level, 0 bar; the extension of this interval is about 165 degrees.

The extension of the second interval is smaller than the previous one; it represents the pressurization phase, where the vane is moving from the inlet environment to the outlet environment. This interval can be subdivided in three further sections (Figure 173). Section a) can be approximated as a linear function, the second section, b), which contains the pressure overshoot can be matched by using a sinusoidal function, as well as the last section, c), which represents the stabilization of the pressure level.

After the pressurization phase, the pressure trend assumes the typical ripple trend (3rd interval) which is characterized by the number of pump vanes; this pressure ripple is defined by using the Fourier series approach. Basically, the frequency content of the pressure signal has been study for several operating conditions and a correlation law has been developed. The correlation law is able to find out the amplitude and phase of the main terms which characterize the pressure ripple.

The last interval is the depressurization phase, where the vane space is gradually closed to the outlet environment and begins the approaching to the inlet environment. This interval can be divided in two sections (Figure 174); the trend of the first section is sketched by using a cubic function, d), on other hand, the second section has been drawn by a linear law, e).
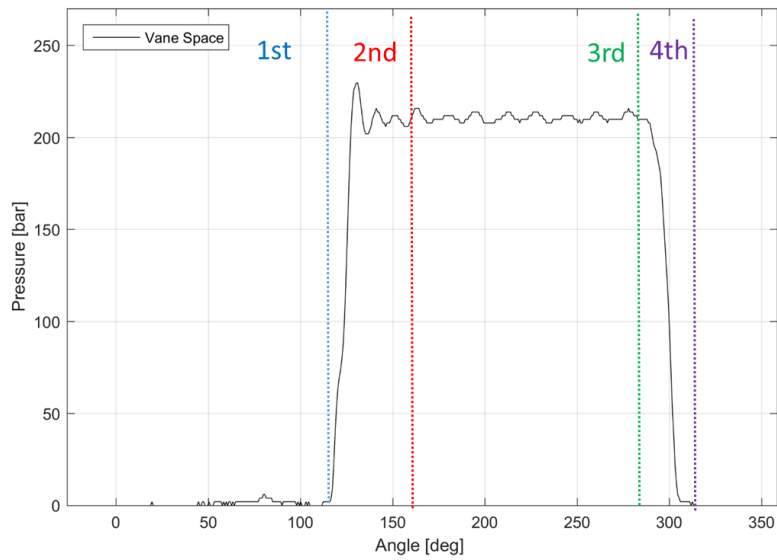
Figure 172. Subdivision of the vane space reference pressure trend.
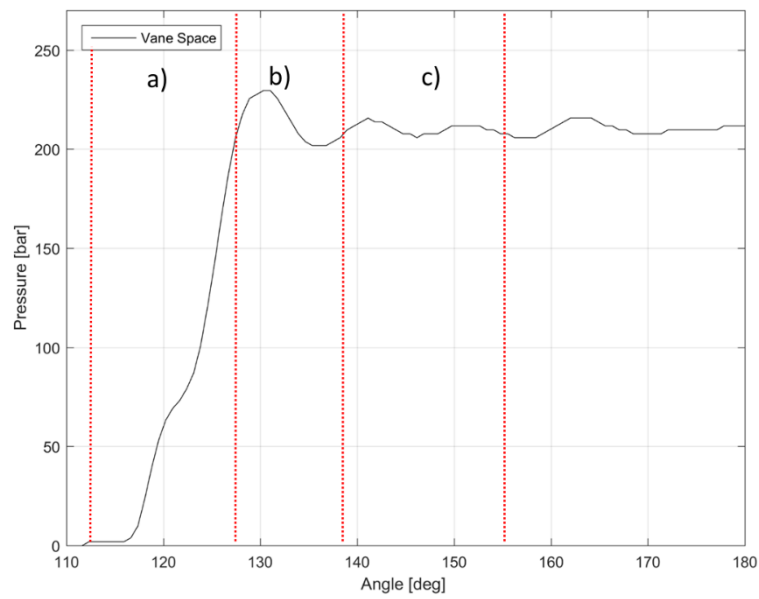
Figure 173. Subdivisions of the pressurization interval.
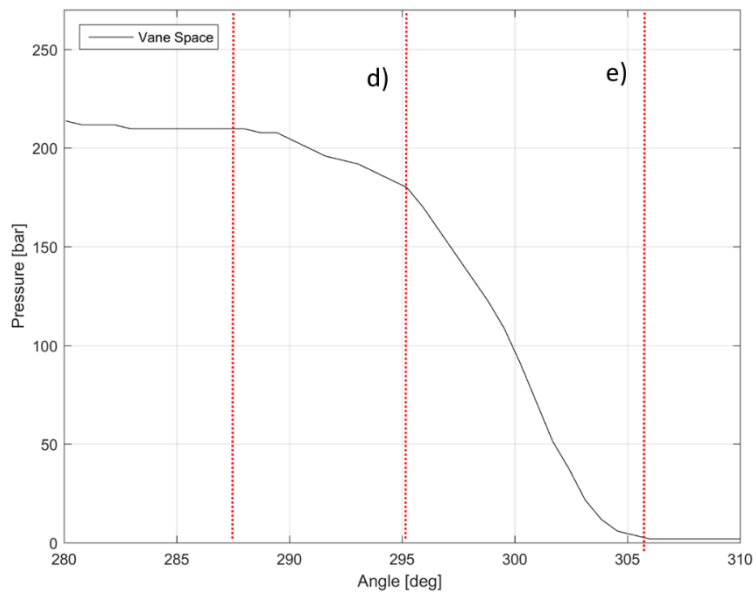
Figure 174. Subdivision of depressurization interval.

The approach used for the vane spaces has been applied for the pressure trend within the rotor holes. Even for the rotor holes the pressure trend has been divided in four main intervals (Figure 175).

The first interval is the easiest to reproduce and the least interesting from the dynamic point of view: basically, in this situation the rotor hole is communicating with the inlet duct.

The second interval - in which there is the pressurization of the hole volume - is characterized by several different trends. Since in this case the angular extension is wider than in the case of vane spaces, a finer subdivision is needed. Figure 176 shows how the interval has been split. There are five sections: the first one, a), is characterized by a linear trend; the second one, b), contains the pressure overshoot and is replicated by a sinusoidal law; the third section, c), is a harmonic function which contains two pressure peaks after the overshoot peak; the fourth section, d), in which the pressure level is steady; the last section, e), defined by pressurization sections b) and c) of the vane space trend.

The third interval is the ripple trend, that perfectively matches the pressure ripple measured in the vane space.

Finally, in the depressurization phase, the rotor hole stops to communicate with the outlet environment. The depressurization trend must be reproduced by two sections (Figure 177): the first one can be matched by using a cubic law; on other hand, the second section can be drawn by a linear law.
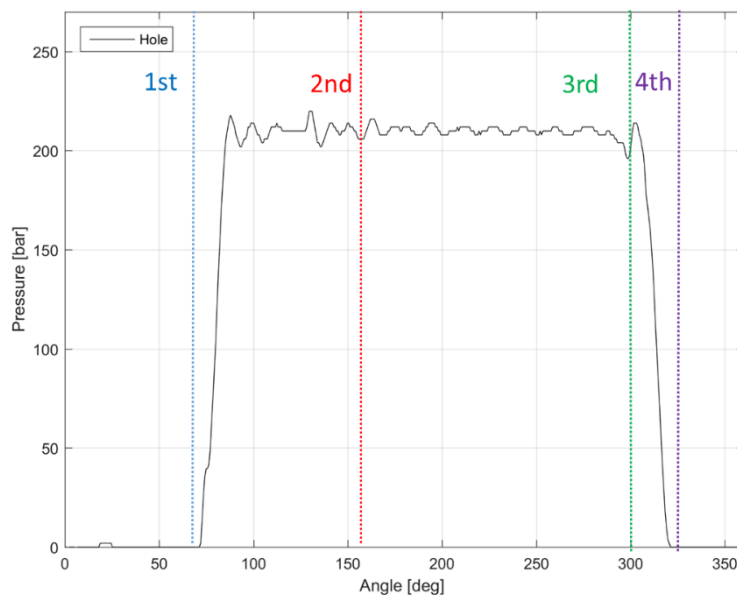
Figure 175. Subdivision of the hole reference pressure trend.
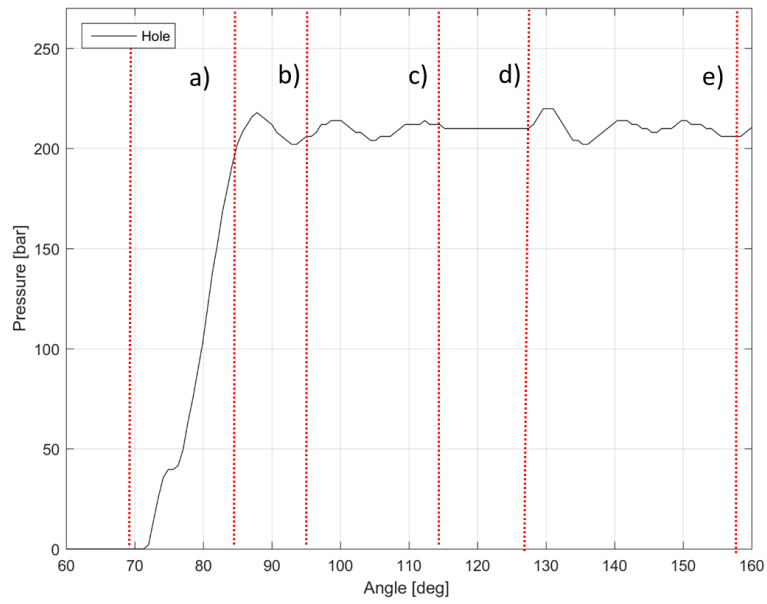
Figure 176. Subdivisions of the pressurization interval.
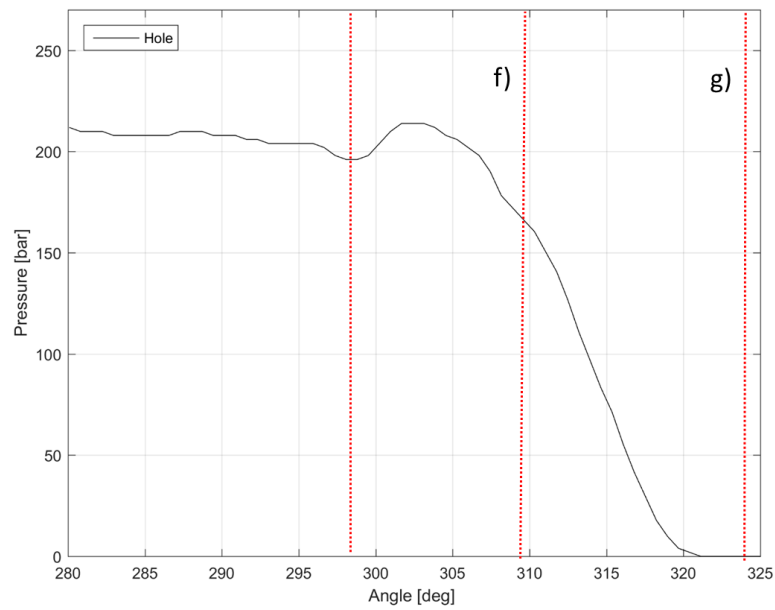
Figure 177. Subdivision of depressurization interval.

B.2.4.   Implementation of the Model

An experimental campaign carried out on three different pump models (namely, 01PHV05-16cc, 01PHV1-32cc, PSP3-100cc) made it possible to develop a synthesis tool, able to evaluate the pressure distribution within the vane spaces and rotor holes, for a family of positive displacement vane pumps manufactured by Berarma s.r.l. The comparison of the results concerning these pumps highlights that the pump displacement affects only the pressure overshoot during the pressurization phase, but it has not influence on the other intervals of the pressure distribution. The increasing of the pump displacement enhances the pressure overshoot on both the analyzed volumes, vane spaces and rotor holes. The model can be used for pumps which have the following features:

- Working pressure level: 160 to 250 bar.
- Displacement: 16 to 125 cc.
- Distributor geometry: type PHV or PSP.
- Pump speed: 1500 rpm.

Now we focus on Matlab code "ModelloCC.m" which determines the pressure distribution. The launch of the Matlab file "ModelloCC.m" initializes the set-up procedure for the definition of the pump features; the user must insert the following pump data:

- Pump displacement
- Working pressure level
- Number of vanes
- Rotor width
- Rotor external diameter
- Stator internal diameter
- Rotor eccentricity

The model firstly computes the pressure distribution within the vane space, beginning with the linear law of the pressurization phase by means of the following code lines:

```
%%(1)Definition of pressure run up
p_s=[100 160 210 250]; %pressure range [bar]
%Definition of the run up start angle
y1=[1.00339*fi_external_outlet.carving_start
0.99153*fi_external_outlet.carving_start
0.98644*fi_external_outlet.carving_start
0.97966*fi_external_outlet.carving_start];
%Evaluation of the regression linear law
[a1,b1,d1]=regression(p_s,y1); %a1 slope, b1 intercept term,
d correlation coefficient
fi1=a1*p_es +b1; %fi1 starting angle
```

Vector `p_s` contains four pressure levels from 100 to 250bar; vector `y1` contains the starting angles for each working pressure level of vector `p_s`. Vector `y1` takes into account the effect of the port plate geometry, because each term of the vector is defined by a coefficient and the angular value where the outlet carving begins. The previous vectors have been used for defining the slope (`a1`) and the intercept term (`b1`) of the regression line by using the least-squares method; thus, considering the working pressure level (`p_es`), the starting angle of the pressurization phase is defined (`fi1`). A similar approach has been applied for the evaluation of the ending angle of the linear interval. The Matlab script containing the definition of the regression linear law is the following:

```
%%(2)Definition of the pressure run up
%Definition of the pressure run up ending angle
y2=[0.92852*fi_external_outlet_start
0.94192*fi_external_outlet_start
0.95309*fi_external_outlet_start
0.95905*fi_external_outlet_start];
% Evaluation of the regression linear law
[a2,b2,d2]=regression(p_s,y2); %a2 slope, b2 intercept term,
d2 correlation coefficient
fi2=a2*p_es +b2; %fi2 ending angle
```

The evaluation of the beginning (`fi1`) and ending angle (`fi2`) of the pressurization phase makes it possible to draw the connection line. The following script reports the definition of the first interval as well as the linear trend of the second interval of the pressure trend of the vane space:

```
%%(3)Definition of the first and the second intervals of the
vane space pressure trend.
fi_a=linspace(0,fi1,1000);
p_a=ones(1,length(fi_a)); %p_a inlet steady state
fi_b=linspace(fi1,fi2,1000);
p_b= 1+((fi_b-fi1)./(fi2-fi1))*(p_es-1); %linear law.
```

Eq(18) represents the linear law which connects the beginning angle and the ending angle; Figure 178 shows the pressure trend at this point.

$$p_b = 1 + \frac{(f_{ib} - f_{i1})(p_{es} - 1)}{f_{i2} - f_{i1}} \qquad (18)$$
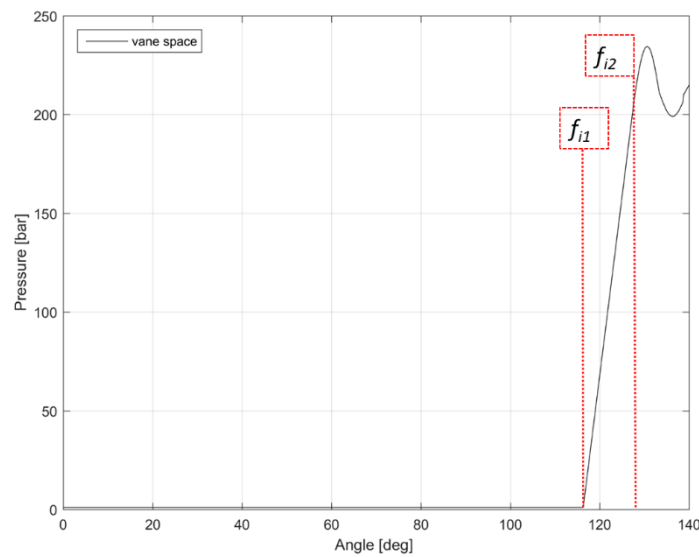
Figure 178. Definition of the vane space pressure trend (PHV32), 1st interval and 2nd a) interval.

The next step concerns the evaluation of the overshoot pressure and the angular positioning of this peak. The overshoot depends on the working pressure level and the pump displacement as well. The overshoot is defined by using two vectors (p_max_perc1, p_max_perc2) which contain the overshoot percentage over the working pressure level for the three displacements (Table 18).

16cc		32cc		100cc	
p[bar]	**%p$_{max}$**	**p[bar]**	**%p$_{max}$**	**p[bar]**	**%p$_{max}$**
210	8.8	210	10.3	210	25
250	6.2	250	9.1	250	20

Table 18. Percentage overshoot (experimental data).

These data allow the definition of the regression line over the pump displacement (`cc`) for each working pressure level, put together in vector `p_max_perc_cc_es`. The interpolation of the regression lines gives the percentage pressure overshoot over the working pressure level (Eq(19)), `p_max_perc`) and finally its absolute value (Eq(20), `p_max`):

$$P_{\max\%} = \frac{\left(P_{\max\%\_250bar} - P_{\max\%\_210bar}\right)\left(P_{es} - 210\right)}{250 - 210} + P_{\max\%\_210bar} \qquad (19)$$

$$p_{\max} = \left(\frac{P_{\max\%}}{100} + 1\right) P_{es} \qquad (20)$$

```
%%(4)Definition of the overshoot pressure level max
cc_s=[16 32 100]; %Displacements
p_max_perc1=[8.8 10.3 25]; % percentage overshoot @ 210bar
p_max_perc2=[6.2 9.1 20];% percentage overshoot a @ 250bar
%regression line for the working pressure levels 210bar and
250bar
[a3,b3,d3]=regression(cc_s,p_max_perc1);
[a4,b4,d4]=regression(cc_s,p_max_perc2);
%vectors of regression lines due to the working pressure
level 210 e 250 bar
p_max_perc_cc_es =[a3*cc+b3 a4*cc+b4];
% evaluation of the percentage overshoot
p_max_perc = ((p_max_perc_cc_es(2)-
p_max_perc_cc_es(1))*((p_es-210)/(250-
210)))+p_max_perc_cc_es(1);
%Evaluation of the overshoot pressure
p_max=(((p_max_perc)/100)+1)*p_es;
```

The procedure for the evaluation of the pressure overshoot has been also applied for the evaluation of the first pressure undershoot, as shown in the following code lines:

```
%(5)Definition of the first pressure undershoot
p_1min_perc1=[3.4 4 15]; %percentage undershoot 210 bar
p_1min_perc2=[3.7 4.6 10]; %percentage undershoot 250 bar
% regression line for the working pressure levels 210bar and
250bar
[a5,b5,d5]=regression(cc_s,p_1min_perc1);
[a6,b6,d6]=regression(cc_s,p_1min_perc2);
% vectors of regression lines due to the working pressure
level 210 e 250 bar
p_1min_perc_cc_es =[a5*cc+b5 a6*cc+b6];
% evaluation of the percentage undershoot
p_1min_perc = ((p_1min_perc_cc_es(2)-
p_1min_perc_cc_es(1))*((p_es-210)/(250-
210)))+p_1min_perc_cc_es(1);
% Evaluation of the undershoot pressure
p_1min=p_es*(1-p_1min_perc/100);
```

The experimental data for the evaluation of the regression line which determines the pressure undershoot are presented in Table 19.

16cc		32cc		100cc	
p[bar]	**%p$_{min}$**	**p[bar]**	**%p$_{min}$**	**p[bar]**	**%p$_{min}$**
210	3.4	210	4	210	15
250	3.7	250	4.6	250	10

Table 19. Percentage undershoot (experimental data).

After the first oscillation, a further oscillation interval is present before the pressure ripple. Looking at the experimental data (Figure 179), is it clear that, after the pressure overshoot and undershoot, the pressure trend can be drawn by a damped harmonic function. Basically, this interval can be divided in four periods; each period is characterized by a sinusoidal law. The third order characterizes the sinusoidal law of this transitional phase. Eq(21) defines respectively the periods which contain the second and the third peak of the pressure trend; on other hand Eq(22) draws the periods which contain the second and third valley of the damped harmonic function.

$$p(\varphi)_{peaks\_period} = k_{i\_peaks} \left(p_{\max} - p_{es} \right) \sin\left(3 z_{vanes} \omega t \right) \qquad (21)$$

$$p(\varphi)_{valleys\_period} = k_{i\_valleys} \left(p_{working\_level} - p_{\min} \right) \sin\left(3 z_{vanes} \omega t \right) \qquad (22)$$
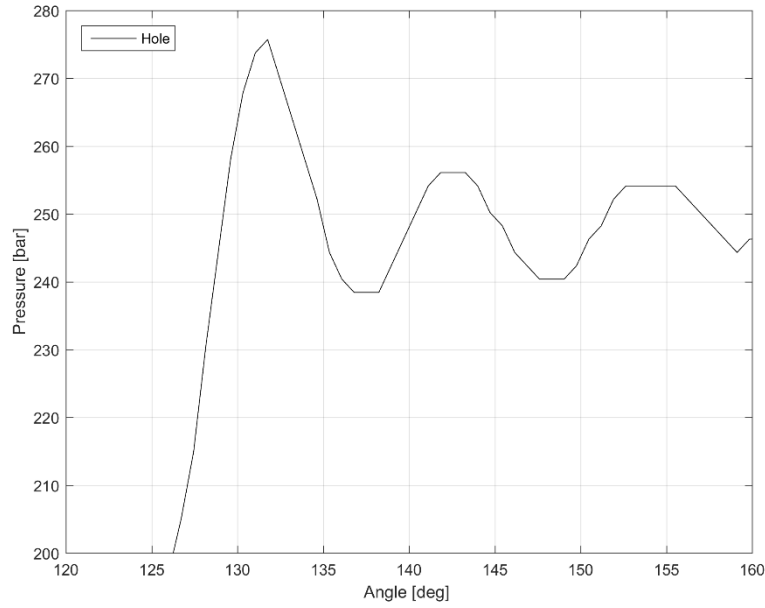
Figure 179. Experimental data, 250bar working pressure level, first peaks of the pressure trend.

Coefficients k_{i_peaks} and k_{i_valleys}, which allow the tuning of the amplitude over the pump displacement, are defined in Table 20. These coefficients are the ratio between the variance of the peak or valley with respect to the working pressure level and the variance of the overshoot or undershoot with respect to the working pressure level. Table 21 contains the values obtained by means of the experimental data. The values of the peaks and valley coefficients are compute by using a linear interpolation. The following Matlab lines implement the definition of the coefficients and the evaluation of the pressure trend.

$k_{2\text{nd}\_peak}$	$k_{2\text{nd\_valley}}$	k_{3rd_peak}	k_{3rd_valley}
$\dfrac{p_{2nd\_peak} - p_{working\_level}}{p_{\max} - p_{working\_level}}$	$\dfrac{p_{working\_level} - p_{2nd\_valley}}{p_{working\_level} - p_{\min}}$	$\dfrac{p_{3rd\_peak} - p_{working\_level}}{p_{\max} - p_{working\_level}}$	$\dfrac{p_{working\_level} - p_{3rd\_valley}}{p_{working\_level} - p_{\min}}$

Table 20. Coefficients of the peaks and valley of the pressure trend.

displacement	k_{2nd_peak}	k_{2nd_valley}	k_{3rd_peak}	k_{3rd_valley}
16cc	0.20	0.30	0.10	0.55
32cc	0.30	0.50	0.15	0.40
100cc	0.65	0.80	0.40	0.35

Table 21. Peaks and valleys coefficients of the experimental data.

```
%(6)Definition of the oscillation trend which contain the
second and third peaks.
%knmax=(pn-p_es)/(p_max-p_es)
%knmin=(p_es-pn)/(p_es-p1min)
% Second peak definition
p_2max_perc_s=[20 30 65]; %2nd peak ratios
% regression line for the 2nd peak
[a6,b6,d6]=regression(cc_s,p_2max_perc_s);
% percentage 2nd peak
p_2max_perc=a6*cc+b6;
% 2nd peak coefficient
k_2max=p_2max_perc/100;
 % Second valley definition
p_2min_perc_s=[30 50 80]; %2nd valley ratios
% regression line for the 2nd valley
[a7,b7,d7]=regression(cc_s,p_2min_perc_s); %2nd valley ratios
% percentage 2nd valley
p_2min_perc=a7*cc+b7;
% 2nd valley coefficient
k_2min=p_2min_perc/100;
 % Third peak definition
p_3max_perc_s=[10 15 40];
% regression line for the 3rd peak
[a8,b8,d8]=regression(cc_s,p_3max_perc_s); %3rd peak ratios
% percentage 3rd peak
p_3max_perc=a8*cc+b8;
% 3rd peak coefficient
k_3max=p_3max_perc/100;
 % Third valley definition
p_3min_perc_s=[55 40 35]; %3rd valley ratios
% regression line for the 3rd valley
[a9,b9,d9]=regression(cc_s,p_3min_perc_s);
% percentage 3rd valley
p_3min_perc=a9*cc+b9
% 3rd valley coefficient
k_3min=p_3min_perc/100;
```

Figure 180 contains the pressure trend drawn at this point.
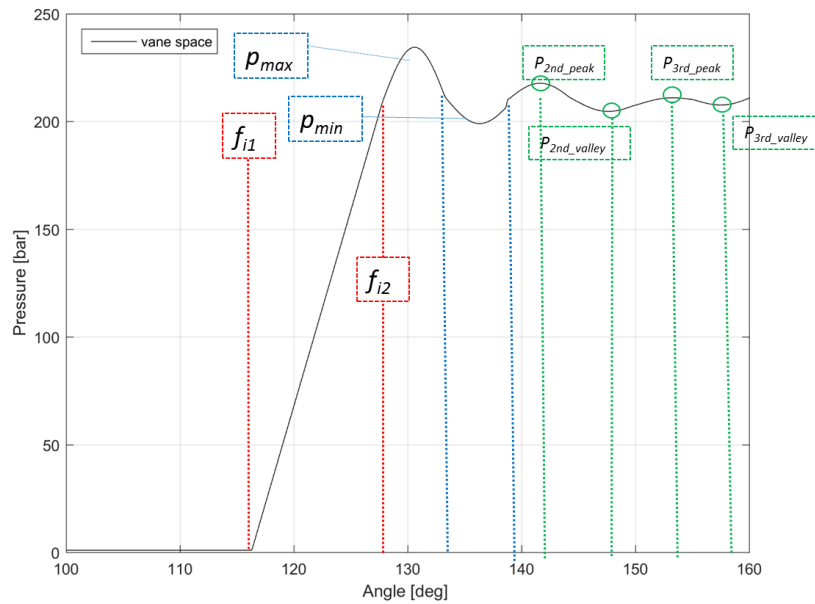
Figure 180. Model results for working pressure level 210bar PHV32(pressurization phase).

After the pressurization phase, the pressure ripple interval is defined. The evaluation of the pressure ripple is based on the frequency analysis of the pressure signals. For instance, Figure 181 and Figure 182 depict the single side spectrum of the pressure ripple signal of pump 01PHV32cc for three different working pressure levels. The spectrum highlights the principal harmonic components ($11^{th}, 22^{th}$ and 33th order). The experimental data lead to define the pressure ripple by taking into account the principal orders plus the static component. The amplitude terms of Eq(23) have been defined by averaging the experimental data.
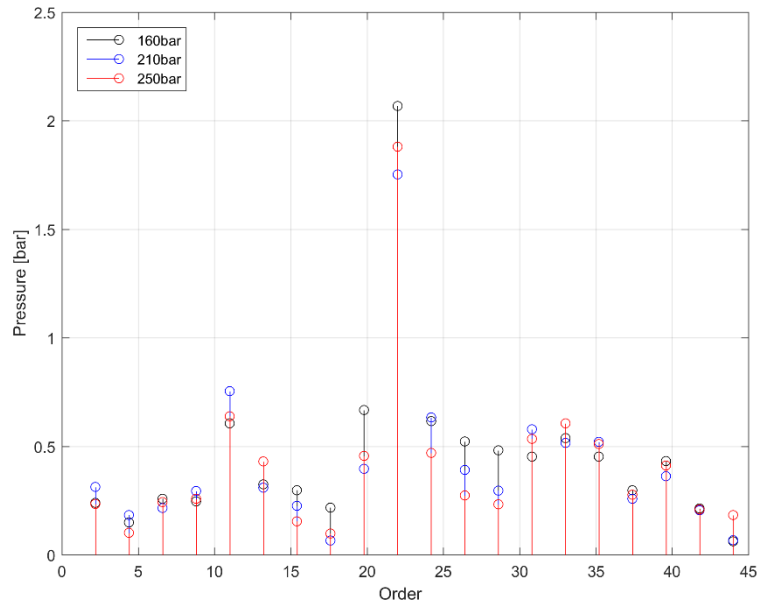
Figure 181. Spectrum (Amplitude) of the pressure ripple signal, for three different pressure level.
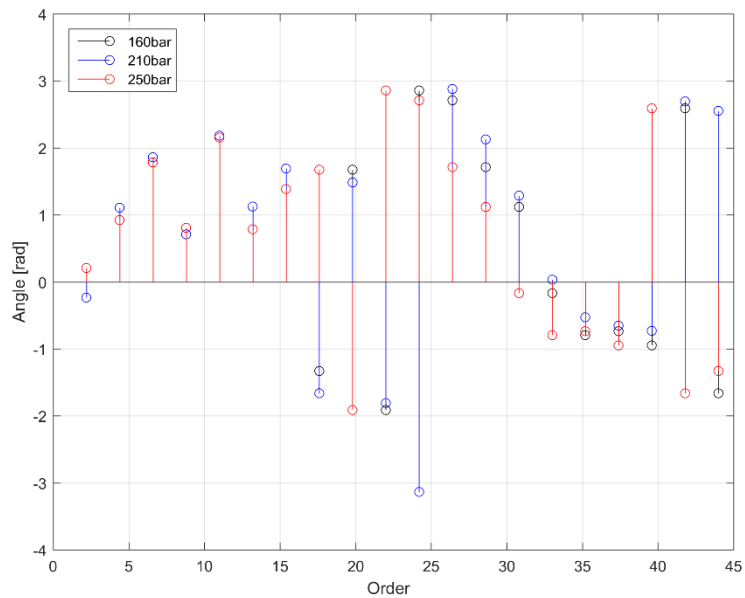
Figure 182. Spectrum (Phase) of the pressure ripple signal, for three different pressure level.

$$p(\varphi)_{ripple} = p_{es} + A_{11}\sin\left(3z_{vanes}\omega t + \alpha_{11}\right)...$$
$$...+ A_{22}\sin\left(3z_{vanes}\omega t + \alpha_{22}\right) \tag{23}$$
$$...+ A_{33}\sin\left(3z_{vanes}\omega t + \alpha_{33}\right)$$

The drawing implementation of the pressure ripple interval (using the Matlab code) has been reported in the following lines:

```
%(7)Pressure ripple interval
% definition of time vector
time2=linspace(0,(fi3-deg11(end))/(f_rot*360),1000);
deg2=f_rot*time2*360+deg11(end); % starting angle
% Pressure ripple equation
press2=p_es+A1v*cos(2*pi*f_rot*n_pal*time2+alfa1v)+A2v*cos(2*
pi*2*f_rot*n_pal*time2+alfa2v)+A3v*cos(2*pi*3*f_rot*n_pal*tim
e2+alfa3v);
```

The Figure 183 displays the pressure ripple trend obtained for pump PHV32cc and working pressure level 210bar.
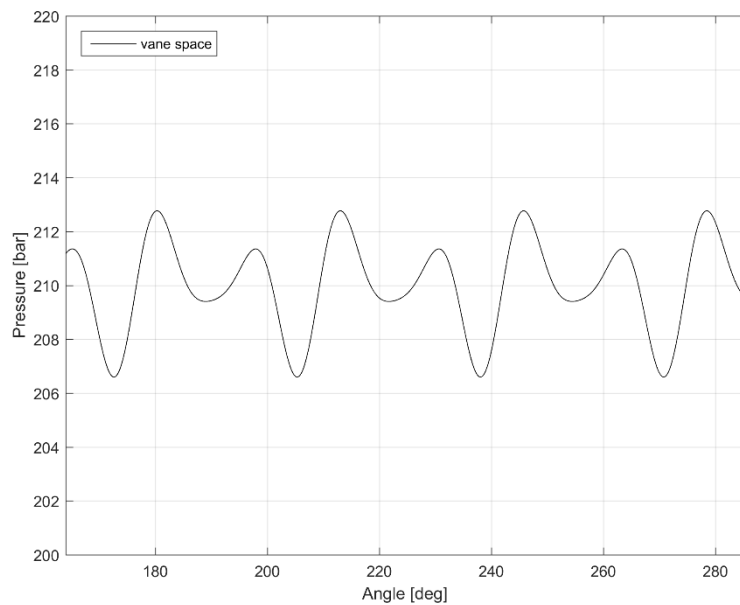
Figure 183. Pressure ripple draw by the empirical model for PHV32cc and working pressure level 210bar.

The depressurization interval is the last line to draw. This phase is characterized by two different trends: the first one is defined by using a cubic law; the second one is a linear law. Let us start to analyze the first part: the beginning of the depressurization phase is due to the inlet carving design and the last pressure value of the ripple trend; no further parameters affect the cubic law. Eq(24) represents the cubic law implemented into the empirical model, where p_{ripple_end} is the last value of the pressure ripple interval and coefficient c_{dep} is obtained by averaging the experimental data. The second part depends only on the distributor design and on the working pressure level; thus the regression line approach, already developed for the pressurization law, has been implemented. The following Matlab lines implement the depressurization phase. Moreover, Figure 184 and Figure 185 represent respectively the depressurization phase and the entire pressure trend within the vane space, obtained by using the empirical model.

$$p(\varphi)_{dep\_f} = p_{ripple\_end} - c_{dep}\varphi^3 \qquad (24)$$

```
%(8)Definition of the depressurization interval
%Definition of the depressurization trend cubic law
fi_g=linspace(fi3,fi_external_inlet.carving_start,100);
c=0.1 ; %experimental coefficient
%Cubic law design
p_g=p_c(end) -c*(linspace(0,fi_external_inlet.carving_start-
fi3,100)).^3;
%Definition of the ending angle
y6=[0.96593*fi_external_inlet_start
0.96753*fi_external_inlet_start
0.97135*fi_external_inlet_start
0.97389*fi_external_inlet_start];
%Evaluation of regression law
[a11,b11,d11]=regression(p_s,y6);
fi6=a11*p_es +b11;%ending anlge
%Linear law design (depressurization)
fi_h=linspace(fi_external_inlet.carving_start,fi6,1000);
p_h= 1+((fi_h-fi6)./(fi_external_inlet.carving_start-
fi6))*(p_g(end)-1);
%Definition of the constant intake pressure trend
fi_i=linspace(fi6,360,1000);
```
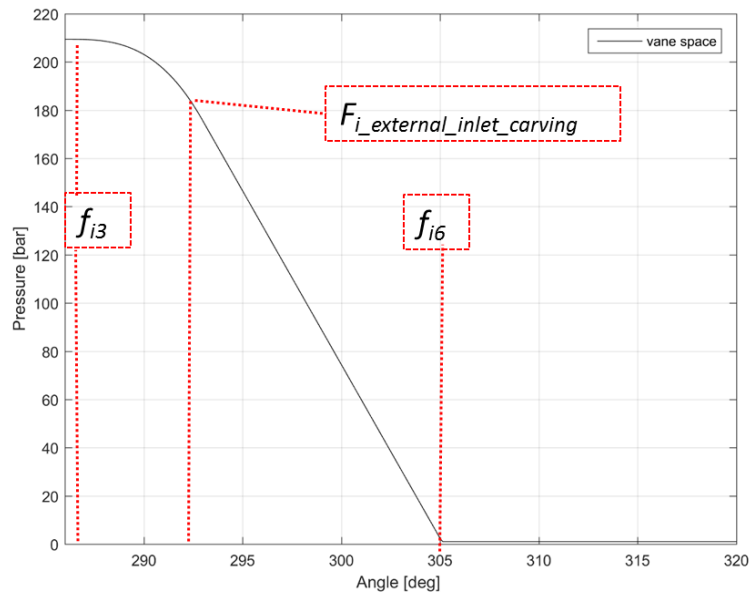
Figure 184. Depressurization interval compute by using the empirical model.
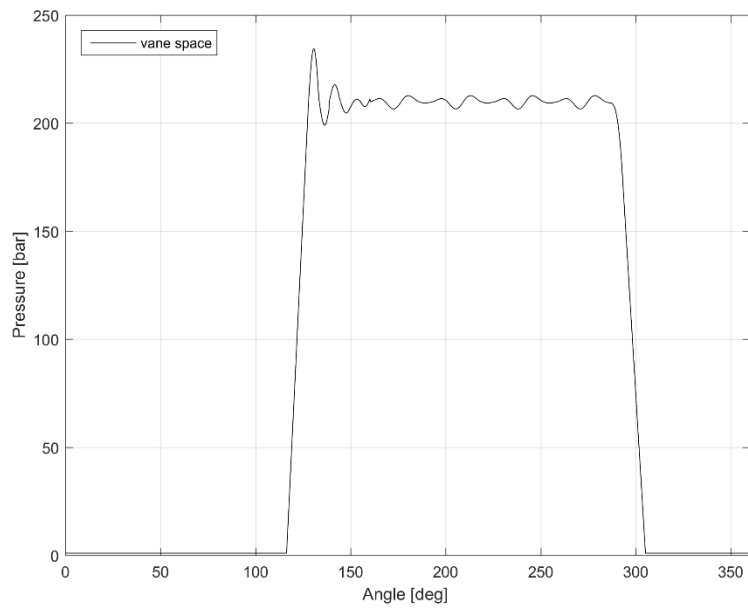
Figure 185. Model results, pressure trend within vane space for working pressure level 210bar.

Now we move to describe the procedure for the estimation of the pressure within the rotor holes. The pressure trend of the rotor holes has an interval which is in common with the pressure trend of the vane space; thus, the definition of the pressure intervals not in common will be illustrated.

Basically, the design of the pressurization phase is composed of four sections (Figure 186). The first one is the linear increasing of the pressure over the pump rotation angle, the second section contains the overshoot and the undershoot of the pressurization phase, the third section is defined by a damped oscillating trend, and the last section (before the matching with the space vane pressure trend) is a sinusoidal function (Figure 187), characterized by the 22nd rotational speed order and a very small amplitude. The observations concerning the influence of pump parameters on the pressure trend of the vane space are valid for the rotor holes as well. The following Matlab lines implement the drawing of the pressurization phase of the rotor hole.
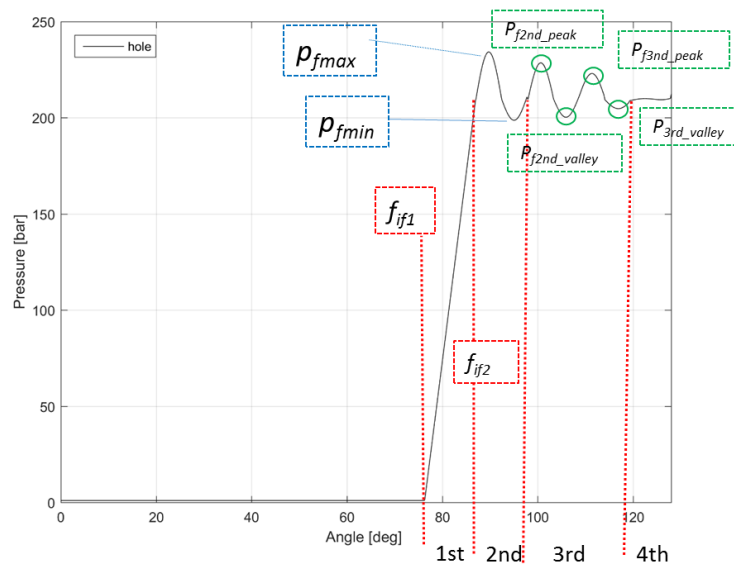
Figure 186. Subdivision of the pressurization phase for the rotor hole pressure trend.
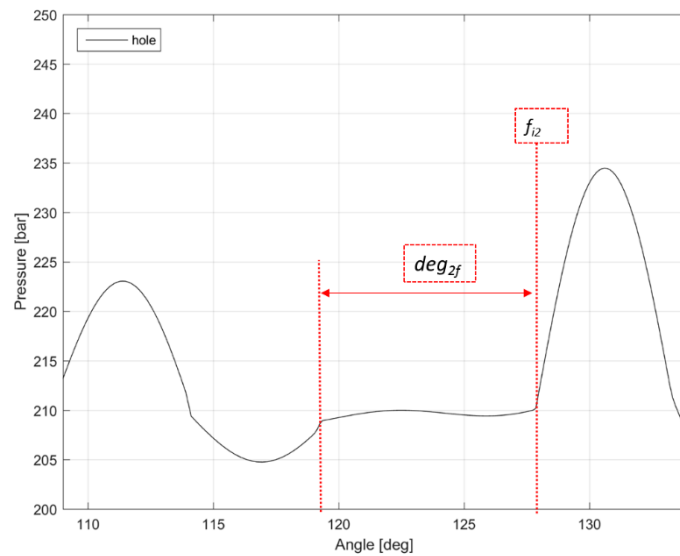
Figure 187. Focus on the last section of the pressurization phase (rotor hole).

```
%%(1)Definition of pressure run up(Hole)
y7=[1.05306*fi_internal_outlet.carving_start
1.04218*fi_internal_outlet.carving_start
1.03810*fi_internal_outlet.carving_start
1.03401*fi_internal_outlet.carving_start];
%Definition of the run up angle
[a12,b12,d12]=regression(p_s,y7); %a1 slope, b1 intercept
term, d correlation coefficient
fif1=a12*p_es +b12 %fif1 starting angle
%%(2)Definition of the pressure run up (Hole)
%Definition of the pressure run up ending angle
fif2=0.84058*fi_internal_outlet_start %fif2 ending angle
%%(3)Definition of the overshoot and undershoot intervals
(Hole)
fif_a=linspace(0,fif1,1000); %angles vector overshoot
pf_a=ones(1,length(fif_a)); %pressure vector overshoot
fif_b=linspace(fif1,fif2,1000); %ending angle undershoot
pf_b= 1+((fif_b-fif1)./(fif2-fif1))*(p_es-1); pressure vector
undershoot
%%(4)Definition of undershoot and overshoot pressure level
(Hole)
pf_max_perc1=[3 8.3 59.8]; % percentage overshoot @ 210bar
pf_max_perc2=[2.38 7.2 47];% percentage overshoot @ 250bar;
% regression line for the working pressure levels 210bar and
250bar
[a13,b13,d13]=regression(cc_s,pf_max_perc1);
[a14,b14,d14]=regression(cc_s,pf_max_perc2);
%%vectors of regression lines due to the working pressure
level 210 e 250 bar
pf_max_perc_cc_es =[a13*cc+b13 a14*cc+b14];
```

```matlab
% evaluation of the percentage overshoot
pf_max_perc = ((pf_max_perc_cc_es(2)-
pf_max_perc_cc_es(1))*((p_es-210)/(250-
210)))+pf_max_perc_cc_es(1);

%Evaluation of the pressure overshoot
pf_max=(((pf_max_perc)/100)+1)*p_es;

%(5)Definition   of   the   first   pressure   undershoot   (Hole)

pf_1min_perc1=[3.8 5.71 10]; %%percentage undershoot 210 bar
pf_1min_perc2=[3.4 5 9]; %percentage undershoot 250 bar
% regression line for the working pressure levels 210bar and
250bar
[a15,b15,d15]=regression(cc_s,pf_1min_perc1);
[a16,b16,d16]=regression(cc_s,pf_1min_perc2);
%%% vectors of regression lines due to the working pressure
level 210 e 250 bar
pf_1min_perc_cc_es =[a15*cc+b15 a16*cc+b16];
%% Evaluation of the percentage undershoot
pf_1min_perc = ((pf_1min_perc_cc_es(2)-
pf_1min_perc_cc_es(1))*((p_es-210)/(250-
210)))+pf_1min_perc_cc_es(1);
% Evaluation of the undershoot pressure
pf_1min=p_es*(1-pf_1min_perc/100);
%(6)Definition of the oscillation trend which contain the
second and third peaks(Hole).
%kf_max=(pn-p_es)/(p_max-p_es)
%kf_min=(p_es-pn)/(p_es-p1min)
% Second peak definition
pf_2max_perc_s=[100 58 46]; %2nd peak ratios
% regression line for the 2nd peak
[a19,b19,d19]=regression(cc_s,pf_2max_perc_s);
pf_2max_perc=a19*cc+b19; % percentage 2nd peak
kf_2max=pf_2max_perc/100; % 2nd peak coefficient
% Second valley definition
pf_2min_perc_s=[100 84 33]; %2nd valley ratios
% regression line for the 2nd valley
[a20,b20,d20]=regression(cc_s,pf_2min_perc_s);
pf_2min_perc=a20*cc+b20; % percentage 2nd valley
kf_2min=pf_2min_perc/100; % 2nd valley coefficient
% Third peak definition
pf_3max_perc_s=[60 33 19];
% regression line for the 3rd peak
[a21,b21,d21]=regression(cc_s,pf_3max_perc_s);

pf_3max_perc=a21*cc+b21; % percentage 3rd peak

kf_3max=pf_3max_perc/100; % 3rd peak coefficient
% Third valley definition
pf_3min_perc_s=[10 22 50]; %3rd valley ratios
% regression line for the 3rd peak
[a22,b22,d22]=regression(cc_s,pf_3min_perc_s);
pf_3min_perc=a22*cc+b22; % percentage 3rd valley
kf_3min=pf_3min_perc/100; % percentage 3rd valley
```

```
%last oscillating section
time2f=linspace(0,(fi2-deg11f(end))/(f_rot*360),1000); %time
vector
deg2f=f_rot*time2f*360+deg11f(end); %angle interval
%Definition of the last oscillating trend
press2f=p_es+A2p1*cos(2*pi*2*f_rot*n_pal*time2f+alfa2p1);
fif_c=[deg1f(1:end-1) deg11f(1:end-1) deg2f]; %overall
oscillating trend (pressurization)
%Definition of the pressure trend during the pressureization
phase
pf_c=[press1f(1:end-1) press11f(1:end-1) press2f];
```

Table 22 and Table 23 contain the experimental data used in order to define the pressurization phase.

16cc		32cc		100cc	
p[bar]	%p$_{max}$	p[bar]	%p$_{max}$	p[bar]	%p$_{max}$
210	3.00	210	8.30	210	57.9
250	2.28	250	7.20	250	47.0

Table 22. Percentage overshoot (experimental data).

16cc		32cc		100cc	
p[bar]	%p$_{min}$	p[bar]	%p$_{min}$	p[bar]	%p$_{min}$
210	3.80	210	5.71	210	10.1
250	3.40	250	5.90	250	9.00

Table 23. Percentage undershoot (experimental data).

After the pressure ripple, the depressurization phase takes place. The decreasing pressure trend of the rotor hole is different with respect to that of the vane space. Basically, in this case the descending trend must be divided in three different sections (Figure 188). The first section is defined by a sinusoidal law which contains the last valley of the pressure ripple, the second section is still a sinusoidal law but it contains the last peak of the pressure ripple, and finally the last section is characterized by a linear law which represents the pressure decay from the working pressure level to the inlet working level. The angular extension of the sinusoidal trends (fig_g1, fif_g2), during the depressurization phase, depends only on the inlet carving design; the angular ranges for the first and second sinusoidal law are respectively $\pi/2$ and π; these laws are shown in Eq(25) and Eq(26).

$$p(\mathit{fif}_{g1}) = pf_{3\min} + \left(pf_{3\min} - pf_{3\min} \right) \sin([\pi/2 : \pi]) \qquad (25)$$

$$p(\mathit{fif}_{g2}) = pf_{3\min} + \left(pf_{3\min} - pf_{5\max} \right)\sin([0:\pi]) \qquad (26)$$
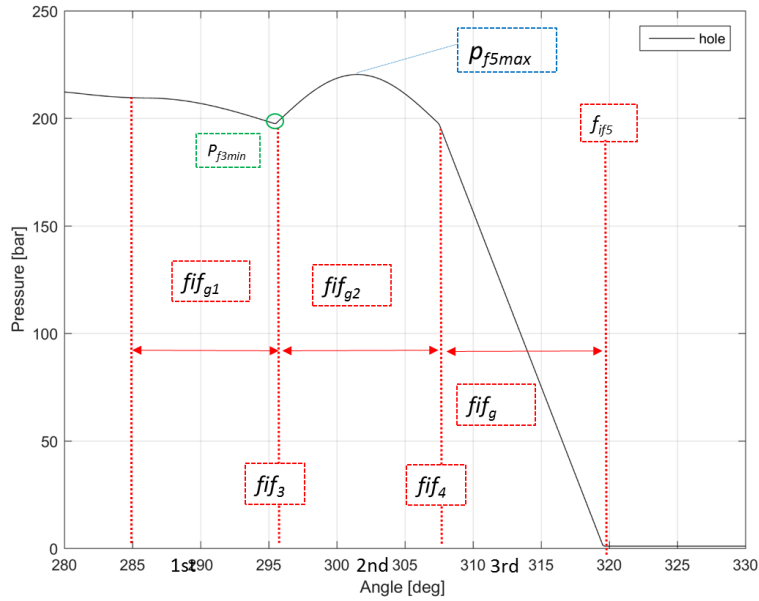
Figure 188. Depressurization interval compute by using the empirical model.

The minimum pressure value present within the first interval has been defined by using the experimental data, showing that it is not affected by any pump parameters, but it is almost the 6% below the working pressure level. On other hand, the last pressure overshoot depends on the pump displacement and the working pressure level; thus, the evaluation of this parameter requires the regression line approach. The experimental data implemented into the Matlab code are reported in Table 24. The following Matlab lines implement the depressurization trend for the rotor hole.

16cc		32cc		100cc	
p[bar]	%p$_{max}$	p[bar]	%p$_{max}$	p[bar]	%p$_{max}$
210	1.85	210	7.54	210	9.00
250	1.68	250	6.80	250	7.50

Table 24. Experimental data concerning the last pressure overshoot

```matlab
%%(7)Definition of depressurization trend(hole)
%last undershoot angle
fif3=0.97589*fi_internal_outlet.carving_end;
% sinusoidal law end (angle)
fif4=0.99571*fi_internal_outlet.carving_end;
% extension of the first depressurization interval
fif_g1=linspace(fif_f(end),fif3,1000);
% extension of the second depressurization interval
fif_g2=linspace(fif3,fif4+(fif4-fif3),1000);
%last undershoot pressure level
pf_3min=p_es-((p_es/100)*6);
% Definition of overshoot pressure level (Hole)
pf_max_perc5=[1.85 7.44 9]; % percentage overshoot @ 210bar
pf_max_perc6=[1.68 6.8 7.5];% percentage overshoot @ 250bar;
%% regression line for the working pressure levels 210bar and
250bar
[a17,b17,d17]=regression(cc_s,pf_max_perc5);
[a18,b18,d18]=regression(cc_s,pf_max_perc6);
% vectors of regression lines due to the working pressure
level 210 e 250 bar
pf_max_perc5_cc_es =[a17*cc+b17 a18*cc+b18];
% evaluation of the percentage overshoot
pf_5max_perc = ((pf_max_perc5_cc_es(2)-
pf_max_perc5_cc_es(1))*((p_es-210)/(250-
210)))+pf_max_perc5_cc_es(1);

%Evaluation of the pressure overshoot
pf_5max=(((pf_5max_perc)/100)+1)*p_es;

%First sinusoidal trend
pf_g1=pf_3min+(pf_f(end) -
pf_3min)*sin(linspace(pi/2,pi,1000));

%Second sinusoidal trend
pf_g2=pf_3min -(pf_3min-pf_5max)*sin(linspace(0,pi,1000));

%Extension of linear law of depressurization law
fif_g=[fif_g1 fif_g2];


%Drawing of the first and second depressurization interval
pf_g=[pf_g1 pf_g2];
%%Definition of the ending angle
y8=[1.00508*fi_internal_inlet.carving_start
1.01015*fi_internal_inlet.carving_start
1.01301*fi_internal_inlet.carving_start
1.01745*fi_internal_inlet.carving_start];
%Evaluation of regression law
[a20,b20,d20]=regression(p_s,y8);
fif5=a20*p_es+b20; %Ending angle
%Linear law design (depressurization)
fif_h=linspace(fif_g(end),fif5,1000);
pf_h= 1+((fif_h-fif5)./(fif_g(end)-fif5))*(pf_g(end)-1);
%%Definition of the constant intake pressure trend
```

```
fif_i=linspace(fif5,360,1000);
pf_i=ones(1,length(fif_i));
```

The pressure trend within the rotor hole (in case of 210bar working pressure) is displayed in Figure 189, where the red circles delimit the portion of the pressure trend shared with that of the vane space.
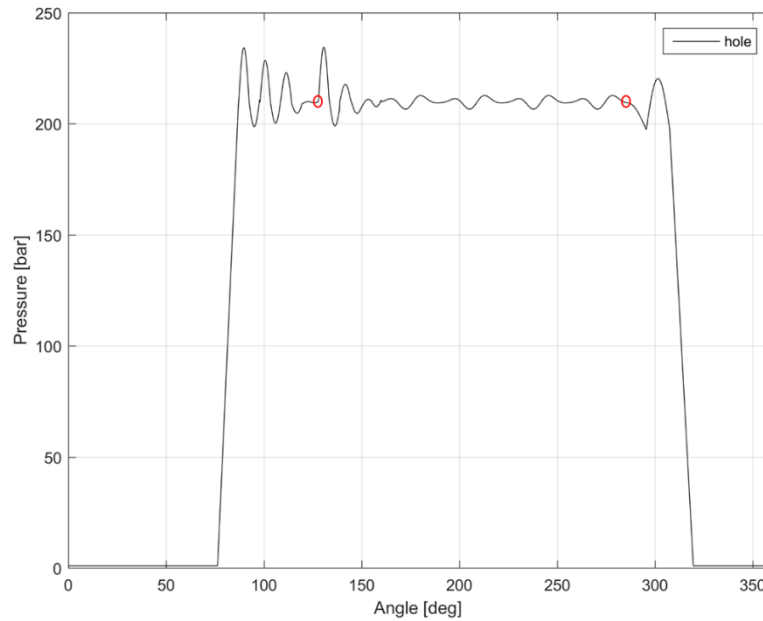
Figure 189. Model results, pressure trend within rotor hole for working pressure level 210bar.

B.2.5.   Model validation by Comparison with Test Results

The model has been validated by performing the comparison between the model and experimental results for three different pumps of the same family (16cc, 32cc and 100cc); for each pump three working pressure levels have been investigated (160bar, 210bar, 250bar). The model accuracy is defined by using the Percentage of Good Point (PGP) index [26]: this approach defines a tolerance area, using the reference experimental data and choosing an appropriate percentage tolerance. Thus, the tolerance area is defined by two threshold lines, called

respectively "lower deviation" and "upper deviation" line. The lower and upper lines are traced by shifting the experimental line respectively down and up of the percentage tolerance, which is selected as 2% of the working pressure level:

$$\delta = \frac{p_{es}}{100} 2 \qquad (27)$$

Figure 190 shows the example of the tolerance area. The PGP index is defined by computing the percentage of the model points which are included within the tolerance area; the points below level 5 bar are not taken into account because they are not relevant for our purposes. The model validation has concerned only the full flow working condition, because during the pump durability test, the displacement was kept steady at the maximum flow rate value. The PGP index has been evaluated for the vane spaces and the rotor holes as well. If PGP index is above the 70%, the model can be considered efficient for the pressure trend prediction. Table 25 and Table 26 contain the PGP index results for the vane space and rotor hole: the PGP values are always above the 75%; that means a good agreement between the experimental results and the numerical ones.

Furthermore, the model accuracy is proved by the following diagrams, exhibiting the positive matching between the numerical and experimental trends.
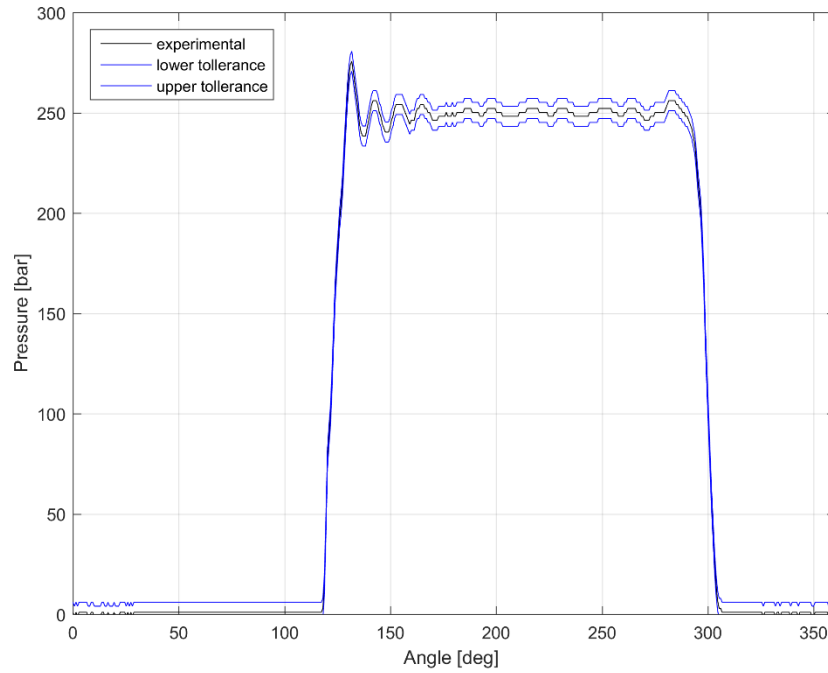
Figure 190. Example of the tolerance area.

Pressure working level	PHV05 16cc	PHV01 32cc	PSP100
160bar	80,29%	75,44%	76,43%
210bar	80,77%	80,56%	78,90%
250bar	80;07%	81,76%	82,77%

Table 25. PGP index results for the vane space pressure trend.

Pressure working level	PHV05 16cc	PHV01 32cc	PSP100
160bar	76,12%	75,01%	75,02%
210bar	82,35%	77,58%	77,32%
250bar	87,79%	81,36%	80,91%

Table 26. PGP index results for the rotor holes pressure trend.

In particular, Figure 191, Figure 192, Figure 193, Figure 194, Figure 195 and Figure 196 show the comparison between the model and experimental results for the middle size pump of 32cc, which is taken as a reference for the subsequent research concerning the evaluation of the lubrication regime between the vane tips and the stator ring.
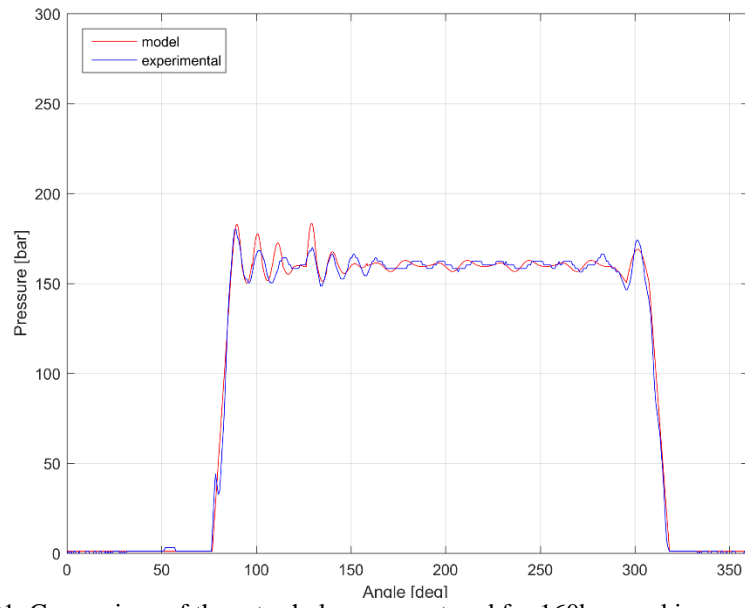
Figure 191. Comparison of the rotor hole pressure trend for 160bar working pressure level (Pump32cc).
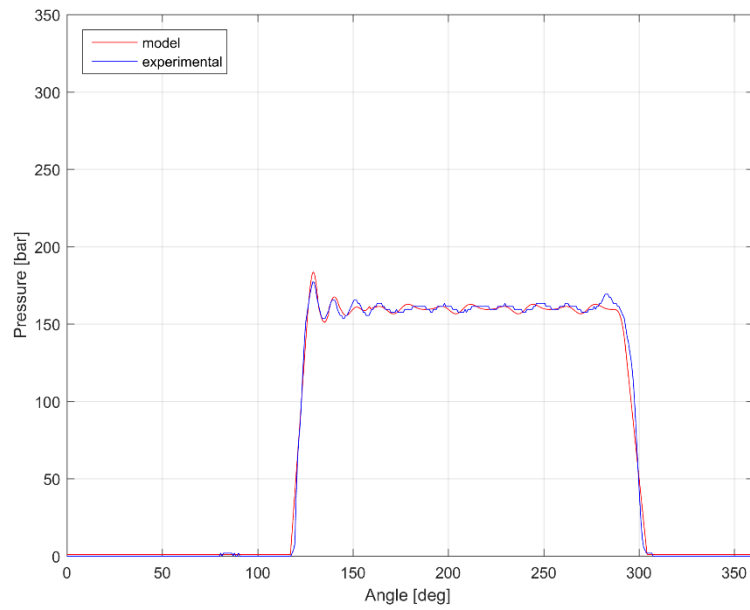
Figure 192. Comparison of the vane space pressure trend for 160bar working pressure level (Pump32cc).
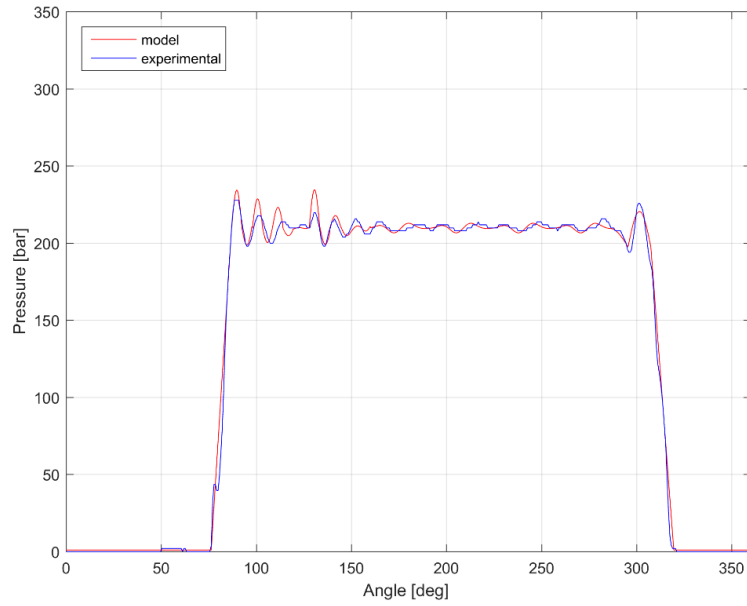
Figure 193. Comparison of the rotor hole pressure trend for 210bar working pressure level (Pump32cc).
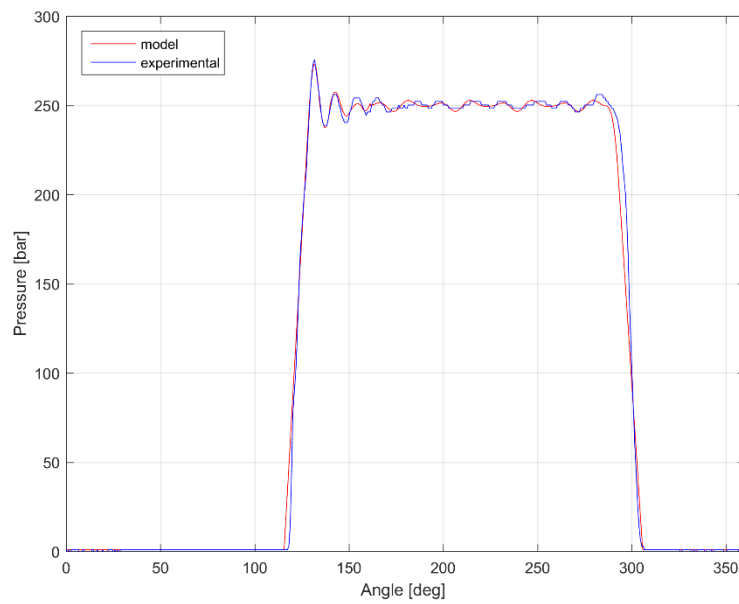
Figure 194. Comparison of the vane space pressure trend for 210bar working pressure level (Pump32cc).
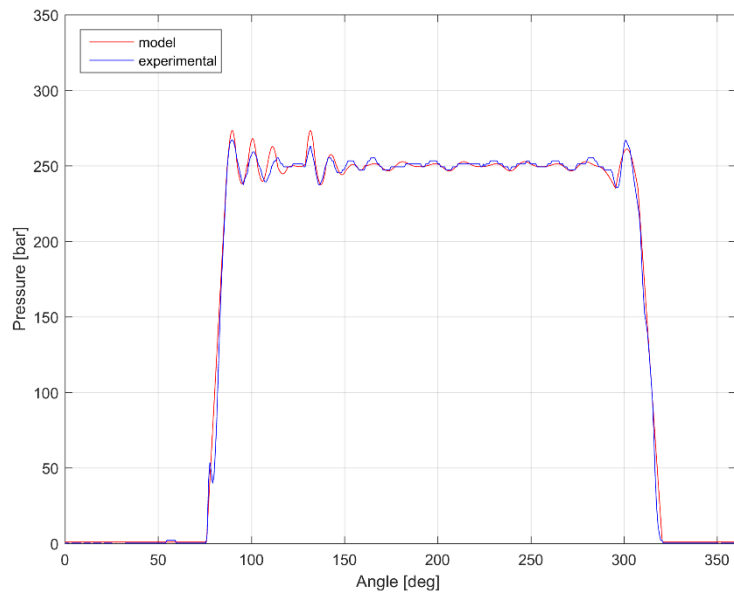
Figure 195. Comparison of the rotor hole pressure trend for 250bar working pressure level (Pump32cc).
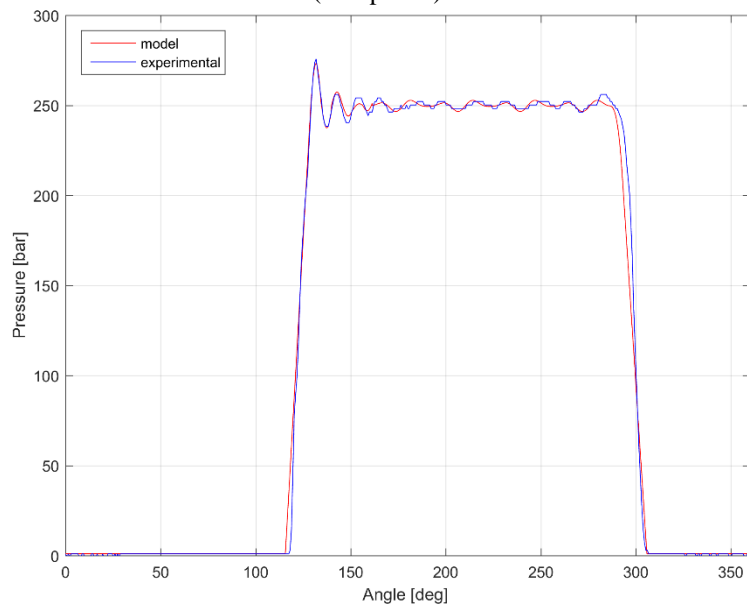
Figure 196. Comparison of the vane space pressure trend for 250bar working pressure level (Pump32cc).

CHAPTER B.3
ANALYSIS OF THE WEAR AND LUBRICATION REGIME

B.3.1.   Introduction and Methodology

This chapter deals with an experimental methodology for the analysis of the lubrication regime and wear that occur between vanes and pressure ring. This first paragraph gives an overview of the wear issue on variable displacement vane pumps and it describes the methodology based on Archard's equation, used in order to identify the lubrication regime between vanes and ring. The second paragraph (B.3.2) is focused on the evaluation of the normal contact forces between the vane tips and the stator ring by using the empirical model. Hereafter the third paragraph (B.3.3) depicts the procedures for the evaluation of the parameters of Archard's equation. The fourth paragraph (B.3.4) presents the application of an EHD model, used in order to verify the goodness of the developed methodology for the estimation of lubrication regime. The last paragraph (B.3.5) illustrates and discusses the obtained results.

In high pressure variable displacement vane pumps, the evidence of wear tracks can be found on the internal surface of the pressure ring as well as on the top of the vanes, as a consequence of the sliding contact between pressure ring and vanes (Figure 197). The wear phenomenon is a rather difficult topic to be understood, especially if all of the possible physical and chemical influence parameters are taken into account.
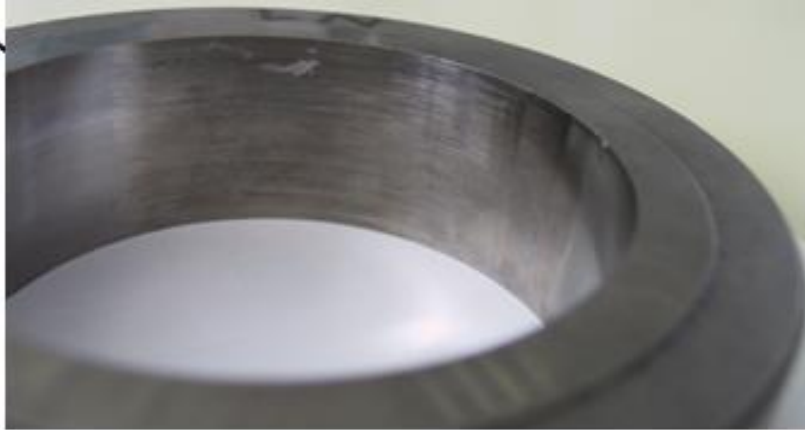
Figure 197. Evidence of wear tracks in the pressure ring internal surface.

In the manufacturing sector, energy costs continue to rise, and companies are being asked to improve profitability through greater cost control. The reduction of energy consumption has become a key component in cost control, especially at manufacturing facilities with higher energy costs. Nowadays the target of the designer consists in the development and implementation of the best ways to make the manufacturing sector, specifically of pumping systems, as energy efficient as possible. In order to help designers to improve the performance of high pressure vane pumps by reducing the wear, increasing the volumetric efficiency and decreasing the maintenance cost, it is necessary to know what kind of lubrication regime exists in the vane-pressure ring contact, Figure 198. Thus, the selection of the adequate materials and suitable design methodologies is desired, in order to achieve optimized wear. For example, wear reduction can be achieved by improving surface material performance if boundary lubrication regime exists or by modifying the surface geometry in case of hydrodynamic lubrication regime.
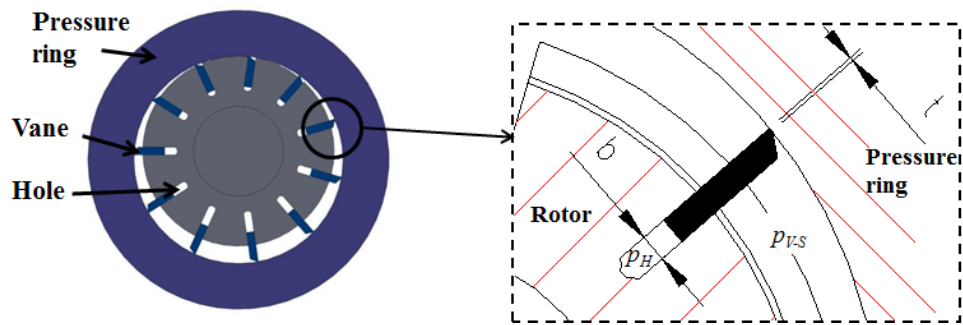
Figure 198. Sketch of the pressure ring (stator), rotor, vanes and holes.

In the literature, many approaches have been adopted in order to estimate wear in kinematic joints. The main equations of the wear models use the methods of solid mechanics, most include material properties, thermodynamics quantities and other engineering variables. H.C Meng and K.C Ludema in [27] describe how wear models have been improved over years. The first wear equations were developed in Europe by German authors such as Toon [28], Holm [29] and by Russian authors such as Kruschov and Barbichev [30]. A big step in the wear equation enhancement occurred in 1967 with the fatigue theory, which takes into account the contact roughness [31]. Originally, the wear equations were derived using data taken from experimental tests [32,33]. Then, wear equations were proposed based on Young's modulus and hardness of kinematic joint materials like Archard's equation [34]. Specifically, for vane pumps, the works in [19,35] regards the wear prediction in the contact between vanes and stator and the relative comparison with experimental data, assuming that wear is caused by shear effects in the surface regions of contacting bodies in relative motion. Then, till 1981 several authors have developed wear models that included new material phenomena like dislocation mechanisms, fatigue brittle-fracture and corrosion properties [36-39]. Nowadays, finite element method takes advantage of a number of wear equations. In this context, the first simulation of mild wear in spur gears has been referred to Flodin and Anderson in [40]. Specifically, for vane pumps, concerning the prediction of lubrication regime in kinematic joints, experimental methods based on optical interferometry in the contact region of sliding/rolling point contact can be found in [41-44]. In

particular, by such a methodology the geometry of the lubricant passageway can be fully estimated. A different experimental approach concerns the electrical resistance technique, which has been used to aid the identification of the lubrication regime [45]. Furthermore, several analytical methods based on elasto-hydrodynamic (EHD) empirical equations obtained by experimental data have been deduced. They calculate the minimum film thickness and they predict the lubrication regime by comparison with surface roughness [46].

It is now outlined the methodology used in this chapter for the identification of the lubrication regime between vanes and pressure ring, based on Archard's equation. It is well known that the Archard's wear model correlates the wear volume with the hardness of the sliding bodies, the applied normal load and the sliding distance. When Archard's wear approach is concerned, it should be highlighted that this linear wear model was firstly possessed by Holm [29], although it has been usually named as Archard's wear equation. Archard's wear equation represents a macroscopic model, since the microscopic effects like asperities deformations and materials tearing are not directly taken into account. This model was developed and based on experimental tests and it states that [47]:

$$V = \frac{K \, F_N \, s}{H} \qquad (28)$$

where V is the wear volume [m³] concerning one of the surfaces, s is the sliding distance [m], K is the dimensionless generalized wear coefficient, F_N represents the normal contact force [N] and H is the material penetration hardness [N/m²] of the surface which is worn away. The generalized wear coefficient depends on the lubrication regime as shown in Table 26. High values of such a coefficient correspond to unlubricated joints, while low values to hydrodynamic lubrication, squeeze film [48] or elasto-hydrodynamic lubrication [49].

Type of lubrication	Range of wear coefficient K
Hydrodynamic	$<10^{-13}$
Squeeze film	$<10^{-13}$
Elasto-hydrodynamic	10^{-9}-10^{-13}
Boundary (commercial lubricant)	10^{-6}-10^{-10}
Solid film lubricant	10^{-6}
Dry bearing material	10^{-2}-10^{-7}
Unlubricated	10^{-2}-10^{-4}

Table 27. Generalized wear coefficient K as a function of the lubrication regime (see also reference [50]).

In this work, the Archard's wear equation is used to estimate the generalized wear coefficient in order to define the lubrication regime that is established in the sliding contact between vanes and pressure ring (Figure 199), taking advantage of data in Table 27. The other parameters in the Archard's equation have been numerically calculated or experimentally measured: surface material hardness H was measured by hardness tests, sliding distance s was determined by the knowledge of the rotor angular velocity and the test duration, F_N was obtained by an empirical model and wear volume V was measured with high resolution measuring machine. In this research, vane pumps of the PHV series were tested at the output pressure of 230 bar, rotational speed of 1500 rpm for a duration of 40 h supplying the full flow of 50 l/min, by using commercial Shell Tellus ST46 as pumping oil.
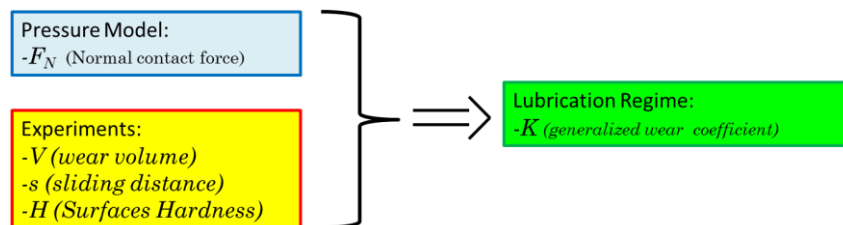
Figure 199. Scheme of the numerical and experimental methodology foe evaluation of lubrication regime for the vane and stator ring contact.

These conditions were very stressful for pump components, as outlined before, so it was possible to assess the vane and pressure ring wear within a short operational time. Three different types of pressure ring were tested that differ in the surface coating type; all of them were made of 41CrAlMo7-10 steel. The first was made by using a 41CrAlMo7-10 nitriding steel (Figure 200). The nitriding steel pressure ring was subjected to an isothermal annealing to confer 3000 HB (Brinnell Hardness), a hardening and tempering treatment to give ultimate tensile strength of 1200÷1300 N/mm² and lastly a nitriding treatment to obtain 1100÷1200 HV (Vickers Hardness). The second type of pressure ring was made of TiN-coated steel (Figure 201), obtained through a physical vapor deposition, which places a thin coating (3μm thick) on the working area of the pressure ring; the hardness of this material is about 2300 HV. The third type used a DLC-coated steel (Figure 202). DLC (diamond-like carbon) coating is a structurally amorphous low friction carbon-hydrogen based film. It is a thin and inert coating (3μm thick); moreover, the DLC coating has a hardness of 1300 HV. The material of the vane was the same for each test: the vanes were made from HS6-5-2C high speed steel, quenched and tempered to 63 HRC (Rockwell C Hardness).

Figure 200. Nitinding pressure stator ring.
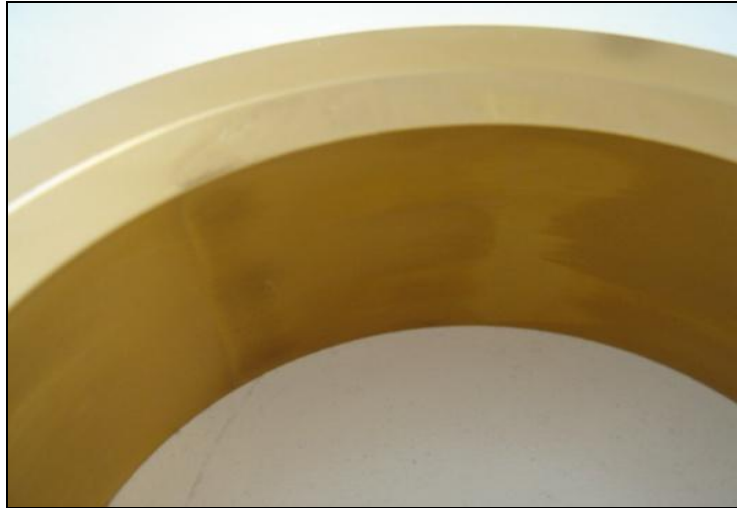
Figure 201. TiN pressure stator ring.
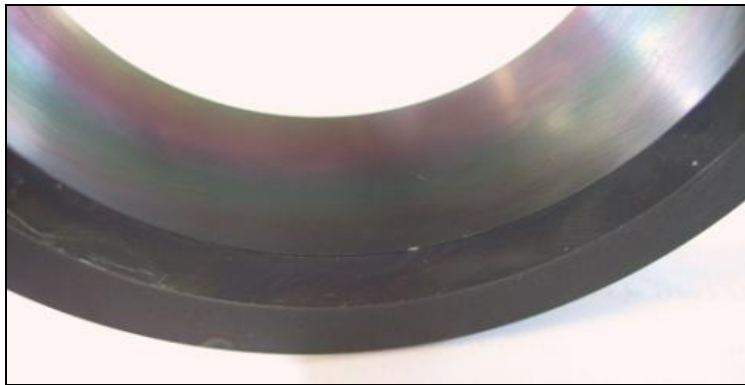
Figure 202. DCL pressure stator ring.

B.3.2.   Evaluation of Contact Forces by the Empirical Model

These paragraph explains how the results of the empirical model are used for the evaluation of normal contact forces between the stator ring internal surface and the vane tips. Normal contact force F_N of Eq (28) is obtained as the difference between the force on the vane base due to the pressure in the hole (Figure 203), $F_{V\text{-}B}$, Eq(30), and the force due to the pressure acting on the tip of the vane, $F_{V\text{-}T}$,(31) , taking into account the inertial force of the vane, i.e. the centrifugal force, $F_{V\text{-}C}$, Eq(32):

$$F_N = F_{V-B} - F_{V-T} + F_{V-C} \qquad (29)$$

with:

$$F_{V-B} = p_H(\varphi)bw \qquad (30)$$

$$F_{V-T} = p_{V-S}(\varphi)(b - t_{tip})w \qquad (31)$$

$$F_{V-C} = m_v \omega^2 R_m \qquad (32)$$

where p_H (φ) is the hole pressure acting on the vane base and p_{V-S} (φ) is the pressure of the vane space acting on the vane tip at angular reference φ, w and b and are width and thickness of the vane, respectively, t_{tip} is the thickness of the vane tip, mv is the vane mass, ω is the rotor angular speed and R_m is the mean distance between the center of mass of the vane and the shaft rotational axis.
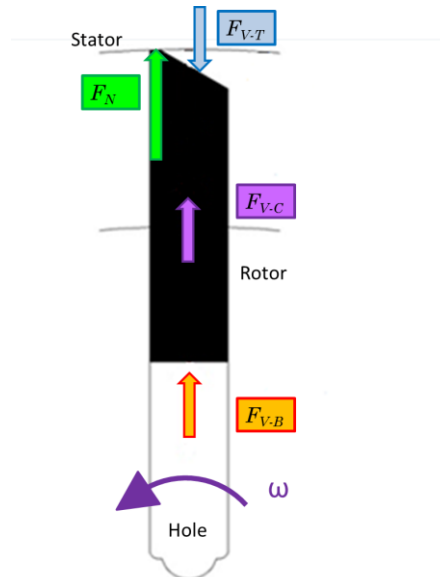
Figure 203. Representation of the force balance between pump vane and stator pressure ring.

Thus, in order to calculate the normal contact force, the pressure evolution in holes and in vane spaces during a complete rotation of the rotor is needed. The empirical model described above has been used in

order to predict the pressure evolution inside the pump by using an approach focused on industrial applications. In case of working pressure level of 250bar and full flow rate, Figure 204 depicts the normal contact force evolution for a complete revolution. In more detail, also the normal contact force can be subdivided into four regions: Inlet region (I), characterized by the atmospheric pressure in vane spaces and holes; Inlet-Outlet transition region (I-O), where the pressure in vane spaces and holes increases from inlet to outlet pressure; Outlet region (O), characterized by the outlet pressure in vane spaces and holes; Outlet-Inlet transition region (O-I), where the pressure in vane spaces and holes decreases from outlet pressure to inlet pressure. Region I (from fi_{f5} to fi_{f1}) is characterized by a low contact normal force, since the inlet pressure acts on both surfaces (the vane tip and vane base). Region I-O (from fi_{f1} to fi_2) has a high contact normal force; in this region the pressure rapidly changes from the inlet to the outlet pressure, where the former acts on the tip vane, while the latter acts on the vane base. Region O (from fi_2 to fi_3) has a lower value than region I-O, since the outlet pressure acts on the tip and on the vane base. Region O-I (from fi_3 to fi_{f5}), being a transition between outlet and inlet pressure, has a high contact normal force.
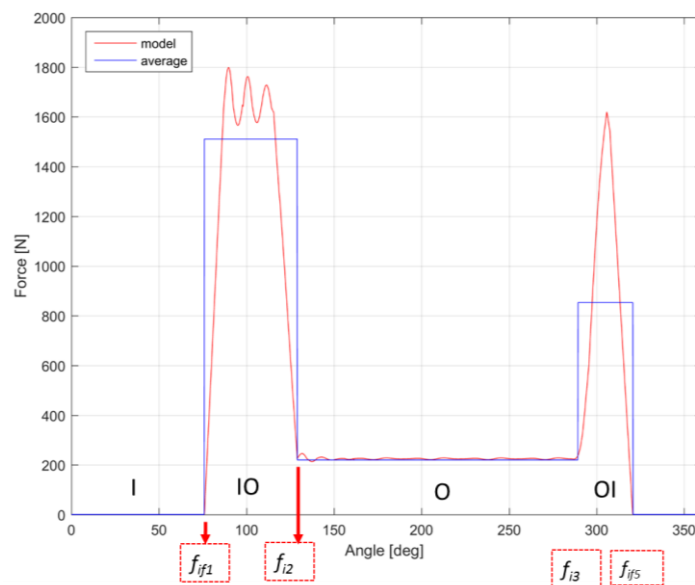
Figure 204. Normal contact force between pressure ring internal surface and vane computed by empirical model and the simplified one.

B.3.3.   Evaluation of the Parameters of Archard's Equation

The evaluation of remaining Archard's equation parameters will be illustrated in this paragraph, beginning with the wear volumes of the four regions. Measurements were made by Mitutoyo LEGEX9106 coordinate measure machines, which has the maximum measurable volume of 1005×905×605 mm, resolution of 0.01 µm and maximum permissible error of length measured (MPE_E index) MPE_E=(0.48+L/1000) [µm], where L is the measured length in mm. The internal profile of each pressure ring has been measured before and after the pump operational test described in Paragraph B.3.1; then the average value of wear volume for each region (Inlet, Inlet-Outlet, Outlet and Outlet-Inlet) has been calculated. In order to increase the robustness of the results, for each type of pressure ring (nitriding steel, TiN, DLC), two specimens were tested and for each specimen, profile measurements were evaluated on three sections of the pressure ring (Figure 205), namely L1, L2 and L3. Section L1 was positioned at a quarter of the pressure ring axial length (8 mm from ring face), section L2 in the middle (15 mm) and the last section (L3) at three quarters of the pressure ring length (22 mm). Then, wear average values between the sections and between the specimens belonging to the same pressure ring type were considered.
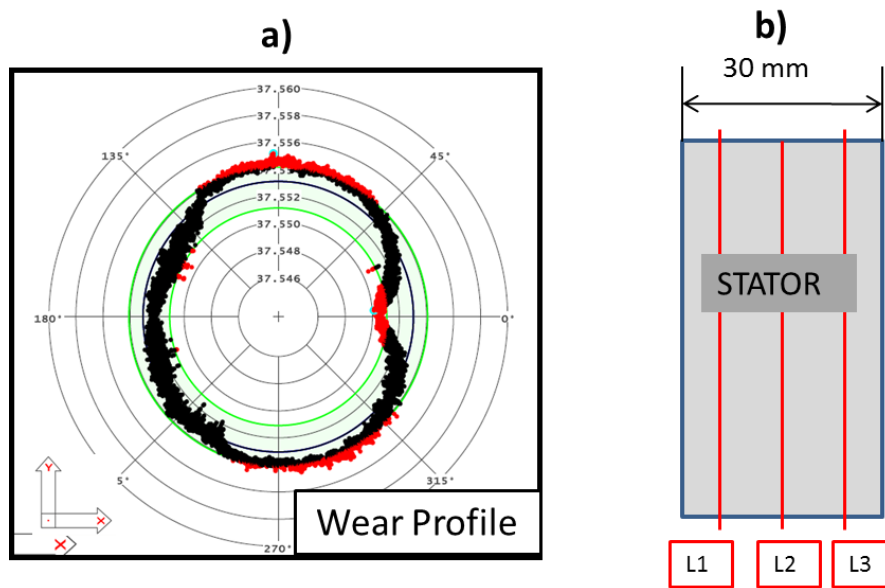
Figure 205. a) Inner stator pressure ring wear profile, b) measurement section of the inner stator profile.

The total sliding distance (s_{total}) regarding the pressure ring is obtained by multiplying the value of sliding velocity ($v_{sliding}$) for the test duration of 40 h (t_{test}) and the number of vanes (z_{vanes}):

$$s_{total} = v_{sliding} z_{vanes} t_{test} = 0,00589 \cdot 11 \cdot (40 \cdot 3600) \cong 9326 \text{ km} \qquad (33)$$

The sliding distance for each region (s in Eq (28)) was obtained from this total sliding distance by the proportional subdivision with respect to the circumferential region lengths (I, I-O, O, O-I). It has to be specified that pump operational tests have been made in full flow condition with the maximum eccentricity between pressure ring and rotor, so in this case the sliding velocity is different during the rotation. However, because of the low value of eccentricity between pressure ring and rotor axis, equal to 4 mm, the assumption of constant sliding velocity is acceptable. The considered value of sliding average velocity is 5.89 m/s ($v_{sliding}$), which is the sliding velocity in zero flow condition without eccentricity.

Finally, Vickers hardness tests have been used in order to measure the hardness of the internal profile of the three types of pressure ring being tested.

The generalized wear coefficient for the vane related to each particular pressure ring has been computed as well by using the same methodology described for pressure ring. In particular, the wear volume has been experimentally obtained by comparing the thickness of the vane measured by optical microscopy after the wear process (Figure 206) with the nominal value given by the 3D-CAD. Figure 206 clearly highlights that wear occurs mainly in the vane centre. The material hardness has been obtained by Vickers hardness tests. The product $F_N s$, which appears in Archard's equation (Eq(28)), has been calculated as follows:

$$F_N s = F_{Inlet} s_{Inlet} + F_{Inl-Out} s_{Inl-Out} + F_{Outlet} s_{Outlet} + F_{Out-Inl} s_{Out-Inl} \qquad (34)$$

where the sliding distance (s) has been subdivided into the four regions of sliding circumference: s_{Inlet} is the sliding distance of the Inlet region, $s_{Inl-Out}$ is sliding distance in the Inlet-Outlet region, s_{Outlet}, $s_{Out-Inl}$ are the sliding distances of the Outlet and Inlet-Outlet region, respectively. Thus, each distance referring to a region was multiplied by the relative average normal contact force acting in each region: F_{Inlet} in the Inlet region, $F_{Inl-Out}$ in the Inlet-Outlet region, F_{Outlet}, $F_{Out-Inl}$ in the Outlet and Outlet-Inlet region, respectively.
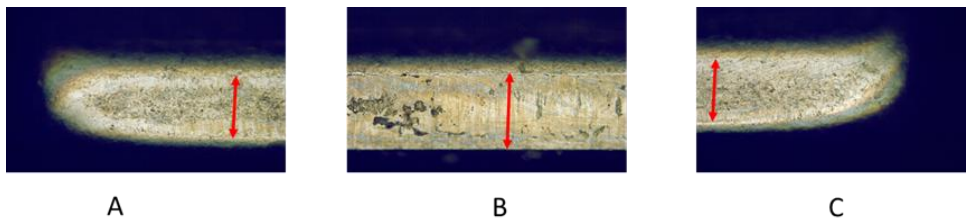
Figure 206. Photo of vane surface (A is the left side of the vane tip, B is the centre and C is the right side). The values refer to the mean dimensions of vane

tip thickness measured by optical microscopy. The nominal vane tip thickness is 200 µm.

B.3.4.   Application of an EHD model

An analytical model based on elasto-hydrodynamic lubrication (EHD) has been used in order to estimate the minimum lubricant film thickness (h_0) established between the vane and the pressure ring in operational conditions. The minimum film thickness together with the roughness of the surfaces in contact (R_{a1} and R_{a2}) were used for the estimation of parameter λ [51]:

$$\lambda = \frac{h_0}{\sqrt{R_{a1}{}^2 + R_{a2}{}^2}} \qquad (35)$$

In the literature, parameter λ is correlated to the type of EHD lubrication. In particular, values of λ lower than 1 indicate direct contact between surface asperities, so surface smearing or deformation accompanied by wear may occur. This is the typical situation of boundary lubrication. Values of λ between 1 and 3 indicate that a lubricating film separates the surfaces, but some contacts between the surface asperities are allowed. This type of lubrication is considered in the literature as mixed or partial EHD lubrication. Finally when λ values become greater than 3, full separation of the surfaces by EHD film can be expected.

The minimum film thickness is obtained by the well-known line contact model [48,49]. The line contact formula uses a similar expression for the estimation of the minimum film thickness with respect to the Hamrock and Dowson's EHD model [52,53]. The formulae derived by Hamrock and Dowson can be applied to several kinds of contact, such as punctual, linear or elliptical, while the line contact model is more specific and can be used when two cylinders are pressed against one another under a normal load, producing a plane rectangular contact area, as in our case (Figure 207).
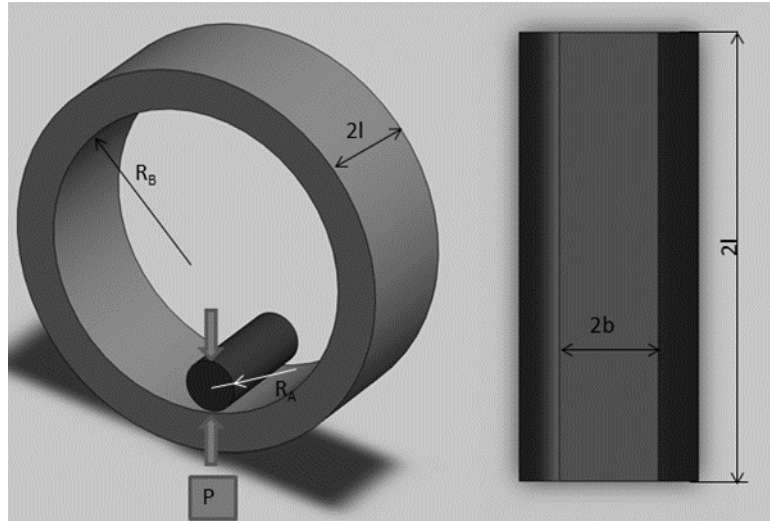
Figure 207. Schematic of the contact model between two cylindrical surfaces (concave and convex).

The numerically derived formula for the minimum film thickness for the line contact model has the following form (see Table 28 for the list of symbols and relative values used in the simulation):

$$\frac{h_0}{R'} = 1.93 \cdot \left(\frac{u\mu_0}{E'R'}\right)^{0.69} \left(\alpha E'\right)^{0.56} \left(\frac{F_N}{E'R'2l}\right)^{-0.1} \tag{36}$$

Pump parameters	Symbols	Values
Roughness of vane	R_{a1}	0.1 μm
Roughness of pressure ring internal surface	R_{a2}	0.11 μm
Pressure-viscosity coefficient	α	16 GPa^{-1}
Viscosity at atmospheric pressure and operational temperature	μ_o	0.02037 Pa s
Radius of curvature for vane	R_A	7.75 mm

Radius of curvature for pressure ring	R_B	-37.55 mm
Poisson's ratio of vane and pressure ring	v_A, v_B	0.3
Young's modulus of the vane	E_A	210 GPa
Young's modulus of the pressure ring	E_B	220 GPa
Vane velocity	u_A	5.887 m/s
Pressure ring velocity	u_B	0 m/s
Contact length	l	30 mm

Table 28. Pump parameters for EHD lubrication model calculation.

where h_0 [m] is the minimum film thickness, $u=u_A+u_B$ (the subscripts A and B refer to the velocities of vane and pressure ring, respectively), μ_0 [Pa·s] is the viscosity at the atmospheric pressure and operational temperature of the lubricant, E' [Pa] is the reduced Young's modulus, R' [m] is the reduced radius of curvature, a [m²/N] is the pressure-viscosity coefficient, F_N [N] is the contact load, $2l$ is the contact length (Figure 207). The numerical data for the lubricant has been acquired by the oil datasheet, considering an operational temperature of 60 °C equal to the pump drainage oil temperature. Parameters R', E' are related to the Hertzian contact depending on the contact geometry and material properties. In our case, the geometry can be compared to the contact between two parallel cylinders (Figure 207); hence the Hertzian contact parameters (R', E') assume the following forms:

$$R' = \frac{R_A R_B}{R_A + R_B} \tag{37}$$

$$E' = \left[\frac{1}{2} \left(\frac{1-v_A^2}{E_A} + \frac{1-v_B^2}{E_B} \right) \right]^{-1} \tag{38}$$

where R_A and R_B are the nominal values of the curvature radii of the vane tip and the pressure ring, respectively, v_A is the Poisson's ratio of the vane material, v_B is the Poisson's ratio of the pressure ring material, E_A and E_B [Pa] are the Young's moduli of vane material and pressure ring respectively. It has to be underlined that for this calculation, E_A and E_B are the Young's moduli of the material cores. In the literature, researches trying to experimentally estimate the Young's

modulus of the coating can be found. Usually these material parameters are obtained by nanoindentation techniques [54]. However, the use of Young's moduli of the coating does not influence significantly the results, which remain of the same order of magnitude. Eq(36) is usually written in the following form, by using three non-dimensional groups:

$$\frac{h_0}{R} = 1.93 \cdot (U)^{0.69} (G)^{0.56} (W)^{-0.1} \qquad (39)$$

where U is the non-dimensional speed parameter, G the non-dimensional material parameter and W the non-dimensional load parameter. The variation of the non-dimensional parameters causes variation of the EHD film thickness and pressures, as demonstrated in [48, 49, 52, 53,54].

B.3.5.   Results and Discussion

Before the values of the wear coefficients are presented, the results of the Archard's parameters are shown hereafter.

Concerning the normal contact force, for this research a simplification can be accepted: the average contact normal force for each of the four regions (Figure 204) has been used. The computed values are also shown in Table 29. Regarding the wear volume, Figures 204, 205 and 206 show the wear profile comparison (where r is the radius of the measured profile) before and after the pump operational test, for the three different pressure rings being studied. The wear profiles have been obtained by the coordinate measure machine described in Paragraph B.3.3. By using these quantities, the average wear volume for each type of pressure ring (nitriding steel, TiN, DLC) in the four circumferential regions can be estimated (collected in Table 30).

Region	Average Contact Force (F_N)	Sliding distance (s)
Inlet	3 N	3019 km
Inlet-Outlet	1511 N	1365 km

| Outlet | 207 N | 4241 km |
| Outlet-Inlet | 853 N | 704 km |

Table 29. Average contact forces between pressure ring internal surface and the vane and sliding distance in the different regions.

Material / Region	Nitriding steel (0.4÷0.6mm)	TiN coated (3µm)	DLC coated (3µm)
Inlet	$2.7 \cdot 10^{-10}$ m^3	$8.2 \cdot 10^{-10}$ m^3	$8.9 \cdot 10^{-10}$ m^3
Inlet-Outlet	$11.4 \cdot 10^{-10}$ m^3	$11.1 \cdot 10^{-10}$ m^3	$25.0 \cdot 10^{-10}$ m^3
Outlet	$5.2 \cdot 10^{-10}$ m^3	$26.7 \cdot 10^{-10}$ m^3	$44.0 \cdot 10^{-10}$ m^3
Outlet-Inlet	$1.5 \cdot 10^{-10}$ m^3	$2.0 \cdot 10^{-10}$ m^3	$4.5 \cdot 10^{-10}$ m^3

Table 30. Average values concerning wear volume experimentally obtained by coordinate measurements.

Measurement uncertainty about wear volumes has been computed by using *MPE$_E$* index and considering the error propagation. Measurement uncertainty is equal to $3.0 \cdot 10^{-10}$ m^3 with a confidence level of 95%. Taking as a reference Table 30, it can be noted that the wear volume values concerning the Inlet and Outlet-Inlet regions have the same order of magnitude of the measurement uncertainty for the three types of pressure rings and for the Outlet region in the nitriding steel pressure ring as well. On the one hand, in the Inlet region the contact force has low intensity (3 N, see Table 29) leading to small wear volume values; on the other hand, in the Outlet-Inlet region, a high contact force acts (853 N, see Table 29) but for a short sliding length (704 km), leading again to small wear volume values. Eventually, the measurement uncertainty analysis provides reliable and robust results for the Inlet-Outlet and Outlet regions, where high wear volume occurs, while the results concerning the Inlet and Outlet-Inlet regions have to be considered as an order of magnitude.
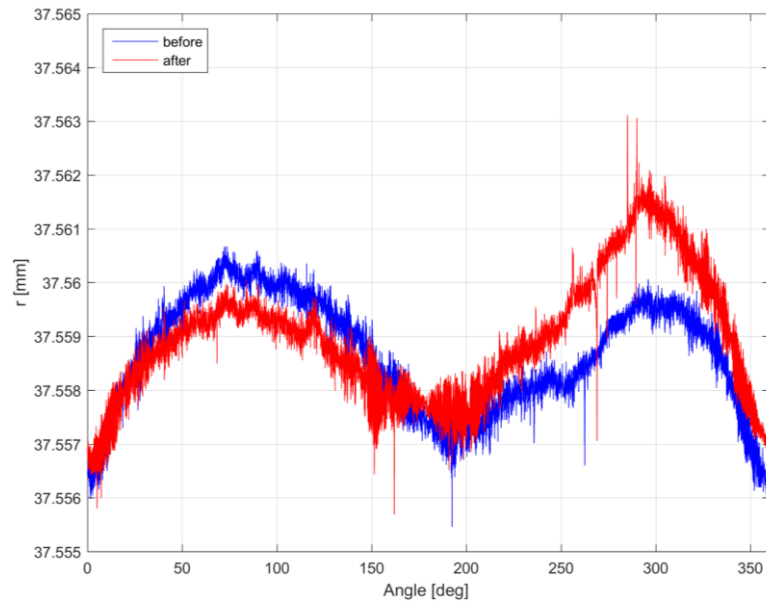
Figure 208. Internal profile of the nitriding steel pressure ring in reference section L1 before and after the pump operational test.
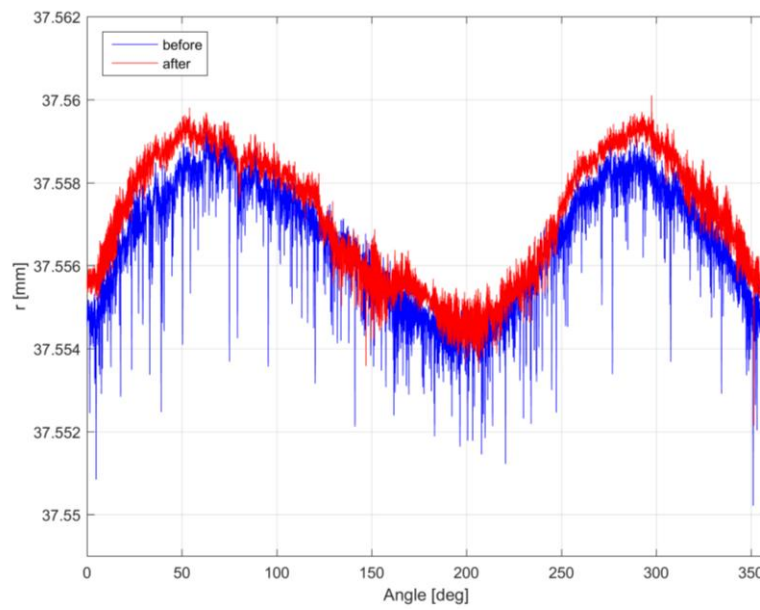
Figure 209. Profile comparison for TiN coated pressure ring in section L1 before and after the pump operational test.
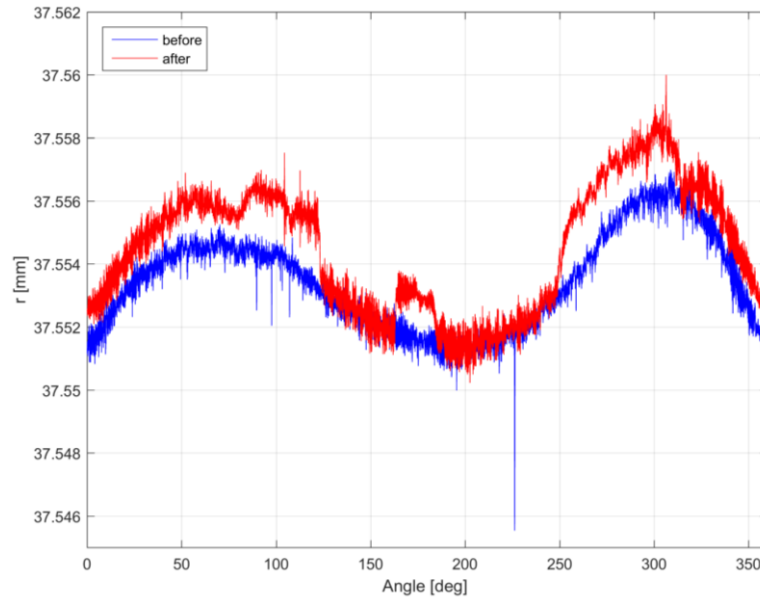
Figure 210. Profile comparison for DLC coated pressure ring in section L1 before and after the pump operational test.

The results concerning the sliding distances for each region are collected in Table 29. The sliding distance of the Inlet region is 30.37% of the total distance, for Inlet-Outlet it is 14.64%, for the Outlet region it is 45.48% and for the Outlet-Inlet region it is 7.51%.

Eventually, the results of the Vickers hardness tests are collected in Table 31.

Material	Hardness
Nitriding steel pressure ring	$1.2 \cdot 10^{10}$ N/m^2
TiN coated pressure ring	$2.3 \cdot 10^{10}$ N/m^2
DLC coated pressure ring	$1.3 \cdot 10^{10}$ N/m^2
High speed steel vane	$8.35 \cdot 10^{9}$ N/m^2

Table 31. Vickers hardness concerning the different material types being studied.

The values of the wear coefficients for pressure rings have been calculated using the above data (see Table 29-Table 31). The results are shown in Table 32, where the lubrication regime for each value is reported as well (see also Table 27). A few comments can be drawn. The pressure ring with DLC coating has the higher values of wear

coefficient for each region of sliding circumference leading to a boundary lubrication regime. The nitriding steel pressure ring has the lower wear coefficients: in the Inlet-Outlet, Outlet and Outlet-Inlet regions the wear coefficients assume values correlated to elasto-hydrodynamic lubrication (EHD) and boundary lubrication. In the Inlet-Outlet region, with the TiN-coated pressure ring, the elasto-hydrodynamic lubrication regime does not establish; this evidence can be justified by the high hardness of the surface, which admits lower deformation than the other coating treatments. In fact, taking as a reference the Archard's equation, in the Inlet-Outlet region, the wear volumes for nitriding steel and TiN-coated pressure rings are similar (see Table 29), the contact force and the sliding distance are the same, while the material hardness are different: $1.2 \cdot 10^{10}$ N/m^2 for the nitriding steel and $2.3 \cdot 10^{10}$ N/m^2 for the TiN coating. Therefore, the generalized wear coefficients become different and boundary lubrication is established for the TiN-coated pressure ring. The generalized wear coefficients for the Outlet-Inlet and Inlet regions have to be considered as an order of magnitude due to the high measurement uncertainty in the wear values (see Table 30). However, the identified lubrication regimes foresee in the different regions (see Table 32) remain the same when the measurement uncertainty is accounted in the calculation.

Material / Region	Nitriding steel (0.4÷0.6mm)	TiN coated (3μm)	DLC coated (3μm)
Inlet	$3.5 \cdot 10^{-7}$ (Boundary)	$1.8 \cdot 10^{-6}$ (Boundary)	$1.3 \cdot 10^{-6}$ (Boundary)
Inlet-Outlet	$6.6 \cdot 10^{-9}$ (Boundary-EHL)	$1.3 \cdot 10^{-8}$ (Boundary)	$1.4 \cdot 10^{-8}$ (Boundary)
Outlet	$7.1 \cdot 10^{-9}$ (Boundary-EHL)	$6.9 \cdot 10^{-8}$ (Boundary)	$6.5 \cdot 10^{-8}$ (Boundary)
Outlet-Inlet	$3.4 \cdot 10^{-9}$ (Boundary-EHL)	$7.5 \cdot 10^{-9}$ (Boundary-EHL)	$1.1 \cdot 10^{-8}$ (Boundary)

Table 32. Generalized wear coefficients K for pressure ring internal surfaces.

Concerning the wear coefficient of the vane for the three types of pressure ring being tested, they are collected in Table 33. Furthermore, Table 33 collects the average values of the wear coefficient for the

entire pressure ring and not specified for each region. They are obtained by using Eq(34) in the Archard's equation. The wear coefficient concerning the vane indicates that the lubrication regime in the nitriding steel pressure ring is intermediate between boundary lubrication and elasto-hydrodynamic lubrication. For the other two types, the lubrication regime nears the boundary lubrication. Although the numerical values of the averaged generalized wear coefficients regarding pressure ring and vane are different, they refer to the same type of lubrication regime, as detailed in the Table 33. Since the goal of this research is the estimation of the lubrication regime in vane pumps, the agreement in the results can be considered satisfactory.

Pressure ring material	Average K for the pressure ring	Average K for the vane
Nitriding steel	$7.2 \cdot 10^{-9}$ (Boundary-EHL)	$5.8 \cdot 10^{-9}$ (Boundary-EHL)
TiN coated pressure ring	$3.1 \cdot 10^{-8}$ (Boundary)	$1.4 \cdot 10^{-7}$ (Boundary)
DLC coated pressure ring	$2.9 \cdot 10^{-8}$ (Boundary)	$9.7 \cdot 10^{-9}$ (Boundary)

Table 33. Average of generalized wear coefficients K for the pressure ring internal surfaces and vanes.

The results concerning the EHD line contact model are hereafter described. They are calculated by using the numerical data collected in Table 28. In this research, experimental roughness data, used for the calculation of parameter λ, were available only for the nitriding steel pressure ring. Therefore, the application of the EHD model has been limited to this type of pressure ring. In particular, the roughness of the tip vane is 0.0001 mm and 0.00011 mm for the inner surface of the nitriding steel pressure ring. Roughness has been experimentally obtained at the end of the wear process.

In order to use the line contact model defined by Eq(39), one has to verify that the non-dimensional parameters lie in a typical range. For the line contact model, such ranges are 10^{-11}-10^{-10}, 1500-6000, 10^{-6}-10^{-5} for U, G, W, respectively [49]. Table 34 collects the values of the non-dimensional parameters calculated for the four circumferential regions of the pressure ring. It can be noted that the values always lie in the typical range reported above, except that in the Inlet region where the low level of contact force determines a low value of the non-dimensional load parameter. Therefore, the EHD line contact model

cannot be applied in such a region. Moreover, Table 34 collects the λ values in the three regions where the line contact model can be applied. The λ values range from 1.8 to 2.26. On the basis of the considerations outlined above, a lubrication condition between elasto-hydrodynamic and boundary is established as confirmed by the experimental results reported above.

Eventually, it has to be underlined that the value of R' is dominated by the curvature radius of the vane (R_A), which can vary during the pump test due to the increase of the wear process. Moreover, also the oil temperature, which strongly affects the viscosity value of Eq (36), can change during the pump test. On the contrary, the calculation of the minimum film thickness in Eq. (36) and of the type of lubrication regime have been carried out considering constant values for oil temperature and reduced curvature radius. In order to take into account their variability, Figure 211 presents the influence of oil temperature T and vane tip radius R_A on the minimum film thickness h_0 for the line contact model. The response surface of the figure informs on the relevance of the oil temperature, with respect to the minimum film thickness, in particular at higher values of tip vane radius. Maintaining constant the vane tip radius, the minimum film thickness increases if the oil temperature decreases. Moreover, it is interesting to note that an increase of 100% of R_A with respect to its nominal value, determines an increase of λ (Eq(35), Eq(36)), which remains in the range between 1 and 3, leading to the same conclusions about the type of lubrication regime. Thus, the approximation of considering constant values for R_A and R_B can be considered acceptable.

Region	U	G	W	λ
Inlet	$2.60 \cdot 10^{-11}$	3896	$4.33 \cdot 10^{-8}$	/
Inlet-Outlet	$2.60 \cdot 10^{-11}$	3896	$2.18 \cdot 10^{-5}$	1.87
Outlet	$2.60 \cdot 10^{-11}$	3896	$2.99 \cdot 10^{-6}$	2.26
Outlet -Inlet	$2.60 \cdot 10^{-11}$	3896	$1.23 \cdot 10^{-5}$	1.80

Table 34. Values of the non-dimensional parameters and λ for the line contact model applied to the contact between nitriding steel pressure ring and vane.
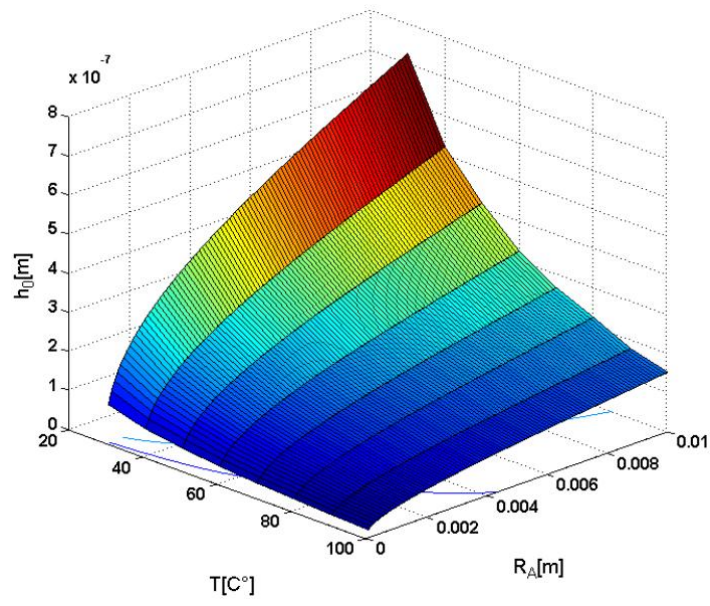
Figure 211. Response surface concerning lubricant temperature, minimum film thickness and vane radius for the line contact model.

CONCLUSIONS

This dissertation has presented different modelling methodologies for the simulation of pressure evolution in rotary positive displacement pumps. The aim of such models is the accurate dynamic simulation of the pressure evolution inside the pump and in the inlet and outlet ducts, as a function of rotor position in working conditions. The model results can be used for the analysis of the vibro-acoustic excitations, the optimization of the structural design, as well as the assessment of wear and lubrication regime. In this thesis, modelling methodologies based on a lumped parameter approach and an empirical approach have been developed and applied to practical cases of industrial interest, in order to assess their specific features. Moreover, model applications for estimating, improving and optimizing pump performances have been presented.

In the following, the **results about the features of the models developed according to the different approaches** are firstly outlined and compared; then the specific results about the performance analysis of the two kind of pumps - carried out by using the models - are summarized.

The **lumped parameter (LP) approach** has been developed and applied to an external gear pump for automotive applications: the fluid volume of the pump is divided in several control volumes and a system

of continuity equations is solved in Matlab environment. This model simulates the pressure evolution inside the control volumes for a complete turn of the pump. The benefits and the most remarkable results of this work are resumed below.

- The pressure distribution computed by the LP model makes it possible to characterize the main excitation sources of vibration and noise. This aspect makes the model a robust and suitable tool for designer in order to improve the NVH behaviour of the mechanical system.

- Since a specific Matlab code has been implemented for the gear drawing on the basis of the parameters of the cutting tools, every kind of external spur gear pump can be accounted.

- The modelling of the laminar flows was supported by a CFD simulation campaign which consolidates the validity of the laminar flow hypothesis done in the LP model development.

- The comparison of the experimental and numerical results, in terms of outlet pressure ripple and pump efficiency, proves the validity of the numerical model.

- The LP model makes it possible to investigate the effects due to the variation of design and functional parameters.

On the other hand, an **empirical approach** has been studied and adopted in the case of a family of variable displacement vane pumps. This approach is not based on physical laws but on the parametrization of experimental data concerning a family of pumps of different size, tested in different working conditions: correlation rules are established between the characteristics of the pressure evolution into the vane spaces and the rotor holes and the design and functional parameters, as number of vanes, distributor geometry, displacement, rotational speed,

and operational pressure. The pros and cons of the empirical model with respect to the LP approach can be summarized as follows.

- This model is an useful tool for designers in order to foresee the pressure trends, as it is fast to develop and easy to use.

- The empirical model is based on experimental data, thus it is able to foresee only the pressure distribution of a certain family of vane pumps.

- The correlation rules, implemented in a Matlab code, can be easily updated by using new experimental data.

- The validation analysis proves the reliability of the model, exhibiting high values of PGP index for several pumps.

Thus, both modelling approaches give reliable results, useful for the analysis of the vibro-acoustic excitations, the optimization of the structural design, as well as the assessment of wear and lubrication regime. It is worth noting that, on the one hand, the lumped parameter approach allows the simulation of the behaviour of pumps of different type and design and makes it possible to account for a wide range of modifications, to be considered for optimization purposes. On the other hand, empirical models are less flexible than lumped parameter models, as they are applicable only to a single family of pumps; however, they represent efficient tools for R&D in industrial environment, due to faster development time and more friendly use.

Concerning the **results of the sensitivity analysis, carried out on the external gear pumps by using the LP model**, the following conclusions can be outlined about the effects of some functional and design parameters.

- *Oil Temperature:* The sensitivity analysis about the oil temperature shows that lower temperature leads to higher pressure spikes within gear pockets during the pressurization phase, and it increases the pressure drops below the atmosphere pressure during the depressurization phase. Furthermore, the analysis shows that the higher the temperature, the higher the leakage flows as well as outlet pressure ripple. These aspects lead to the decreasing of the pump efficiency, as expected.

- *Gear Eccentricity:* This analysis pointed out how the radial clearances affect the pump efficiency. In fact, the configuration with high radial clearances leads to a dramatic reduction of the pump efficiency, due to the raising of the laminar tip flows in correspondence of the low pressure sealing line. This increase of the leakage flows delays the pressurization of the gear pockets but has no effect on the outlet pressure ripple.

- *Epsilon Groove Depth:* The epsilon groove depth acts on several aspects of the gear pump operation. For instance, the configuration with the deepest epsilon groove is characterized by the lowest efficiency and the highest amplitude of the outlet pressure ripple. Furthermore, the epsilon groove depth affects the pressurization phase and the pressure oscillations within the gear pockets, because tight axial clearances determine high pressure overshoots and high pressure oscillations within the gear pockets as well. Basically, this analysis demonstrates how much important the right choice of this parameter in order to reach the best compromise between volumetric efficiency and dynamic excitation.

- *Outlet Epsilon Groove Extension:* The extension of the outlet epsilon groove has a relevant effect on the pressurization phase: wider configurations produce more anticipated pressurization with sharper pressure spikes. It is interesting to underline how the groove extension affects the waveform of the outlet pressure ripple while keeping the pump efficiency constant.

Concerning the evaluation of the wear and lubrication regime between vane tips and stator ring in the variable displacement vane pump, an original method has been developed. It is based on Archard's wear model, which associates the wear coefficient to the contact forces given by the empirical model, the wear rate and the material hardness, experimentally measured. The results of the method have been then compared with the outcomes obtained from an EHD lubrication model in order to evaluate the film thickness and the lubrication regime. The most important concluding remarks are given below.

– The proposed methodology allows the identification of the lubrication regime, which occurs between vanes and pressure ring in high pressure variable displacement vane pumps by using wear measurements. Measurement uncertainty has been estimated. The identified lubrication regimes foreseen in the different regions remain the same when the measurement uncertainty is accounted in the calculation.

– The best performance in terms of wear and friction is given by the nitriding steel pressure ring, which allows the establishment of the partial elasto-hydrodynamic lubrication in the high load regions (Inlet-Outlet and Outlet-Inlet regions).

– Coated pressure rings (TiN, DLC) have been selected and used since they guarantee low friction in dry condition. In the vane-pressure ring contact, they have shown higher wear volumes than the nitriding steel, due to the different lubrication regime. The coated pressure rings suffer a greater wear due to the establishment of boundary lubrication. Moreover, the higher hardness of the coated pressure rings (TiN, DLC) caused a wide wear volume on the vanes not acceptable for costumers.

– The results experienced for the TiN coating pressure ring may be due to the high hardness of the coating and the high roughness of the surface.

– The results experienced for the DLC coating pressure ring may be due to the high percentage of graphite and the low cohesion between coating and base material.

– The EHD model used in this research states that a lubrication condition between elasto-hydrodynamic and boundary is established in the sliding contact between vanes and pressure ring in three of the four regions the pressure ring is divided. This is in agreement with the results of the proposed experimental method. In the Inlet region, the EHD model cannot be applied since the non-dimensional load parameter lies outside its typical range, due to the low level of normal contact force.

– Although these quantitative results concern a particular vane pump, the proposed methodology about the estimation of the lubrication regime in sliding contact has a general meaning from the qualitative point of view: it can be applied to a large variety of vane pumps and gives useful guidelines for similar applications.

BIBLIOGRAPHY

[1] Mucchi. E, D'Elia. G, Dalpiaz. G, " Simulation of the running in process in external gear pumps and experimental verification", *Meccanica* (2011), Volume 47: pp. 621-637.

[2] Mucchi. E; " Dynamic analysis of external gear pumps by means of non linear models and experimental techniques". *PHD Thesis* (2007), Engineering Department of University of Ferrara, Italy.

[3] Falfari. S, Pelloni. P., "Setup of a 1D Model for Simulating Dynamic Behaviour of External Gear Pumps," *SAE Technical Paper* 2007-01-4228, 2007, doi:10.4271/2007-01-4228.

[4] Mancò. S, Nervegna. N, "Simulation of an external gear pump and experimental verification". *JHPS. International Symposium on Fluid Power Tokio*, (1989).

[5] Zardin. B, "Modellazione Numerica e Caratterizzazione Sperimentale di Macchine e Componenti Oleodinamici.(2008), ALMA Mater Studiorum Bologna, Italy.

[6] Yuqiao. Z, Wai Lam. L, Thong-See. L, " CFD Simulation Of A Pump With Wankel Engine Geometry". *The 11th Asian International Conference on Fluid Machinery and Paper Number 10. The 3rd Fluid Power Technology Exhibition* November 21-23, 2011, IIT Madras, Chennai, India.

[7] Alekseev. D P, Guvernyuk. S V, Chyulunin. A U. Sheypak. A A, " "Calculation of characteristic gear pump based on two-dimensional

and three-dimensional simulation". *Mathematical and Computer Modeling for Systems and Machines* (2013).

[8] Ghazanfarian. J, Ghanbari. D, " Computational Fluid Dynamics Investigation of Turbulent Flow Inside a Rotary Double External Gear Pump", *Journal of Fluids Engineering* (2011), Volume 137: Paper No: FE-14-1077; doi: 10.1115/1.4028186.

[9] Del Campo. D, Castilla. R, Raush. G A, Gamez Montero. P J, Codina. E, "Numerical Analysis of External Gear Pumps Including Cavitation", *Journal of Fluids Engineering* (2013), Volume 137(8). doi: 10.1115/1.4007106.

[10] Wurtenberger. S H, "Simulation of Cavitating Flow in Vane Pumps" , EACC *3rd European CFD Automotive Conference* (2007), Frankfurt(Germany).

[11] Frosina. E, Senatore.A, Buono. D, Uncini Manganelli. M, Olivetti. M, "A Tridimensional CFD Analysis of the Oil Pump of an High Performance Motorbuke Engine", *Energy Procedia* (2014), Volume 45: pp. 938-948.

[12] Paladino. E E, De Lima. J A, Pessoa. P, Almeida. " Computational Three Dimensional Simulation Of The Flow Within Progressive Cavity Pumps", Proceedings of COBEM 2009 20th International Congress of Mechanical Engineering (2009). Gramado(Brasil).

[13] Mucchi. E, Dalpiaz. G, "Analysis of the evolution of pressure forces in variable displacement vane pumps using different approaches", *Proceedings of the ASME 2013 International Design Engineering Technical Conferences & Computers and Information in Engineering Conference IDETC/CIE 2013*, (2013) August 4-7, Portland, Oregon, USA.

[14] Mucchi. E, Cremonini. G, Delvecchio. S, Dalpiaz. G, "On the Pressure Ripple Measurement in Variable Displacement Vane Pumps", *J. Fluids Eng.* (2013) 135(9), , DOI: 10.1115/1.4024110

[15] Mucchi. E, Agazzi. A, D'Elia. G, Dalpiaz. G, "On the wear and lubrication regime in variable displacement vane pumps", *Wear* (2013).Vol. 306, pp. 36-46, doi: 10.1016/j.wear.2013.06.025

[16]   Nelik. L , "Centrifugal & Rotary Pumps: Fundamentals With Applications".(1999), pp.4.

[17]   Frith RH, Scott W; "Comparison of an external gear pump wear model with test data". *Wear* (1996), Volume196: pp. 64–71.

[18]   Frith RH, Scott W; "Wear in external gear pumps". *Wear* (1994), Volume 172: pp121–126.

[19]   Gellrich R, Kunz A, Beckmann G, Broszeit E; "Theoretical and practical aspects of the wear of vane pumps. Part A. Adaptation of a model for predictive wear calculation". *Wear* (1995), Volume 181–183:862–867.

[20]   Vacca.A, Guidetti.M; "Modelling and experimental validation of external spur gear machines for fluid power applications". *Simulation Modelling Practice and Theory* (2011), Volume19(9): pp 2017-2031.

[21]   P. Casoli, A. Vacca, G.L. Berta, A numerical model for the simulation of flow in hydraulic external gear machines, in: PTMC2006 Power Transmission and Motion Control, 13–15 September 2006, University of Bath (GB), 2006.

[22]   Gopal. M ; "Control systems: principles and design". *2nd ed. Tata McGraw-Hill*, (2002). pp 159.

[23]   Nof. S Y, Wilhelm. W E, Jürgen Warnecke. H. "Industrial assembly". *Springer* (1997). pp 174.

[24]   Zhang. P; "Industrial Control Technology: A Handbook for Engineers and Researchers". *William Andrew, Inc.* (2008). pp 91.

[25]   Ohio Electric Motors. "Brushless DC Motors Used in Industrial Applications". *Ohio Electric Motors*. (2012).

[26]   Bussola, R., and Tiboni, M.,. "Parametrical identification for a complex mathematical model of indexing cam mechanisms by means of genetic algorithm". (1999) *Tech. rep., Eurogen, Jyv¨askyl¨a*, Finland, May 30 - June 3.

[27]   Meng. H.C, Ludema, K.C. "Wear models and predictive equations: their form and contents", *Wear* (1995). Volume 181-183, pp.443–457.

[28]   Toon. W. Z. Metallkunde. 29 (1937) pp. 196–198

[29]   Holm. R. "Electrical contacts " Electrical contact handbook, (1946) Gerbers, H., Stockholm.

[30]   Kruschov, M.M., Babichev, M.A.. "Friction and Wear in Machinery", (1941) pp. 89-96.

[31]   Kragelsky. I.V, Nepomnyaschy. E.F, Kharach. G.M, "The fatigue mechanism and a short methodology for the analytical evaluation of wear", Academy of Sciences Press. (1967) U.S.S.R, Moscow.

[32]   Barwell. F.T, "Wear of metals". *Wear* (1958) Volume 1 pp.317–322.

[33]   Rhee. S.K, "Wear equation for polymers sliding against metal surface", *Wear*. (1970), Volume16, pp.431-445.

[34]   Archard, J.F. "Contact and rubbing of flat surfaces". *Journal of Applied Physics,* (1953*)* Vol. **24**, pp. 981–988.

[35]   Gellrich. R, Kunz. A, Beckmann. G, Broszeit. E, "Theoretical and practical aspects of the wear of the vane pumps Part B. Analysis of wear behaviour in the Vickers vane pump test", *Wear*. (1995) Volume 181-183, pp.868–875.

[36]   Suh. N.P, "The delamination theory of wear", *Wear*. (1973) Volume 25, pp.111-124.

[37]   Hornbogen. E, "The role of fracture toughness in the wear of metals, *Wear*. (1975) Volume 33, pp.251-259.

[38]   Challen. J.M, Oxley. P.L.B, "An explanation of the different regimes of friction and wear using asperity deformation models", *Wear*. (1979) Volume 53, pp.229-243.

[39]   Evans. A.G, Marshall. D.B, "Fundamentals of friction and wear of material", D.A. Rigney (Eds), American Society for metals, (1981).

[40]   Flodin. A, Andersson. S, "Simulation of mild wear in spur gears", *Wear*. (1997) Volume 207, pp.16-23.

[41]   Young. A, Bair. S, "Experimental investigation of friction in entrapped elastohydrodynamic contacts", *Tribology International*. (2010) Volume 43, pp.1615–1619.

[42]   Jobault. I, Molimard. J, Lubrecht. A.A, Mansot. J.L, Vergne. P, "In situ pressure and film thickness measurements in rolling/sliding lubricated point contacts, Tribology Letters". (2003) Volume 15, pp.421–429.

[43]   Luo. J, Wen. S, Huang. P, "Thin film lubrication Part I: Study on the transition between EHL and thin film lubrication using a relative optical interference intensity technique", *Wear* (1995) Volume 194, pp.107-115.

[44]   Chaomleffel. J.P, Dalmaz. G, Vergne. P, "Experimental results and analytical film thickness predictions in EHD rolling point contacts", *Tribology International*. (2007) Volume 40, pp.1543-1552.

[45]   Jisheng. E, Gawne. D.T, "Influence of lubrication regime on the sliding wear behaviour of an alloy steel", *Wear*. (1997) Volume 211, pp.1-8.

[46]   Pylios. T, Shepherd,. Prediction of lubrication regimes in wrist implants with spherical bearing surfaces, Journal of Biomechanichs. 37 (2004) 405-411.

[47]   Peterson. M, Winer. W, ASME, Wear Control Handbook, (Eds), 1981.

[48]   Stachowiak. G.W, Batchelor. S.W, Engineering Tribology, third ed., Elsevier Butterworth-Heinemann, 2005.

[49]   Gohar. R, Elastohydrodynamics, second ed, Imperial College Press, London, 2001.

[50]   Dunaevsky. V, Generalized wear coefficient, , in: I Booser, E Richard (Eds.), Tribology data handbook, 1997, pp. 455-461.

[51]   Tellian. T.E, "On competing failure modes in rolling contact", *ASME transaction*. (1967) Volume 10, pp.418–439.

[52]   Hamrock. B.J., Dowson. D.,. "Isothermal and elastohydrodynamic lubrication of Point Contacts",(1977) Journal of lubrication Technology, Vol. 99, pp. 264–276.

[53]   In book, Hamrock, B.J., Dowson, D., "Ball bearing lubrication: the elastohydrodynamics of elliptical contacts". (1981) John Wiley & Sons.

[54]   Ichimura. I, Ando. I, "Mechanical properties of arc-evaporated CrN coatings": Part I – nanoindentation hardness and elastic modulus, *Surface and coatings technology*. (2001) Volume 145, pp.88-93.

[55] In book, Grubin, A.N., "Fundamentals of the Hydrodynamic Theory of lubrication of Heavi-ly Cylindrical Surfaces", (1949) Ketova, K. F., ed. Traslation of Russian book No. 30

[56] Fernandez Del Rincon. A., Dalpiaz. G., "A Model for the Elastodynamic Analysis of External Gear Pumps", *Proceedings of ISMA2002 - International Conference on Noise & Vibration Engineering*, 16-18 September, 2002 -: Katholieke Universiteit Leuven - Departement Werktuigkunde, ISBN 90-73802-79-2, pp. 1387-1396.

[57] Dalpiaz. G, Fernandez del Rincon. A., Mucchi. E, "Modeling Meshing Phenomena in Gear Pumps", *Proceedings of ISMA* September 20-22, 2004. Leuven, Belgium, Editors: P. Sas, B. van Hal, Heverlee (Belgium).

[58] Dalpiaz. G., Fernandez del Rincon. A., Mucchi. E., Rivola. A., "Model-Based Analysis of Dynamic Phenomena in Gear Pumps", *Proceedings of 5th International Conference on Acoustical and Vibratory Surveillance Methods and Diagnostic Techniques*, October 11-13, 2004. Senlis, (France).

[59] Mucchi. E, Dalpiaz. G, Pizzotti. S, 2007, "Updating an elastodynamic model of gear pumps to helical gear prototypes", *Proceedings of the ICSV14*, July 9-12, 2007. Cairns (Australia).

[60] Mucchi. E, Venturi. V, Dalpiaz. G, "A hybrid LP/FE model for the dynamic analysis of external gear pump", *Proceedings of the International Mechanical Engineering Congress & Expositions IMECE2007*, November 11-16, 2007. Seattle, Washington, USA.

[61] Mucchi. E, Dalpiaz. G, Fernàndez del Rincòn. A, "Elasto-dynamic analysis of a gear pump. Part I: pressure distribution and gear eccentricity", *Mechanical Systems and Signal Processing*, Vol. 24, No. 7, pp. 2160-2179, 2010, ISSN: 0888-3270, doi:10.1016/j.ymssp.2010.02.003.

[62] Mucchi. E, Dalpiaz. G, Rivola. A, "Elasto-dynamic analysis of a gear pump. Part II: meshing phenomena and simulation results", *Mechanical Systems and Signal Processing*, Vol. 24, No. 7, pp. 2180-2197, 2010, ISSN: 0888-3270, doi:10.1016/j.ymssp.2010.02.004;

(anche pubblicato in Preprints del Dipartimento di Ingegneria di Ferrara, Pubbl. n°177, Aprile 2010).

[63]   Mucchi. E , Dalpiaz. G. "Numerical vibro-acoustic analysis of gear pumps for automotive applications", *Proceedings of ISMA2012*, September 17-19, 2012, Leuven (Belgium).

[64]   Mucchi. E, Dalpiaz. G. "An assessed model for the vibro-acoustic analysis of gear pumps", *Proceedings of the ASME 2013 International Design Engineering Technical Conferences & Computers and Information in Engineering Conference IDETC/CIE 2013*, August 4-7, 2013, Portland, Oregon, (USA).

[65]   Mucchi. E, Rivola. A, Dalpiaz. G. "Modelling dynamic behaviour and noise generation in gear pumps: Procedure and validation", *Applied Acoustics* 77 (2014) 99-111, DOI: 10.1016/j.apacoust.2013.10.007.

[66]   Tosi. G, Mucchi. E , D'Ippolito. E, Dalpiaz. G (2015). "Dynamic behavior of pumps: an efficient approach for fast robust design optimization", *Meccanica*, Vol. 50 (8) (August 2015), ISSN: 0025-6455 (Print) 1572-9648 (Online), DOI: 10.1007/s11012-015-0142-z (published online 11 March 2015).

[67]   Vassena. A, Vacca. A, "Design optimization of the sliding elements of external gear machines", in: 6th FPNI–PhD Symposium, 2010, West Lafayette (IN), USA.

[68]   Zardin. B, Paltrinieri F, Borghi M, et al. "About the prediction of pressure variation in the inter-teeth volumes of external gear pumps". In: 3rd FPNI-PhD *Symposium on Fluid Power*, Terrassa, Spain, 2004.

[69]   Mancò S and Nervegna N. "Pressure transients in an external gear hydraulic pump". *In: 2nd JHPS International Symposium on Fluid Power*, Tokio, Japan, 1993.

[70]   Arakere. N.G, Nataraj. C. "Numerical simulation of nonlinear spur gear dynamics". *In: ASME Design Engineering Technical Conferences*, Las Vegas, Nevada, USA, 1999.

[71]   Theodossiades. S, Natsiavas. S, "Non-linear dynamics of gear-pair systems with periodic stiffness and backlash". *Journal of Sound and Vibration* 2000; 229(2):287-310.

[72]   Theodossiades. S, Natsiavas. S, ”On geared rotordynamic systems with oil journal bearings”. *Journal of Sound and Vibration* 2001; 243(4):721-745.

[73]   Kahraman. A, Singh. R. ”Interactions between time-varying mesh stiffness and clearance nonlinearities in a geared system”. *Journal of Sound and Vibration* 1991; 146:135-156.

[74]   Childs. D, Moes. H and Van Leeuwen. H. ”Journal bearing impedance descriptions for rotordynamic applications”. *ASME Journal of Lubrication Technology* 1977; 99:198-210.

[75]   Van de Vorst .E L B, Fey. R H B, De Kraker. ,“A et al. Steady-state behavior of flexible rotordynamic systems with oil journal bearings.” *Nonlinear Dynamics* 1996; 11:295-313.

[76]   Kuang. H, Yang. T. ”An estimate of mesh stiffness and load sharing ratio of a spur gear pair”. *In: International Power Transmission and Gear Conference*, 1992; pp. 1–9.

[77]   Fernandez del Rincon. A, Viadero. F, Iglesias. M. et al. ”A model for the study of meshing stiffness in spur gear transmissions”. *Mechanism and Machine Theory* 2013; 61:30-58.

[78]   Chang L, Liu G, Wu L. ”A robust model for determining the mesh stiffness of cylindrical gears. Mechanism and Machine Theory” 2015; 87:93-114.

[79]   Bastani. Y, De Queiroz. M. ”A new analytic approximation for the hydrodynamic forces in finite-length journal bearings”. *ASME Journal of Tribology* 2010; 132:1-9.

[80]   Lahmar M, Haddad. A, Nicolas. D. ”An optimized short bearing theory for nonlinear dynamic analysis of turbulent journal bearings”. Eur. J. Mech. A/Solids 2000; 19:151–177.

[81]   Chasalevris. A, Sfyris. D. ”Evaluation of the finite journal bearing characteristics, using the exact analytical solution of the Reynolds equation”. Tribology International 2013; 57:216-234.

[82]   Borghi. M, Milani. M, Paltrinieri. F et al. ”Studying the axial balance of external gear pumps”- *SAE paper* 2005-01-3634, 2005.

[83]   Bidhendi. M, Foster. K, Taylor. R. ”Computer prediction of cyclic excitation sources for an external gear pump”. *Journal of Engineering Manufacture* 1985; 199(3):175-180.

[84] Takahashi. Y. "On the trapping of fluid between the teeth of the involute gear pump". *Trans. of the Japan Society of Mechanical Engineers* 1940; 3(6):6-10.

[85] Dhar. S, Vacca. A, "A novel CFD-axial motion coupled model for the axial balance of lateral bushings in external gear machines" Elsevier Simul. Model. Pract. Theory, 26 (2012), pp. 60–76.

[86] Hooke. C.J , Koc. E, "End plate balance in gear pumps" *Proceedings of the Institution of Mechanical Engineers*, 198B (1984), pp. 55–60.

[87] Zecchi. M, Vacca. A, Casoli. P, "Numerical analysis of the lubricating gap between bushes and gears in external spur gear machines", *in: Proc. ASME Symposium on Power Transmission and Motion Control*, 2010.

[88] Mucchi. E, Dalpiaz. G . "Elasto-dynamic analysis of a gear pump–Part III: Experimental validation procedure and model extension to helical gears", *Mechanical Systems and Signal Processing*, Vol. 50-51 (January 2015), pp. 174-192, DOI: 10.1016/j.ymssp.2014.05.048 (published online 30 June 2014).

[89] S. Dhar, A. Vacca. "A fluid structure interaction EHD model of the lubricating gaps in external gear machines: formulation and validation. Tribol. Int., 62 (2013), pp. 78–90.

[90] Schweiger. W, Scheofman. W, Vacca. A, "Gerotor pumps for automotive drivetrain applications: a multi domain simulation approach", in: SAE 2011 Commercial Vehicle Engineering Congress, September 13–14, 2011, Rosemont, IL, (USA).

[91] Singhal. A.K, Athavale.M.M, Li. H.Y, Jiang. Y, "Mathematical basis and validation of the full cavitation model" *ASME Trans. J. Fluids Eng.*, 124 (3) (2002), pp. 617–624.

[92] Zwart. P.J, Gerber. A.G, Belamri. T, "A two-phase flow model for predicting cavitation dynamics", in: *Proceedings of the Fifth International Conference on Multiphase Flow*, Yokohama, Japan, 2004.

[93] Schnerr. G.H, Sauer. J, "Physical and numerical modeling of unsteady cavitation dynamics", in: *Fourth International Conference on Multiphase Flow*, 2001, New Orleans, USA,.

[94]   Campo. D, Castilla. R, Raush. G.A, Gamez-Montero. P.J, Codina.
        E, "Numerical analysis of external gear pumps including
        cavitation". *ASME Trans. J. Fluids Eng.*, 134 (8) (2012), p. 081105.

[95]   Zhou. J, Vacca. A, Manhartsgruber. B, ,"A novel approach for the
        prediction of dynamic features of air release and absorption in
        hydraulic oils", *ASME Trans. J. Fluids Eng.*, 135 (9) (2013), p.
        091305.

[96]   Vacca. A, Klop.R, Ivantysynova. M, "A numerical approach for
        the evaluation of the effects of air release and vapour cavitation on
        effective flow rate of axial piston machines, Int. J. Fluid Power, 11
        (1) (2010), pp. 33–46.

[97]   Tillner. W, Fritsch. H, Kruft. R, Lehman. W, Masendorf. D.G,
        ,"The Avoidance of Cavitation Damage", MEP, London (1993).

[98]   Mucchi. E, Dalpiaz. G, Rivola. A, 2011, "Dynamic behavior of
        gear pumps: effect of variations in operational and design
        parameters", *Meccanica*: Volume 46, Issue 6 (2011), Page 1191-
        1212, ISSN: 0025-6455, doi: 10.1007/s11012-010-9376-y (published
        online 19 November 2010).

[99]   Casoli. P, Vacca. A, Franzoni. G, Guidetti. M, "Effects of some
        relevant design parameters on external gear pumps operating:
        numerical predictions and experimental investigations", in: *Proc.
        6IFK Internationales Fluidtechnisches Kolloquium*, 2008, Dresden,
        (Germany).

[100]   Idelchik I.E., Handbook of hydraulic resistance, 3rd Edition.

[101]   Dearne R., The fine art of gear pump selection and operation,
        World pumps, June 2001, 38-40.

[102]   The Mathworks, Matlab (PDF Manual), Version 2015rB, Release
        12.1,

Dottorati di ricerca

UNIVERSITÀ DEGLI STUDI DI FERRARA
· EX LABORE FRUCTUS ·

Il tuo indirizzo e-mail

gzzlsn@unife.it

Oggetto:

Dichiarazione di conformità della tesi di Dottorato

Io sottoscritto Dott. (Cognome e Nome)

Agazzi Alessandro

Nato a:

Ferrara

Provincia:

Ferrara

Il giorno:

24/09/1986

Avendo frequentato il Dottorato di Ricerca in:

Scienze dell'Ingegneria

Ciclo di Dottorato

27

Titolo della tesi:

Positive Displacement Pumps: Pressure Modelling for Performance Analysis

Titolo della tesi (traduzione):

Pompe Volumetriche: Modellazione della Pressione per l'Analisi delle Prestazioni

Tutore: Prof. (Cognome e Nome)

Dalpiaz Giorgio

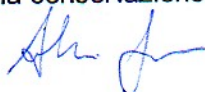Settore Scientifico Disciplinare (S.S.D.)

ING-IND/13

Parole chiave della tesi (max 10):

Modellazione, Pompe a ingranaggi esterni, Pompe a palette a cilindrata variabile, Distribuzione di pressione, Fluttuazioni di pressione, Validazione sperimentale, Analisi di sensibilità, Regime di lubrificazione. Modelling, External gear pumps, Variable displacement vane pumps, Pressure distribution, Pressure ripple, Experimental validation, Sensitivity analysis, Lubrication regime.

Consapevole, dichiara

CONSAPEVOLE: (1) del fatto che in caso di dichiarazioni mendaci, oltre alle sanzioni previste dal codice penale e dalle Leggi speciali per l'ipotesi di falsità in atti ed uso di atti falsi, decade fin dall'inizio e senza necessità di alcuna formalità dai benefici conseguenti al provvedimento emanato sulla base di tali dichiarazioni; (2) dell'obbligo per l'Università di provvedere al deposito di legge delle tesi di dottorato al fine di assicurarne la conservazione e la consultabilità da parte di terzi; (3) della

procedura adottata dall'Università di Ferrara ove si richiede che la tesi sia consegnata dal dottorando in 2 copie, di cui una in formato cartaceo e una in formato pdf non modificabile su idonei supporti (CD-ROM, DVD) secondo le istruzioni pubblicate sul sito : http://www.unife.it/studenti/dottorato alla voce ESAME FINALE – disposizioni e modulistica; (4) del fatto che l'Università, sulla base dei dati forniti, archivierà e renderà consultabile in rete il testo completo della tesi di dottorato di cui alla presente dichiarazione attraverso l'Archivio istituzionale ad accesso aperto "EPRINTS.unife.it" oltre che attraverso i Cataloghi delle Biblioteche Nazionali Centrali di Roma e Firenze. DICHIARO SOTTO LA MIA RESPONSABILITA': (1) che la copia della tesi depositata presso l'Università di Ferrara in formato cartaceo è del tutto identica a quella presentata in formato elettronico (CD-ROM, DVD), a quelle da inviare ai Commissari di esame finale e alla copia che produrrà in seduta d'esame finale. Di conseguenza va esclusa qualsiasi responsabilità dell'Ateneo stesso per quanto riguarda eventuali errori, imprecisioni o omissioni nei contenuti della tesi; (2) di prendere atto che la tesi in formato cartaceo è l'unica alla quale farà riferimento l'Università per rilasciare, a mia richiesta, la dichiarazione di conformità di eventuali copie. PER ACCETTAZIONE DI QUANTO SOPRA RIPORTATO

Dichiarazione per embargo

36 mesi
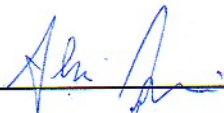
Richiesta motivata embargo

2. Tesi previo accordo con terze parti

Liberatoria consultazione dati Eprints

Consapevole del fatto che attraverso l'Archivio istituzionale ad accesso aperto "EPRINTS.unife.it" saranno comunque accessibili i metadati relativi alla tesi (titolo, autore, abstract, ecc.)
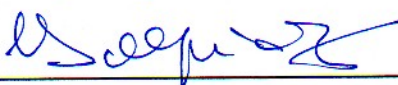
Firma del dottorando

Ferrara, li 21/03/2016 Firma del Dottorando _____

Firma del Tutore

Visto: Il Tutore Si approva Firma del Tutore _____

Università degli Studi di Ferrara

UFFICIO DOTTORATI DI RICERCA

AL MAGNIFICO RETTORE
UNIVERSITÀ DEGLI STUDI DI FERRARA
UFFICIO DOTTORATO
Via delle Scienze, n. 41/B – 44121 Ferrara

Richiesta di embargo della tesi di dottorato oltre i 12 mesi			
(da allegare alla dichiarazione di conformità)			
Nome e cognome del dottorando:	Alessandro Agazzi		
Corso di dottorato:	Scienze dell'Ingegneria		
Matricola:	073531		
Ciclo:	27		
E-mail per contatti:	gzzlsn@unife.it		
Anno dell'esame finale:	**2016**		
Nome e cognome del Tutore:	**Giorgio Dalpiaz**		
Titolo della tesi:			
Positive Displacement Pumps: Pressure Modelling for Performance Analysis			
Periodo di secretazione:	☐ **18 mesi**	☐ **24 mesi**	☑ **36 mesi**

Motivo dell'embargo:		
Tesi in corso di pubblicazione	☐	Tesi già sottoposte a un editore che non consenta l'accesso aperto prima dell'avvenuta pubblicazione
Motivi di pubblica sicurezza	☐	Quando la tesi può mettere a rischio la sicurezza pubblica e/o nazionale o per motivi di rispetto della Legge vigente
Tutela della proprietà intellettuale	☐	Diritto d'autore, brevetti, copyright etc.
Tesi previo accordo con terze parti	☑	Lavoro prodotto nell'ambito di un progetto di ricerca per il quale sia stato stipulato un accordo con un ente di ricerca esterno o con un ente finanziatore che preveda la divulgazione della tesi solo dopo il completamento dell'intero progetto di ricerca
Privacy	☐	Qualora la ricerca verta su una o più persone per cui si tema di violare il diritto alla riservatezza

Descrizione dettagliata della richiesta di secretazione:

Indicare in modo esaustivo le ragioni per cui si chiede l'embargo, citando gli estremi di eventuali accordi editoriali, contratti commerciali, progetti di ricerca etc. per cui sia richiesta la non accessibilità temporanea ai contenuti del lavoro

Parte del lavoro è stato prodotto nell'ambito di un contratto di ricerca commissionata dalla Società TRW Automotive Italia Srl – Divisione Automotive Pumps - condotto nel 2014.

Si chiede l'embargo in quanto il contratto prevede un impegno di riservatezza di 5 anni dal termine del contratto e nella dissertazione sono contenuti dati sensibili di prodotti industriali che rientrano in tale impegno di riservatezza.

Data:	15/03/2016
Firma del dottorando:	
Firma del Tutore:	

Come previsto dal Regolamento in materia di Dottorato di Ricerca dell'Università di Ferrara, che stabilisce l'obbligo di deposito delle tesi di Dottorato nell'archivio istituzionale d'Ateneo ad accesso aperto, la presente istanza dovrà essere sottoposta all'eventuale approvazione da parte del Consiglio di "IUSS Ferrara 1391"